The University Of Sheffield.

Access to Electronic Thesis

Author: Qian Wang

Thesis title: Advanced Optical and 3D Reconstruction Diagnostics for Combustion and Fluids Research

Qualification: PhD

Table of Contents

Declaration

No portion of the work referred to in the thesis has been submitted in support of an application for another degree or qualification of this or any other university or institute of learning.

Copyright

Publications

Journal paper:

1. Q. Wang, Y. Zhang, **High Speed Stereoscopic Shadowgraph Imaging and Its 3D Reconstruction**, *Measurement Science and Technology*, 22 (2011) 065302 (9pp).

2. Q. Wang, H. Gohari Darabkhani, L. Chen, Y. Zhang, **Vortex Dynamics and Structures of Methane/air Jet Diffusion Flames with Air Coflow**, *Experimental Thermal and Fluid Science*, doi:10.1016/j.expthermflusci.2011.10. 006.

3. H. Gohari Darabkhani, Q. Wang, L. Chen, Y. Zhang, **Impact of Co-flow Air on Buoyant Diffusion Flames Flicker**, *Energy Conversion and Management*, 52 (2011), 2996-3003;

4. H.W. Huang, Q. Wang, Y. Zhang, M. Zhu, H.J. Tang, **Characterization of External Acoustic Excitation on Diffusion Flames Using Digital Colour Image Processing**, *Fuel* , 2011, in press;

5. Q. Wang, H.W. Huang, Y. Zhang, H.J. Tang, M. Zhu, **Nonlinear Response of Buoyant Diffusion Flame under Acoustic Excitation**, *Fuel*, 2011, under review;

6. Q. Wang, Y. Zhang, **Spark Characteristics Investigation of a Gas Turbine Igniter**, *Combustion Science and Technology*, 2011, under review;

7. Q. Wang, H.W. Huang, Y. Zhang, M. Zhu, H.J. Tang, **Visualisation of Diffusion Flame/Vortex Structure and Dynamics under Acoustic Excitation**, *Combustion Science and Technology*, 2011, under review;

8. Q. Wang, H.W. Huang, Y. Zhang, **Impinging Flame Ignition and Propagation Visualization Using Schlieren and Colour-enhanced Stereo Imaging Techniques**, *Fuel*, 2011, under review;

9. L. Chen, Q. Wang, Y. Zhang, **Flow Characterization of Diffusion Flame in a Standing Wave**, *Experiments in Fluids,* 2011, under review;

10. L. Chen, Q. Wang, Y. Zhang, **Flow Characterisation of Diffusion Flame under Non-resonant Acoustic Excitation**, *Experiments in Fluids,* 2011, under review.

Conference paper:

1. Q. Wang, HW Huang, Y. Zhang M. Zhu, HJ Tang, **3D Visualisation of Diffusion Flame Structure and Dynamics under Acoustic Excitation**, *23rd ICDERS Conference*, 2011, oral presentation;

2. Q. Wang, Y. Zhang, **High Speed Stereoscopic Shadowgraph and Its Digital 3D Reconstruction**, *23rd ICDERS Conference,* 2011, oral presentation.

Acknowledgements

The research work has been funded by The University of Sheffield, The University of Manchester and BP Alternative Energy International Ltd. The funding support is essential for the research activities and is gratefully acknowledged. The equipment loan from EPSRC is also acknowledged.

I would like to express my sincere appreciation to my supervisor, Prof. Yang Zhang, for his continuous guidance and encouragement during my research. I am extremely grateful for everything he taught me, in work and in life, for the past three years. I have benefited greatly from his outstanding knowledge in combustion field.

I must also thank Prof. Min Zhu, Dr. Kevin Hua-Wei Huang, Dr. Rong Wang (Zoe), Dr. Huimin Guo, Dr. Jizhao Li, Dr. Hamid Darabkhani, Mr. Liwei Chen, Mr. Hussain Saeed, Miss. Chloe McDaid, Mr. Haojie Tang, for their valuable guidance and comments on my research, especially at the meetings. Their suggestions helped my research project to be more complete and sound. It has been an honour and pleasure to work with them.

I deeply appreciate the support from my beloved family and dearest friends. The achievement of this dissertation is both theirs and mine.

Abstract

Imaging based optical diagnostics have played an important role in combustion and fluids studies. However, most imaging techniques are two dimensional. The increasing interest in accurate whole field measurement has heightened the need for developing three dimensional methods. Furthermore, many flows are inherently 3D in nature. One aim of this study is to develop an innovative 3D schlieren/shadowgraph system based on conventional schlieren/shadowgraph techniques. Furthermore, several research issues related to fluid mechanics and combustion are investigated using multi optical methods, including high speed direct/schlieren imaging, stereo imaging and 3D reconstruction and PIV techniques, etc.

Firstly, a stereoscopic shadowgraph system has been developed using two sets of conventional z-type schlieren configurations. The test volume is set at the intersection of two inclined converging beams formed by two pairs of parabolic mirrors. Two synchronised high speed cameras are used to record the shadowgraph image pairs simultaneously. A precisely etched metal mesh plate is used to calibrate the stereoscopic shadowgraph system. The fully developed MATLAB code is employed to obtain calibration parameters and 3D coordinates reconstruction. A crystal block with internal 3D images is acted as a static model for point reconstruction. The 3D coordinates obtained are in good agreement with the real dimensions. The technique has been subsequently applied to investigate the bursting dynamics of a bubble. The 3D curve reconstruction is also accomplished successfully. The stereoscopic shadowgraph technique has been shown to be an effective method for both 3D visualisation and quantitative measurement.

Secondly, the spark induced hot gas jet of a gas turbine combustor igniter has been investigated using optical methods with the combination of high speed schlieren and stereo imaging. A spherical shockwave and a hot gas jet are observed after spark initiation. The 3D velocity vectors of the flying off metal bits are calculated by a stereo imaging and reconstruction algorithm. It has been found that the amount and velocity distributions of the eroded metal bits are very different even at a fixed input

voltage to the igniter, which contrasts with the quite consistent hot gas jet development. The 3D structures of the interaction boundaries between hot gas and ambient air are reconstructed for the first time using stereoscopic shadowgraph technique.

Thirdly, the vortex dynamics and structures of methane-air diffusion flames are investigated under different co-flow conditions. The schlieren and PIV images show that the visible flame flickering is dominated by the dynamics of the external toroidal vortices outside. The co-flow air is observed to push the initiation point of toroidal vortices beyond the visible flame height and suppress flame flickering completely. The velocity vectors and vorticity contours at different air flow rates are presented and analysed. The shedding frequency of the toroidal vortex is found to be consistent with the result obtained from a photomultiplier. The investigation indicates that co-flow helps to depress flame instability by changing the vortex evolution.

Finally, a laminar diffusion flame is studied under external acoustic excitation at different frequencies (6 Hz-100 Hz). The flame structures and vortex evolutions are investigated using high-speed stereo/schlieren imaging and digital imaging processing techniques. The flame frequency shows obvious nonlinear response to both the excitation frequency and amplitude. Several typical nonlinear phenomena were observed and analysed, which may serve as proof for relevant numerical simulation.

List of Figures

List of Tables

Nomenclature

Symbol	Meaning
A	Camera intrinsic matrix
A_e	Amplitude of the acoustic excitation
C	Intersecting corner of the two inner mirrors
Ca	Capillary number
e	Base of the natural system of logarithms
f	Flame flickering frequency/vortex shedding frequency
f (Chapter 5)	Distance from O" to optical axis of the camera O
f_1, f_2	Frequency of signals
f_m	Dominant flame flickering frequency
f_e	Acoustic excitation frequency
h (Chapter 5)	Film thickness
h (Chapter 7)	IPTV height
$h_{\max}$	Maximum IPTV height
k	Arbitrary parameter
L	Extent along the optical axis
l, m, n	Distances in the camera optical system
l (Chapter 5)	Bubble diameter
m	A point in image plane
$\tilde{m}$	Augmentation of m vector by adding 1 as the last element
M	An object point in space
$\tilde{M}$	Augmentation of M vector by adding 1 as the last element

Symbol	Meaning
n	Number of positions of the calibration board
n	Refractive index
N	Buoyancy frequency
O	Real camera optical center
O"	Virtual camera optical center
P1 to P23	Points selected for 3D reconstruction
R	Radius
R,t (Chapter 2)	Camera extrinsic matrix
R_O	Right outer mirror
R_I	Right inner mirror
Re	Reynolds number
s	Arbitrary scale factor
$S(\gamma)$	Calculated function of γ
t	Time
U (Chapter 5)	Film retracting velocity
U (Chapter 7)	Air flow velocity
u,v	Cartesian/pixel coordinates in image plane
v_a	Velocity of air
v_f	Velocity of fuel
u_0, v_0	Cartesian/pixel coordinates of the image plane origin
V_a	Co-flow air velocity
V_f	Fuel velocity
Vx	Velocity along X coordinate

Symbol	Meaning
Vy	Velocity along y coordinate
Vz	Velocity along Z coordinate
w	Weight fraction
W_{max}	Maximum width of the flame bulge
We	Weber number
x (Chapter 2)	Mole fraction
x, y	Coordinates of X, Y axes
X, Y, Z	Cartesian coordinates in space
X, Y, Z	Refer to X, Y and Z axes
X_1, X_2	Amplitudes of signals
$x(t), x_1(t), x_2(t), y_n(t)$	Functions of signals
X, X_1, X_2, Y_n	Arbitrary amplitudes of signals
∂	Partial differential

Greek	Meaning
α	Scale factor for u
β	Scale factor for v
γ	Skew parameter of the two image axes
γ (Chapter 5)	Surface tension
δ (Chapter 3)	Discrepancy angle
δ	Standard deviation error
ε	Deflection angle
θ	Angle

θ_1	An angle of incidence
θ_2	An angle of refraction
λ (Chapter 2)	Air equivalence ratio
λ	Parameter of parabolic mirror
μ	Viscosity of the liquid
ρ	Density
ρ_0	Atmospheric density
ϕ	Fuel equivalence ratio
ϕ_n, ϕ_1, ϕ_2	Arbitrary initial phase angles of signals
$\omega, \omega_1, \omega_2$	Phase angles of signals

Abbreviation	**Meaning**
2D	Two Dimension/Dimensional
3D	Three Dimension/Dimensional
BOS	Background Oriented Schlieren
CCD	Charge Coupled Device
C-MOS	Complementary Metal Oxide Semiconductor
CT	Computed Tomography
DoF	Degrees of freedom
ECT	Electrical Capacitance Tomography
FFT	Fast Fourier Transform
et al	Et alii (and others)
fps	Frame per second

Abbreviation	Meaning
HFV	Holographic Flow Visualisation
HPIV	Holographic PIV
IPTV	Initiation Point of Toroidal Vortex
LIF	Laser-induced fluorescence
PIV	Partical Image Velocimetry
PMT	Photomultiplier
SPLIF	Stereoscopic Planar Laser-Induced Fluorescence
slpm	Standard litre per minute

Chapter 1 Introduction

1.1 Motivation

Human being have known and utilized flame and fire since ancient times. Today, the burning process is widely used on industrial applications. About 90% of the energy utilization is related to combustion, such as internal combustion engine, gas turbine engine, etc. Due to the important role of combustion plays in modern industry, many methods and models have been developed by researchers in order to understand the theories and behaviours of this complex phenomenon. Combustion is a rapidly developing area, which covers a wide range of topics from ignition, flame dynamics, flame quenching to chemical reaction mechanism. The development in combustion science contributes greatly to fuel efficiency improvement, alternative energy development and pollutant emission reduction.

Combustion diagnostics have provided tremendous information in experimental research, which is essential for physical understanding and numerical modelling

validation. Among all combustion diagnostic techniques, optical diagnosis plays an important role and receives increasing attention as it has apparent advantages such as being non-intrusive, intuitiveness and providing large data sets compared to single-point measurement from devices such as pressure or temperature transducers. More recently, optical methods, such as schlieren/shadowgraph, PIV and PLIF, have been widely used to visualise the combustion process both qualitatively and quantitatively. With the combination of optical visualisation, high speed imaging and image processing, the understanding of combustion characteristics can be increased. However, most of the optical techniques are two-dimensional (2D) based and the measurement of combustion flame dynamics in three-dimensional (3D) space is a relatively new concept. Many recent studies have focused on developing 3D diagnostics with some specific techniques, such as stereoscopic techniques(Nishimoto and Shirai, 1987, Ng and Zhang, 2003a), tomography (Waterfall et al., 2001, Atcheson et al., 2008) and visual hull (Laurentini, 1994). However, most studies have been devoted to direct imaging, while rather less attention has been paid to 3D measurement based on density gradients, which is the principle of schlieren and shadowgraph.

Each diagnostic technique has its own advantages and limitations. For example, high speed stereoscopic imaging is able to visualise the visible flame in three dimensions but is not able to obtain the information in the invisible part of the flame. Schlieren and shadowgraph are capable of visualising the invisible mixing process of hot gas/fuel/air of a flame clearly due to the density variations but they are mainly restricted to 2D views. 3D schlieren investigations have been attempted in the 1950s but they were abandoned due to the complex experimental setup and lack of

quantitative data analysis methodology at that period of time. Thus there is no effective way to get the 3D invisible hot gas structures, which is important for further understanding of the flame dynamics and structures. In order to overcome this shortcome, one aim of the present investigation is to design an innovative stereoscopic schlieren/shadowgraph system together with 3D digital reconstruction and analysis.

One single technique is obviously not able to supply all the information that is needed. The application of multi-diagnostics on the same phenomena is an inevitable trend in combustion/fluids research. The other aim of this study is to gain physical insights into combustion/fluids phenomena using a combination of optical diagnostics.

1.2 Objectives

Based on the background information raised in the previous section, the main objectives of the research carried out in this study are listed below:

- To briefly review basic combustion theory and several widely used optical diagnostic methods.
- To explore an innovative stereoscopic schlieren/shadowgraph technique.
    - To study the projective geometry theory, camera calibration and reconstruction algorithms of stereo technique.

- To design the specific stereoscopic schlieren/shadowgraph experimental setup based on a conventional z-type schlieren system.

- To manufacture a calibration board with high accuracy and suitable for stereo shadowgraph/schlieren calibration process.

- To explore the calibration and reconstruction processes based on the stereoscopic shadowgraph/schlieren images.

- To apply the newly developed stereoscopic schlieren/shadowgraph technique on different test cases.

- To investigate the shockwave and hot gas kernel development of a surface-discharge spark igniter using high speed stereo, schlieren and stereoscopic schlieren diagnostics.

- To explore the vortex dynamics and structures of the co-flow diffusion flames using high speed schlieren imaging and PIV techniques.

- To study the flame dynamics of diffusion methane flames under external acoustic excitations using high speed stereo and schlieren imaging techniques.

1.3 Outline of the thesis

Chapter 1 includes the motivation and objectives of this study. The feasibility of establishing a novel technique of high speed stereoscopic schlieren/shadowgraph imaging has been proposed. How to apply multiple diagnostic methods in

combustion research to gain valuable physical insights is another main objective of this study. Thereafter, the objectives of the study are listed.

Chapter 2 presents a brief review of basic combustion theory and several optical diagnostics which are widely applied in combustion research, especially for schlieren/shadowgraph and stereo imaging techniques.

Chapter 3 introduces background theories and main algorithms of stereo technique based on a stereo adapter, including camera calibration and 3D reconstruction.

Chapter 4 demonstrates the experimental setup of the novel stereoscopic schlieren/shadowgraph method and its 3D reconstruction procedure.

Chapter 5 demonstrates examples of the application of stereoscopic shadowgraph technique, including point reconstruction and curve reconstruction. The application on a bubble bursting process is presented.

Chapter 6 investigates the electrical spark characteristics using high speed stereo, schlieren and stereoscopic shadowgraph imaging techniques.

Chapter 7 incorporates the high speed direct and schlieren imaging as well as PIV technique into studies of vortex dynamics and structures of co-flow methane diffusion flames.

Chapter 8 presents the application of high speed stereo and schlieren technique to the acoustic excited diffusion flames. The nonlinear responses of the flame under different excitations are analysed.

Chapter 9 summarises the work reported in this thesis and proposes possible future works for the study.

Chapter 2 Literature Review

2.1 Combustion background

2.1.1 Introduction

Combustion is a complex sequence of exothermic chemical reactions between a fuel and an oxidant, during which heat and light are emitted to form a flame, where the light flickers. During a chemical reaction, the atoms are exchanged between colliding molecules. In a typical chemical reaction, for example,

$$CH_4+2O_2=CO_2+2H_2O \quad (2\text{-}1)$$

the amount and category of the atoms (C, H and O) are conserved before and after the reaction, while the molecules are changed from (CH_4 and O_2) to (CO_2 and H_2O).

The reaction occurs usually in a small fraction of the available volume in the reaction zone or flame. Reaction may produce intermediates with chemiluminescence or

particles that glow and hence the colour of flames. Examples of combustion systems are shown in Table 2-1. The combustion systems can be categorised simply in terms of the preparation of the fuel/oxidiser mixture: premixed and non-premixed (Warnatz J., 2006). For any combustion process the equivalence ratio, ϕ, is defined based on the ratio between fuel and oxidizer. If the fuel and oxidizer consume each other completely, it is called stoichiometric (ϕ=1). If there is an excess of fuel, the system is fuel-rich (ϕ>1) and if there is an excess of oxidizer, it is fuel-lean (ϕ<1). The relevant subjects to this study of flame dynamics and instability will be discussed in the following sub-sections.

Table 2-1 Basic combustion types and examples (Warnatz J., 2006)

Fuel/Oxidizer Mixing	Fluid Motion	Examples
Premixed	Turbulent	-Spark-ignited gasoline engine -Gas turbine
	Laminar	-Flat flame -Bunsen flame
Non-premixed	Turbulent	-Pulverized coal combustion -Diesel engine -Aircraft turbine
	Laminar	-Candle -Wood fire

2.1.2 Premixed flames

One of the simple laboratory flames is the laminar premixed flame in which the fuel and oxidiser are mixed before chemistry begins. There is an un-burnt zone with reactants and a burnt zone with products. The motion of the flame front is a superposition of flame propagation and fluid convection. An example is a Bunsen burner in fuel lean conditions as shown in Figure 2-1. Turbulent flames can be

formed at higher speeds of flame propagation and fluid convection, which also have intensified heat and mass transfer. The combustion in a spark-ignited engine is a model of turbulent premixed flames. The fuel and air are mixed in the pipes before they enter the combustion chamber. Considering both improving the energy utilization and reducing exhaust pollution, a precise control of the combustion process in a spark-ignited engine is of significant importance. The premixing process makes the control of combustion process such as fuel equivalence ratio ϕ and the time of ignition, etc., to be easier, more precise and time responsive. An important issue in premixed combustion is that the mixing process can only be operated under low temperature. Once the fuel and air mixtures are in the region of flammability limits, high temperature or unexpected spark could cause uncontrollable combustion. Generally, the ranges of flammable mixtures are from ϕ=0.5 to ϕ=1.5 (Warnatz J., 2006). The safety risk must be taken into account in practical applications.

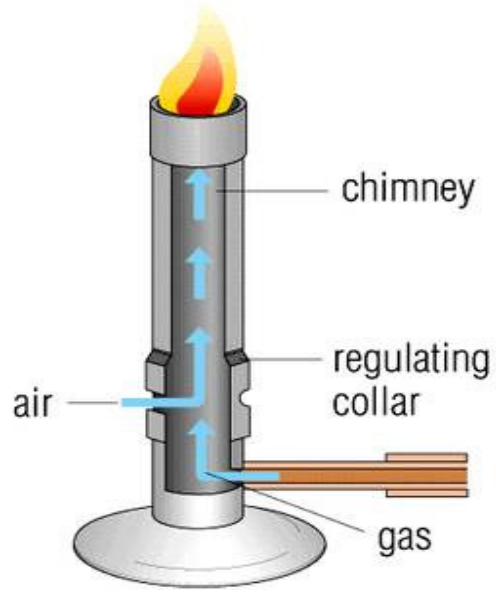

Figure 2-1 Schematic illustration of a classical Bunsen burner (RM, 2011)

2.1.3 Non-premixed/diffusion flames

Flames where the fuel and oxidiser are initially separate are called diffusion flames, which can be safer and form a very large percentage of combustion applications. In non-premixed flames, the fuel and oxidizer mixing and the combustion process occur at the same time. Unlike the propagation of a premixed flame, the diffusion flame is formed at the interface of the fuel and oxidiser streams (often air). Non-premixed flames are very often diffusion-controlled or mixing-controlled, rather than kinetically-controlled in premixed flames. In non-premixed flames, the fuel equivalence ratio covers from zero on the air side and to infinite on the fuel side. Thus, lean combustion takes place near the air side, rich combustion near the fuel side and stoichiometric in the middle. The flame front, which is recognised from the strongest luminosity, has the highest temperature and exists in stoichiometric combustion (Warnatz J., 2006).

As shown in Table 2-1, many types of industrial equipment (e.g. pulverized coal combustion, diesel engines and aircraft turbines, etc.) use the turbulent non-premixed combustion process, which is able to avoid the potential danger mentioned above for premixed cases. In most non-premixed flames, the combustion takes place in rich fuel conditions. Thus the flames have yellow luminance and rich soot exhaust because of the fuel rich chemical reaction in rich domains (Warnatz J., 2006). Laminar non-premixed flames are used as models to gain insight into the flame structure of more complicated turbulent non-premixed flames. There are two models that are widely used in laboratory to investigate laminar non-premixed flames: laminar counter-flow and non-premixed co-flow, which are illustrated in Figure 2-2.

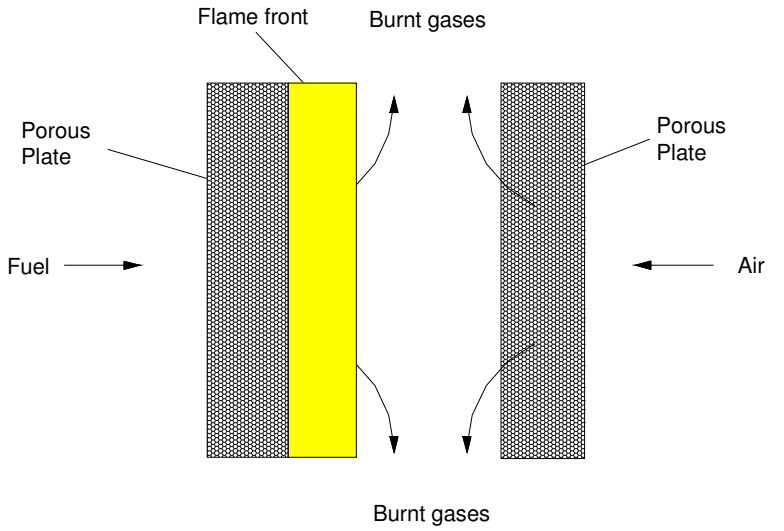

(a)

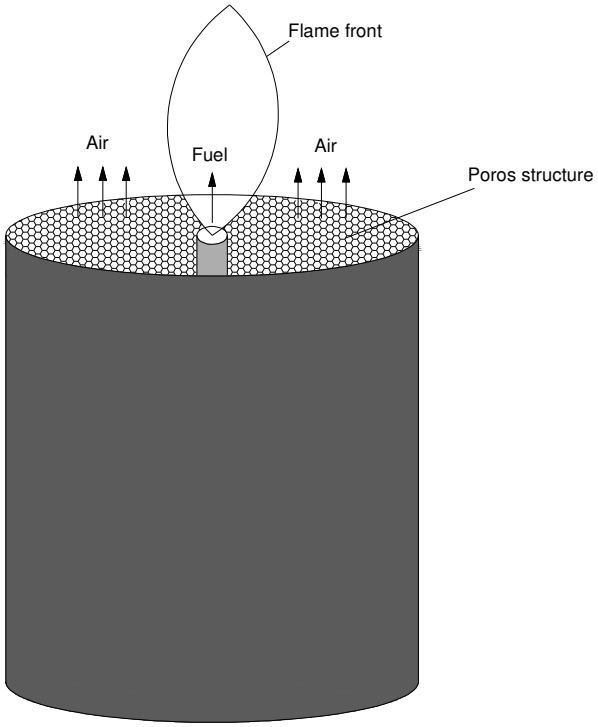

(b)

Figure 2-2 Schematic illustration of laminar non-premixed
(a) Counter-flow flame and (b) Co-flow flame

2.1.4 Laminar, turbulent and transitional flames

Combustion can take place in a laminar or a turbulent flow environment, including laminar-to-turbulent transitional flow conditions. Laminar flow, which is steady and smooth, occurs when a fluid flows in parallel layers, without lateral mixing between

the layers. On the contrary, turbulent flow is a regime characterised as chaotic, with adjacent layers continually disturbing each other. Vortical structures can usually be observed in turbulent flow field. Reynolds number (*Re*) is a widely used dimensionless parameter, which measures the relevant importance of inertial force to viscous force. The laminar flow is dominated by viscous force (low *Re*), while turbulent flow is inertial force dominated (high *Re*). In certain conditions, the flow field is partly laminar and partly turbulent, which forms a transition flow from laminar to turbulent taking place. The critical Reynolds number, at which transition occurs, is only approximate and depends on the smoothness of the surface and the level of disturbances in the flow.

The effect of Reynolds number on flame dynamics is more complex than in non-reacting flow. The flame behaviours can be affected by both fuel flow conditions and the chemical reaction process induced buoyancy forces. Although the Reynolds number at a certain reference point in the flow field, e.g. jet nozzle exit, can be used to categorise different flow conditions, it is not able to represent the reacting flow properly. For example, a jet flame, which is laminar near the jet nozzle exit, can become fully turbulent downstream due to the combustion effects. The effects of Reynolds number on a jet flame is illustrated in Figure 2-3. As shown in Figure 2-3 (a), a typical jet diffusion flame is formed by injecting a jet of fuel (usually pure) into ambient air. The measured flame length *Lf* are illustrated in Figure 2-3 (b) as a function of the Reynolds number (H.C.Hottel, 1949). It can be seen that a laminar flame is formed at relatively low *Re*. With the increasing of *Re*, the transition regime from laminar to turbulent can be observed. When the Reynolds number is high enough, the flow becomes turbulent completely. With further increasing *Re*, a lifted

flame can be established, with the flame detaching from the nozzle exit. The flame can be finally blown-off at a critical high *Re*.

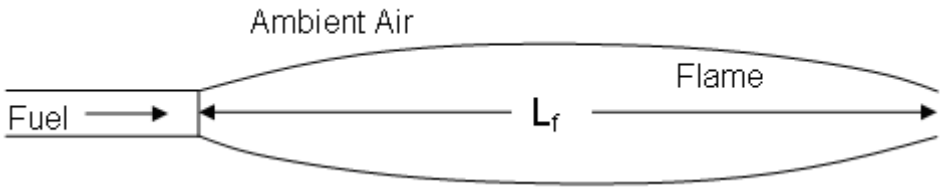

(a)

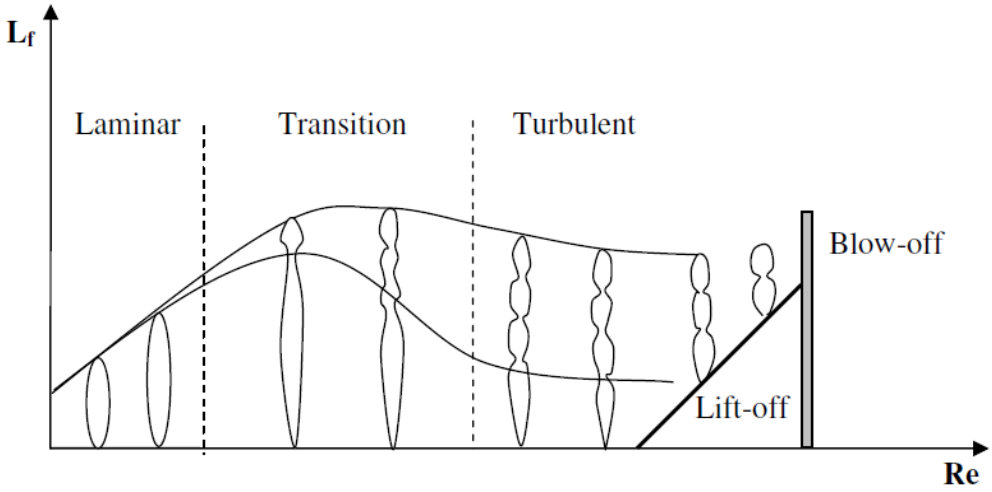

(b)

Figure 2-3 (a) Jet flame configuration; (b) Jet flame length Lf as a function of the jet Reynolds number (H.C.Hottel, 1949)

2.2 Optical experimental methods in fundamental combustion research

Observational science in experiments has been identified by Leonardo da Vinci (1452-1519) during the era of the Renaissance. He was the first to sketch or describe many typical phenomena in flow visualisation, such as formation of eddies, the profiles of free jets and the propagation of waves, etc. One of the most important

applications of flow visualisation was due to Osborne Reynolds, a prominent innovator in fluid dynamics, in 1883. He investigated the circumstances of the transition from laminar to turbulent flow by injecting a liquid dye into the water flowing through a long horizontal pipe. From these experiments came the famous dimensionless Reynolds number for dynamic similarity (Yang, 1989). Many other historically important discoveries in flow phenomena were similarly made through the application of rather simple methods of flow visualisation.

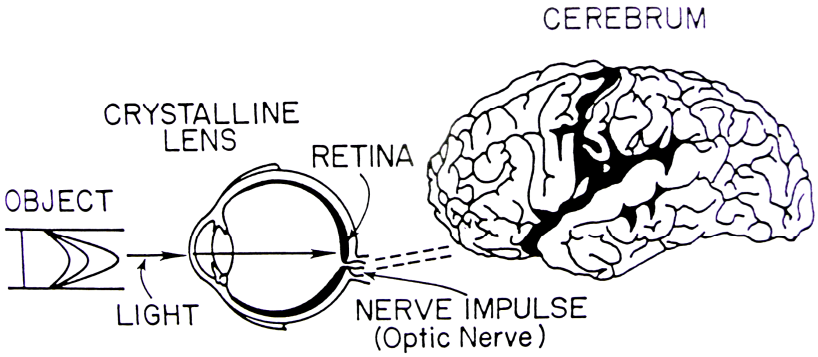

(a)

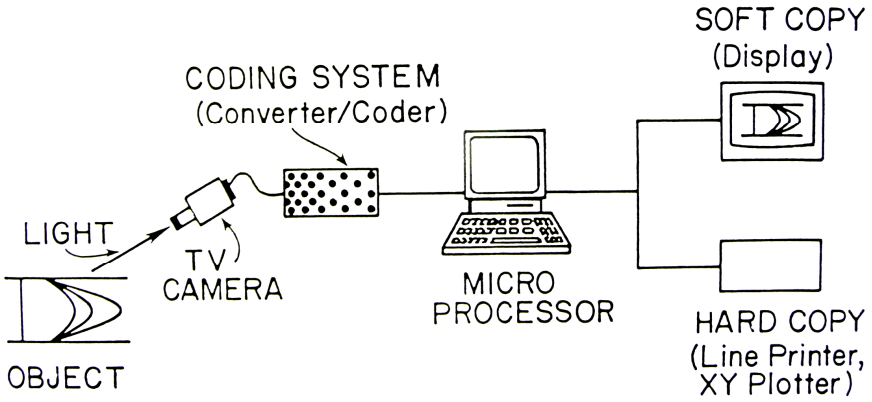

(b)

Figure 2-4 Digital image processing and its bionics (Yang, 1989)

In conventional flow visualisation techniques, different substances are introduced into the flow field as a contrast medium or as a tracer to distinguish the object to be observed. Most of the flow field needs to be illuminated in order to achieve high contrast and resolution in the final image. Recently, with the rapid development of computational techniques and computer colour graphics, the flow visualisation techniques have been advanced to a new era. Digital image processing and its bionics are depicted in Figure 2-4. The process of identifying an object with the human eye takes the steps shown in Figure 2-4 (a). Light rays reflected from the object pass through the crystalline lens to be focused on the retina. Light rays stimulate millions of optical receptors in the retina. The stimuli are then transmitted through the optic nerves to the cerebrum, where the image of the object is identified. Figure 2-4 (b) shows a schematic diagram of digital image processing. For automatic identification of an object, it is necessary to have a system similar to that of human vision. The image input is equivalent to that of the human eye. The input system consists of a television camera and a coding unit. This device functions to convert the image of an object into a signal. An electronic computer analyses, identifies and judges the signal. An output device is needed for judgment of the results of the image processed by the computer. Thus the computer and the output device together serve the functions of the cerebrum (Yang, 1989). Recently, the development of optical diagnostic techniques have been playing an essential role in flow visualisation, velocity measurements, temperature and pressure distribution, species concentration and so on. The visualisation results contribute to reveal important flow physics, guide intuition into complex phenomena, inspire formulation of theories, and provide valuable feedback for engineering designs.

Optical diagnostics have been applied to combustion research for decades. In combustion phenomena, besides visible light emission, the invisible flow pattern also affects the ignition and combustion processes greatly. Since combustion involves chemical reaction and high temperature, the nonintrusive optical diagnostics thus show the great advantages to obtain the whole field visualisation and measurement. One of the powerful flow visualisation tools is schlieren/shadowgragh technique, which is able to visualise 'invisible' density gradients and has been applied widely to study combustion, aerodynamics and fluid mechanics, etc. Recently, the laser-based diagnostics have been developed rapidly and widely applied in combustion research. The laser sheet makes it possible to resolve the flow field on a specific section plane in great detail. Particle Imaging Velocimetry (PIV) is served as a standard technique for velocity measurement by introducing tiny particles into the flow field. Planar Laser Induced Fluorescence (PLIF) is able to tackle the distribution of specific species through recognising the corresponding light emission. However, most of the diagnostics are two dimensional. Great efforts have been made in developing diagnostics such as stereo imaging and tomography that are able to obtain three-dimensional information. Great efforts are needed in exploring and developing three dimensional diagnostics. In the following section, several advanced optical diagnostic techniques that are widely applied to flame dynamics will be reviewed briefly, mainly concentrating on the ones that are photography and/or imaging based.

2.2.1 Schlieren & shadowgraph

2.2.1.1 Conventional schlieren and shadowgraph methods

Many problems of science and engineering involve substances that are colourless, transparent and non-luminous, so that their observation by direct visual or photographic methods is difficult. For example, the combustion outside the visible flame, the motion of air past models of aeroplane wings or compressor blades, problems of convection, the mixing of liquids or gases and the detection of faults in glass windows. In such cases, the phenomena that are of interest frequently involve changes of the refractive index across the field to be investigated, which can then be visualised or photographed by using optical methods that depend on the effects of the refractive index changes on the transmission of light. The most widely used techniques are schlieren and shadowgraph.

2.2.1.2 Schlieren

The schlieren technique remains to be one of the most powerful flow visualisation techniques due to its relatively easy implementation, high and variable sensitivity, low cost and the use of conventional light sources. The first schlieren system was invented by Robert Hook in the 17^{th} century and the schlieren technique was developed as a visualisation technique in the 19^{th} century by Toepler (Settles, 2002). Since then, the technique has been applied widely to tackle different kinds of problems in many research areas, such as combustion (Davis and Rerkshanandana, 1993, Strozzi et al., 2008), aerodynamics (Settles, 1985, Kleine and Gronig, 1991) and fluid mechanics (Fiedler et al., 1985, Peters et al., 1992), etc.

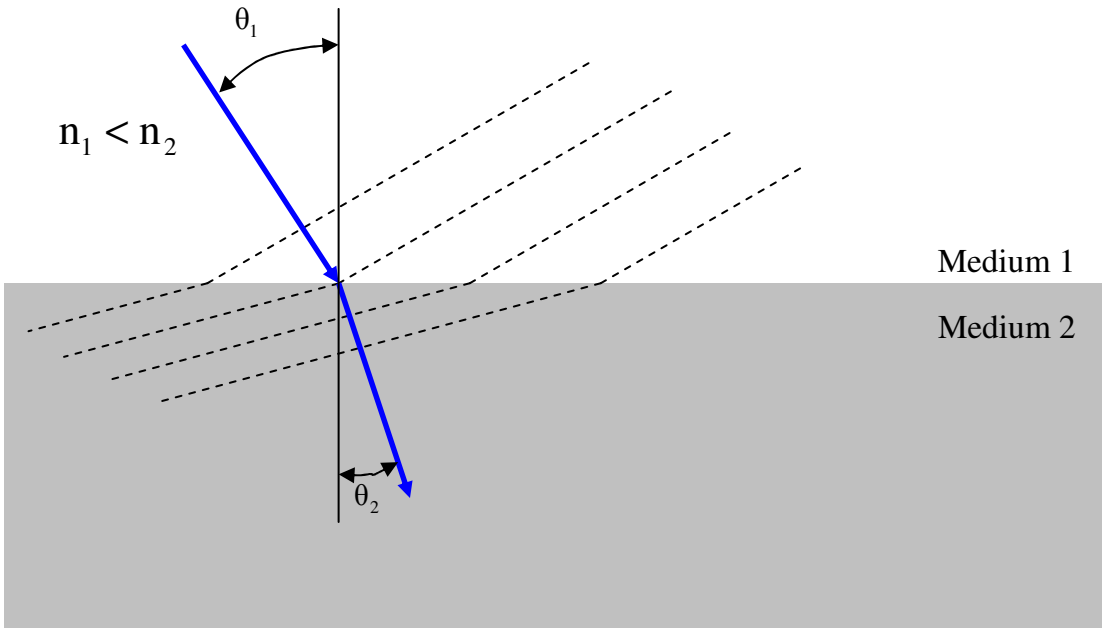

Figure 2-5 Schematic of light refraction theory

Schlieren techniques are based on the principle of light refraction. As shown in Figure 2-5, when light from medium 1 passes through medium 2, if the refractive index of the two mediums n_1 and n_2 are different, the light will change its original direction. According to Snell's law, the angle changed depends on the refractive index difference:

$$n_1 \sin\theta_1 = n_2 \sin\theta_2 \tag{2-2}$$

According to the Gladstone-Dale relation, for specific species the refractive index n has linear relationship with density ρ:

$$n - 1 = k\rho \tag{2-3}$$

Thus, the angle changed by refraction is proportional to the density differences of the mediums. The refractivity (n-1) of a gas, from Equation 2-8, depends on gas

thermodynamics parameters, such as temperature, pressure and composition, etc. The simple perfect-gas state equation ($p/\rho = RT$) can be applied in most cases. The estimated refractivity values of some common species and the refractive index ratios between them and standard air are listed in Table 2-2. The larger the density differences, the less sensitivity is required for the visualisation.

Table 2-2 Refractive index ratio between different species and air

Category	Refractive index	Refractive index ratio (n1/n2)
Air	1.000292	1.00000
Hydrogen	1.000132	0.99984
Helium	1.000035	0.99975
Nitrogen	1.000298	1.00001
Carbon dioxide	1.000449	1.00016
Methane	1.000444	1.00015
Carbon tetrachloride vapour	1.001768	1.00148
Shockwave front	1.0003~1.0015	1.00001~1.00121
Flame	1.0015~1.0021	1.00121~1.00181
Water	1.3	≈ 1.29962
Glass	> 1.3	> 1.29962

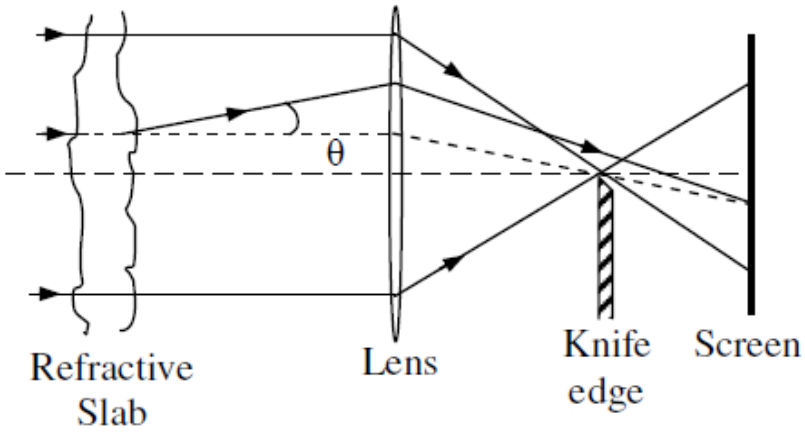

Figure 2-6 Schlieren imaging apparatus

A simple schlieren system is built up with two lenses, geometric optics, a knife-edge and a point light source as shown in Figure 2-6. The beam from a point source is collimated by a lens. A second lens refocuses the beam to an image of the point source. A knife-edge is placed on the focal point of the second lens. From there, the beam proceeds to a viewing screen where a real inverted image of the test area is formed. Since the knife edge removes part of the background rays, the background intensity loss applies evenly to the screen if the test area has uniform refractive indexes. However, if higher refractive index exists in the test area, then the light will be refracted downward and be blocked by the knife-edge. Thus, a darker spot will be formed at the screen. On the other hand, if the light is refracted upward, a brighter spot will be formed finally. Darker and brighter spots appearing on the screen correspond to positive and negative refractive index gradients in the direction normal to the knife-edge.

For a two dimensional x-y plane schlieren of extent L along the optical axis, the relationship is formed:

$$\varepsilon_x = \frac{L}{n_0}\frac{\partial n}{\partial x}, \quad \varepsilon_y = \frac{L}{n_0}\frac{\partial n}{\partial y} \tag{2-4}$$

where n_0 is the refractive index of the surrounding medium, ε_x and ε_y are the angle deflected on x and y directions.

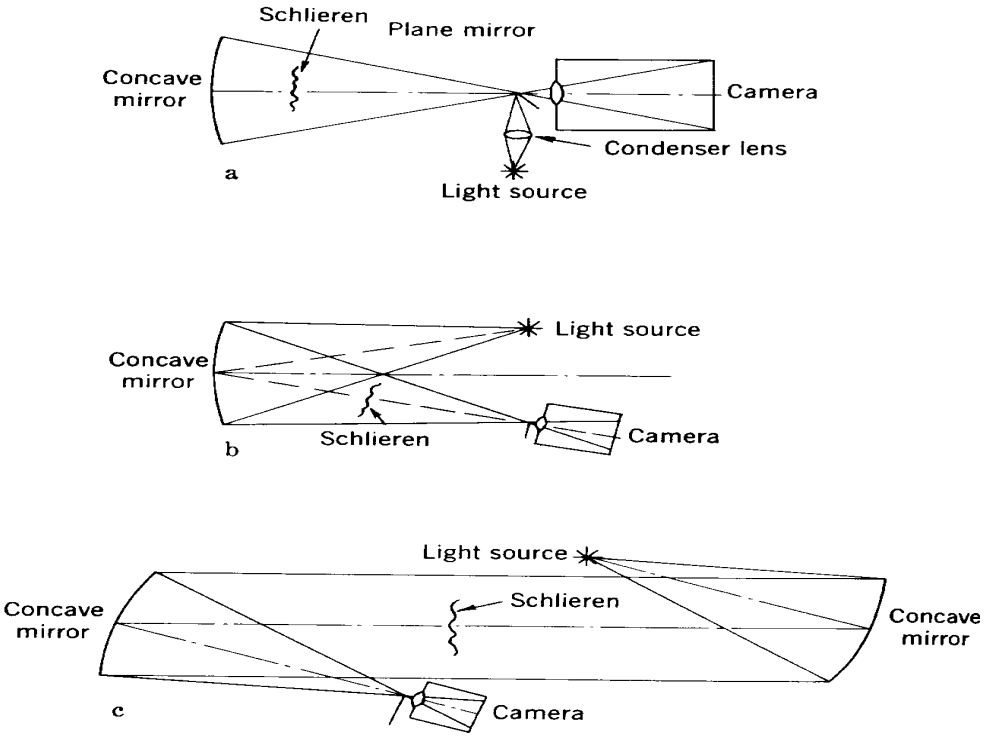

Figure 2-7 Three schlieren systems with concave mirrors (Settles, 2002)

Due to the partial spectrum that is cut off by the knife-edge, the chromatic aberration is a problem even for the sensitive achromatic lenses. Moreover, modern multi-element lenses require high internal quality, which makes the cost of lenses very high. For these reasons, most schlieren systems are built up on mirrors, which only need one polished surface and little internal quality (Settles, 2002). Three types of schlieren systems are schematically listed in Figure 2-7. The systems of Figure 2-7 (a) and (b) are single, spherical mirror, dual pass schlieren systems. The point light source is placed at the mirror focal length. The light returning from the mirror is

deflected to a cut off knife-edge and then recorded by a camera. Figure 2-7 (c) shows the most popular arrangement of z-type schlieren system with a pair of parabolic mirrors. The light source is placed on the focal point of the mirror on the right hand, while the knife-edge on the focal point of the left hand mirror. A parallel beam is formed between the two mirrors, which casuses the test area to be larger than that in the single mirror systems. With the convergence of the mirror on the left hand, the beam will be focused and partially cut off and arrive the camera at the end. Figure 2-8 shows an example of direct and schlieren photographs of a burner flame. The schlieren image is able to show more information of the invisible parts, which are absent on the direct image.

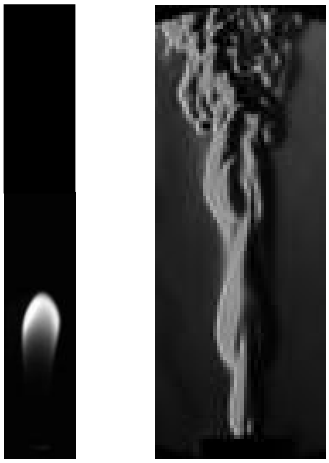

Figure 2-8 Direct and schlieren imaging of a burner flame

2.2.1.3 Shadowgraph

A type of parallel-light direct shadowgraph is shown in Figure 2-9. The shadowgraph system is so simple and only composed of a light source, a lens, a test object and a screen to observe the images. Without a test object in the beam, the parallel light will be projected on the screen evenly-illuminated. In Figure 2-9, the

test object is a soap bubble containing a heavier gas such as carbon dioxide, which has higher refractive index than the surrounding air. When the light beam passes through the bubble, the light will be focused according to Snell's law above. The strongest light refraction is at the boundary between the bubble and surrounding air. No refraction occurs outside the bubble or exactly at its center. A dark circular shadow marks the periphery of the bubble. Inside it follows a brighter illuminance ring, which is the light displaced from the dark circular shadow. If we define the deflection angle as ε, it is shown that deflection angle ε is proportional to refractive index gradients in the observation zone. Consequently it is the gradient of the deflection angle $\partial\varepsilon/\partial x$ or $\partial\varepsilon/\partial y$. Otherwise written, this is the second spatial derivative of the refractive index, $\partial^2 n/\partial^2 x$ or $\partial^2 n/\partial^2 y$. Though it is less sensitive than schlieren in general, particular circumstances can make it more sensitive. For example, $\partial^2 n/\partial^2 x$ can be much larger than $\partial n/\partial x$ in gas flows involving shockwaves or turbulence around supersonic projectiles (Settles, 2002). An example of shadowgraph of a bullet is shown in Figure 2-10, in which the shockwaves could be observed clearly.

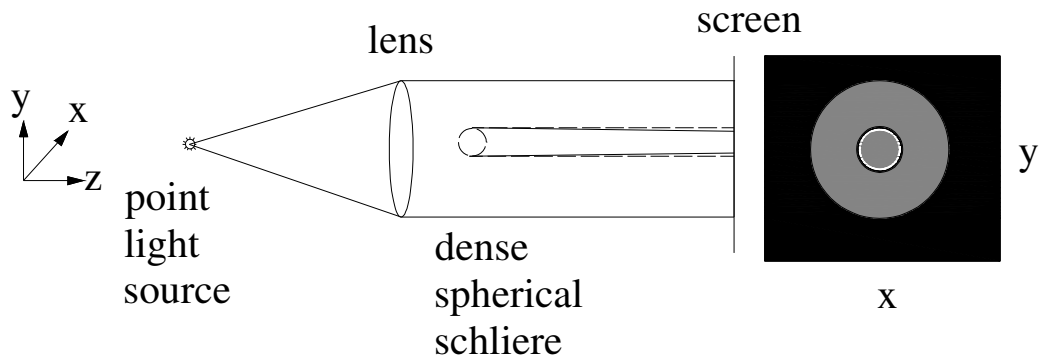

Figure 2-9 Diagram of parallel-light direct shadowgraph of a dense spherical object (Settles, 2002)

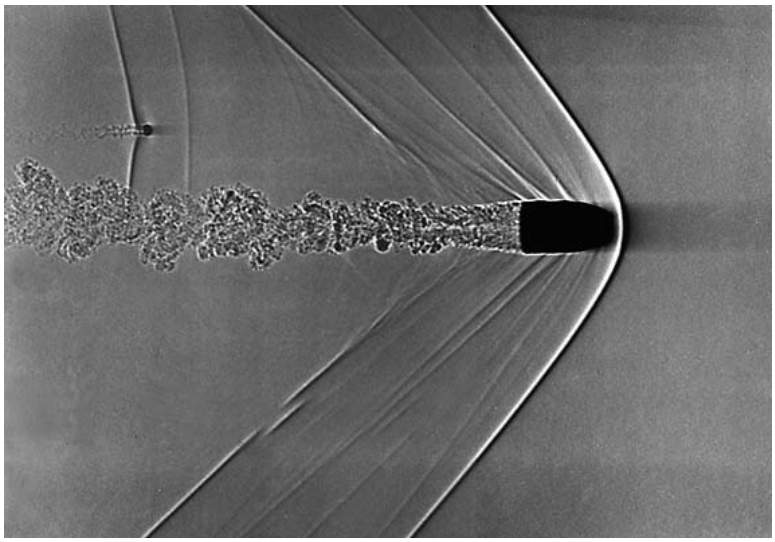

Figure 2-10 Shadowgraph of the bullet (Davidhazy, 2011)

2.2.1.4 Distinctions between schlieren and shadowgraph

Schlieren and shadowgraph are two techniques which are related closely and always developed together. However, there are several distinctions between them. First, a knife edge is required in schlieren methods to cut off part of the refracted light, where there is no such cutoff in shadowgraph. Second, the brightness difference in a schlieren image responds to the first spatial derivative of the refractive index in the test area, while shadowgraph responds to the second spatial derivative of the refractive index. Accordingly, the schlieren image displays the deflection angle while the shadowgraph displays the ray displacement resulting from the deflection. Generally, schlieren is more sensitive than shadowgraph and is able to show weaker disturbances. Therefore, when using schlieren systems, relative still air conditions is required in the lab as any gradients along the optical path will affect the final image. However shadowgraph is able to show the salient features of a subject without gross changes in illumination and is more sensitive in particular circumstances (Settles, 2002). Thus the application of schlieren or shadowgraph depends on the actual characteristics of the test field and the objective of the investigation.

2.2.1.5 Quantitative schlieren

Despite the schlieren technique being primarily conceived as a visualisation technique, it has also been used to obtain quantitative density data in flows. Since the temperature is related to the density field, schlieren can be used to obtain the temperature field as well. The use of schlieren systems to obtain direct measurements of the gradients in the flow has been discussed frequently. However, the measurement of density gradient has been limited to low accuracy (no better than 5%) for some fundamental reasons (Settles, 2002). The conventional schlieren methods measure the total angular deflection experienced by a light ray across the test section. Even for two dimensional flows, the light ray is not refracted continuously. For three dimensional flows, the density variations are more complicated along the optical path. The measurement of the total angular deflection of the rays can be attempted in several ways such as background-oriented schlieren, calibration schlieren, colour schlieren, interference schlieren, fringe schlieren and synthetic schlieren, which will be reviewed briefly in the following sections.

2.2.1.6 Background-oriented schlieren (BOS)

Background oriented schlieren (BOS) is a visualisation technique based on schlieren with some photographic background. It shares the similar principle of conventional schlieren on the points of light refracting passing through a region of density gradient and being sensitive to those components of the first spatial derivative of the index of refraction. With some mathematical techniques applied on following, the density fields of testing area can be measured by BOS both qualitatively and quantitatively.

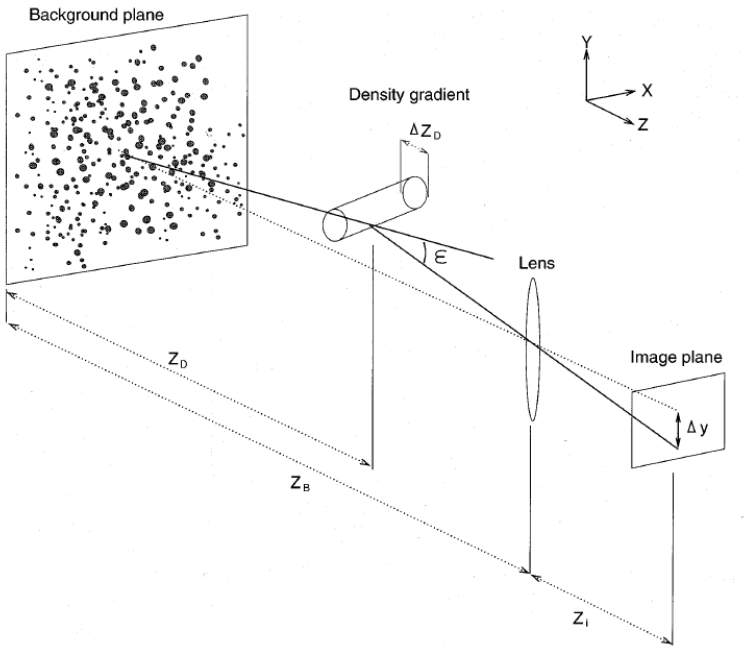

Figure 2-11 Sketch of BOS optical setup (Raffel *et al.*, 2000)

The optical setup of a typical BOS system is shown in Figure 2-10. A parallel beam is passing through the background plane and the inhomogeneous medium. The background pattern usually consists of tiny and randomly distributed dots. In order to get the density information through light distortion, two recordings have to be conducted. First, a reference image will be recorded as the background pattern observed through air at rest before the experiment. In the second step, an additional exposure through the flow under investigation leads to a displaced image of the background pattern. The density gradients of the tested flow induce distortion to the image of the background pattern. The resulting images of both exposures can then be evaluated by correlation methods (Raffel *et al.*, 2000). The existing evaluation cross-correlation algorithm, which have been developed and optimized e.g. for particle image velocimetry (PIV), tomography, can be used to determine background image displacements.

Comparing to conventional schlieren, BOS uses simple optics, high accuracy and could be applied on large scale, but with poorer resolution. The background oriented technique was successfully applied to study different types of flow (Raffel et al., 2000, Venkatakrishnan, 2005).

2.2.1.7 Calibration schlieren

The illumination in the schlieren image of the flow is related to the angular deflection of the light rays. The deflections may be determined by examining a photographic negative of the image with a densitometer. In order to compensate for the effects of diffraction, a number of 'standard schliere' with known or calculable angular deflections, such as a series of glass wedges, or bubbles of known size containing suitable gases, may be used (Schardin, 1942). The images of these 'standard schliere' on the photographic negative are then used as reference points when examining the negative with a densitometer. Nowadays, with the application of digital cameras, the intensity detection becomes easier and more accurate.

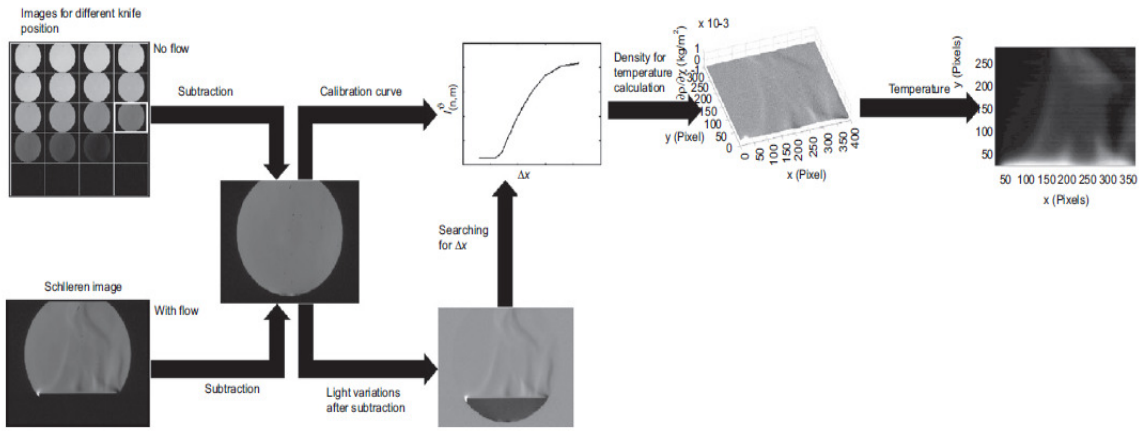

Figure 2-12 Flowchart for temperature fields calculation
(Alvarez-Herrera *et al.*, 2009)

An alternate schlieren technique used in the measurement of density fields has been proposed in (Alvarez-Herrera et al., 2009, Garg and Cattafesta Iii, 2001). It is based on a calibration procedure that relates light variation at the observation plane to transverse knife position. The calibration of this method consists of recording the light level in the schlieren image for several knife-edge positions ranging from no cutoff (maximum brightness) to full cutoff with no flow. The schlieren image at approximately half-cutoff under no flow conditions is chosen to be a reference image. It is found that the change of intensity in illumination from its undisturbed value is related to the flow induced density gradient. Thus, by subtracting the undisturbed intensity from the measured intensity distribution, the density deviation could be worked out. The flowchart of the method is illustrated in Figure 2-12.

2.2.1.8 Colour schlieren

In alternative ways of schlieren setup, the knife edge may be replaced by a colour band filter. Schardin (Schardin, 1942) proposed a cut-off mask composed of several colour filter strips arranged in a lattice (Kleine and Gronig, 1991) which codes the colours of the image directly to the magnitudes of light refractions in the schlieren object plane. Unfortunately, high sensitivity can only be obtained with narrow lattice strips which destroy the image resolution. Thus quantitative measurements using the lattice cut-off are practical only if the schlieren gradients are strong. Figure 2-13 gives an example of the contrast between conventional schlieren and colour schlieren images of the same flow pattern. The colour image is more informative indicating the light deflection comparing to the monochromic image.

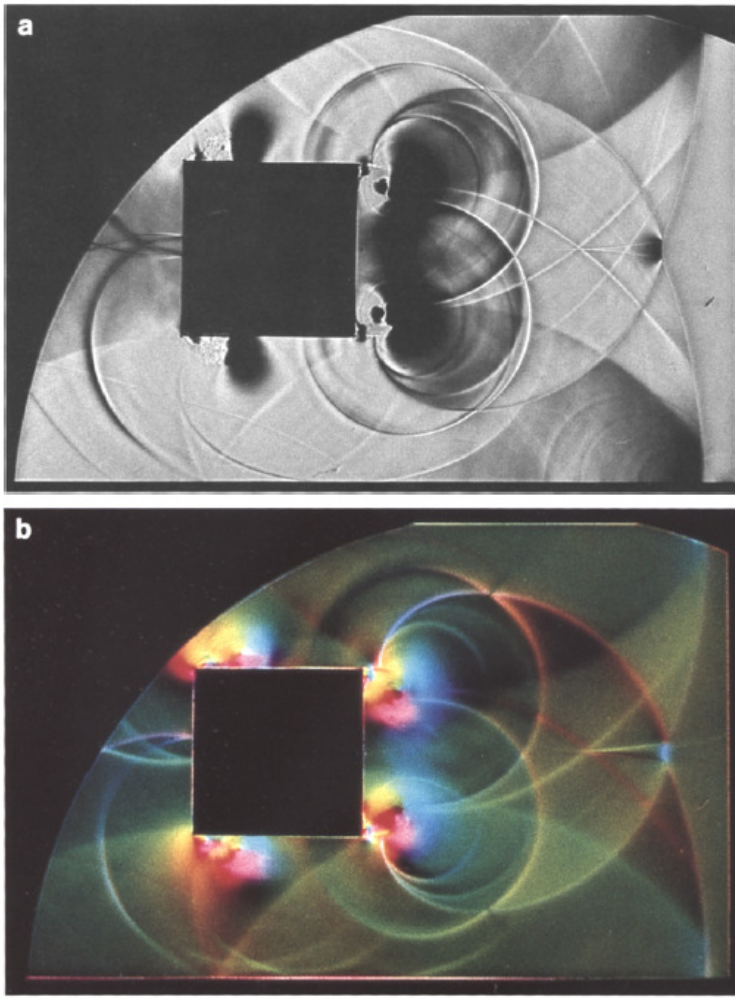

Figure 2-13 Interaction of a shockwave with a square cylinder
(a) black-and-white method; (b) colour schlieren method (Kleine and Gronig, 1991)

2.2.1.9 Interference schlieren

In Mach-Zehnder interferometer method, a light beam that has passed across the flow and a reference beam with different phases are observed to interfere. Similarly, some methods, for example, the phase-contrast method (Bouyer, 1956, Sauders, 1956) and the field-absorption method (Gayhart, 1949) have developed by using a different principle for producing the interference in schlieren images. A certain portion of the light passing through the object plane undergoes special treatment in the plane of the image of the light source. In the final image, this light can interfere

with the untreated light. Under certain conditions, the density in the flow can be determined from the interference pattern. Due to the complicated apparatus of this method, it is rarely used in practical experiments.

2.2.1.10 Fringe schlieren

The Moire fringe method (Burton, 1949, Mortensen, 1950, Sakai, 1990) represents an optically simpler alternative to the classical schlieren. As shown in Figure 2-14, a set of two accurately aligned masks replace the pair of parabolic mirrors and knife edge in the conventional schlieren setup introduced in section 2.2.1.2. A diffuse light source is instead of the point light source as well. One mask is positioned in front of the test section and the other one is on the other side. Due to camera parallax, the lines on the mask in front of the tank are more closely spaced than those to the rear of the tank. The two masks are positioned and scaled to have the same line spacing for a fixed observer and no perturbations to the flow. When the flow is initiated the density field is perturbed and the light rays reaching the observer originate from a different location on the mask behind the tank. This location may result in either more or less light reaching the observer depending on the magnitude and direction of $\nabla\rho'$ and the phase relationship between the two masks. Such a situation is illustrated in Figure 2-14, where the phasing of the lines on the two masks has been selected so as to increase the mean intensity (averaged over a region larger than the line spacing) for positive $\partial\rho'/\partial\uparrow$ (here $\uparrow$ represents the direction perpendicular to the lines). If there had been no phase difference between the two sets of lines then the image would have got darker for either sign of $\partial\rho'/\partial\uparrow$, while a 180º phase difference

would have started from a black image and got brighter for $\left|\partial\rho'/\partial\uparrow\right| > 0$ (Dalziel et al., 2000).

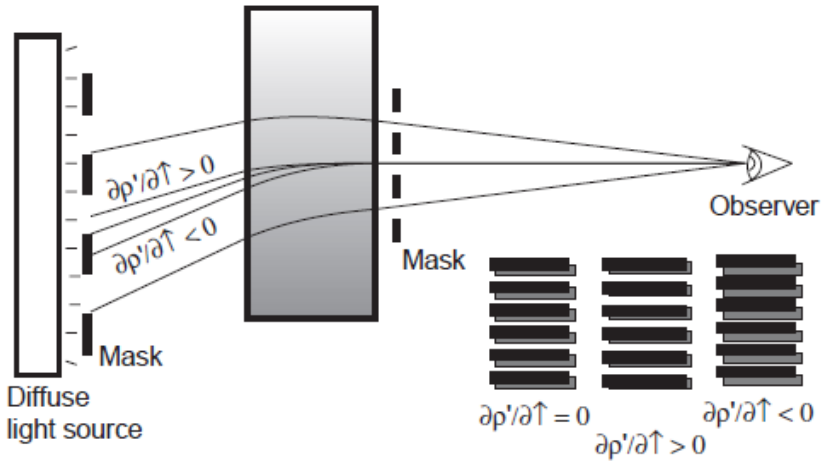

Figure 2-14 Sketch of optical arrangement for Sakai's Moire method (Dalziel et al., 2000)

The Moire fringe method is cheaper to implement and may be scaled up to cover larger domains more readily than classical schlieren. If carefully set-up, the Moire fringe method is capable of producing high quality visualisation with excellent spatial resolution. The main difficulty is that the alignment between the apparent positions of the two masks are critical and non-trivial, especially if light entering the camera is not approximately parallel or if the stratification is nonlinear so that the line spacings are not related by a simple scale factor (Dalziel et al., 2000).

2.2.1.11 Synthetic schlieren

Synthetic schlieren is a digital implementation of 'Moire fringe schlieren' that was recently developed for quantitative investigations of two-dimensional, linear

internal-wave fields (Dalziel et al., 2000, Sutherland BR, 1999), and qualitative visualisation of nonlinear internal waves (Peacock T. and Weidman, 2005).

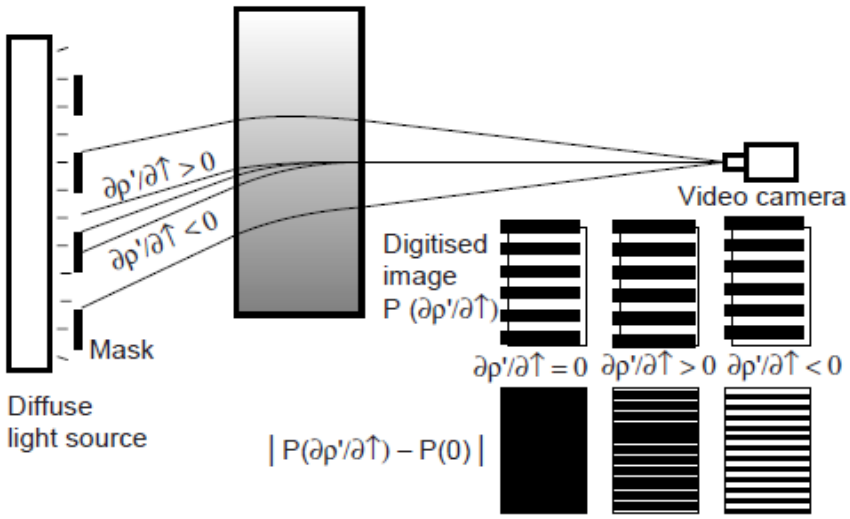

Figure 2-15 Sketch of optical arrangement for line-mode synthetic schlieren (Dalziel *et al.*, 2000)

Only one mask is required in synthetic schlieren and is placed between the light source and the tank, while a virtual mask is captured on digitized image from the appearance of the real mask in the absence of perturbations to the quiescent state. The method is more sensitive than shadowgraph. As shown in Figure 2-16, the thermal convection between a hand and the ambient air could be visualised through the synthetic schlieren images. By relating the digital images with and without flow perturbations, it is able to determine the apparent vertical displacement field quantitatively. An example has been given in Figure 2-17, in which a cylinder is oscillating in a uniformly stratified fluid with buoyancy frequency *N*.

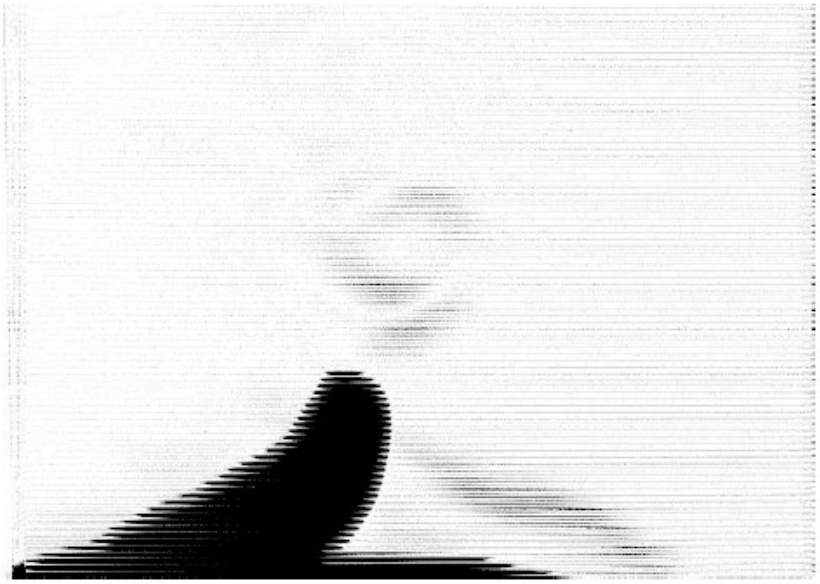

Figure 2-16 Thermal convection from a hand (Dalziel *et al.*, 2000)

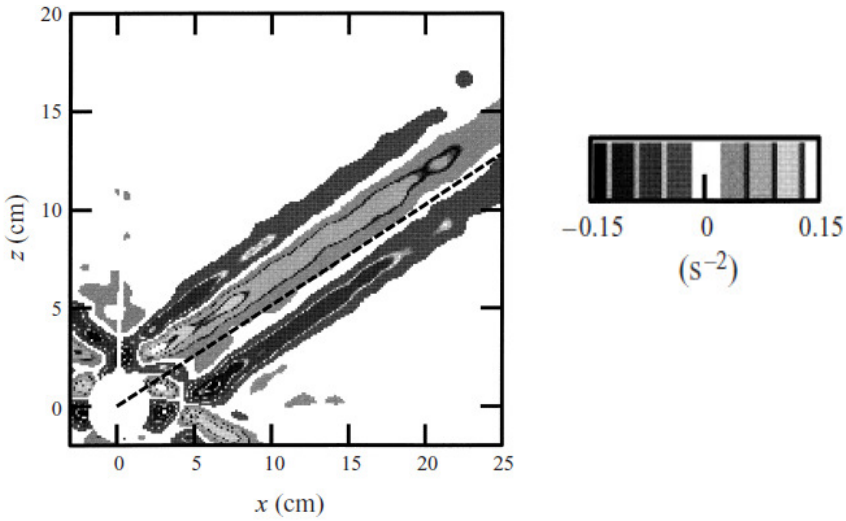

Figure 2-17 Quantitative result (N^2) deduced from vertical displacement field (Sutherland BR, 1999)

2.2.2 Stereoscopic imaging technique

Stereoscopy was first invented by Charles Wheatston in 1838 and was used for entertainment through the production of stereograms. In 1950s, David Brewster invented a box shaped viewer that was popular at the time. Nowadays, the stereoscopic technique is applied widely on 3D games, movies and televisions.

Stereoscopic, or 3D photography, works because our brain is capable of creating the illusion of depth by presenting a slightly different image to each eye. As shown in Figure 2-18, a pair of stereoscopic photographs are projected on the screen and each eye only receives one image with the help of specific glasses. The 3D illusion is created from the 2D images in our brain.

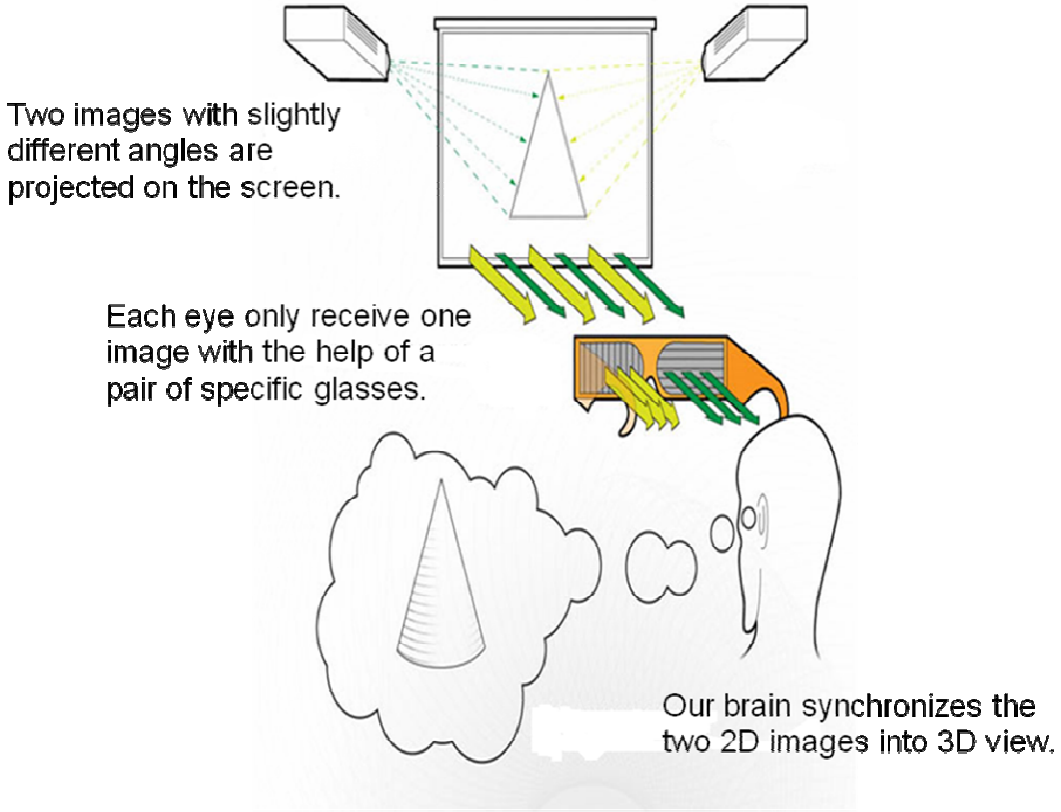

Figure 2-18 Illustration of stereoscopic images to create 3D view

The principle of stereoscopic imaging technique is to extract and recover the out-of-plane information of the subject from two views. Thus it is necessary to take two photographs for a stereoscopic image pair. Stereoscopic motion pictures can be produced through a variety of different methods.

A common means of obtaining stereo image pairs is to synchronize two cameras with same parameter setting. The two cameras are either fixed in lateral

displacement, known as the translation systems, or in angular displacement, known as the rotational systems (Prasad, 2000). The Fujifilm FinePix Real 3D W1 (or Fuji W1), launched in July 2009, is the first easily available and usable sterescopic digital camera. It has two lenses and an auto-stereoscopic display which directs pixels of the image towards the left and right eyes separately. Two-camera stereo systems have better spatial resolution and a comparative wider common FoV (Field of View) than stereo optical systems with one camera. However the specification of the two cameras are unavoidable different in some extent, such as focal length, zoom level and exposure time, etc. The differences will bring difficulty in establishing correspondences between the two images (Lee and Kweon, 2000) . In addition, the synchronization mechanism will also add extra time difference of the two images, which may affect the reconstruction accuracy greatly for the motion object.

Considering the disadvantages of two-camera systems, more researches and implementations have been turned to stereo optical systems of a single camera, with different external devices fixed in front of the camera lens. As shown in Figure 2-19, for static observed object, a single camera with a glass plate (Nishimoto and Shirai, 1987) or a mirror (Teoh and Zhang, 1984) rotating to two different positions was used to take two different images. Because of the time delay at taking two images, it is not suitable to investigate dynamic motion objects, such as flame. A mechanism that uses one camera to obtain two concurrent images for motion objects was proposed by Gosthasby and Gruver (Goshtasby and Gruver, 1993) . Two mirrors were placed symmetrically to the optical axis in front of the camera to form two virtual cameras in a rotational displacement. The disadvantage of this system is that it is complicated to align the mirrors with the camera. It may also be difficult to

handle and relocate the system during the observation for keeping the assembled parts in the exact position to each other. The similar-structure stereo systems were proposed with elliptical, hyperbolic and parabolic mirrors respectively (Nene and Nayar, 1998). Though the systems of non-planar reflecting surfaces provide wider FoVs than a planar mirror system, the calibration of the arrangement is much more complicated. Additionally non-planar mirrors need high precision production and cost a lot.

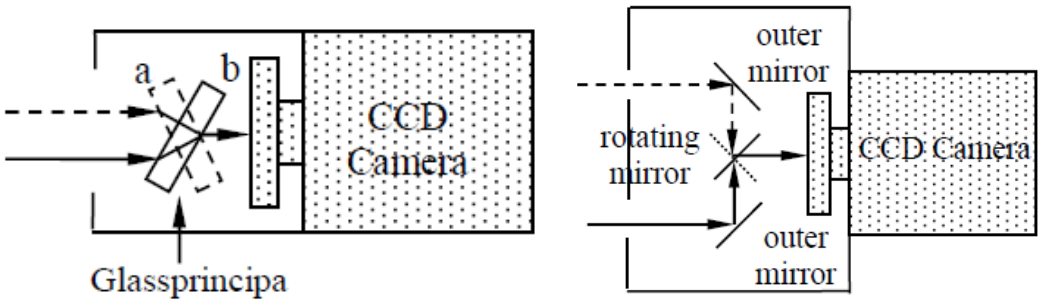

(a) (b)

Figure 2-19 Single camera stereo system with (a) glass plate (b) rotating mirror

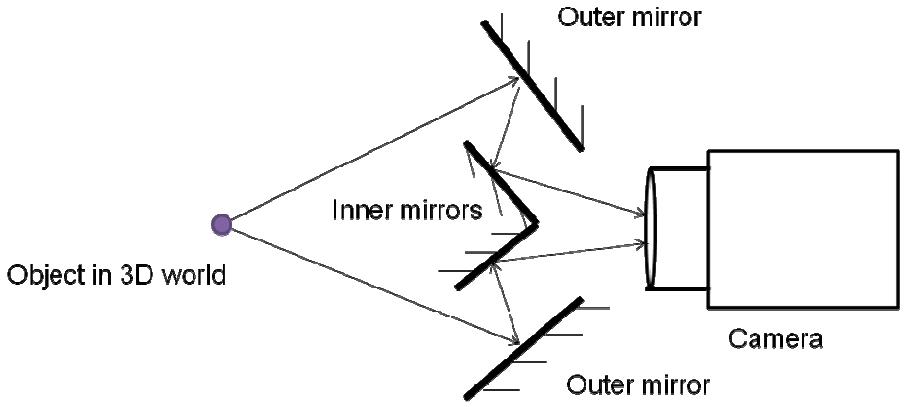

Figure 2-20 Schematic diagram of the four-mirror stereo adapter

The following two systems are both applicable to motion objects and easy to implement in practical experiments. A novel single-camera stereo system was designed using a biprism in front of the camera (Lee *et al.*, 1999). Rays from the object proceed through the biprism and are split into two optical paths by coming out

two side surfaces. Thus two views of the subject via different optical diffraction paths are imaged by the camera. However, serious colour aberration and distortion exists in the images of the biprism stereo system for nonlinear angle variation and different lateral displacement. A more mature single camera stereo system was proposed with a four-mirror stereo adapter (Inaba *et al.*, 1993). As shown in Figure 2-20, the adapter consists of four flat mirrors: two outer ones and two inner. Two different views are formed by the reflected rays among the outer and inner mirrors. Once the camera with the adapter is maintaining at the same setting, the rotation and translation between the two views can be assumed fixed. Hence the motion parameters between two views could be calibrated and used afterward in reconstruction. The adapter has been applied to visualise and reconstruct the 3D surface topology of turbulent diffusion flames by Ng and Zhang (Ng and Zhang, 2003b) recently. The stereo adapter was attached in front of the lens of a high-resolution digital camera. A pair of stereo images were formed through the same lens system and recorded simultaneously on the charge coupled device (CCD) chip. After calibration process and a series of corresponding and reconstruction process, the 3D surface could be reconstructed and observed. A pair of stereo images of the impinging flame and its reconstructed 3D flame surface viewed from different angles is shown in Figure 2-21.

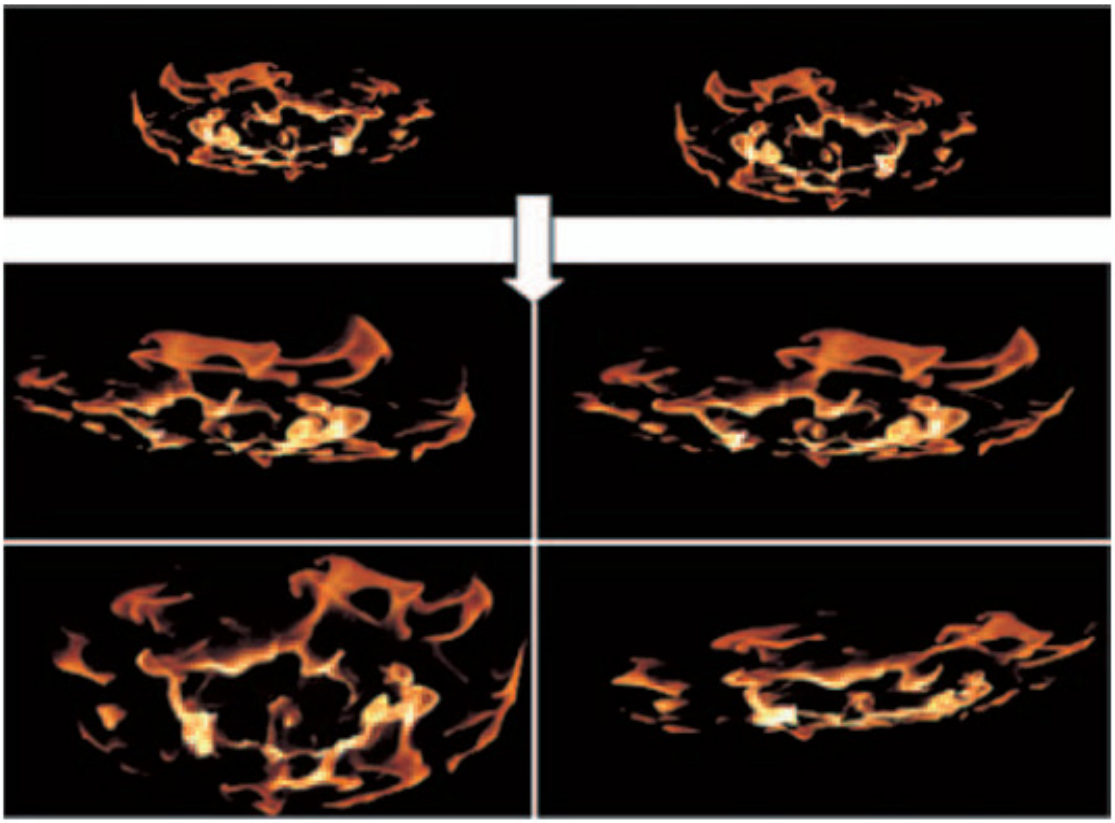

Figure 2-21 Some snapshots of the 3D flame model in different spatial orientations (Ng and Zhang, 2003b)

At the same time, stereoscopic viewing could be combined with other optical diagnostic systems such as Stereoscopic Planar Laser-Induced Fluorescence (SPLIF) (Tanahashi et al., 2004) (Hult *et al.*, 2005), Stereoscopic Particle Imaging Velocimetry (SPIV) (Reeves and Lawson, 2004), etc.

2.2.3 Three-dimensional schlieren technique

2.2.3.1 Tomography BOS

A new optical flow diagnostics method in three dimensional was invented by Bradley Atcheson et al. with the combination of BOS and tomography with 16 cameras in a 180º arc as shown in Figure 2-22 (Atcheson *et al.*, 2008). As we have

mentioned above, BOS could obtain the 2D deflection vectors by taking a reference image of high frequency noise patterns without the tested flow and one more image with the tested flow. In tomography technique, the reconstruction of spatial gradient information could be recovered if multiple view points of BOS are available simultaneously. With a newly designed camera synchronization method, the synchronized images from 16 view points are taken in the experiments. Consequently, with the combination of computer graphics technique, the time-varying density differences of a non-stationary gas flow on a dense grid were captured, as shown in Figure 2-23. However, the complicated apparatus and high demand on many view angles would limit its practical application.

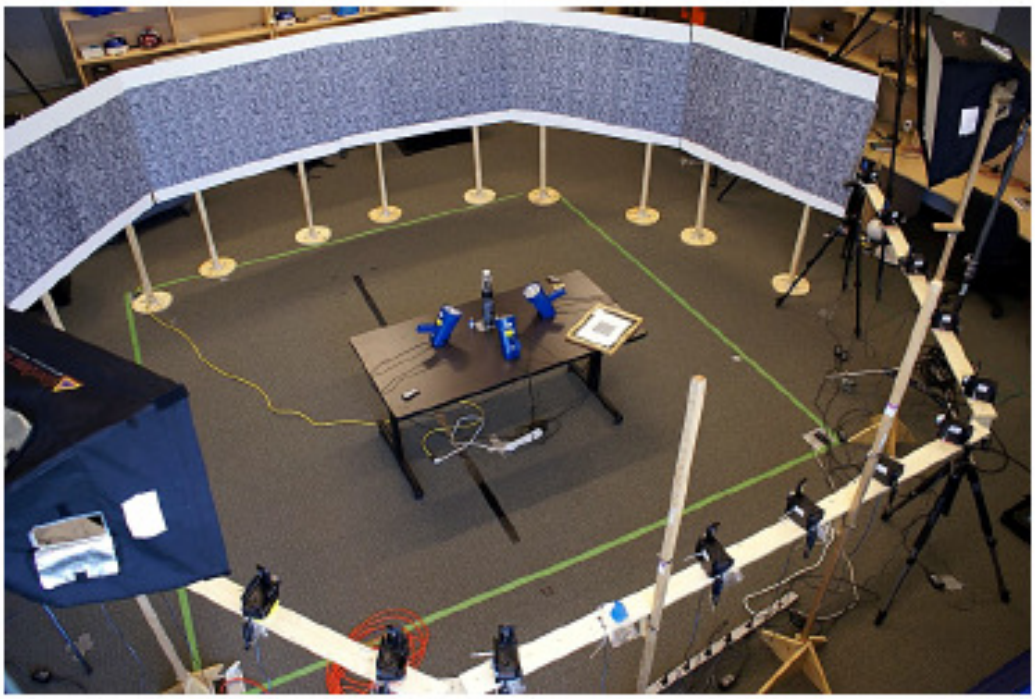

Figure 2-22 Experiment system setup (Atcheson *et al.*, 2008)

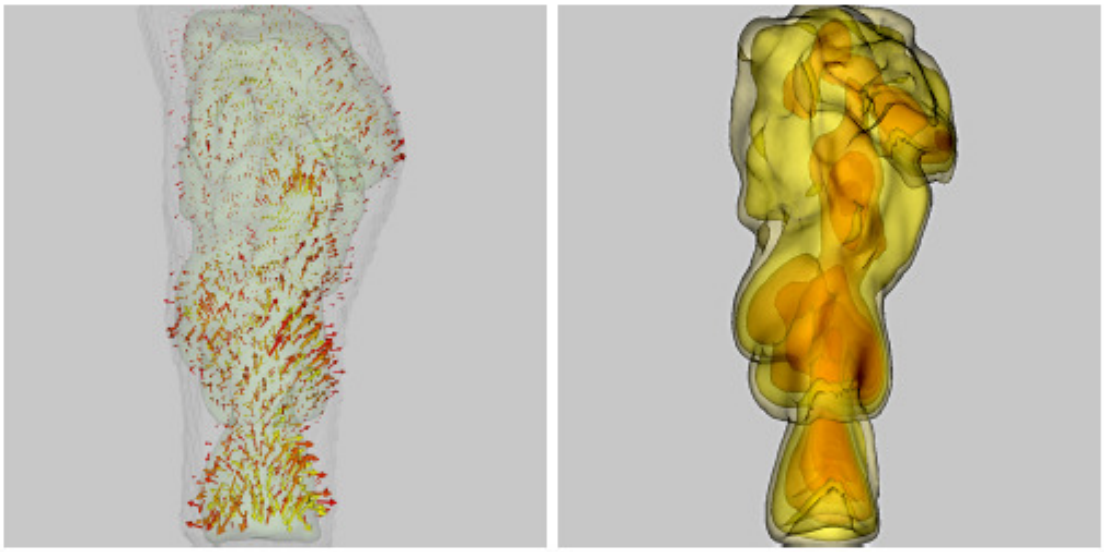

Figure 2-23 Measurements of the hot air flow above a gas burner
Left: 3D gradient field tomographically reconstructed from 16 cameras.
Right: volume rendering of the final refractive index field after Poisson integration.
(Atcheson et al., 2008)

2.2.3.2 Stereoscopic schlieren technique

In conventional schlieren techniques, the image resulting from a system using parallel light will give the impressions of superimposed cross sections of the flow. In a complicated flow the light rays may follow tortuous paths, and the deflections at exit from the working section may not be a true indication of the strengths of the disturbances. It is then desirable to assign positions along the beam of light to the various flow phenomena. Stereoscopic schlieren techniques have been devised to enable this to be done. A stereoscopic method was first developed by Lyot and Francon for examining discs of glass, by taking photos from two different directions with a single parallel beam (B. Lyot, 1948). As shown in **Error! Reference source not found.**Figure 2-24 (a) and (b), the apparatus consists of either a single parallel beam of light used to photograph the flow in the working section from two different directions or two inclined beams used to take photos from two directions simultaneously. Due to the time delay between the two images, the single parallel

beam is not suitable for unsteady phenomenon. Figure 2-24**Error! Reference source not found.** (c) shows the stereoscopic schlieren system setup by John H. Hett (Hett, 1951). The system consists of a pair of parabolic mirrors and 10 flat mirrors and is able to take two images from two directions simultaneously. Besides the complicated apparatus of this system, the test section is much smaller than the parabolic mirror diameter. Though it had been applied to combustion consequently, due to the lack of processing power at that time, the photographs could only been viewed separately. Another apparatus was constructed with two pair of parabolic mirrors, as shown in **Error! Reference source not found.** Figure 2-24 (d) (Veret, 1952). This setup was applied on aerodynamics and a pair of stereoscopic images obtained are shown in Figure 2-25. It can be observed that the shockwaves demonstrate slightly different angles in the two images. Although the technique supplied effective qualitative visualisation at two directions, it should be emphasized that it was still in an early stage of development; the full quantitative potential could not be realised at that time.

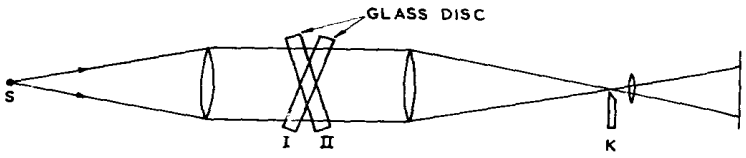

(a) (B. Lyot, 1948)

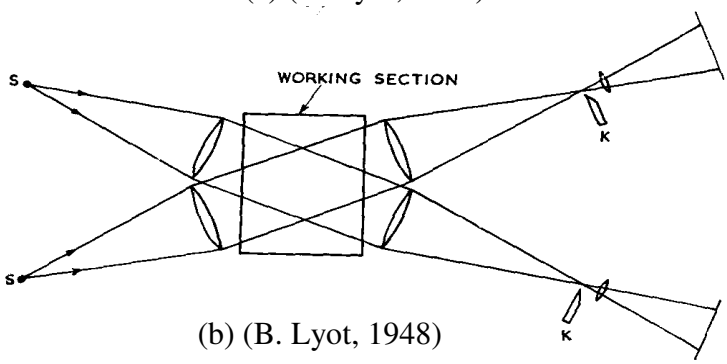

(b) (B. Lyot, 1948)

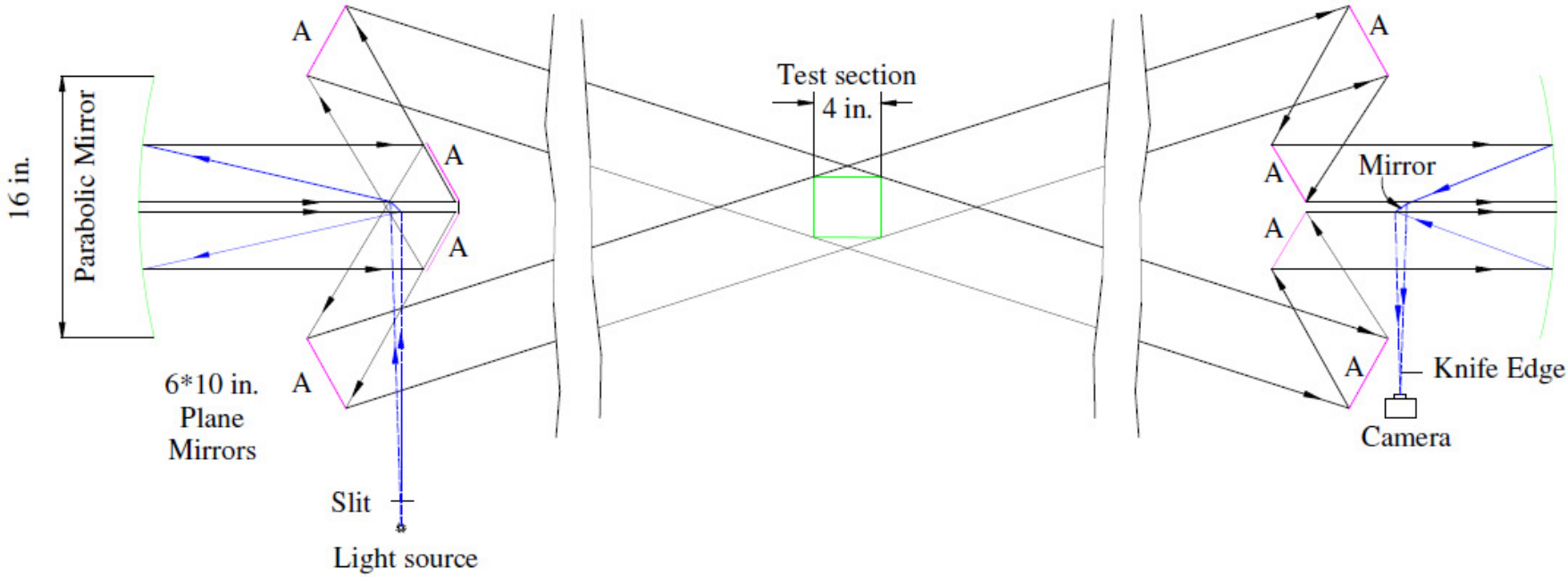
16 in.
Parabolic Mirror
A
A
A
A
6*10 in.
Plane
Mirrors
Slit
Light source
Test section
4 in.
A
A
Mirror
A
A
Knife Edge
Camera

(c) (Hett, 1951)

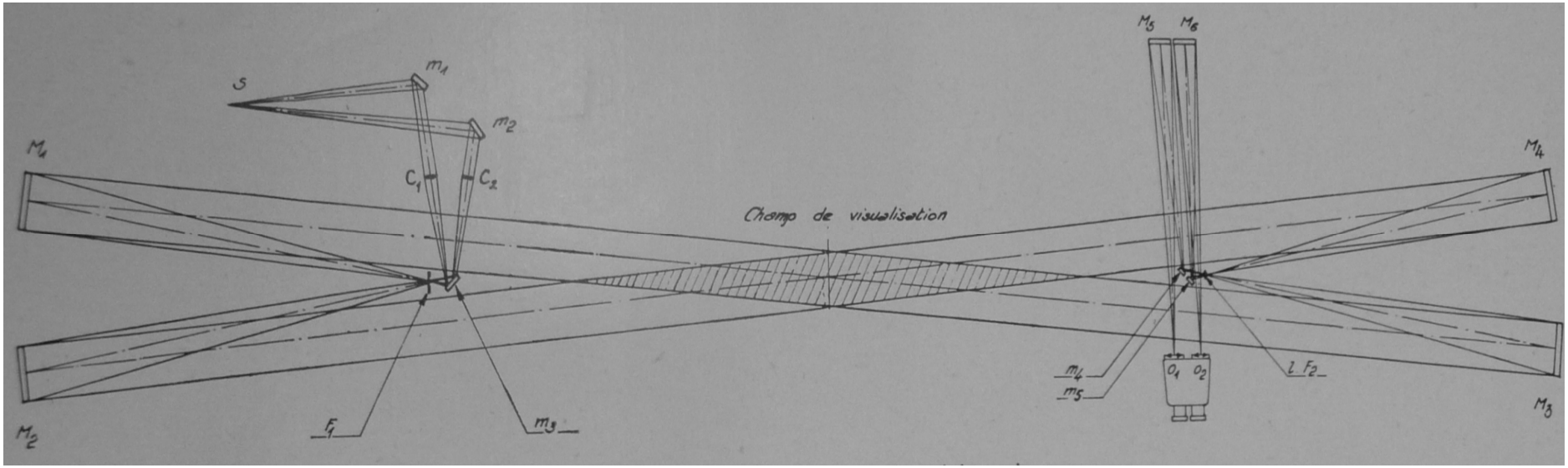

S: light source m: plan mirror M: parabolic mirror F: knife edge
(d) (Veret, 1952)

Figure 2-24 Stereoscopic schlieren apparatus

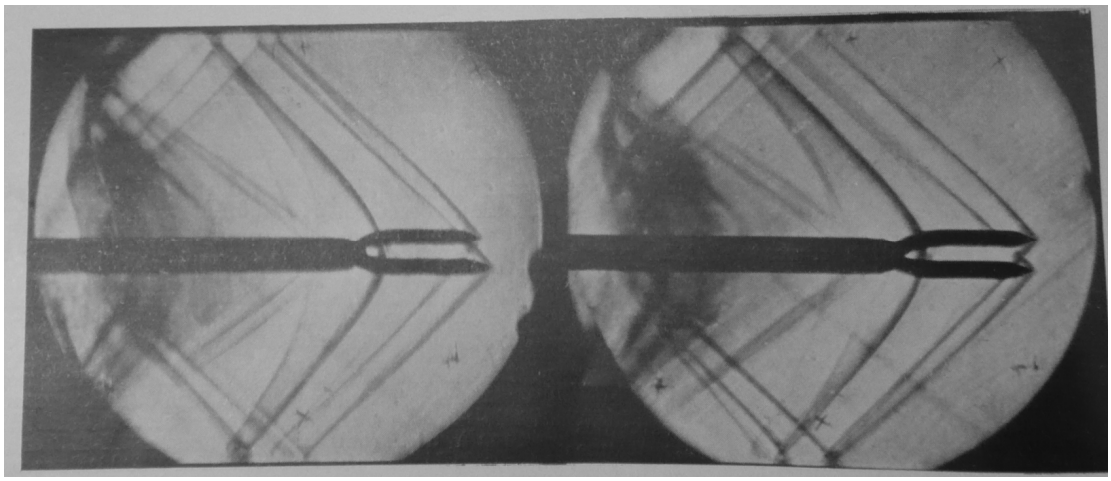

Figure 2-25 A pair of ‘stereoscopic’ schlieren images (Veret, 1952)

However, it must be pointed out that the test sections of the stereoscopic schlieren systems mentioned above were all in the cross section of the two collimated beams. Thus the two images do not satisfy the characteristics of projective geometry, which is the basis of stereoscopic method for 3D reconstruction. Strictly speaking, the techniques are not actually ‘stereoscopic’.

2.2.4 Laser Induced Fluorescence (LIF)

In Laser-induced fluorescence (LIF) technique, the molecules are excited by specific wavelengths of laser light because of the absorption of electromagnetic radiation. The optical emission from the excited molecules is recorded to make quantitative measurements of the analyte concentrations. The intensity of light emitted from the tested region of flow is proportional to the intensity of the excitation energy and the analyte concentration. Assume the excitation energy is locally uniform, then the emitted light intensity could be converted to analyte concentration through a simple

calibration. Since the good sensitivity of LIF, it is applied widely both scientifically and technically in monitoring gas-phase concentrations in the atmosphere, flames, and plasmas. Planar LIF (PLIF) is a particularly well established imaging method in combustion research. It is used to visualise concentration distributions in a variety of flames and combustion engines as well as around single fuel droplets or droplet arrays. Figure 2-26 shows a typical PLIF system with a laser, an arrangement of lenses to form a sheet, fluorescent medium, collection optics and a camera. The laser sheet is used to illuminate the medium, which is usually made up of fluorescent material. The imaged are captured by a CCD camera. Figure 2-27 shows the result of OH radicals in the H2/O2 premixed flame above a micro burner with PLIF method. Three dimensional LIF is also developed to observe the flow characteristics as well (Van Vliet *et al.*, 2004).

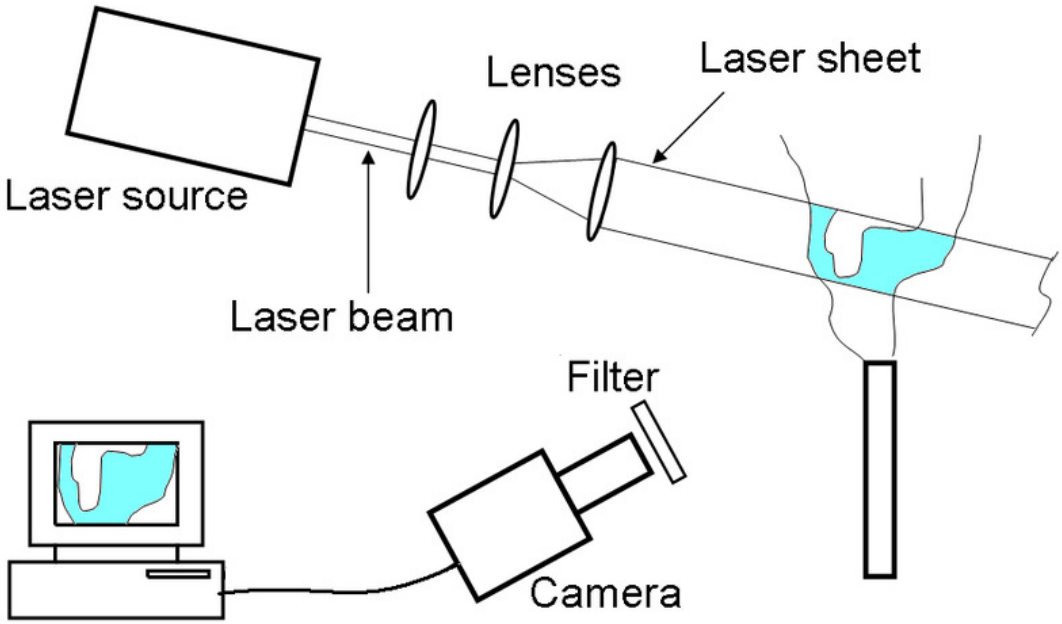

Figure 2-26 PLIF system

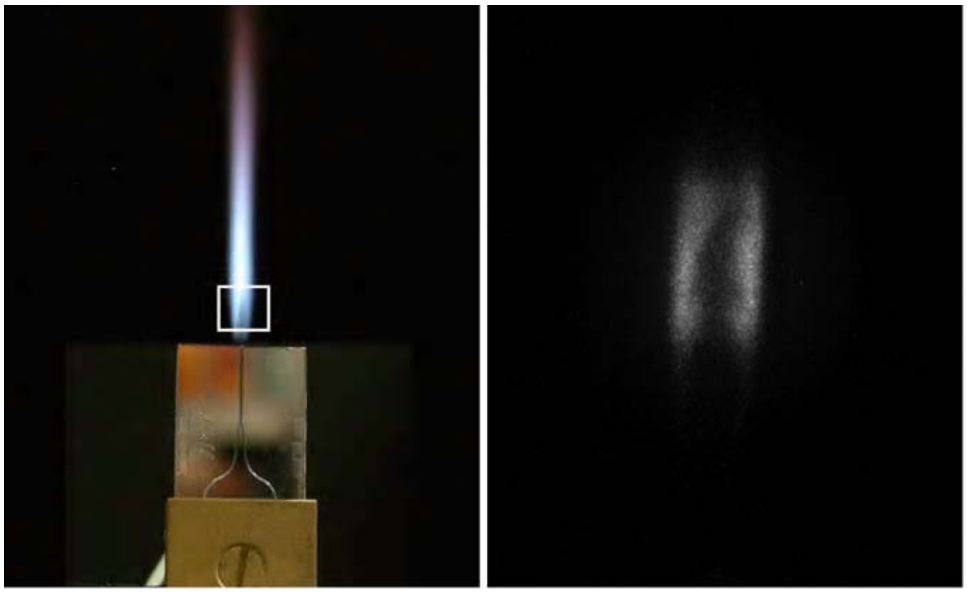

a b

Figure 2-27 (a) Photograph of the microburner with flame (b) consecutive PLIF images of OH radicals in the H2/O2 premixed flame above the microburner. The white rectangle in (a) indicates the area of the PLIF images (Paa, Muller et al. 2007)

2.2.5 Particle Image Velocimetry (PIV)

The PIV technique provides a quantitative, instantaneous, whole-field visualisation and two dimensional description of the flow. This technique has a large range of applications, from slow flows modelled in a laboratory environment to transonic and supersonic flows produced in industrial wind tunnels and turbine engines, widely used to measure velocities of the fluid flow field. Typical PIV apparatus consists of several subsystems. Figure 2-28 shows a schematic of a typical PIV system. The light source is normally acted by a high power laser. A light sheet is formed by optical parts such as a cylindrical lens. The laser acts as a photographic flash for the imaging system, which is usually a digital camera. In most applications, tracer particles have to be added to the flow. These particles are illuminated by the light sheet in the flow at least twice recorded either on a single frame or on a sequence of frames. The resolution of the captured images depends on the camera spatial

specification and the size of the flow area captured. The displacement of the particle images between the light pulses has to be determined through evaluation of the PIV recordings. In order to be able to handle the great amount of data which can be collected employing the PIV technique, sophisticated post-processing is required. In general, accuracy of the PIV data is a function of image resolution and timing of the pulse separation (Raffel M., 2007). The velocity vector maps of a methane/air diffusion flame are presented in Figure 2-29.

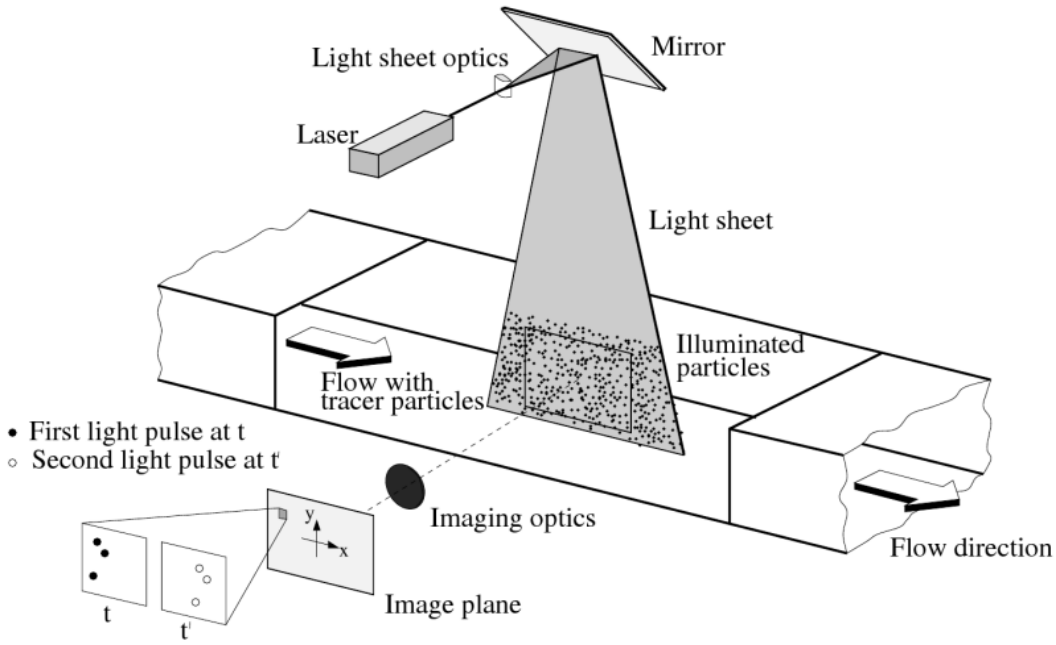

Figure 2-28 PIV system in a wind tunnel (Raffel M., 2007)

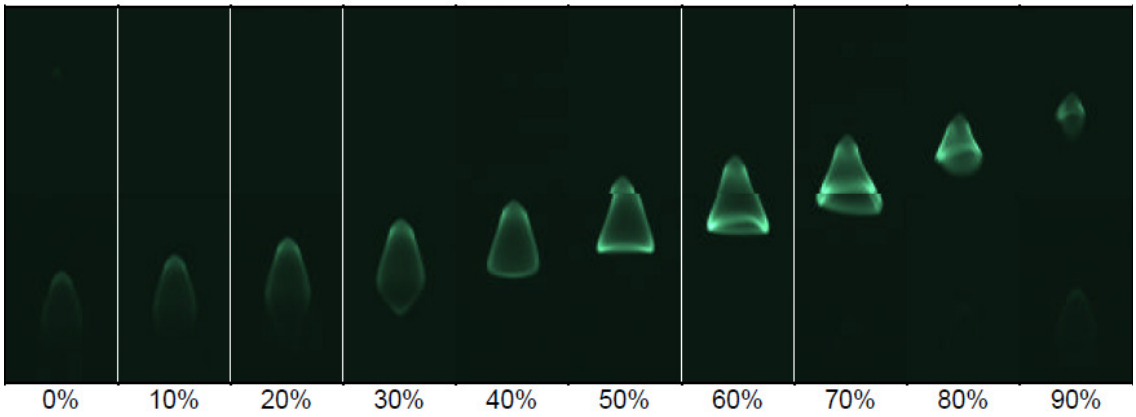

(a)

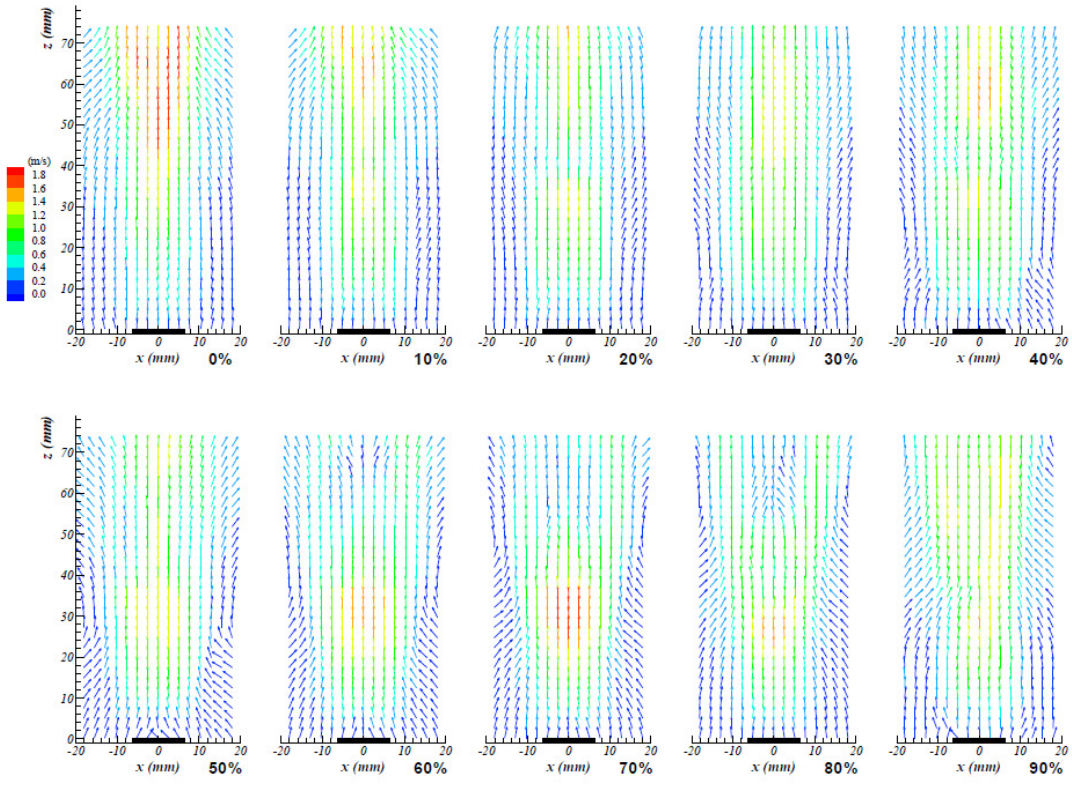

(b)

Figure 2-29 (a) Direct images of the flickering flame (b)Vector plots of phase-averaged velocity for the moderately flickering flame (10 phases in an excitation cycle from 0% to 90%) (George Papadopoulos, 2001)

2.2.6 Holographic Technique

Holography was invented by Dennis Gabor [Gabor, 1949] in 1947. Holography consists of two processes: 1) Recording, where the object wave is mixed with a

coherent reference wave to produce interference fringes, which are recorded on the holographic plate, and 2) Reconstruction, where the object wave is reconstructed from the developed hologram. The principle of holography recording is shown in Figure 2-30. In holography, a coherent light beam is divided into two beams by a beam splitter: one beam passing through the object and then falling on the photographic plate, called object beam, and a second light beam, known as the reference beam, also illuminating the recording medium. Thus interference occurs between the two beams. The holography records not only the intensity but also the phase of the light scattered by the object. The phase delay is proportional to line integral of the density along the light path. Once the phase delay is known, the average flow density can be calculated. Afterwards, if the holography is illuminated by a light beam identical to the reference beam, the solid object will be seen on the holography. The time required to produce a correct hologram is dependent on many factors: power of the laser, sensitivity of the film and the reflectance of the object. When the laser beams are coherent, the interference pattern is stationary in space and is recorded correctly on the film.

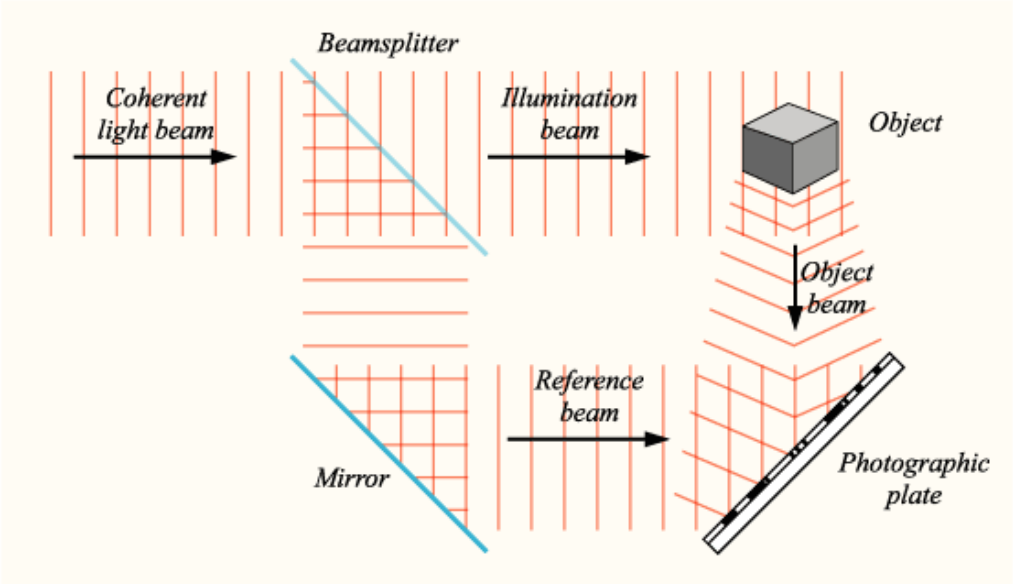

Figure 2-30 Holography recording process

However, when movement is encountered on the optics, film or object, the interference pattern will move and the pattern is obliterated. It is possible to solve this problem by shorten the exposure time, but a more expensive laser would be required. He-Ne laser is often used as the light source of coherent light in holography because it provides visible output and has excellent spatial quality. There are a variety of recording materials which can be used, including photographic film or video CCD cameras.

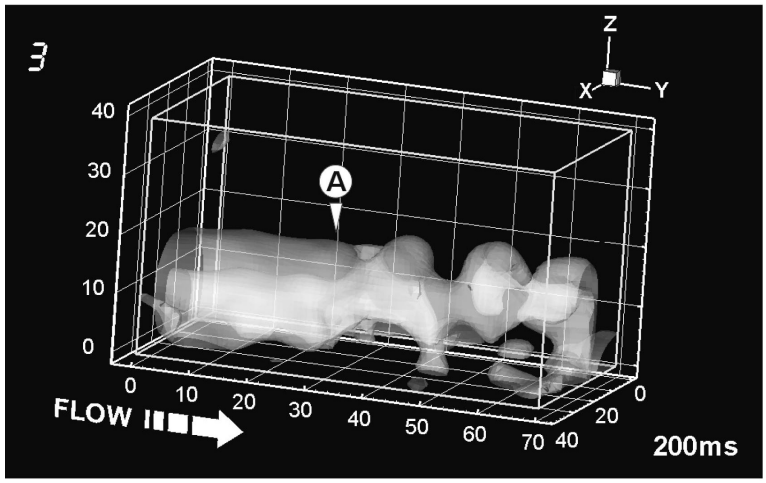

Figure 2-31 Vortex shedding cycle recorded and reconstructed by HFV
(Pu and Meng, 2005)

Nevertheless, holography has been investigated as a useful 3D visualisation tool to observe flow structures. With feeding light scattering particles densely, Meng (Meng *et al.*, 1998) succeeded to reconstruct 3D internal flow structures of a propane jet diffusion flame with their Holographic Flow Visualisation (HFV) technique. A vortex shedding cycle model is shown in Figure 2-31. Since the HFV technique captured the structures by the collection of particles, the flame vortex interactions could be observed clearly. However, the flame front itself often cannot be recorded

by the hologram for lack of particles because the temperature gradients push particles away from the flame front.

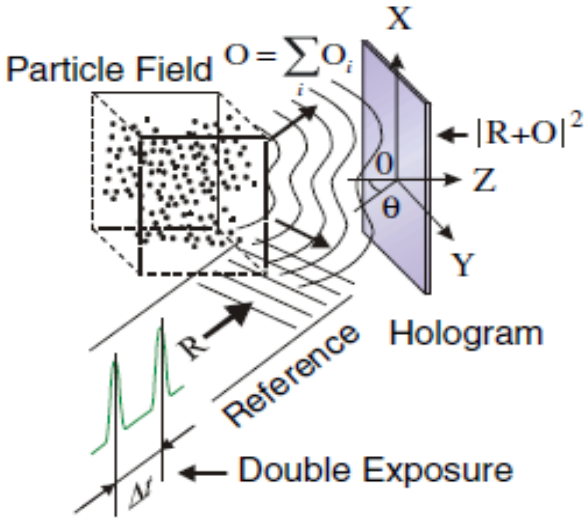

Figure 2-32 Holographic PIV system (Meng *et al.*, 2004)

Another widely developed 3D visualisation technique based on holography is Holographic PIV (HPIV). Holographic PIV instantaneously measures 3D velocities of fluid flows through holographic imaging of small, neutrally buoyant tracer particles dispersed in the flow. Figure 2-32 illustrates the principle of HPIV. An ensemble of neutrally buoyant particles moving with the flow is illuminated with a short-duration laser pulse. In the hologram plane, the light field scattered from the particles (the object wave) interferes with a reference wave, and the intensity of the interference pattern is recorded to form a hologram. 3D positions of these particles can then be reconstructed. Furthermore, from 3D displacements of the particles over two exposures separated by a brief time interval, the instantaneous 3D velocities can be extracted (Meng et al., 2004). The drawbacks of the Holographic-PIV are the process time consuming and somehow inaccurate due to misalignment and distortion when re-positioning the hologram for the object reconstruction. Moreover, the recoding of time-series on film for the study of dynamic flow phenomena is a

technical challenge. Therefore, holographic-PIV studies generally use only a few recordings and do not present velocity statistics.

2.2.7 Tomography

The discovery of X-ray by Dr. Conrad Roentgen in 1901 has provided a revolutionary three-dimension imaging technique in medical application. With the assistant of necessary developments in electronics, Hounslow developed and commercialized the first axial computer tomography in 1972 (EMI-Scanner). Tomography is defined as splitting an object into two-dimensional and cross-sectional images. During the tomographic imaging procedure, the structure of an object on the focal plane between the beam-delivery system and the receiver is sharpened in the image, while structures elsewhere are eliminated. In practice, a series of two-dimensional images are captured from different angles at a constant height. Through algorithms, the common points are compared and reconstructed, and 3D volumes are built by stacking the cross-sectional reconstructed slices.

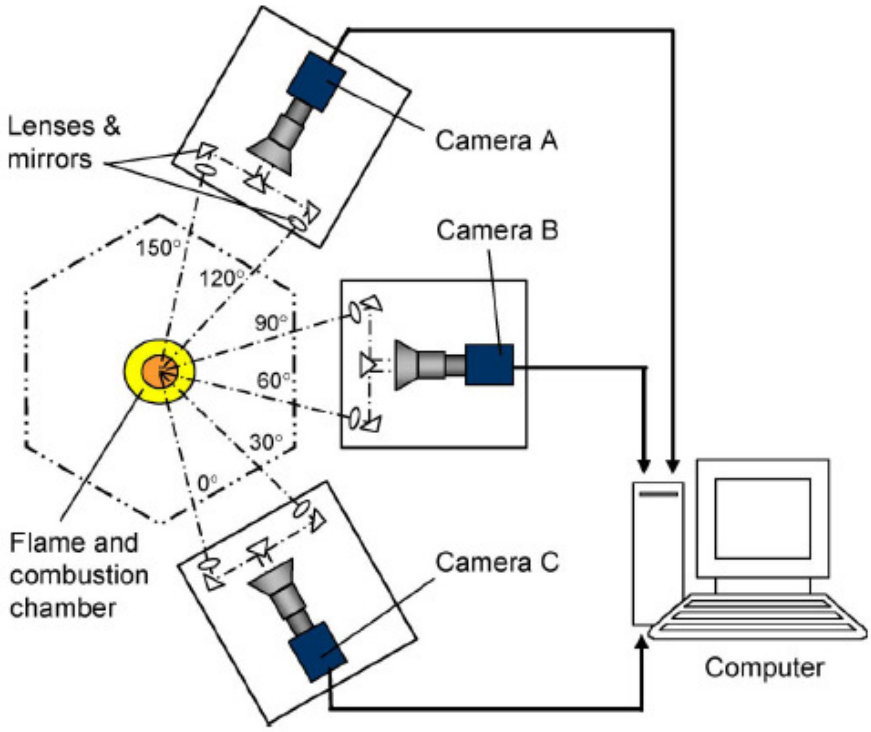

Figure 2-33 Schematic of the flame imaging system (Gilabert *et al.*, 2007)

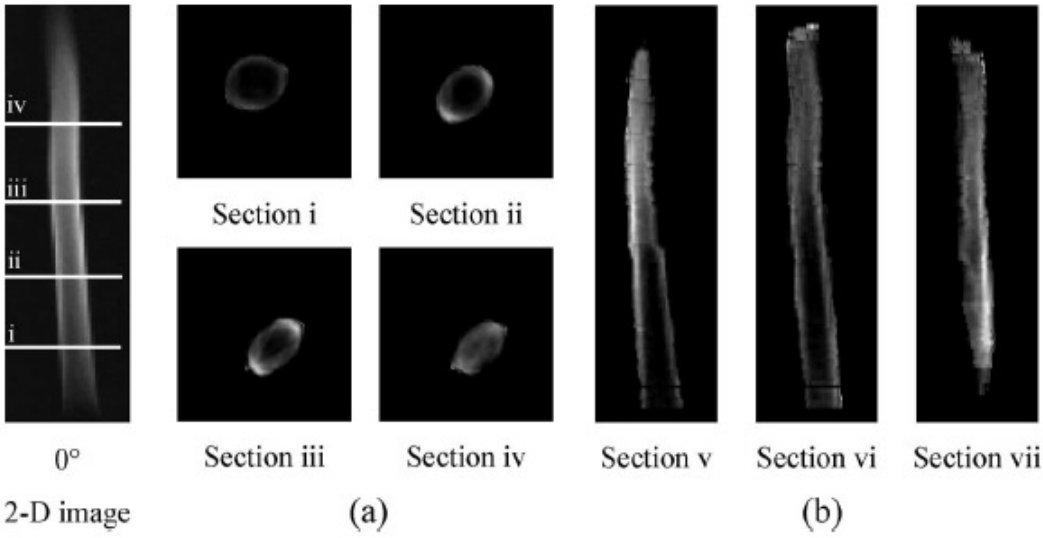

Figure 2-34 Luminosity reconstruction of a gaseous flame
(a) Reconstructed cross sections. (b) Reconstructed longitudinal sections.
(Gilabert *et al.*, 2007)

Recently, some tomographic techniques are used on visualisation in combustion research, such as Computed Tomography (CT) (Gilabert *et al.*, 2007), Electrical Capacitance Tomography (ECT)(Waterfall *et al.*, 2001), and so on. A schematic of

the 3D flame imaging system employed in (Gilabert *et al.*, 2007) is shown in Figure 2-33. The cameras are arranged on one side of the burner with an angle of 60° between two adjacent cameras. The optical transmission unit formed two optical paths for each camera and enabled each camera take images from two different directions with an angle of 30°. With the six flame images recorded concurrently from six directions, 3D reconstruction of the flame luminosity can then be achieved. Figure 2-34 shows the results of gray-level luminosity reconstruction of a gaseous flame by Guillermo Gilabert et al. In combination of PIV, tomgraphic PIV techniques are developed to measure the velocity field of volume spaces.

2.2.8 Visual hull reconstruction

The Visual hull is a geometric entity created by shape-from-silhouette 3D reconstruction technique introduced by Laurentini (Laurentini, 1994). As shown in Figure 2-35, 2D silhouettes of a 3D object S are obtained as a parallel or perspective projection on the image plane. Object reconstruction can be performed using the volume intersection approach, which recovers the volumetric description of the object from multiple silhouettes. However, concave surfaces are not able to be reconstructed properly because they are not observable in projecting lines.

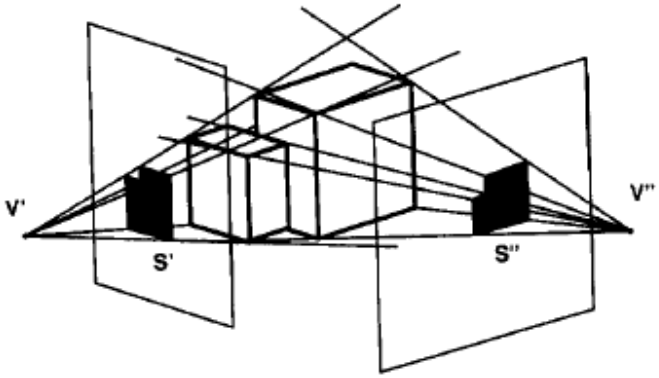

Figure 2-35 The volume intersection approach to object reconstruction

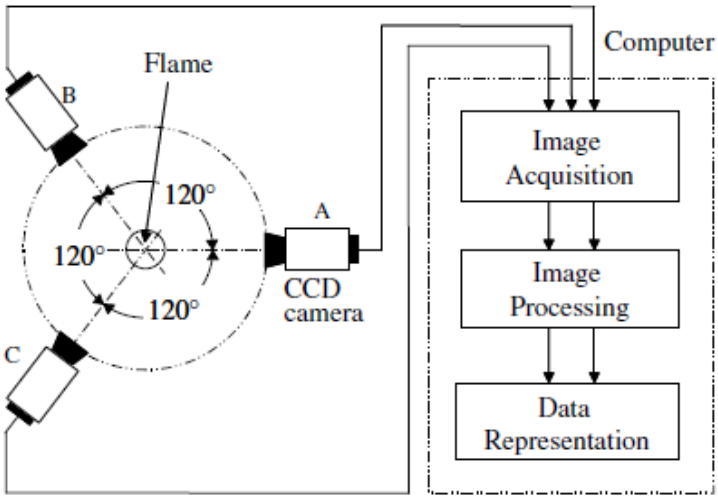

Figure 2-36 System setup

The visual hull techniques have also been developed to measure 3D geometric parameter of flames (Bheemul *et al.*, 2001). As shown in Figure 2-36, the system consists of three CCD cameras, a frame grabber and a computer with dedicated software. The three cameras, placed equidistant and equiangular from each other around the flame being monitored, capture the two-dimensional images of the flame simultaneously from the three different directions. Dedicated computing algorithms have been developed to reconstruct three-dimensional models of the flame using its contours extracted from the two-dimensional images.

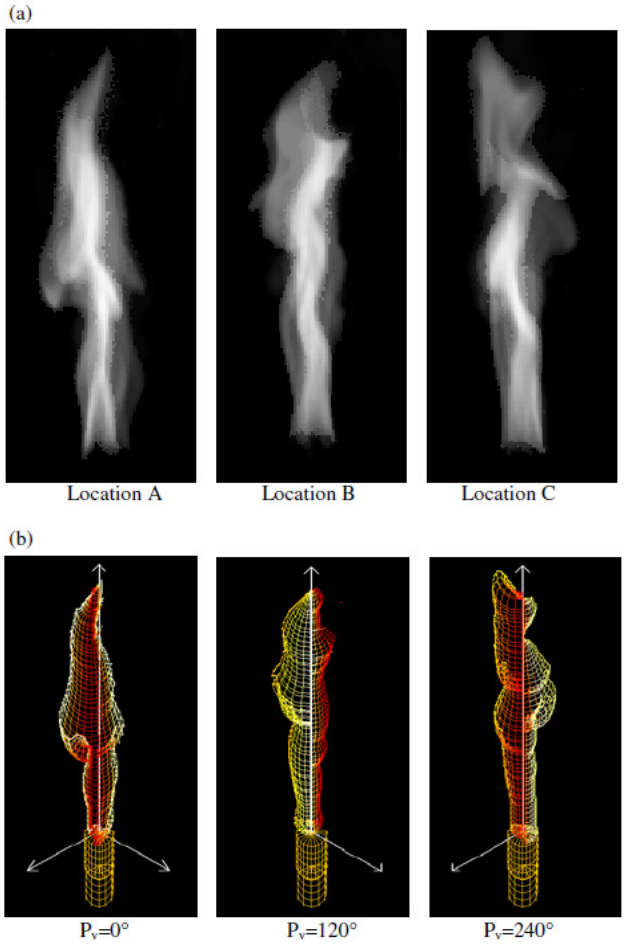

Figure 2-37 Typical flame images and reconstructed 3D model

Figure 2-37 shows the three dimensional reconstructed model of a typical flame shape in 'fishnet' surface. However, the reconstruction accuracy is determined by the information contour extracted from the images, which adds difficulty on flame application for the ambiguity flame shape. Also, the contour tracking algorism is not easy to be applied directly in the presence of noise. Thus the reconstruction of this method may only in low-resolution, which can be adapted for real time processing.

2.3 Comparison of the selected optical techniques used in combustion field

Several applications of popular optical diagnostic methods have been reviewed briefly in Section 2.2. The measurements of dimensions and principles are given in Table 2-3. It is found that most 3D diagnostics are based on the speckle pattern correlation, hologram pattern or multi direct image views. The speckle pattern method usually requires particle feeding in the flow field, such as PIV, which is difficult to achieve in specific circumstances. For the tomography BOS method, multiple views are required for 3D reconstruction and the BOS image resolution is poorer than conventional schlieren images. The technique hires holography, which is high in cost and the recording process is sensitive to disturbance of ambient environment, which calls for significant experience and skills. The stereoscopic schlieren and shadowgraph technique based on conventional schlieren/shadowgraph images is believed to be more reliable and with higher accuracy; but had been stopped at very early stage with critical mistake in the concept (section 2.2.3.2). One aim of this study is to develop an innovative and easy applicable 3D diagnostic by combining schlieren and stereo techniques together.

Table 2-3 Selected optical techniques used in combustion research

Optical Diagnostics	**Dimensions**	**Measurement principles**
Schlieren and shadowgraph	2D	Schlieren/shadowgraph image
Background-oriented schlieren (BOS)	2D	Speckle pattern
PIV/Stereoscopic PIV	2D/3D	Speckle pattern
Tomography BOS	3D	Speckle pattern
Holography	3D	Hologram pattern
Holography PIV	3D	Hologram pattern
Stereo	3D	Direct image
Visual hull	3D	Direct image
Tomography	3D	Direct image

Chapter 3 Principle and Algorithms of 3D Reconstruction Using Stereo Images

Stereo imaging and reconstruction is a technique to obtain 3D information of an object by processing two images taken at slightly different view angles. With fast-developing digital image processing techniques after 1960s and the emerging of digital cameras, stereoscopic imaging gradually joined with computer vision, and turned into a very useful diagnostic method for research and industrial needs. In this chapter, the background theories and typical algorithms related to this thesis are presented briefly.

3.1 Introduction of 3D reconstruction from stereo images

The algorithm designed in this study follows the flowchart presented in Figure 3-1. In order to gain the in-depth information from a pair of stereo images, both camera calibration parameters and correspondence coordinates are required for the 3D

reconstruction. In camera calibration process, the intrinsic and extrinsic parameters are to be calibrated from images taken of a planar pattern. The geometries of the two views in the stereo images can be established from the calibration process. By relating the correspondence coordinates in the test object stereo images, 3D reconstruction can be built based on the geometry parameters.

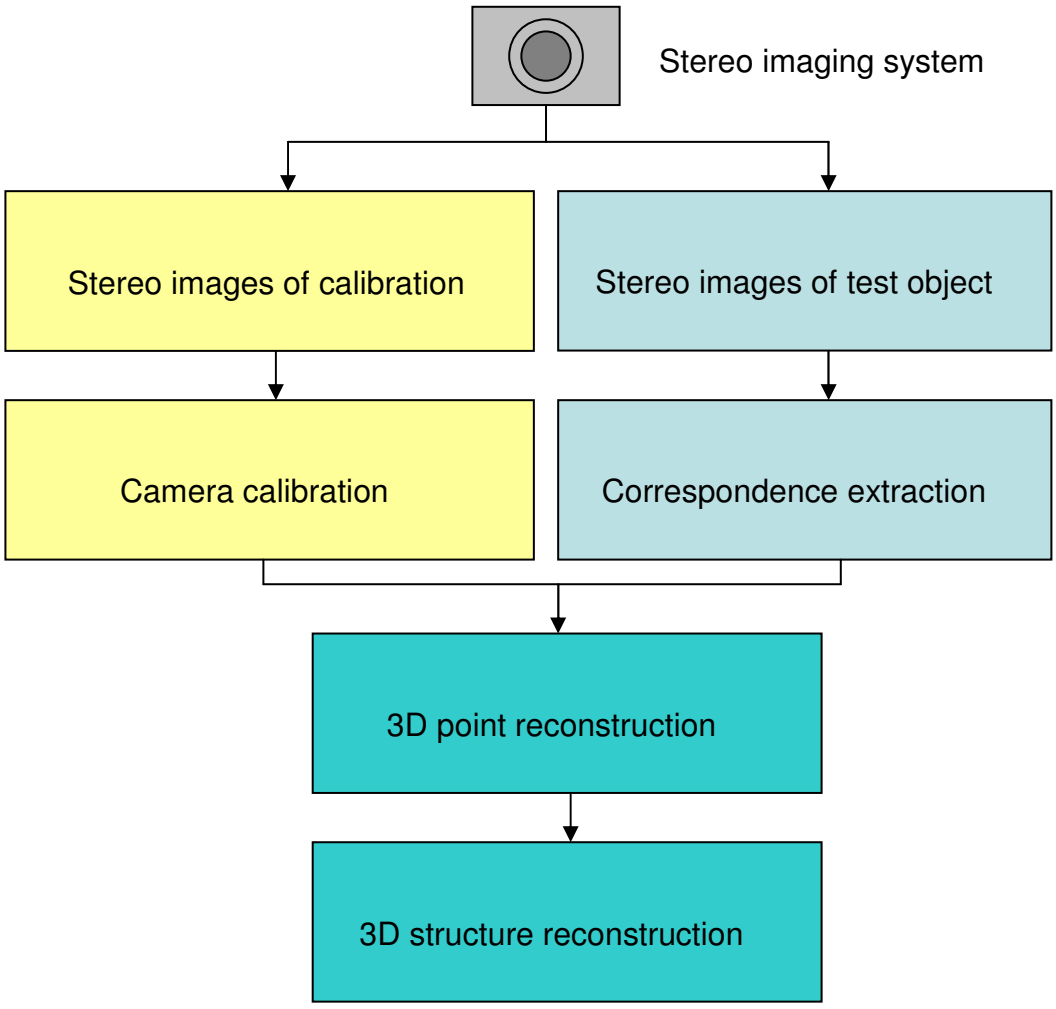

Figure 3-1 Flowchart of 3D reconstruction from stereo images

As reviewed in Section 2.2.2, several methods can be used to take stereo images, including two-camera system and single-camera system. In the two-camera system, for unsteady phenomenon, the two cameras must be synchronised. Thus it requires professional cameras with high configurations. For single-camera system, a stereo adaptor is attached in front of the camera lens to form two different views within one image. Although the image resolution of each view is reduced comparing with the two-camera system, no requirements on synchronization makes it more flexible and feasible in practical applications. The cost of the single-camera system is also much lower than that of the two-camera system. In this thesis, both single-camera and two-camera systems are used for taking stereo images. Both systems share similar principle and algorithms of camera calibration and 3D reconstruction. In this chapter, the stereo imaging and reconstruction algorithms based on single-camera system are introduced briefly.

3.2 Geometry and optical characteristics of the stereo adapter

In this study, the single-camera system consists of an 'Asahi Pentax' 52 mm stereo adapter and a high speed camera. As shown in Figure 3-2, the adapter is attached to the front of the high speed camera lens with a step-out ring. The system is able to record a pair of images simultaneously. In this section, the geometry and basic principles of the four-mirror adapter stereo imaging system will be reviewed. The dimensions and the optical geometry of the adapter is illustrated in Figure 3-3 and Figure 3-4 respectively. The adapter consists of four mirrors: two inside and two outside. There is a discrepancy angle (δ=1.5º) between the inside and outside mirrors. The light rays projected on the outside mirrors will be reflected on the inner mirrors and then go through the camera lens. Thus there will be a pair of images on the

imaging screen. A sample image is shown in Figure 3-5. It could be seen that there are a pair of images of the glass block in the same frame, but in slightly different angles.

Figure 3-2 High speed camera with Pentax stereo adapter attached in front of the lens

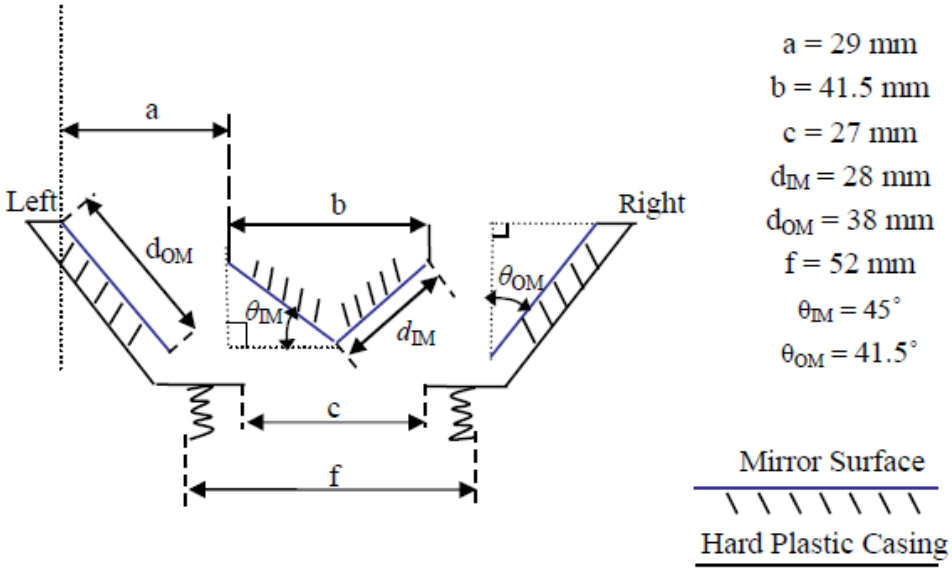

Figure 3-3 Dimension of Pentax stereo adapter (Wang, 2009)

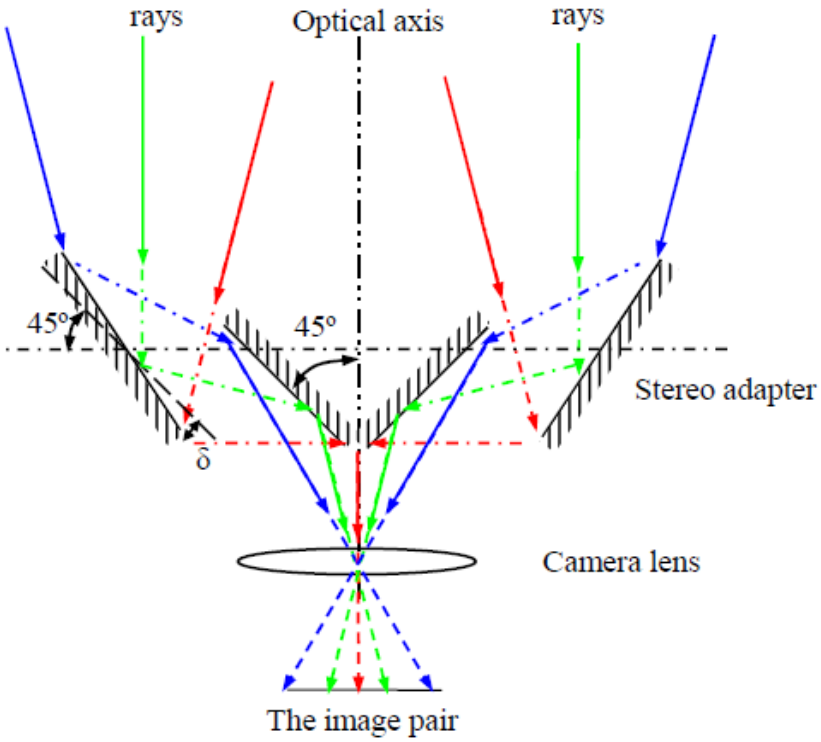

Figure 3-4 The optical geometry of the four-mirror stereo adapter with the camera (Wang, 2009)

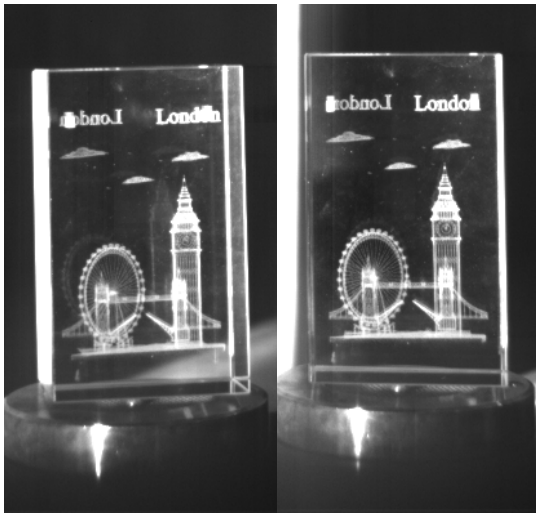

Figure 3-5 Sample image obtained with the stereo adapter

The four-mirror stereo adapter and the camera can be represented as a system of two virtual cameras. Based on the law of reflection, the positions of the two virtual cameras ban be obtained easily. Taking the group of mirrors on right side as an

example, as shown in Figure 3-6, the optical center of the virtual camera can be worked out. We define the intersecting corner of the two inner mirrors as point C, the optical center of the real camera as point O, the right outer mirror as R_O and the right inner mirror as R_I. The distance from point C to mirror R_O in horizontal direction is m and the distance from C to O is n. In converse of the path of rays from object, the virtual camera center O" is obtained by the reflection of real camera center O through inner mirror first and then outer mirror (Wang, 2009).

The distance l from O" along its optical axis to R_O and the distance f from O" to optical axis of the camera O can be described by the equations

$$l = m + n \tag{3-1}$$

$$f = l * \sin\alpha + m = (m+n) * \sin(2\delta) + m \tag{3-2}$$

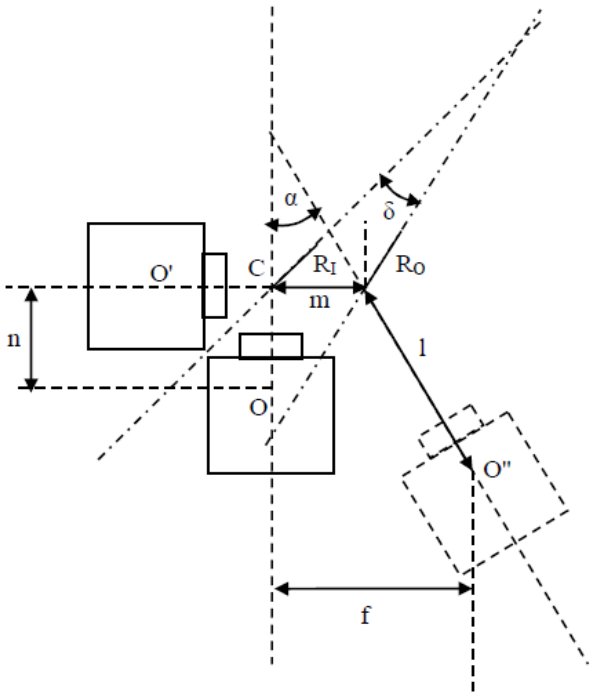

Figure 3-6 Two virtual camera systems (Wang, 2009)

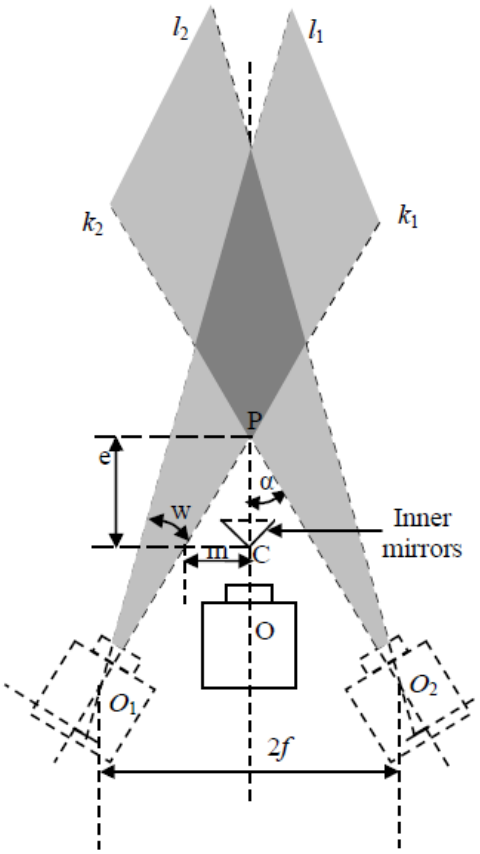

Figure 3-7 Optical structure of two virtual cameras (Wang, 2009)

Figure 3-7 shows the optical structure of the two virtual camera systems. k_1 and k_2 represent the optical axes of the two virtual cameras respectively. The baseline, which refers to the distance between two virtual optical centers, is $2f$. The two virtual cameras will form two equal sized images on the image plane. Each image can only have half FoV of the original camera. As shown in Figure 3-7, we define half angle of the real camera's FoV is w, l_1/ $l_2$and k_1/ k_2 representing the edge rays along the FoV of the virtual camera O_1/O_2. The common FoV of the two virtual cameras, which is the region enhanced by deep shadow, can be observed by the stereo system. The half angle of the stereo system's FoV α is defined as the angle between k_i (i=1, 2) and optical axis of the real camera. The intersection point of rays

k_1 and k_2 , P, is the nearest observable point along the optical axis. The distance e between P and the intersecting corner C of two inner mirrors can be calculated as

$$e = \frac{m}{\tan\alpha} = \frac{m}{\tan(2\delta)} \tag{3-3}$$

It is worth noting that the region restricted by point P and C as well as rays k_1 and k_2, is a blind area of the stereo system. An object placed in this region cannot be seen by either virtual camera.

3.3 Two camera system

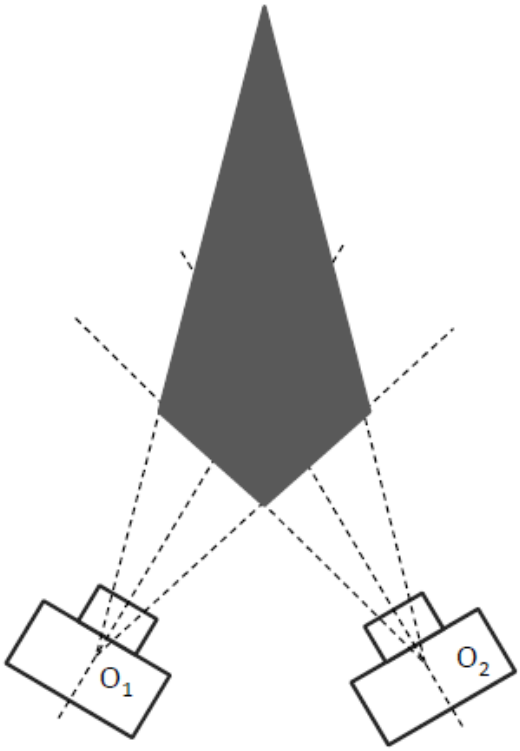

Figure 3-8 Optical structure of two camera systems

Besides the system consisting of a single camera plus a stereo adaptor, the stereo setup can also be made up with two cameras. The optical structure of a two camera system has been shown in Figure 3-8. As illustrated in Figure 3-7, the single camera

system, the two images must share the FoV of the original camera. As indicating by the deep shadow region in Figure 3-8, in a two camera system, each of the two stereo images can have the whole FoV of the camera. Thus a more wide range view field can be covered in a two camera stereo system. However, for investigating unsteady phenomenon, the two cameras must be synchronised properly.

3.4 Algorithms for camera calibration and reconstruction

Camera calibration is an essential step to obtain camera parameters which are required to extract 3D metric information from 2D images. This study has employed a flexible and robust calibration algorithm established by Zhang (Zhang, 2000, Zhang, 1997). The calibration parameters are extracted from a few different orientations of a planar pattern. Combined with the known calibration parameters and the corresponding points in the stereo images, 3D coordinates could be established. The complete MATLAB program is adopted from (Wang, 2009).

3.4.1 Projective camera model

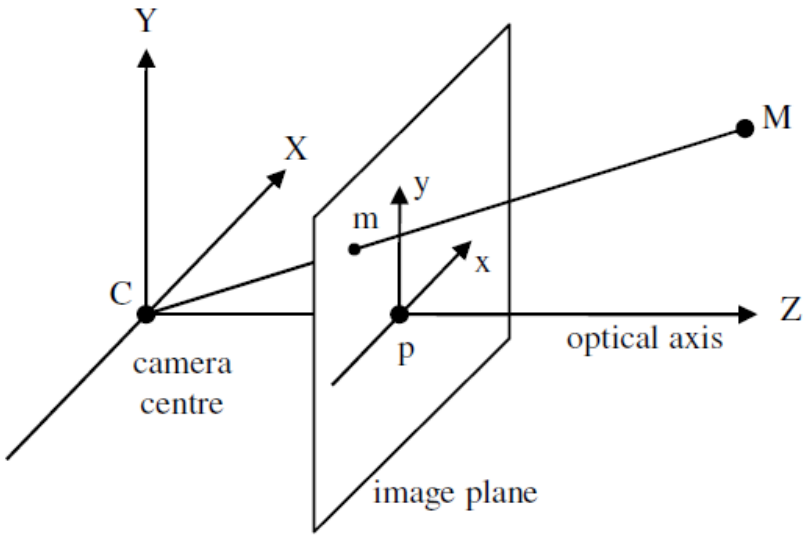

Figure 3-9 Pinhole model

In projective camera model, a 2D point is denoted by $m = [u, v]^T$, while a 3D point is denoted by $M = [X, Y, Z]^T$. The augmented vector is denoted by adding 1 as the last element: $\tilde{m} = [u, v, 1]^T$ and $\tilde{M} = [X, Y, Z, 1]^T$. A pinhole camera model is used by reducing the camera to a point and an image plane, as shown in Figure 3-9. Points in the world coordinates form rays by connecting the camera centre and project images on the image planes. The relationship between a 3D point M and its image projection m is given by

$$s\tilde{m} = A[R \quad t]\tilde{M} \text{ , with } A = \begin{bmatrix} \alpha & \gamma & u_0 \\ 0 & \beta & v_0 \\ 0 & 0 & 1 \end{bmatrix}, \tag{3-4}$$

where s is an arbitrary scale factor, (R, t), namely the extrinsic parameters, the rotation and translation relating the world coordinate system to the camera coordinate system. A is called the camera intrinsic matrix, with $(u_{0,} v_0)$ the coordinates of the principal point, α and β the scale factors for u and v in image, and γ the parameter describing the skew of the two image axes.

In stereo reconstruction, two camera systems are used. We designated one camera coordinate as the world coordinate and the other camera coordinate is related to the world coordinate via the extrinsic parameters (R, t). Then we have

$$\tilde{m}_i = P\tilde{M}_i = A[I \quad 0]M_i \tag{3-5}$$

$$\tilde{m}_i' = P'\tilde{M}_i = A'[R \quad t]M_i \tag{3-6}$$

Without loss of generality, we assume the model plane is on $Z = 0$ of the world

coordinate system. Let's denote the i^{th} column of the rotation matrix R by r_i. From Equation (3-4), we have

$$s\begin{bmatrix} u \\ v \\ 1 \end{bmatrix} = A[r_1 \quad r_2 \quad r_3 \quad t]\begin{bmatrix} X \\ Y \\ 0 \\ 1 \end{bmatrix} = A[r_1 \quad r_2 \quad t]\begin{bmatrix} X \\ Y \\ 1 \end{bmatrix}. \tag{3-7}$$

We still use M to denote a point on the model plane, but $M = [X, Y]^T$ since Z always equals to 0. In turn, $\tilde{M} = [X, Y, 1]^T$. Therefore, a model point M and its image m is related by a homography **H:**

$$s\tilde{m} = H\tilde{M} \quad \text{with } H = A[r_1 \quad r_2 \quad t]. \tag{3-8}$$

3.4.2 Homography between the model plane and the image

Given an image in which image coordinates can be measured and a model plane with known coordinates, the homography can be estimated. A homography H is a 3 by 3 matrix defined to a scale, and has 8 degrees of freedom (DoF). Let's denote it by $H = [h_1 \quad h_2 \quad h_3]$. Each of the two-dimensional point has 2 DoF, thus the minimal number of points correspondences to solve the homography is 4. When more than 4 points are available, no exact solution for homography can be achieved since there exists noise in point measurement. The problem is then tending to be solved by minimizing certain cost functions.

3.4.3 Closed-form solution for intrinsic parameters

From Equation (3-8), we have

$$[h_1 \quad h_2 \quad h_3] = \lambda A[r_1 \quad r_2 \quad t], \tag{3-9}$$

where λ is an arbitrary scalar. Using the knowledge that r_1 and r_2 are orthogonal, we have

$$h_1^T A^{-T} A^{-1} h_2 = 0 \tag{3-10}$$

$$h_1^T A^{-T} A^{-1} h_1 = h_2^T A^{-T} A^{-1} h_2 . \tag{3-11}$$

These are two basic constraints on the intrinsic parameters, given one homography. As the DoF of the intrinsic matrix is 5, therefore at least $n \geq 3$ homographies from *n* images are needed to provide a unique solution of the intrinsic parameters.

Let

$$B = A^{-T} A^{-1} \equiv \begin{bmatrix} B_{11} & B_{21} & B_{31} \\ B_{12} & B_{22} & B_{32} \\ B_{13} & B_{23} & B_{33} \end{bmatrix}$$

$$= \begin{bmatrix} \frac{1}{\alpha^2} & -\frac{\gamma}{\alpha^2\beta} & \frac{v_0\gamma - u_0\beta}{\alpha^2\beta} \\ -\frac{\gamma}{\alpha^2\beta} & \frac{\gamma^2}{\alpha^2\beta^2} + \frac{1}{\beta^2} & -\frac{\gamma(v_0\gamma - u_0\beta)}{\alpha^2\beta^2} - \frac{v_0}{\beta^2} \\ \frac{v_0\gamma - u_0\beta}{\alpha^2\beta} & -\frac{\gamma(v_0\gamma - u_0\beta)}{\alpha^2\beta^2} - \frac{v_0}{\beta^2} & \frac{(v_0\gamma - u_0\beta)^2}{\alpha^2\beta^2} + \frac{v_0^2}{\beta^2} + 1 \end{bmatrix} \tag{3-12}$$

Note that B is symmetric, defined by a 6D vector

$$b = \left[B_{11}, B_{12}, B_{22}, B_{13}, B_{23}, B_{33}\right]^T \tag{3-13}$$

Then the two constraints in Equation (3-10) and Equation (3-11) can be rewritten as 2 homogeneous equations of *b*

$$\begin{bmatrix} v_{12}^T \\ (v_{11} - v_{12})^T \end{bmatrix} b = 0 \tag{3-14}$$

with $v_{ij} = [h_{i1}h_{j1} \quad h_{i1}h_{j2} + h_{i2}h_{j1} \quad h_{i2}h_{j2} \quad h_{i3}h_{j1} + h_{i1}h_{j3} \quad h_{i3}h_{j2} + h_{i2}h_{j3} \quad h_{i3}h_{j3}]^T$,

where h_{mn} is the element in the *m*-th row and *n*-th column of the homography matrix. By given *n* homographies, we have

$$Vb = 0 \tag{3-15}$$

where *V* is a 2n-by-6 matrix. The solution of the equations could be obtained by applying least squares algorithm. Once *b* is estimated, we can compute all camera intrinsic matrix *A* as below:

$$v_0 = (b_2 b_4 - b_1 b_5) / \left(b_1 b_3 - b_2^2\right)$$

$$\lambda = b_6 - [b_4^2 + v_0 (b_2 b_4 - b_1 b_5)] / b_1$$

$$\alpha = \sqrt{\lambda / b_1}$$

$$\beta = \sqrt{\lambda b_1 / (b_1 b_3 - b_2^2)}$$

$$\gamma = -b_2 \alpha^2 \beta / \lambda$$

$$u_0 = \gamma v_0 / \alpha - b_4 \alpha^2 / \lambda$$

The closed-form solution is used to get an initial value of the intrinsic matrix A. Maximum likelihood estimation is applied to refine the result further. Thus the intrinsic parameters could be worked out.

3.4.4 Extrinsic parameters estimation

Once A is known, the initial value of extrinsic parameters for every image can be computed from Equation (3-9). We have

$r_i = \lambda A^{-1} h_i$ where i=1,2

$$r_3 = r_1 \times r_2$$

$$t = \lambda A^{-1} h_3$$

The extrinsic parameters could be refined further based on the coordinates of the measured corresponding image points. By eliminating *M* in Equations (3-5) and (3-6), the following fundamental equation is obtained

$$\tilde{m}_i'^T A'^{-T} TRA^{-1} \tilde{m}_i = 0 \quad , \tag{3-16}$$

where *T* is the skew-symmetric matrix defined by *t*. With the multi-stage algorithm proposed in (Zhang, 1997), the extrinsic parameters could be worked out.

3.4.5 Depth information reconstruction

Metric reconstruction of the scene is possible with the intrinsic and extrinsic parameters obtained by linear triangulation methods. According to Equations (3-5) and (3-6), the two projective matrixes *P* and *P'* for the two cameras are defined as

$$P = A\begin{bmatrix} I & 0 \end{bmatrix} \tag{3-17}$$

$$P' = A'\begin{bmatrix} R & t \end{bmatrix}, \tag{3-18}$$

and can be rewritten in the form

$$\begin{bmatrix} x_1 P_{13}^T - P_{11}^T \\ y_1 P_{13}^T - P_{12}^T \\ x_2 P_{23}^T - P_{21}^T \\ y_2 P_{23}^T - P_{22}^T \end{bmatrix} \tilde{M} = B\tilde{M} = 0 \tag{3-19}$$

where $\{(x_i, y_i)|i=1,2\}$ are the Euclidean coordinates of image points (m_1, m_2) and P_{ij} (i=1,2; j=1,2,3) is the j^{th} row of the projective matrix P_i. However, there are only three unknowns in $\tilde{M} = (X, Y, Z, 1)^T$. The over determined set of equations can be solved by least squares technique.

3.5 Camera calibration process

A calibration board is used for the camera intrinsic and extrinsic parameters calibration. As shown in Figure 3-10, the calibration board is consisted of 64 identical squares, with 8 rows by 8 columns. The distances between the neighbour squares are the same. The ratio of the square width and the length between neighbour squares is 4:3.

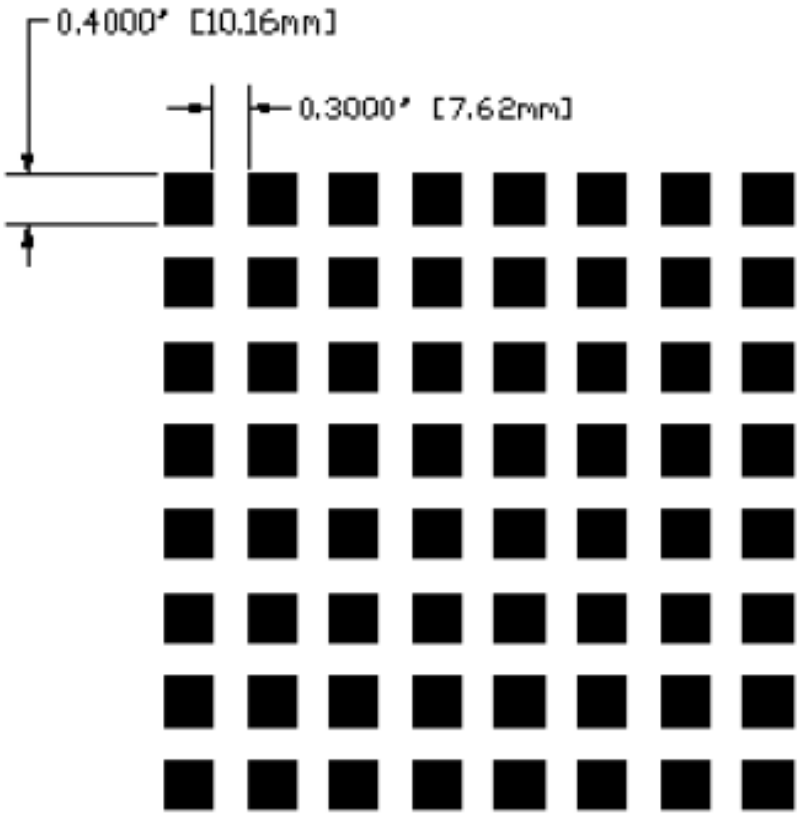

Figure 3-10 Calibration patterns

A corner detection algorithm has been applied to extract the 256 corners of the squares as the known model plane. The details of the corner detection algorithm have been explained in (Wang, 2009). The sample image with the corner detected is shown in Figure 3-11. The 256 corners are extracted successfully and marked with red dots. With the image coordinates of the 256 corners and the known coordinates of the model plane, the homography *H* could be estimated as previously illustrated in section 3.2.2.

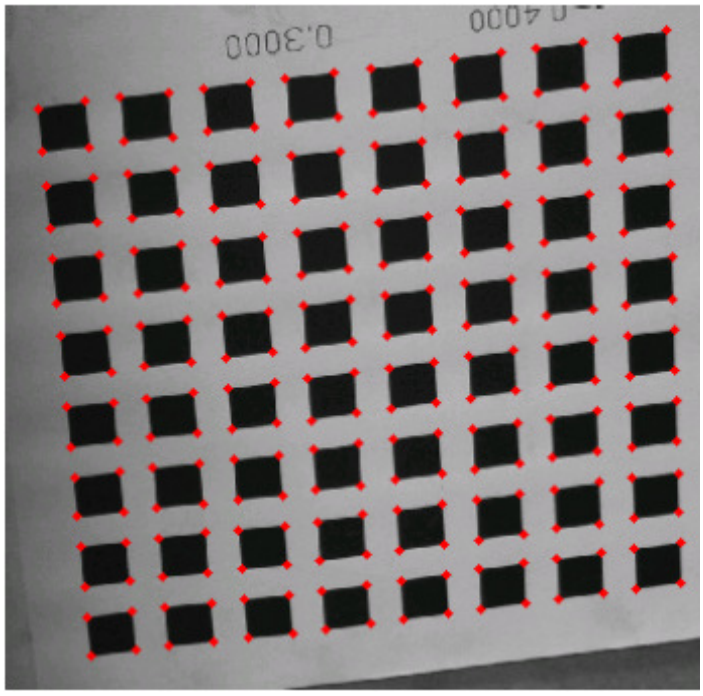

Figure 3-11 Corners extracted from the image

The calibration board was placed arbitrarily at four different positions, resulting four estimated homographies from four model planes, which are sufficient for the camera calibration. The intrinsic matrices *A1* and *A2* of two cameras can be related by Equation (3-20), in which m is the number of pixels per row, and the two matrixes can be solved together combining the constraint. Calibration program reads in the points from 4 left images and 4 right images and performs the algorithms described

in section 3.2. The output of program is the intrinsic parameters of the first virtual camera and the radial distortion parameters. The intrinsic parameters of the second virtual camera can be obtained through Equation (3-20).

$$A2 = A1 - \begin{bmatrix} 0 & 0 & m/2 \\ 0 & 0 & 0 \\ 0 & 0 & 0 \end{bmatrix} \tag{3-20}$$

The obtained calibration parameters are listed below, where *A1* and *A2* are the intrinsic parameters of the two virtual cameras, *R* and *t* the extrinsic parameters indicating the motion between the two cameras.

$$A1 = \begin{bmatrix} 2476.1 & -8.7415 & 516.47 \\ 0 & 2492.6 & 544.41 \\ 0 & 0 & 1 \end{bmatrix}$$

$$A2 = \begin{bmatrix} 2476.1 & -8.7415 & 504.47 \\ 0 & 2492.6 & 544.41 \\ 0 & 0 & 1 \end{bmatrix}$$

$$R = \begin{bmatrix} 0.9424 & 0.011896 & 0.33426 \\ -0.0006381 & 0.99943 & -0.033771 \\ -0.33447 & 0.031612 & 0.94187 \end{bmatrix}$$

$t = \begin{bmatrix} -0.98471 & 0.088197 & 0.15025 \end{bmatrix}^T$.

As discussed in section 3.2.5, the coordinates of the point M in 3D space could be worked out with the calibration parameters and the corresponding coordinates of (m_1,

m_2). Thus the extracted corners could be reconstructed for the validation of the calibration parameters. The reconstruction results of the calibration board at different positions are shown in Figure 3-12. The 3D view of the reconstructed four planes shows very little distortion. The standard deviation defined in Equation (3-21) is then calculated based on the distances between the neighbouring points. The error is less than 5%.

$$\delta = \sqrt{\frac{1}{N}\sum_{i=1}^{N}(x-\mu)^2} \tag{3-21}$$

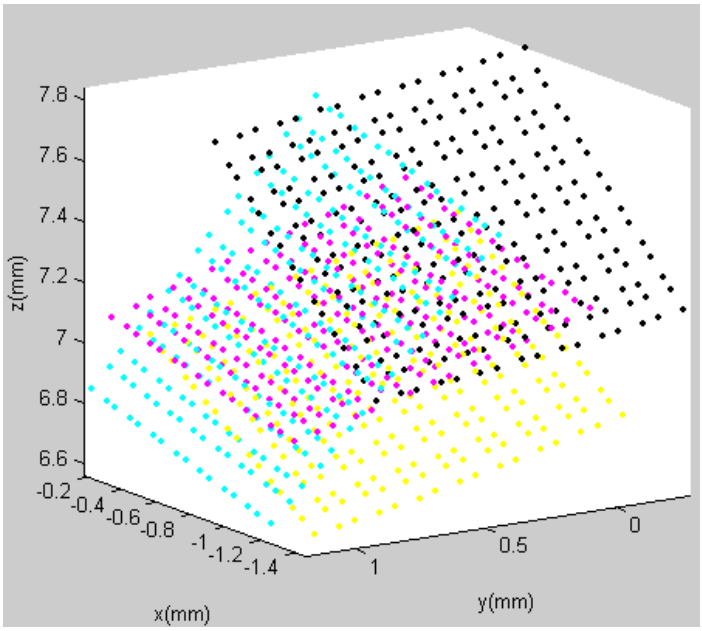

Figure 3-12 Reconstructed planes of the calibration board at different orientations

Stereo camera calibration is a means to determine the intrinsic and extrinsic parameters of the projection. The recommended calibration procedure is as follows:

- Establish the lists of the 2D corner coordinates of the calibration pattern in the real word and their corresponding 2D left and right image coordinates. In this study, the 2D image coordinates is obtained by corner detection.

- The projection matrix P in is determined by direct linear transformation (DLT) and used as the initial values for the Levenberg-Marquardt optimisation.

- Both the intrinsic and extrinsic parameters can be solved by equations that act in the function of projection matrix coefficients (Faugeras, 1993).

3.6 Correspondence problem

3.5.1 Epipolar constraint

The correspondence problem determines which token in the left image corresponds to a given token in the right image. Epipolar constraint is a crucial concept that reduces the number of potential matches for any given point. Figure 3-13 illustrates the epipolar geometry. The two cameras are represented by their optical centres C and C' and the image planes I and I'. The line connecting the camera centres C and C' is referred to as the baseline. The points at which the line through the centers of projection intersects the image planes are called the epipoles e and e'. The 3D point M observed by the two cameras and the two corresponding rays from opitcal centers C and C' define an epipolar plane Π. Point M can lie anywhere on the ray from C through m. However, since the image of this ray in the right image is the epiplar line through the corresponding point m', the correct match must lie on the epipolar line. So this actually restricts the search for the match of m along the corresponding epipolar line. The search for correspondences is thus reduced to a 1D problem.

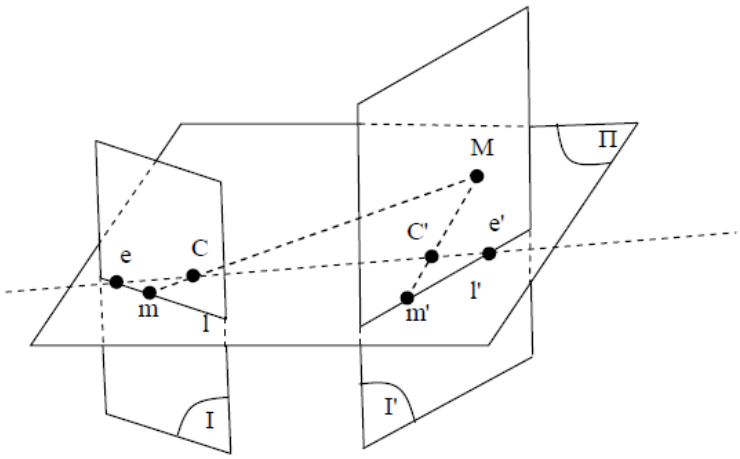

Figure 3-13 Epipolar geometry

3.5.2 Rectification

With the motion parameters given through the extrinsic parameters estimation, corresponding feature points from the image pairs can be reconstructed. However reconstructing numerous feature points only offers a sparse surface model. If a visually surface model is to be reconstructed, standard stereo matching techniques which employ dense disparity matching should be used here.

The system adopted in this study is a verged stereo system, in which the image planes of the two virtual cameras can not be regarded as parallel, as shown in Figure 3-14 (a). However, standard stereo matching techniques deal with the non-verged stereo system, equivalently a translation system, in which the two identical-setting cameras are set parallel to each other, as shown in Figure 3-14 (b). In the non-verged system, the epipoles are at infinity and epipolar lines are parallel to each other.

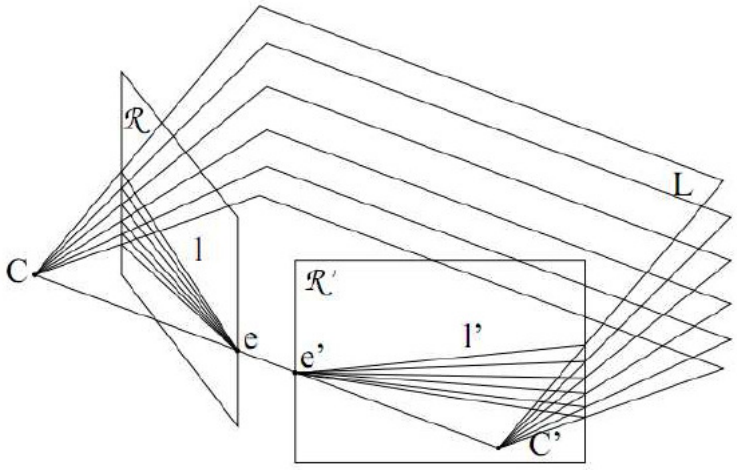

(a)

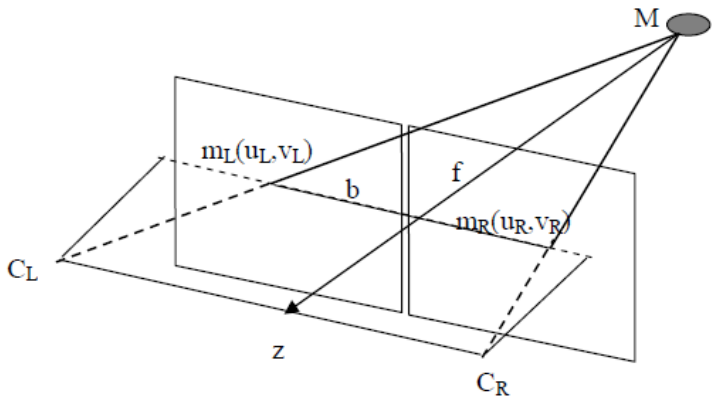

(b)

Figure 3-14 (a) A verged stereo system (b) A non-verged stereo system

The rectification method is to transform images taken with a verged stereo system to rectified images which can be considered as taken with a non-verged stereo system. There are several rectification methods existing, here in this study we use the polar rectification method proposed by Marc Pofelley in [Pollefeys *et al.*, 2004]. The advantage of this approach is that the rectification procedure is relatively simple, and the method guarantees a minimal rectified image size, which will not increase computation in the reconstruction.

To construct the rectified images, a scan-line holding the epipole fixed, rotates and scans gradually down through the image area between the extreme epipolar lines. The extreme epipolar lines are determined depending on the locations of the epipoles to the images. The epipoles of the two images can be obtained through decomposition of fundamental matrix. After each shift, the pixels on the scan-line are transferred to a row in the rectified image. This procedure is illustrated by Figure 3-15. When the left and right images are rectified to a standard geometry, the corresponding points in the two images will lie in the same row. Thus the disparity between them is only one dimensional and easy to compute.

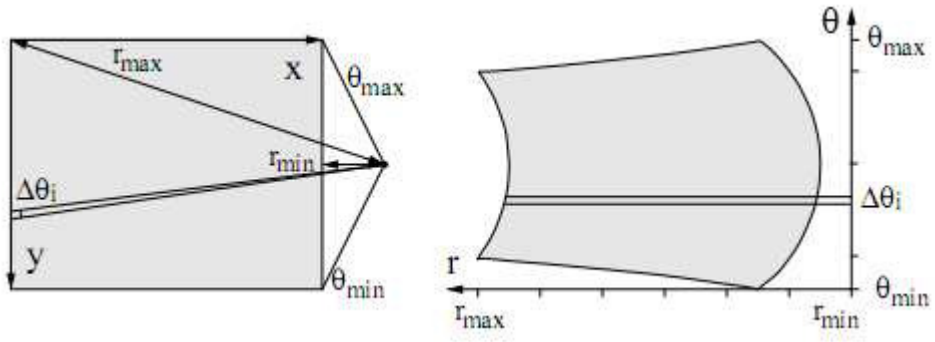

Figure 3-15 Rectification procedure of the image

3.7 Curve reconstruction

Besides points, curves are also important features in scenes. Three dimensional reconstruction based on matching is significant in application in fluid study and research. Curves may be represented by a set of linked points with approximating mathematical equations. B-spline modelling have been applied to curve matching and reconstruction in stereo techniques (Robert and Faugeras, 1991, Bascle and Deriche, 1993, Xiao and Li, 2005). In B-spline curve, certain amounts of knots are distributed along the curve. For the curves on stereo images, the knots $\{ m_i \}$ on one

B-spline curve are selected as sample points. With the epipolar geometry established through the calibration parameters, the matching points $\{ m_i' \}$ on the other curve could be obtained. With the matching primitive sets $\{ m_i \}$ and $\{ m_i' \}$, the 3D points $\{ M_i \}$ can be estimated based on the algorithm of point reconstruction. Then with another B-spline approximation, the 3D curve can be obtained with the set of 3D points.

3.8 Surface reconstruction

Surface reconstruction could supply us the depth information of an object. First, the stereo image pairs are transformed by using the rectification method. In the rectified image pairs, all corresponding points are in the same row and could be searched through area-based correlation methods. Hence each pixel within the matching range in the left image, a corresponding point in the right image will be given. The relative 3D position can then be obtained using the triangulation method. The method works relatively well in surfaces with texture or being non-smooth, however, the correlation approach tends to fail in smooth surfaces without features.

The raw data does not really describe surfaces, but only clouds of point coordinates in three-dimensional space. It is of importance for the data representation to come as close as possible to the actual object and to preserve its topology. Thus the data points must be represented in a structured form suitable for interactive visualisation. The most common structure is the three-dimensional mesh. In this study, the surface is constructed by MATLAB command ‘mesh’ with the three-dimensional

coordinates. An example has been shown in Figure 3-16 , the area of interest of the flame surface has been reconstructed successfully.

(a)

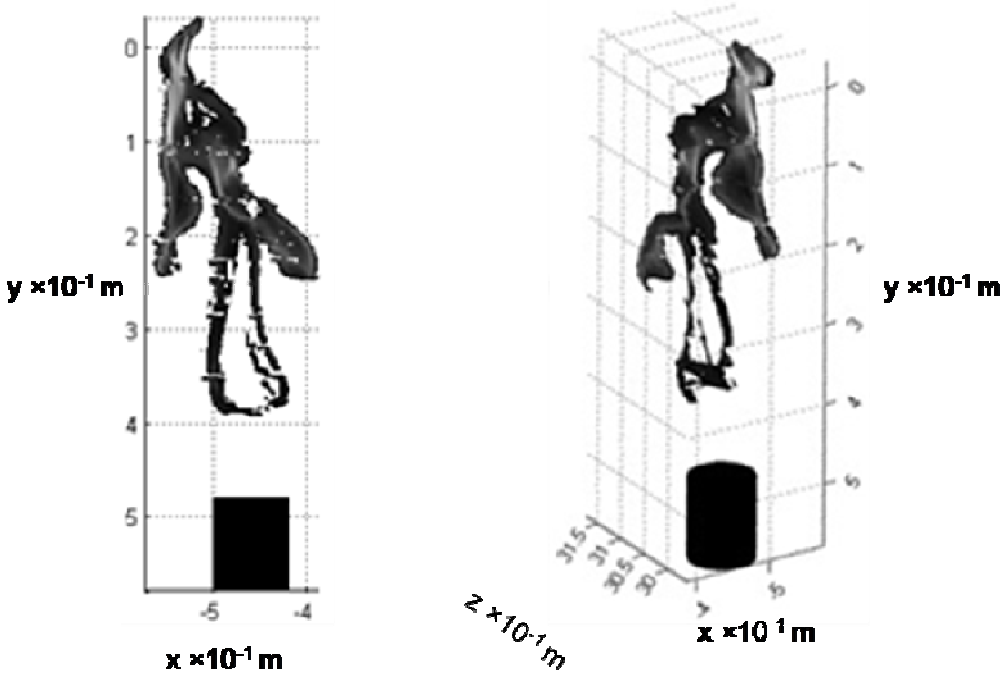

(b)

Figure 3-16 Reconstructed flame surface (a) Stereo images; (b) Reconstructed flame surface at different view angles

The obstacle existing in flame reconstruction is the semi-transparency of flames. The hypothesis of the stereo reconstruction is that the object to be reconstructed is an opaque diffuse object. However, as the flames are semi-transparent, the images taken are influenced by the integration of light along different rays. This fact complicates the matching between image points on two perspective images. Without further information, such as identified features, it is difficult to match the pixels between two images. There remains much work to be done in developing a truly accurate and robust correspondence algorithm (Adelson E, 1990, Richard Szeliski, 1999, Szeliski et al., 2000).

3.9 Summary

In this chapter, the algorithms of 3D reconstruction from stereo images are introduced briefly. The camera calibration process has been presented. With the capability to establish the epipolar geometry between two perspectives, it is possible to reconstruct various features in the diagnostic procedure, such as particle tracking in the flow field, feature curves extraction, flame surface reconstruction, etc.

Chapter 4 Stereoscopic Schlieren/Shadowgraph Imaging System

4.1 Introduction

As reviewed in section 2.2.3.2, stereoscopic schlieren techniques have been attempted in the middle of the 20th century. However, no real 'stereoscopic' images have been obtained. The exploration stopped at very early stage. Although the tomography and synchronization schlieren have been able to provide some specific three dimensional results, the multi view requirement and complex setup have limited their practical applications.

The great progress in stereo reconstruction based on digital image processing has inspired the idea to explore the possibility of developing stereoscopic schlieren diagnostic technique using modern high speed cameras. Rather than only to observe the 3D images in a stereoscope, the quantitative depth information can be extracted

through 3D digital reconstruction. In this chapter, a stereoscopic schlieren/shadowgraph system has been developed by extending the conventional z-type schlieren setup. The test section is chosen at the cross area of the two inclined beams rather than the parallel beams; as a result the shadowgraph images obtained satisfy the projective geometry. The algorithms introduced in Chapter 3 can be applied to the stereoscopic schlieren/shadowgraph system for 3D reconstruction.

4.2 Experimental setup

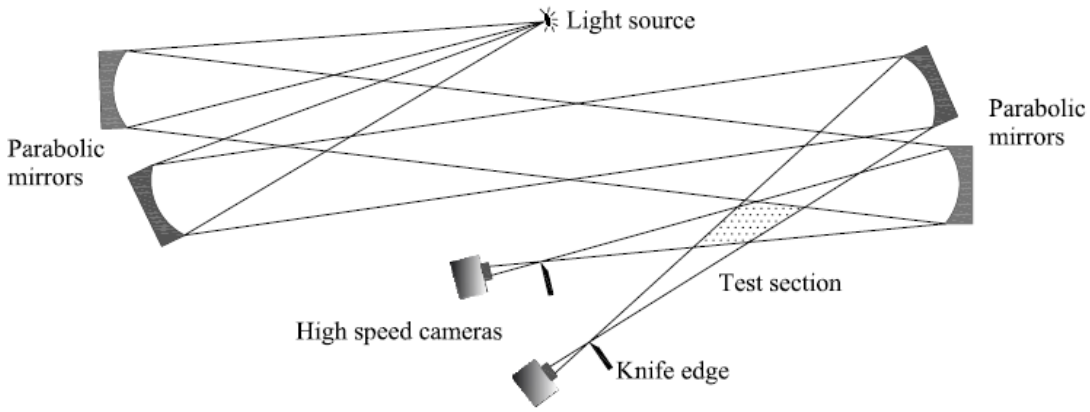

Figure 4-1 Schematic illustration of the stereoscopic schlieren/shadowgraph system

The schematic apparatus of the stereoscopic schlieren system is shown in Figure 4-1. The system consists of four parabolic mirrors, forming two inclined light beams. The test section of the stereoscopic schlieren system is placed at the cross section of the two converging beams. The light source is a 500 W Xenon lamp. The λ/10 parabolic mirrors are 0.3048 m (12 inches) in diameter and 3.048 m (10 feet) in focal length. Two high speed cameras (Photron SA-3) are used to record the schlieren images simultaneously. The converging light beam projects on the camera plane directly. Two knife edges are placed at the focal points of the parabolic mirrors just in front of the cameras. The positions of the knife edges should be adjusted according to the

sensitivity requirements of the test objects. In this thesis, it is more effective to reduce the background noise by leaving the knife edges fully open. Thus the images obtained are actually shadowgraph.

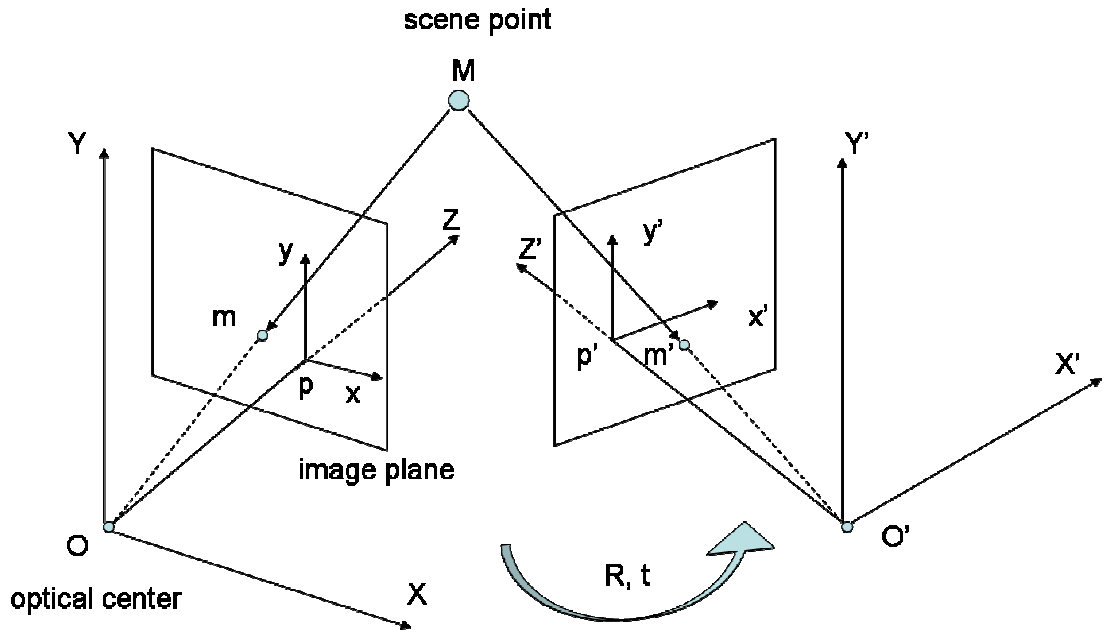

Figure 4-2 Physical and image coordinates

Figure 4-2 shows the physical coordinates of the scene point in the test section (as illustrated in Figure 4-1) and the image coordinates on the image plane. The relationship between the two coordinates satisfies the principles of projective geometry, the same as the pinhole model shown in Figure 3-9.

4.3 Synchronisation of the two high speed cameras

Two Photron SA-3 monochrome high speed cameras are used in the experiments to take schlieren and stereo images simultaneously. The image sensor of the camera is C-MOS. The two high speed cameras are synchronised in master-slave configuration. The connections of the configuration are illustrated in Figure 4-3. One camera is

designated as master, while the other as slave. The master camera will generate a source synchronisation signal for the slave camera so that both cameras can be triggered at the same time with the trigger switch. The frame rate and image resolution of the high speed camera are listed in Table 4-1.

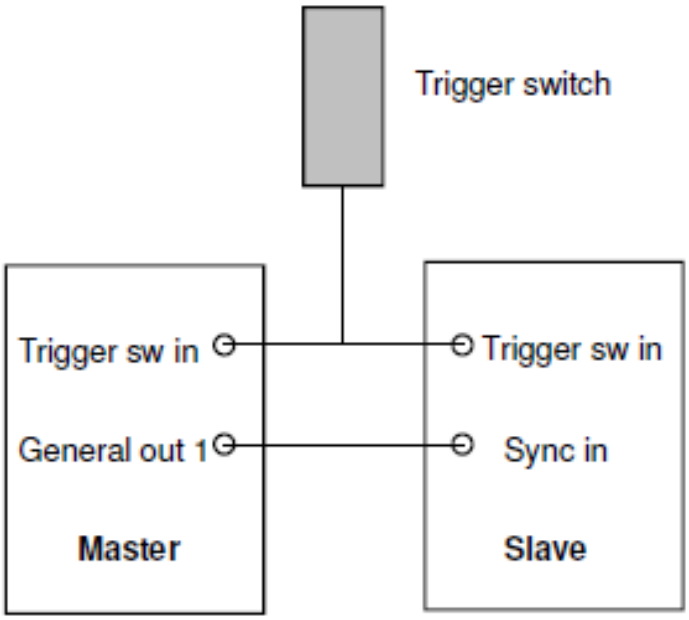

Figure 4-3 Setup of two SA-3 cameras in master-slave configuration

Table 4-1 Frame rate versus image resolution (Photron SA-3)

Frame Rate (fps)	Maximum Resolution (pixels)
2,000	1024 × 1024
3,000	768 × 768
6,000	512 × 512
15,000	256 × 256
120,000	128 ×16

4.4 Camera calibration

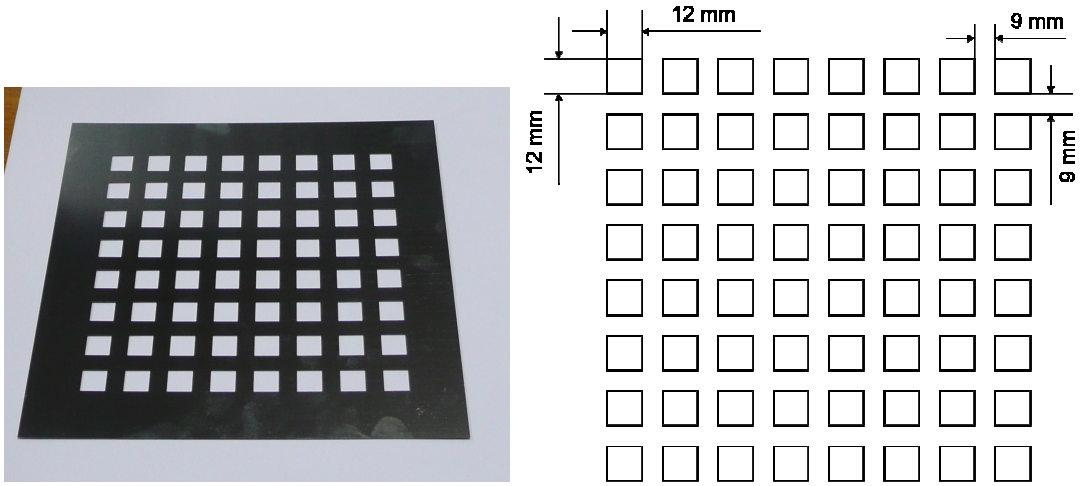

Figure 4-4 (a) Image of the calibration board; (b) Dimensions of the planar pattern on the calibration board

In order to obtain the camera parameters by calibration, a specific accurate planar pattern is required. For supplying the optical path in the stereoscopic shadowgraph system, a steel plate with identical square holes is designed for the calibration process. Avoiding the distortion caused by conventional punching method, the calibration board is manufactured by accurate acid etching on a thin steel plate (0.5 mm in thickness). The error of the square dimension is less than 1 μm. As shown in Figure 4-4, the calibration board consists of 64 identical square holes, with 8 rows by 8 columns. The distances between the neighbouring squares are the same.

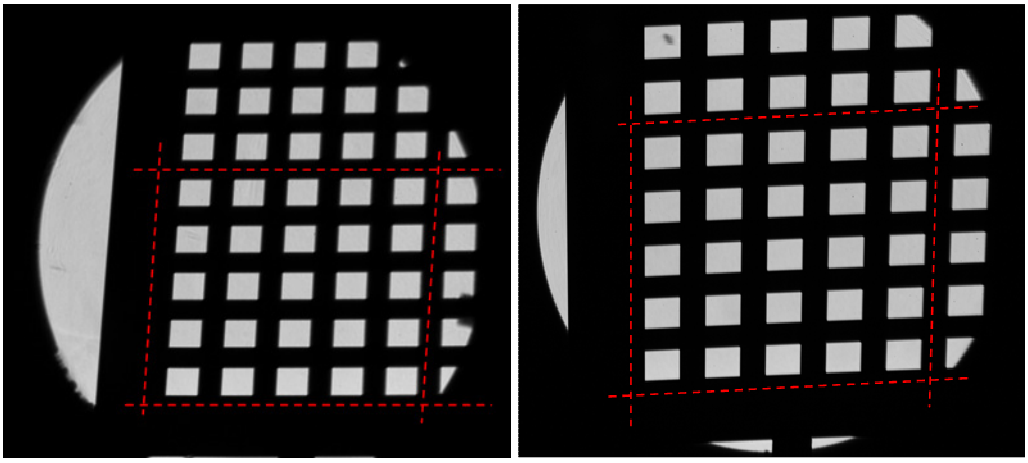

(a) Pose the calibration board right to the two cameras

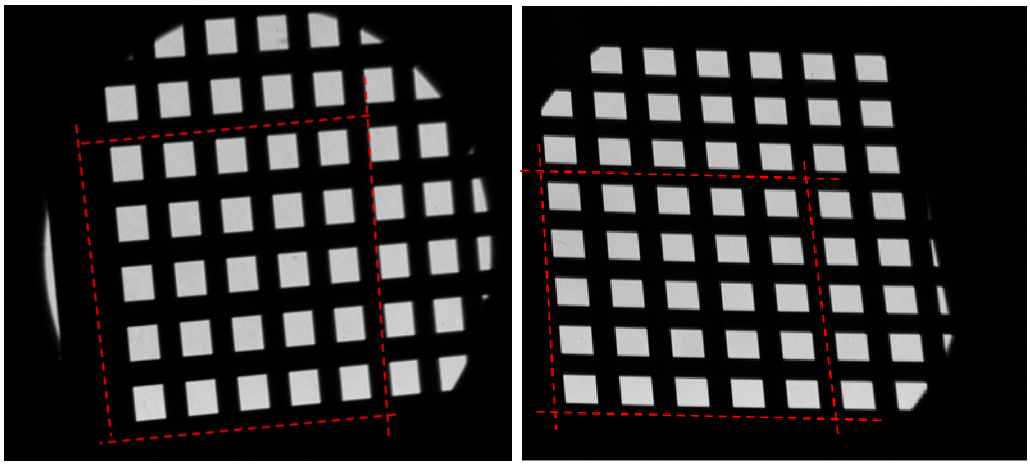

(b) Rotate the calibration board around 30 degrees clockwise

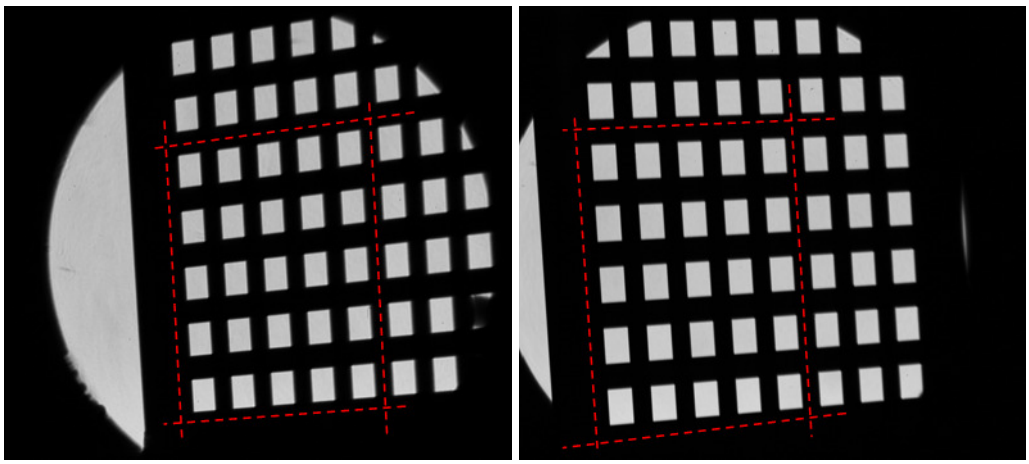

(c) Rotate the calibration board around 30 degrees anticlockwise

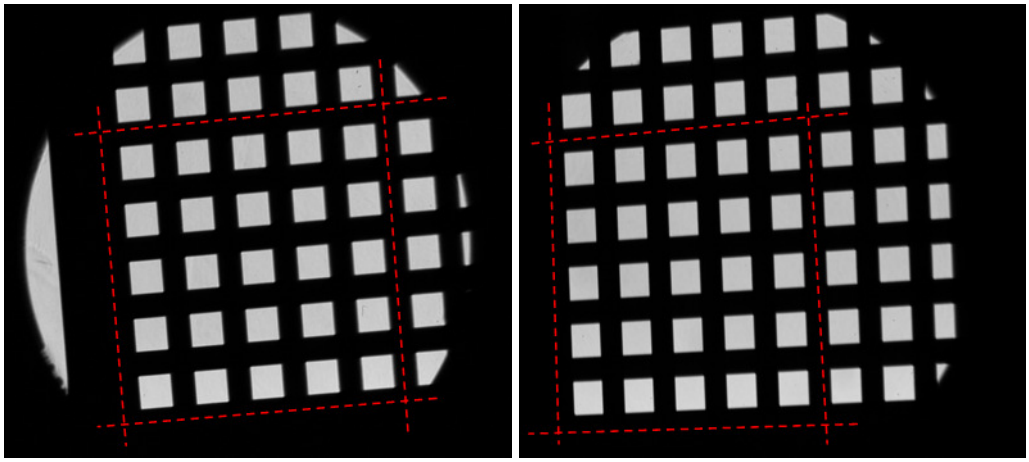

(d) Rotate the calibration board upward around 30 degrees

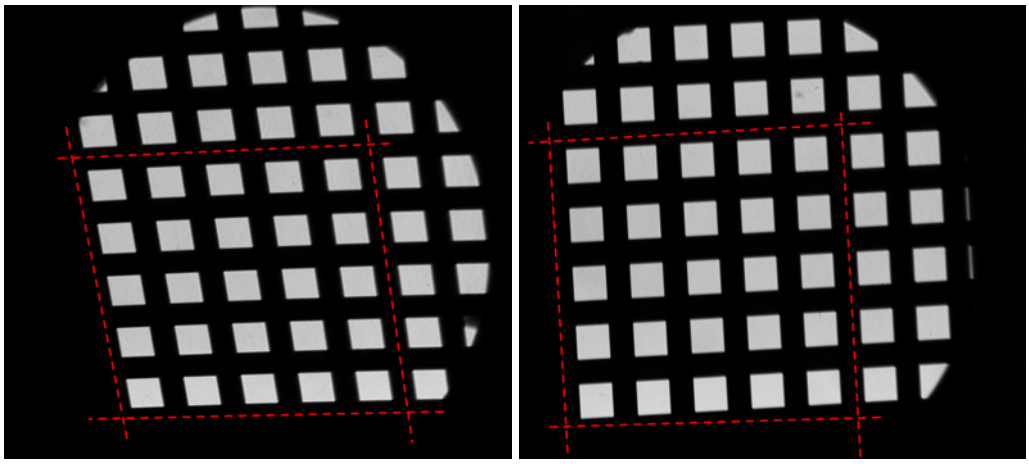

(e) Rotate the calibration board downward around 30 degrees

Figure 4-5 Five pairs of schlieren images of the calibration board

Following the calibration procedures introduced in Chapter 3, the calibration parameters are estimated by placing the calibration board at five different orientations. The schlieren image pairs at five positions are shown in Figure 4-5. Due to the limited dimension of the test section, only 25 squares located at the cross area of the four lines in the lower left corner are selected for the calibration process.

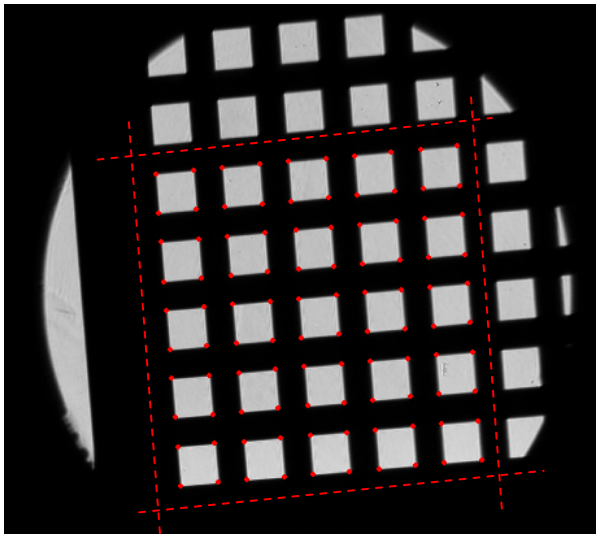

Figure 4-6 Corners extracted for calibration

The MATLAB program with corner detection function was utilized to extract the corners of the selected squares. A sample image with the extracted corners is presented in Figure 4-6. The corners are marked with red spots. The 100 corners of the squares are extracted as the known model plane. The pixel coordinates of all the extracted corners in the five image pairs are saved for the calibration process. As has mentioned in section 3.2.2, the minimum points needed for estimating a homography is 4. The 100 points extracted from the corners are sufficient for the homography estimation. With the corresponding point information and Equation (3-2) to Equation (3-8), the intrinsic parameters of the two cameras could be worked out respectively. The calibration result for this case is as follows:

$$A1 = \begin{bmatrix} 8609.7 & -6.0013 & 1687.6 \\ 0 & 8498.7 & 535.11 \\ 0 & 0 & 1 \end{bmatrix}$$

$$A2 = \begin{bmatrix} 8723.7 & 21.92 & -363.84 \\ 0 & 8702 & 926.68 \\ 0 & 0 & 1 \end{bmatrix},$$

where *A1* is the intrinsic parameters from the left five images and *A2* from right five images. With the intrinsic parameters *A1*, *A2* and the image coordinates of the corresponding points, the extrinsic parameters *R* and *t* could be calculated. The results are listed below:

$$R = \begin{bmatrix} 0.97529 & 0.030322 & -0.21882 \\ -0.042055 & 0.99791 & -0.049162 \\ 0.21687 & 0.05715 & 0.97453 \end{bmatrix}$$

$$t = \begin{bmatrix} 0.98582 & -0.0058141 & 0.16769 \end{bmatrix}^T$$

With the intrinsic and extrinsic parameters, the 3D coordinates of the extracted corners could be worked out. The reconstruction results of the calibration board at five positions are demonstrated in Figure 4-7. Each colour represents a different position. Through the different views of the 3D results, five planes could be observed obviously. The corners are roughly in the same plane of each colour. The rows and columns are orthogonal roughly, which shows the accuracy of the reconstruction results to some extent.

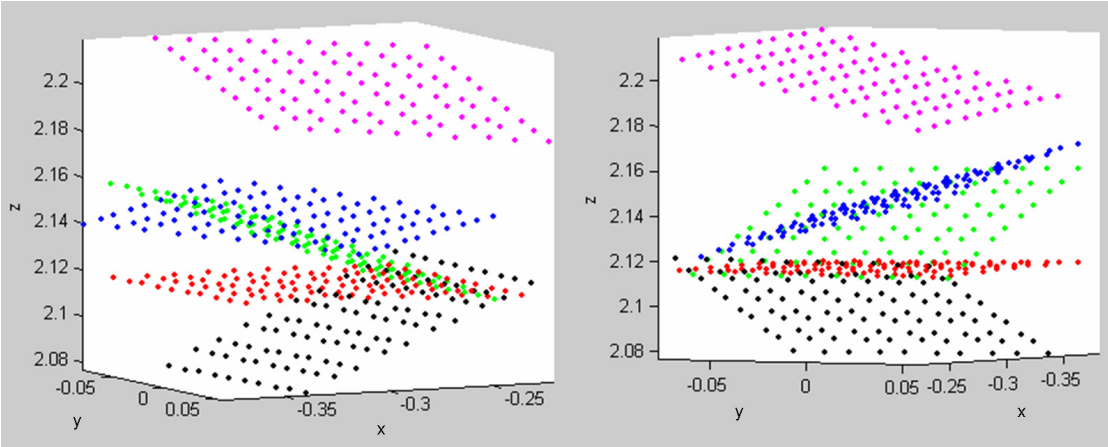

Figure 4-7 Reconstructed planes of the calibration board at different positions

The lengths of the four edges of each square are calculated based on the 3D coordinates obtained. The standard deviation error δ between the reconstruction and real dimensions are calculated according to Equation (3-21). The error obtained shows to be less than 2%. The accuracy of the calibration and reconstruction is reasonable for further application.

4.5 Conclusion

A stereoscopic schlieren system has been established on the basis of conventional z-type schlieren system. The system is calibrated based on projective geometry. A steel calibration board manufactured by accurate acid etching method is used for the calibration. The calibration process and algorithms are introduced briefly. Furthermore, the accuracy of the calibration and reconstruction is analysed based on the calibration results with a standard deviation error of approximately 2%.

The advantage of the stereoscopic schliren/shadowgraph system is to extract the quantitative depth information and thus to reconstruct the 3D coordinates of the object from two schlieren/shadowgraph images. The method has acted as a bridge to combine stereo and shadowgraph successfully, which enables it to broaden the application of stereo technique and to improve the capability of shadowgraph technique. The technique is able to reconstruct the 3D structures in a specific volume rather than only on a surface such as stereoscopic PIV. The synchronization of two high speed cameras makes it possible to obtain time resolved results of unsteady phenomenon. Therefore, it is possible to reconstruct various features extracted in the diagnostic procedure, such as particles tracing to observe the motion of fluid, the feature curves indicating the vortex developing in turbulent flow, etc.

Because the optical geometry is only decided by the mirrors and lenses in the system, both the schlieren and shadowgraph images will share the same projective geometry relationships. The method established in this study should also be applicable to schlieren systems. However, the knife edge influence on the schlieren image requires extra efforts in getting a good pair of stereo images.

Chapter 5 Applications of High Speed Stereoscopic Shadowgraph Technique

5.1 Introduction

In Chapter 4, the experimental setup and calibration process of the high speed stereoscopic shadowgraph system are introduced. In this chapter, applications of the stereoscopic shadowgraph system are investigated using different test cases. A static model is used to conduct the point reconstruction in section 5.2, followed by the investigation of a dynamic bubble bursting process using the high speed stereoscopic shadowgraph technique in section 5.3. In section 5.4, static 3D curve is reconstructed based on curve reconstruction algorithms.

5.2 Point reconstruction in static object

5.2.1 Model introduction

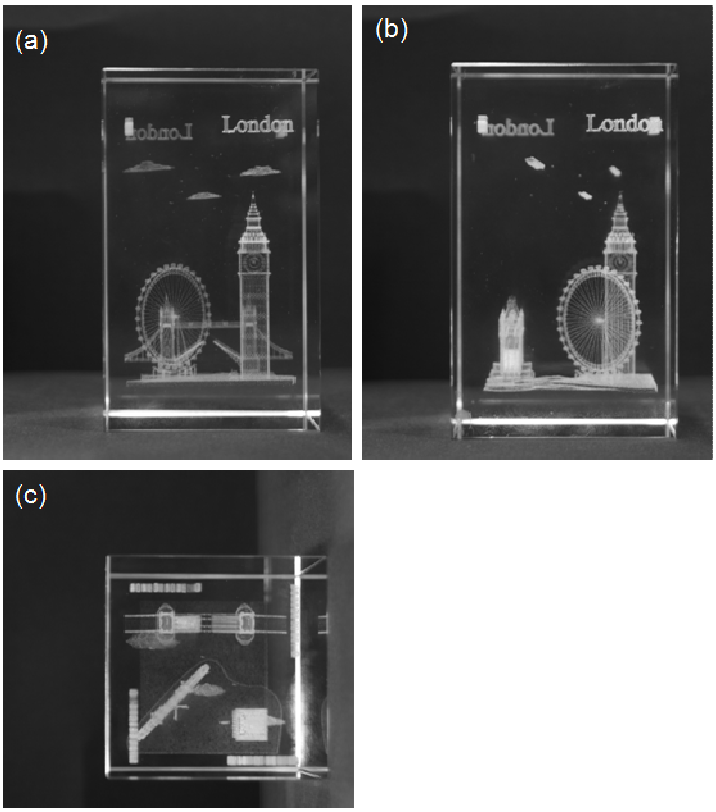

Figure 5-1 Different views of the crystal block
(a) Front view; (b) Side view; (c) Top view

In order to estimate the reconstruction accuracy of the stereoscopic shadowgraph system, a static model with known dimensions is utilized for the test model. Regarding the optical path requirement of the system, a crystal block with internal laser etched 3D figures inside is used as a static model for the application of the experimental apparatus. As shown in Figure 5-1, the crystal block used in this study contains three figures (a tower, a Ferris wheel and a tower bridge), four words of 'London' in different directions and some clouds. The 3D figures are obtained through Sub-Surface Laser Engraving technique. This is the process of having a laser beam penetrate a crystal to create tiny cracks (points or dots) in the glass. Thousands of little cracks represent a unique mosaic of the 3D figures. Since the cracks will

cause density variation, the 3D figures inside the crystal block are visible in the shadowgraph images.

5.2.2 Selected points reconstruction

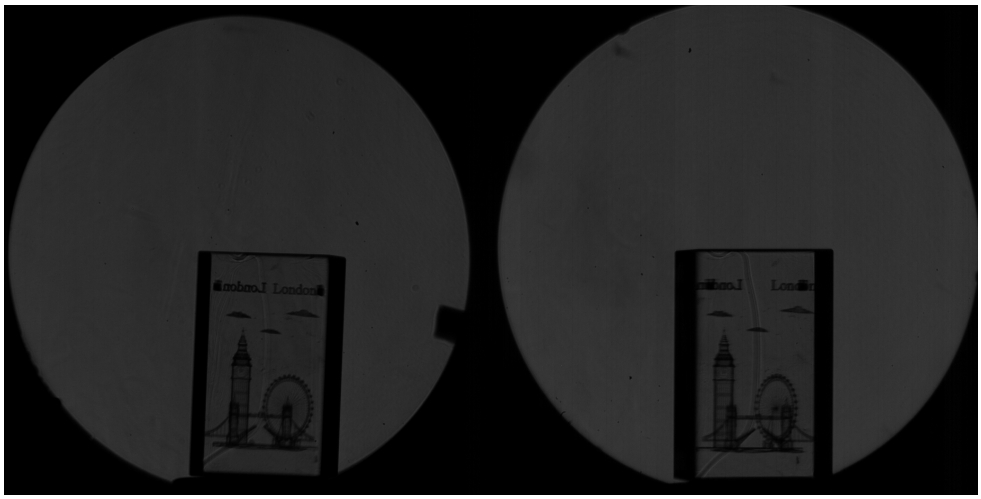

Figure 5-2 Stereoscopic shadowgraph pair of the crystal block

Once the calibration process is completed, the model object is put into the test section. The shadowgraph pairs of the crystal block were taken while the cameras and light beams were kept exactly the same positions as the calibration process. Thus the calibration parameters could be utilized for further 3D reconstruction. A pair of stereoscopic shadowgraph images of the crystal block is illustrated in Figure 5-2. It could be observed that the 3D figures could be seen clearly and the two images are at slightly different angles.

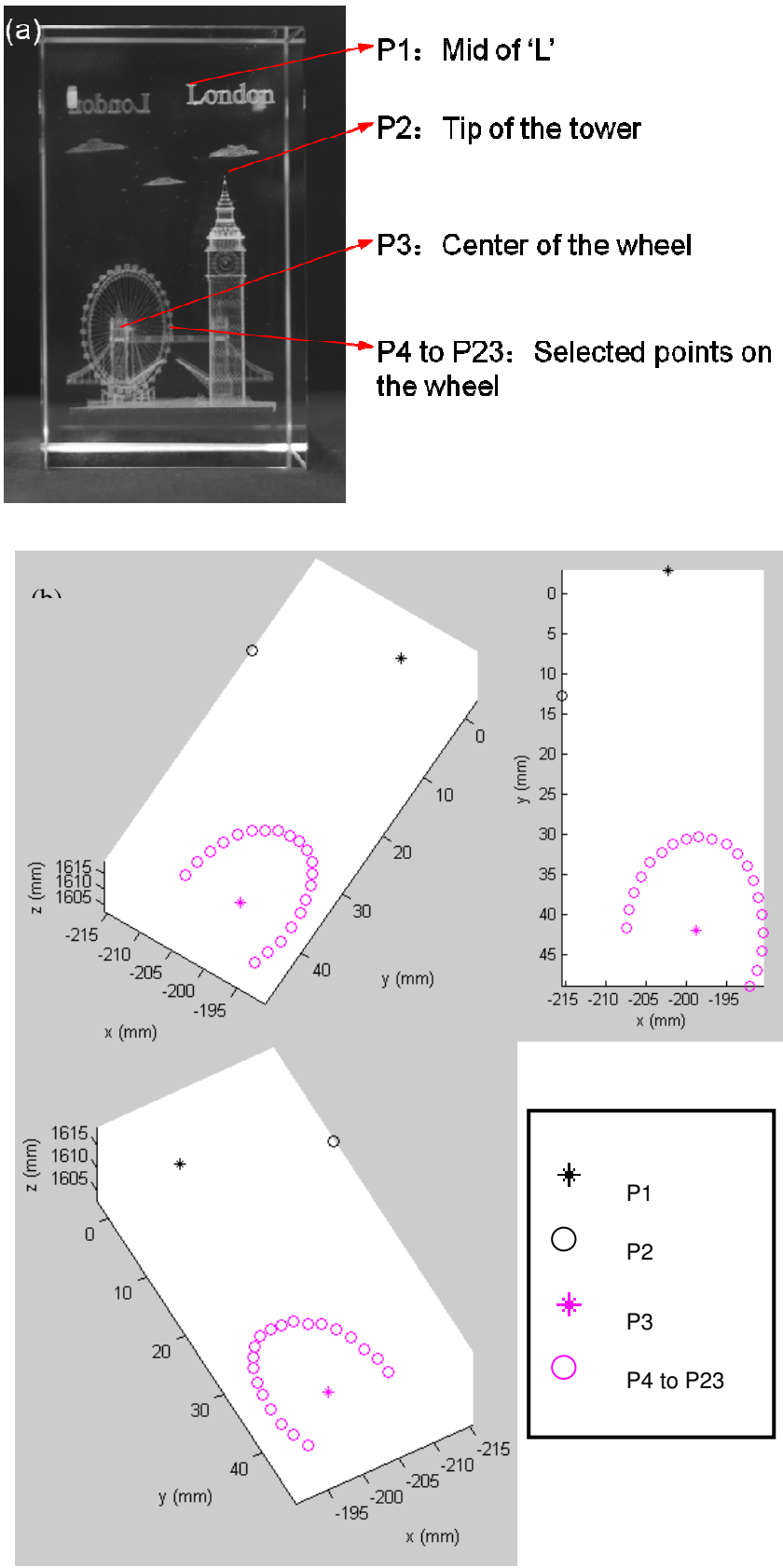

Figure 5-3 3D reconstruction of the selected points from the crystal block

(a) Illustration of the selected points; (b) 3D views of the reconstruction points

As shown in Figure 5-3 (a), some points are selected for the 3D reconstruction and denoted as P1 to P23 respectively. The selected points are convenient to identify in the stereoscopic shadowgraph image pair, and act as the corresponding points for reconstruction. The reconstruction results of the selected points P1 to P23 are illustrated in Figure 5-3 (b). The locations of the reconstructed points match the real positions well, which demonstrates the good reconstruction accuracy.

5.2.3 Error analysis

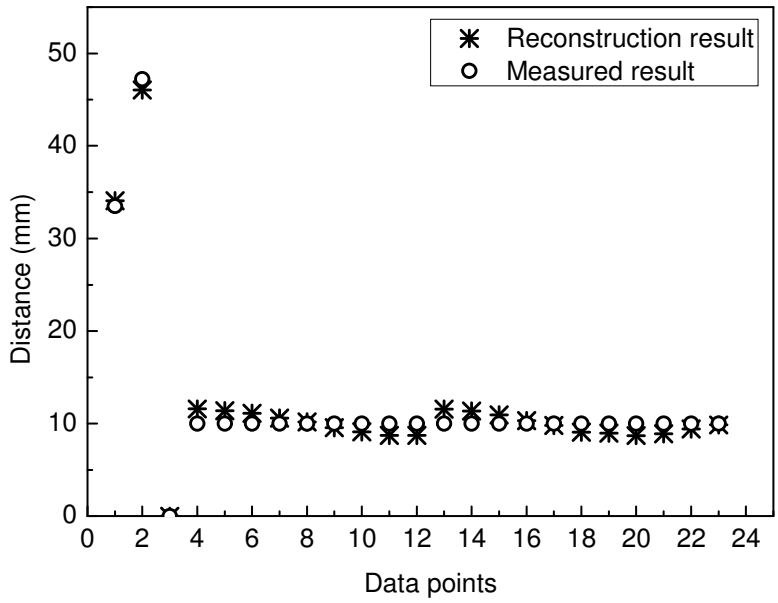

Figure 5-4 The distances between the selected points and P3

The distances between the selected points and P3 are calculated based on the obtained 3D coordinates. The real 3D coordinates are measured by putting the crystal block in the parallel beam from top, front and side views with the conventional schlieren setup. The reconstruction result and the real measured dimensions show consistency throughout, as shown in Figure 5-4. The slight fluctuation deviation at points P4 to P23 may be caused by the point extraction error. The standard deviation error between the reconstruction and measured dimensions is about 5%. The accuracy of the reconstruction depends not only on the calibration

parameters but also the correspondence accuracy of the points on both images. With the calibration parameters fixed, the reconstruction accuracy will be affected by the correspondence accuracy and should be considered more carefully at actual application.

5.3 Bubble bursting investigation based on point reconstruction

5.3.1 Bubble bursting process

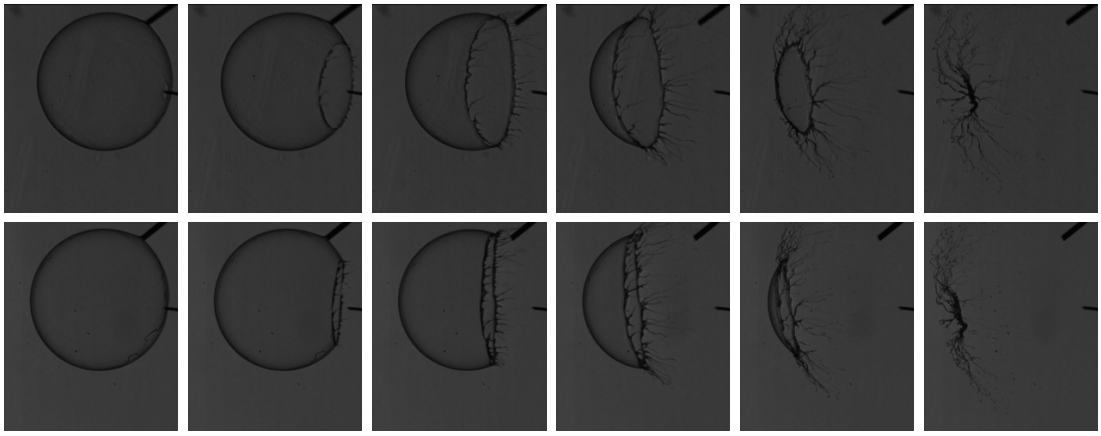

0.2 ms 2.2 ms 4.2 ms 6.2 ms 8.2 ms 10.2 ms

Figure 5-5 Stereo shadowgraph image sequences of bubble bursting

(The Weber number, $We = \frac{\rho U^2 l}{\gamma}$, based on the film retracting velocity U and the bubble diameter l is around 8.6×10^4.)

Thin liquid films, such as soap bubbles, have been investigated as an effective medium for transport processes in physics, chemistry and engineering (de Gennes, 2004, Eggers and Villermaux, 2008, Isenberg, 1978). It is believed that bubble rupture is a source for aerosol droplets (MacIntyre, 1972, Woodcock et al., 1953). Bubble bursting is essential for the foam evolution theories and relevant to health (Angenent et al., 2005) and climate (Wu, 1981). A latest paper on Nature (Bird et al., 2010) pointed out that interfacial bubbles can create daughter bubbles when they rupture, rather than vanishing. The precise measurement on the bubble rupture

process will definitely help us to gain further physical insights and provide data for model validation.

Because of the transparent nature of most soap bubbles, it is difficult to show the bubble bursting boundary clearly with direct imaging since the images could easily be contaminated by background or light reflection. The shadowgraph technique is a good alternative method of investigating bubbles bursting due to the sharp density difference between the liquid and air. The high speed stereoscopic shadowgraph system established in this thesis provides an effective means to study the 3D evolution of the bubble bursting process. In the experiments, a soap bubble was introduced via a thin glass tube. The diameter of the bubble is approximately 44 mm. A sharp tip was used to puncture the bubble and two high speed cameras were synchronised to capture shadowgraph images of the bursting process at 5,000 fps at two different angles. The two shadowgraph image sequences are presented in Figure 5-5 with an interval of 1 ms between each consecutive image. It can be observed that a hole is formed at the bursting initiation point and a rolled-up rim is rapidly moving along the bubble surface, absorbing the unbroken film in its path. The shape of the rim is torus-like with irregular bulges. The bulges turn to ‘finger-like’ liquid lines and become longer while the bubble continues to burst. Some droplets have been torn from the bulges by aerodynamic forces and surface tension. The diameter of the bursting rim increases at first and then reaches the maximum diameter when half of the bubble surface has vanished. After this peak position, the rim begins to decrease gradually. Finally, all the liquid lines and droplets formed by the bulges converge to the same point. The bubble surface vanishing process lasts for about 10.6 ms, after which only residual liquid lines and droplets are left.

5.3.2 Correspondence points

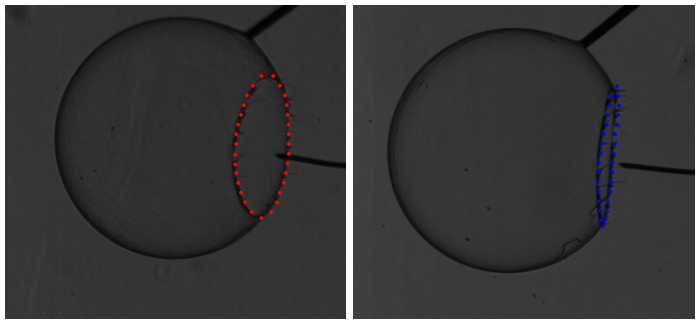

(a)

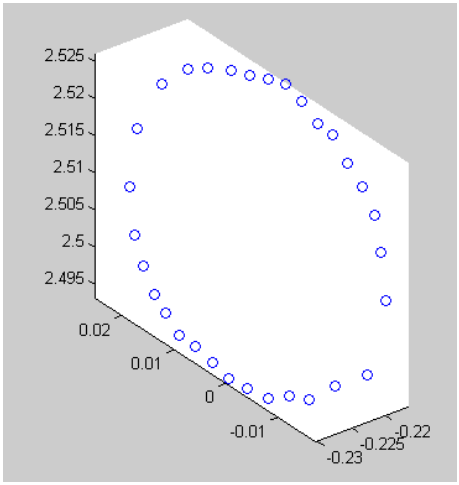

(b)

Figure 5-6 (a) Correspondence points selected on the bursting surface; (b) Reconstructed bursting surface in 3D space

Based on the obtained calibration parameters, the rim can be reconstructed into 3D coordinates once the corresponding points in the bubble bursting rim are matched. First, the image pairs are transferred through rectification under projective geometry restraints. The corresponding points will be located at the same height in the two images. Second, the points in the left image are selected from the image in advance. The coordinates of the selected points are recorded. Third, since the correspondence points in the right image have the same y-coordinate as in the left image, it is then easy to find out the matching points in the rectification image pairs. A sample pair of images with correspondence points is illustrated in Figure 5-6 (a). The points in the left image are selected to distribute on the bursting rim almost evenly. It could be

observed that the matching points in the right image fit the bursting rim quite well, which indicates the accuracy of the point matching. The reconstructed points in 3D space are shown in Figure 5-6 (b). These points are utilized to present the bubble bursting process in the following section.

5.3.3 Bubble bursting rim reconstruction

The time resolved bubble bursting rims are reconstructed based on the correspondence points. The reconstruction results are illustrated in Figure 5-7 at different view angles. The bursting rims from 1.4 ms to 8.6 ms with a time interval of 0.6 ms are reconstructed. The 3D shape of the bursting process indicates that the bubble is bursting along the axis of from initiation point to the bubble center step by step. It can be observed that the time resolved bursting rims on the whole are still in a shape of the original bubble. The shape of the rim at each time step is elliptical but irregular. The irregular structure of the bursting rims could only be well understood by 3D shape, which shows the unique advantage of high speed stereoscopic shadowgraph technique established in this thesis.

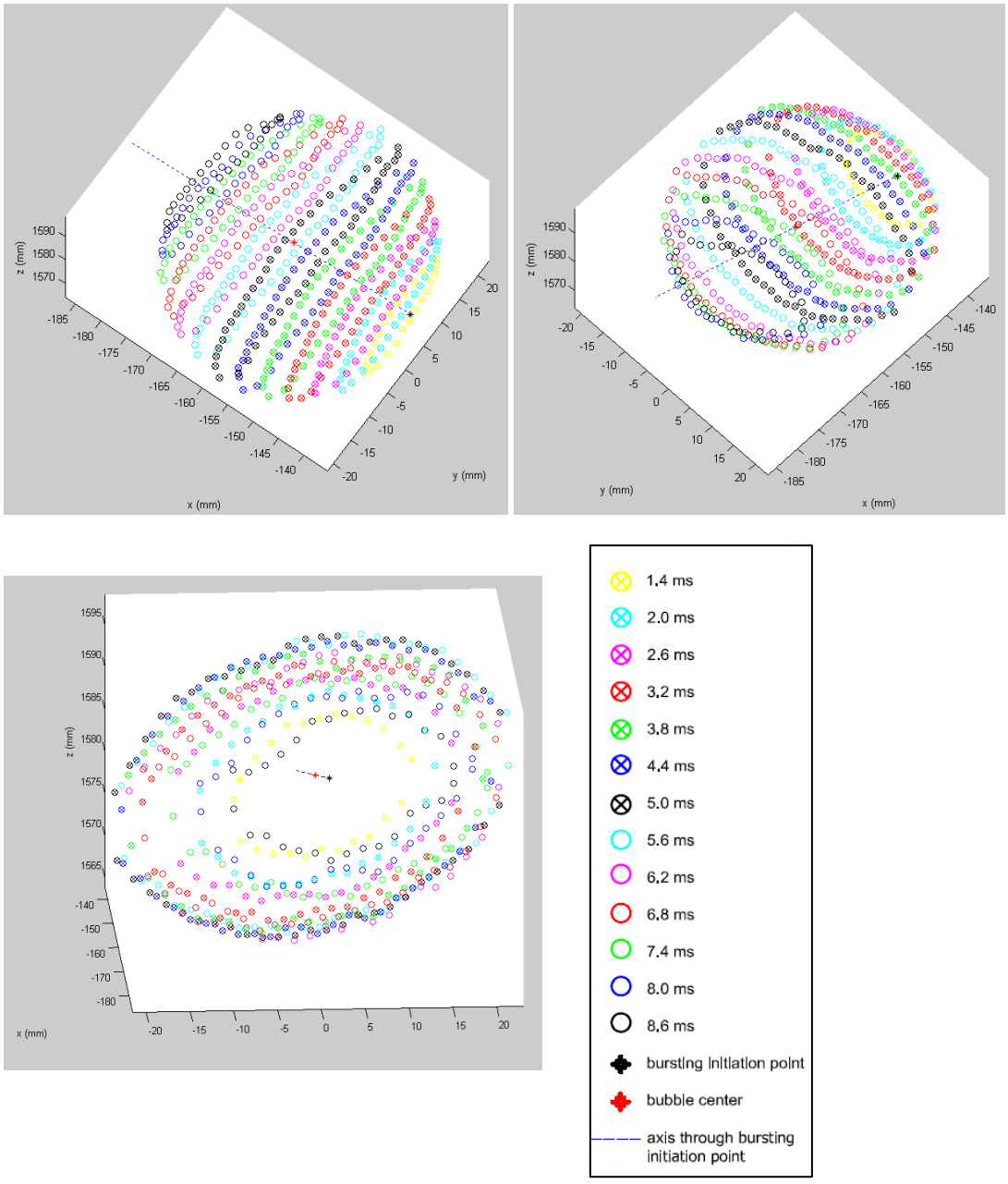

Figure 5-7 Time resolved 3D views of the bubble bursting boundary

5.3.4 Specific point tracing

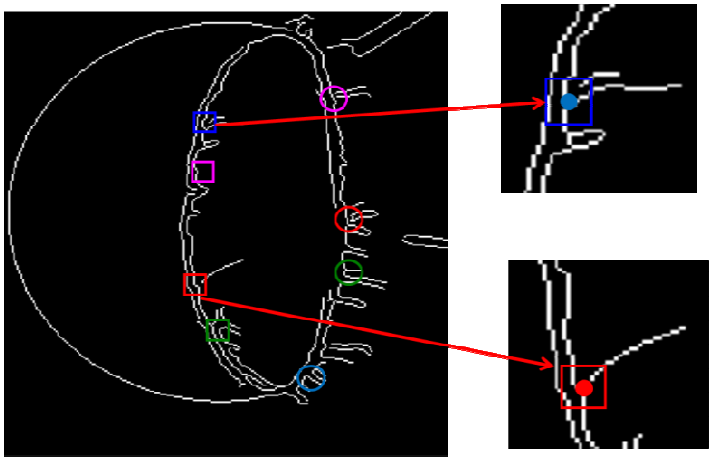

Figure 5-8 The determination of 2D image coordinates of the points selected for tracing

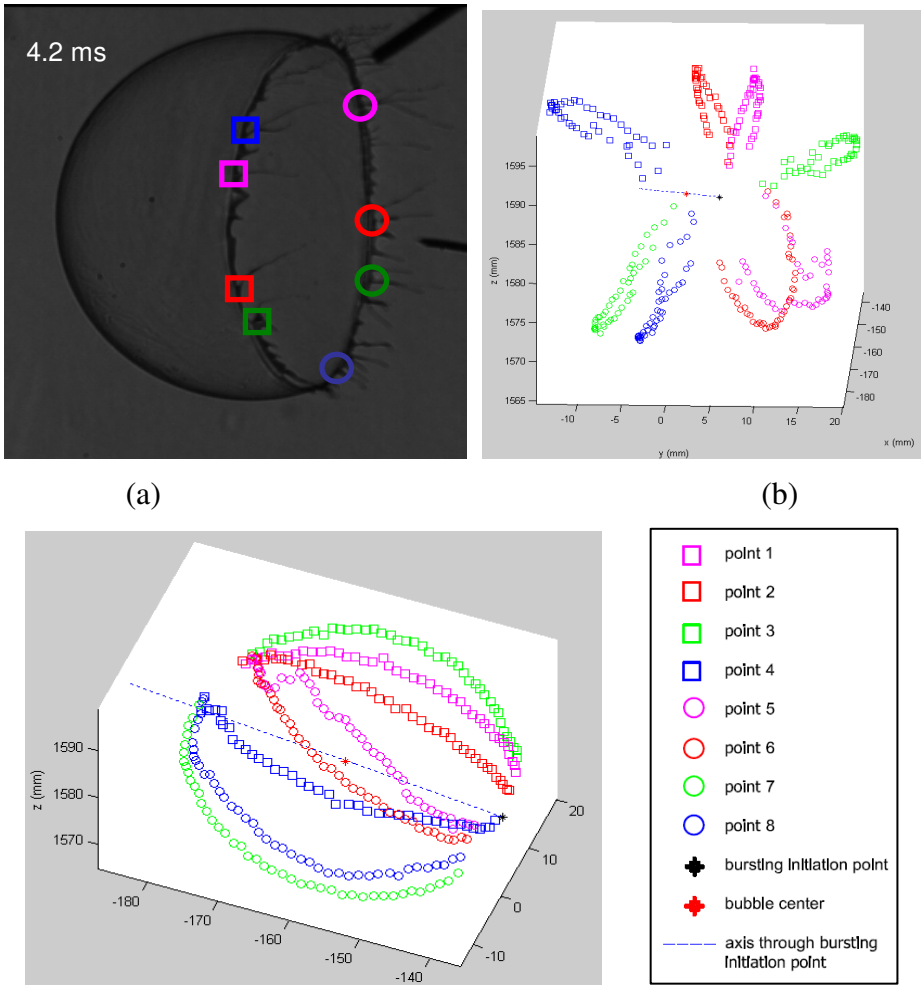

(a) (b)

(c)

Figure 5-9 Point tracing during bubble bursting

(a) Illustration of the points selected for tracing; (b-c) 3D views of the traced points

It can be seen from Figure 5-9 (a) that there are protruding lines on the bursting boundary, which could be matched easily in the stereo image pairs and thus provide good correspondence points for 3D reconstruction. Due to the complicated structure on the bursting surface, it is more reliable to pick up the points manually. As illustrated in Figure 5-8, the image was first transformed to binary image by 'canny edge detection' algorithm in MATLAB. The point of the intersection of protruding lines and the bursting surface rim are selected for reconstruction. Since the protruding lines have a continuous development during the bursting process, the points can be traced at different time steps. Eight points have been selected to trace the bursting process and the locations are illustrated in Figure 5-9 (a). The time dependent movement of the traced points may supply useful information for the understanding of the local bursting structure. The 3D views of the reconstruction results, from 1.4 ms to 9.6 ms with a time interval of 0.2 ms, are shown in Figure 5-9 (b-c). It can be observed that the points are moving mainly along the longitudinal direction on the bubble surface. The movement of the points is more irregular near the end of bursting, due to new bulges appearing and merging with others constantly on the bursting boundary during the process. More merging is observed at the end of the process as the bursting boundary area is decreasing gradually to one point with time.

The dilute water soap solution used in this study has a similar viscosity to water. Thus the bubble should retract in the inertia regime rather than the viscosity regime. In the inertia regime, the retracting velocity of the film is a constant and it can be scaled as $U \propto \sqrt{\frac{\gamma}{\rho h}}$, where ρ is the liquid film density, h is the film thickness, and

γ is the surface tension (Taylor, 1959, Culick, 1960). Based on the 3D coordinates as shown in Figure 5-9 and the time interval of 0.2 ms between two consecutive image pairs, the mean velocity of the tracked points can be calculated. The measurements demonstrate that the film is retracting at a constant speed of 7 m/s, which is consistent with the prediction of the retracting velocity in the inertia regime. Weber number ($We = \frac{\rho U^2 l}{\gamma}$) is a measure of the relative importance of the fluid's inertia compared to its surface tension, which is the product of Reynolds number ($Re = \frac{\rho U l}{\mu}$) and Capillary number ($Ca = \frac{\mu U}{\gamma}$), (i.e., We=Re×Ca), where μ is the viscosity of the liquid. The 'finger-like' structures give an indication of very large Weber number. The 3D measurement of the retraction speed of the bubble rim provides a means to estimate the number accurately. The Weber number based on the characteristic retraction speed of the film (U) and the bubble diameter (l) is around 8.6×10^4, which is quite high as expected.

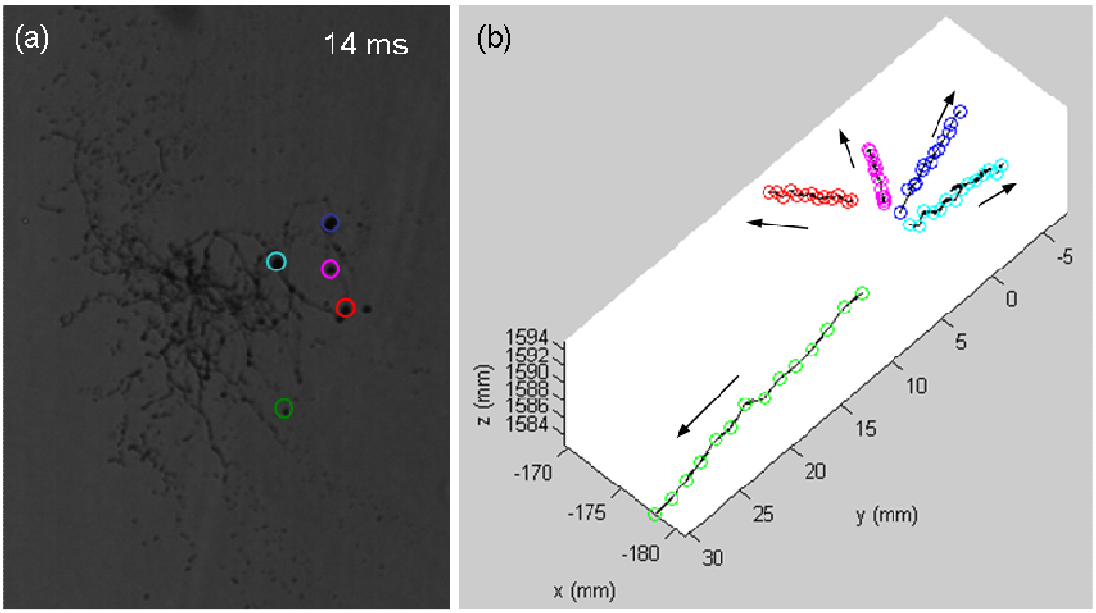

Figure 5-10 Point tracing during bubble bursting (a) Illustration of the selected droplets for tracing; (b) 3D view of traced points

At the end of bubble bursting, the 'finger-like' liquid lines and droplets continue to move after the bubble surface has vanished completely. The 3D movement of 5 selected points illustrated in Figure 5-10 (a) are reconstructed and shown in Figure 5-10 (b). The points are traced from 12 ms to 16.8 ms after bursting initiation. The arrow indicates the moving direction of the traced points. It could be observed that the droplets tending to spread outwardly in different directions. The average velocities are found to vary from point to point in the range of 3 m/s to 4.5 m/s, which are at lower levels than the average bursting velocities. Since the surface tension effect does not play an important role after the bubble surface vanishes, the droplets after that could only move depending on the inertial and aerodynamic forces.

The 3D structure reconstruction, specific point path tracing and velocity calculation is of great help to understand the droplets' moving characteristics, which are difficult to obtain by other conventional techniques. The irregular structures and space movements shown in Figure 5-7, Figure 5-9 and Figure 5-10 demand 3D diagnostics for visualisation and quantitative analysis, since 2D diagnostics is not sufficient and may even be misleading. The 3D reconstruction ability of the stereoscopic shadowgraph method proposed in this study thus has great advantages over conventional 2D shadowgraph techniques.

5.4 Curve reconstruction

Besides points, curves are also important features in scenes. Three dimensional reconstruction based on matching is significant in application in fluid study and research. In this study, two iron wires fixed on a pedestal are used for the model of curve reconstruction. The iron wires are in shape of irregular curves. The stereo

shadowgraph images of the wires are shown in Figure 5-11. It could be observed that the wires show different perceptions in the left and right images.

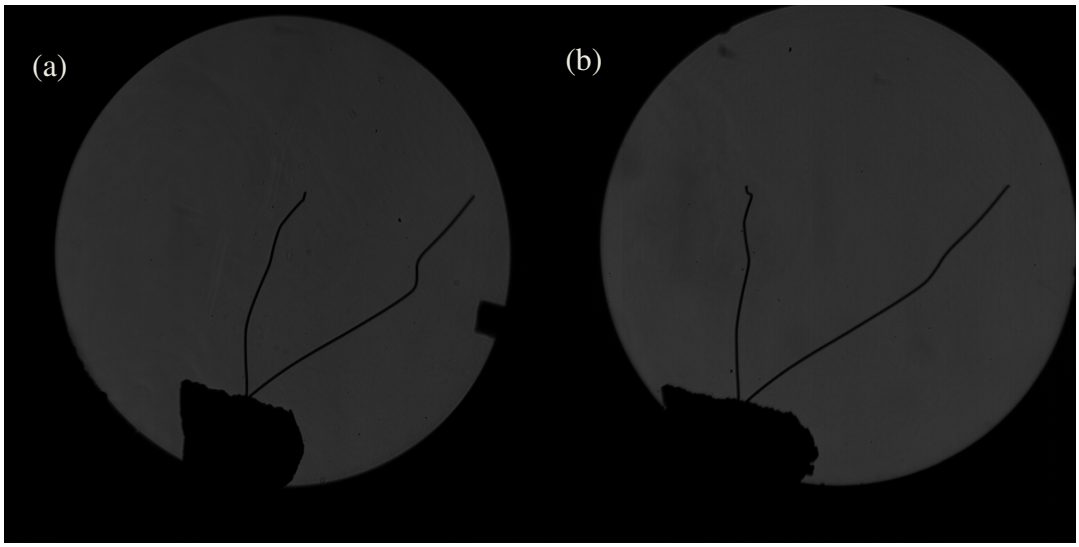

Figure 5-11 Schlieren image pair of two iron wires (a) Left image (b) Right image

5.4.1 Curve extraction

In order to extract the curves from the original schlieren images, the images are converted using colour approximation. The grey colour images are represented by only N colours, as shown in Figure 5-12. In this case, 10 different colours are selected as the indexed colour map. The curves need to be extracted, correspond to 'zero' section in the colour map. The indexed images are then transferred to a binary image, whose pixels are logical 1s if the corresponding pixel colours are 'zero' in the colour map and logical 0s if otherwise. The logical 1s are interpreted as white and 0s as black in the binary image. A skeletonization method is used to reduce the patterns in the binary images to thin-line curves, as shown in Figure 5-13 (a). The discontinuity of the curves is caused by the display factor. The curves are actually continuous after amplified, as shown in Figure 5-13 (b).

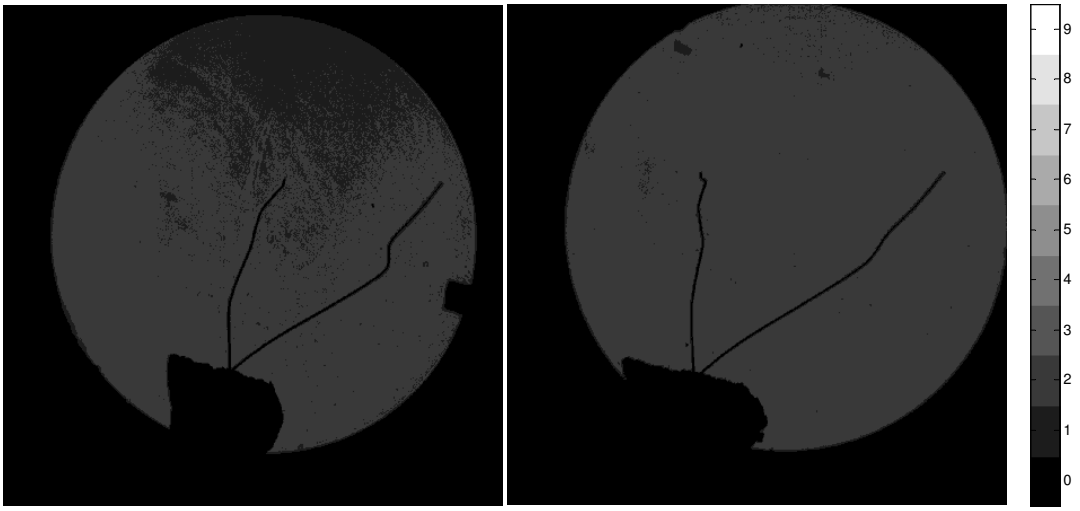

Figure 5-12 Indexed images created from the original grey image

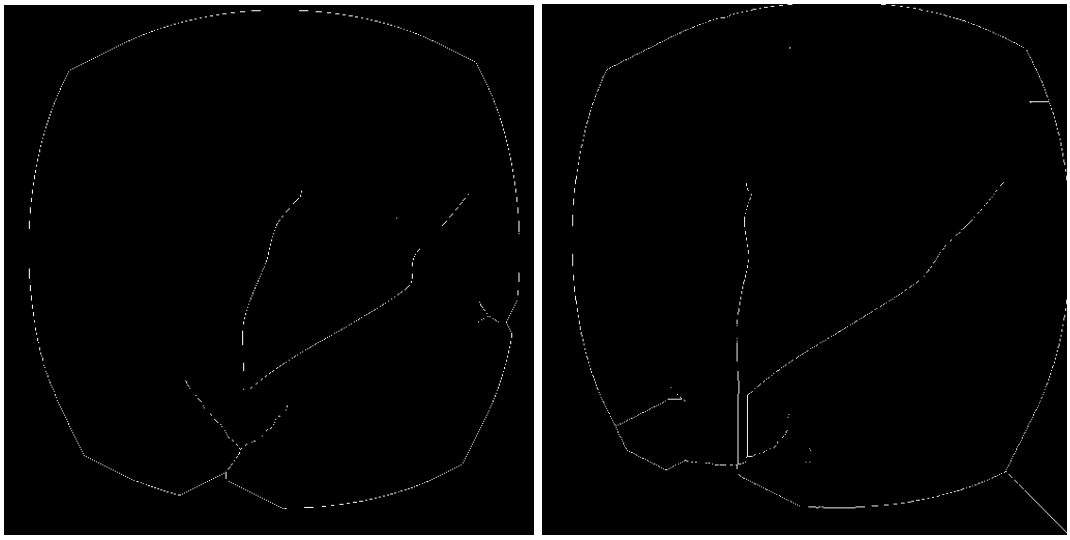

(a)

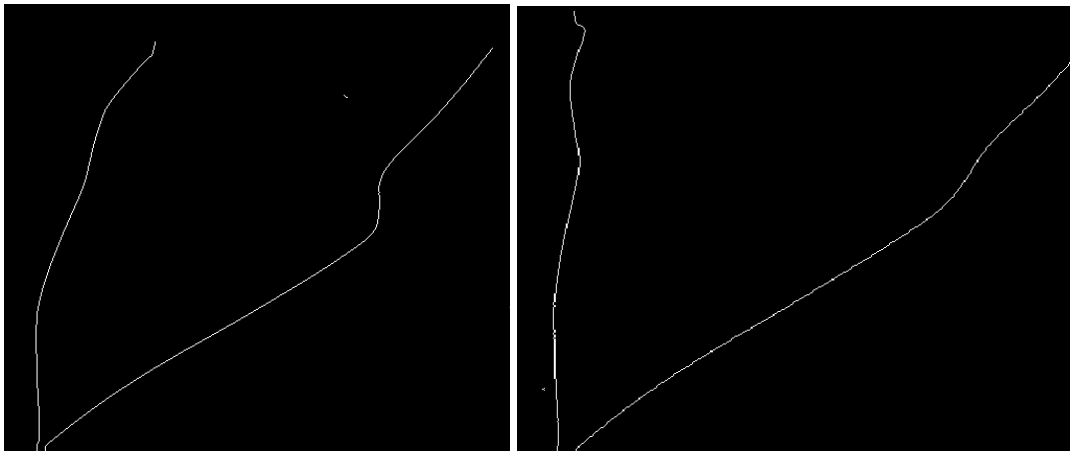

(b)

Figure 5-13 (a) Thin-line representation of binary images; (b) Amplified images of the binary images

5.4.2 Curve picking up from the binary images

A program has been developed to select the pieces of curves from two images and identify the corresponding curve pieces into pairs. A starting point along the curve is required for the curve searching. The program will then search the surrounding pixels and traces the logical '1' pixels. An end point needs to be selected for a complete curve. After the extraction of a complete piece of curve in the left image, the program will switch to the right image and the corresponding curve can be extracted in the similar way. The other pair of curves could also be extracted in the same way. As shown in Figure 5-14, the two pairs of curves are indicated by blue lines. The extracted curves are shown in Figure 5-15 as red lines on the original schlieren images. The result shows good matching with the original curves.

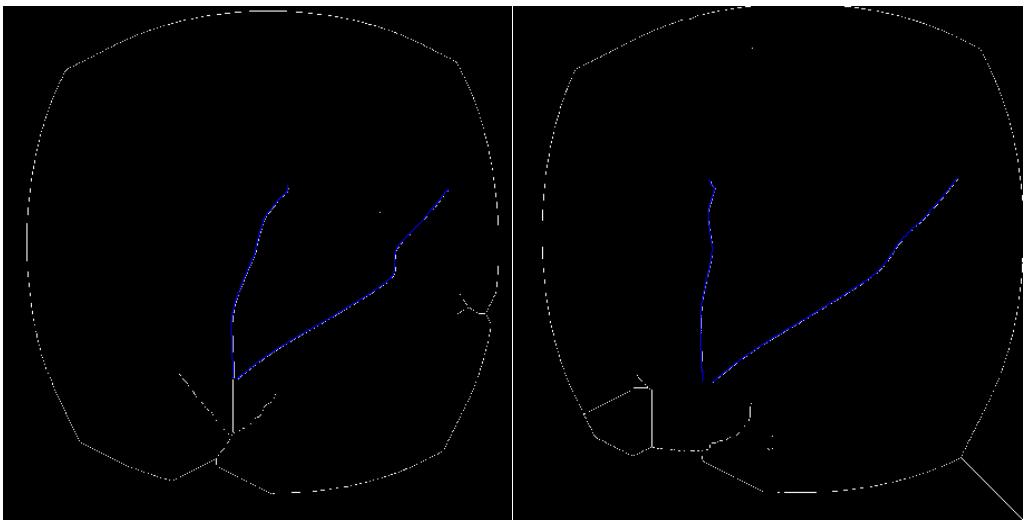

Figure 5-14 Curves extracted from the binary images

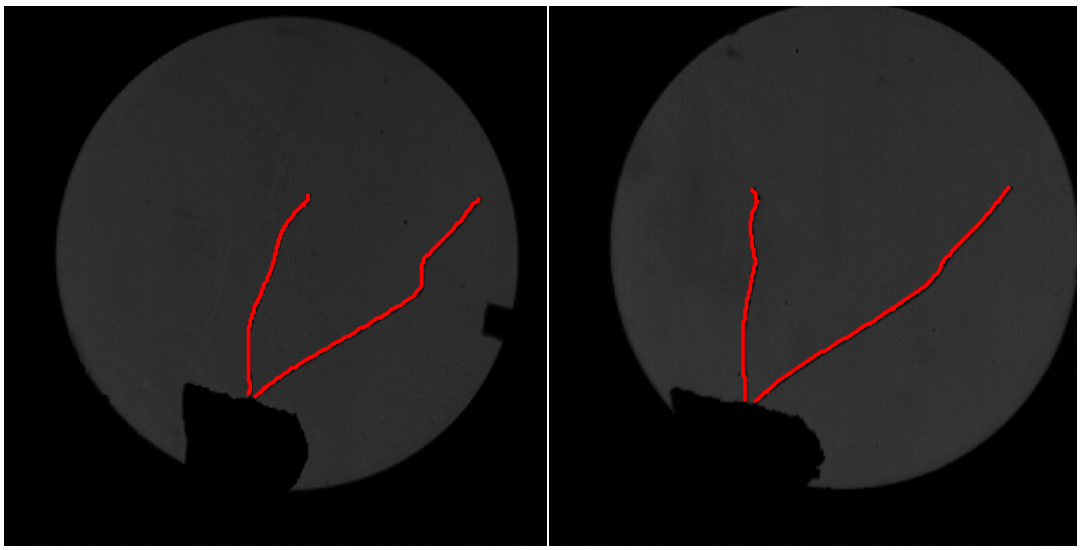

Figure 5-15 Curves marked as red lines in the original image

5.4.3 Curve matching and reconstruction

Curves may be represented by a set of linked points with approximating mathematical equations. B-spline modelling has been utilized to curve matching and reconstruction in stereo techniques (Robert and Faugeras, 1991, Bascle and Deriche, 1993, Xiao and Li, 2005). In B-spline curve, certain amounts of knots are distributed along the curve. For the curves on stereo images, the knots $\{m_i\}$ on one B-spline curve are selected as sample points. With the epipolar geometry established through the calibration parameters, the matching points $\{m_i'\}$ on the other curve could be obtained. With the matching primitive sets $\{m_i\}$ and $\{m_i'\}$, the 3D points $\{M_i\}$ can be estimated based on the algorithm of point reconstruction. Then with another B-spline approximation, the 3D curve can be obtained with the set of 3D points. The reconstruction results of the two curves are shown in Figure 5-16 with different colours. Several views of the curves are illustrated. The curves show different shapes at different view angels. The result indicates that the curve extraction and

reconstruction can be accomplished with the newly built stereoscopic shadowgraph technique and may have potential application in physical curve reconstruction.

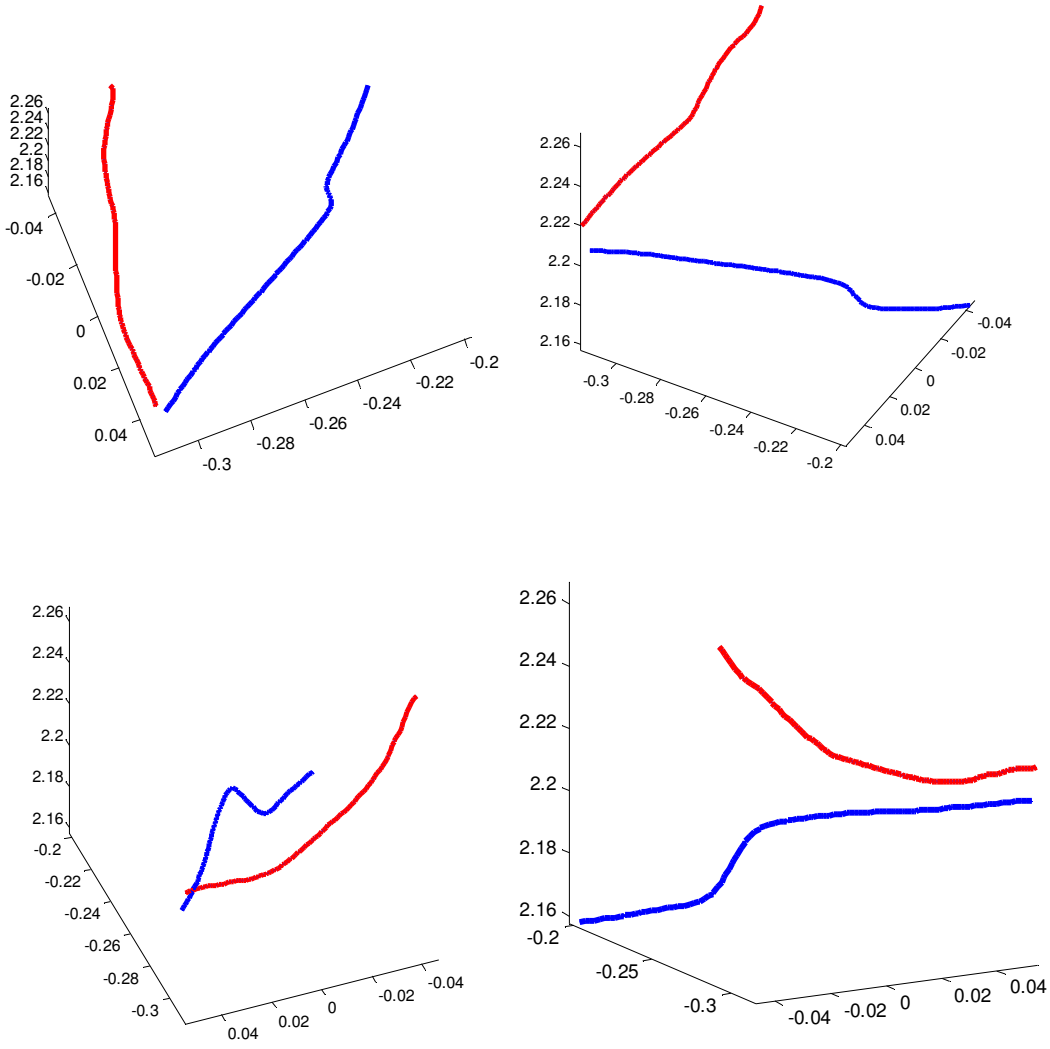

Figure 5-16 Different views of the reconstructed curves

5.5 Summary

Several application cases of the high speed stereoscopic shadowgraph system are investigated in this chapter. A crystal block is used as a static model for the validation of the application. Several points are selected as the matching points in the schlieren image pairs. The reconstruction result of the selected points fits well with

the measured result. The overall error analysis indicates that the accuracy of the reconstruction results is affected by the calibration parameters as well as the feature extraction.

The stereoscopic schlieren system is applied to investigate the bubble bursting process consequently, which approves the ability to study time resolved unsteady phenomena. The time resolved bubble bursting rims have been reconstructed, indicating clearly the whole bursting process. Typical feature points on the bursting rims are selected and tracked during the bursting process. The average velocity of the selected points tends to be at a similar value. The movements of some selected droplets after bursting are reconstructed in 3D space. The droplets are moving outwardly in different directions and at lower velocities than the average bursting velocity. The quantitative information supplies more accurate data of the bubble bursting characteristics investigation.

Other than the static and dynamic point reconstruction, the procedure of curve extraction and reconstruction are introduced in section 5.4. Since curve is also important feature in many research fields, the stereoscopic shadowgraph technique shows the potential application in future studies.

Finally, the application of the stereoscopic schlieren system could be summarised as follows:

- Set up the optical apparatus as the illustration in Chapter 4. The test section is located at the cross area of the two converging beams. Two high speed

cameras are used to take the schlieren/shadowgraph images at two different angles simultaneously.

- Place the calibration board in the test section for at least three positions. Work out the intrinsic and extrinsic parameters based on the images of the calibration board.

- Once the calibration parameters are estimated successfully, the point in space can be reconstructed through the triangulation method. The matching points in the image pairs need to be known in advance. In practice, the matching point coordinates could be obtained by feature extraction.

Chapter 6 Spark Characteristics Investigation of a Gas Turbine Igniter

6.1 Introduction

Spark ignition systems play an important role in aircraft engines, as it is responsible for initiating the combustion process that sustains engine operation. Moreover, a rapid reigniting is required after the flameout at high altitude flight where the ambient air is low both at temperature and pressure. Surface-discharge sparks are effective and powerful ignition systems, which are most widely used for gas turbines and jet engines. In a surface discharge spark, a condenser voltage is applied to initiate a main discharge in the form of an intense plasma arc, by ionizing the gas. A spark kernel formed by ions can be observed. The pressure and temperature at the spark initiation can be as high as in the order of 10^6 Pa and 10^6 K. The high pressure can generate a shockwave, which at its beginning is an intermediate shockwave and then decays into a sonic wave. The decay of the shockwave at the first several

microseconds is very fast (Bayle et al., 1985, Gord et al., 1999). The ignition time for most gases is in the time scale from several hundred microseconds to several milliseconds. Thus the shockwave expansion process is not sufficient to ignite the combustible gas. The energy associated with the high pressure perturbation after shockwave expansion might be important in mixing and igniting the reactive species (Phuoc, 2005). Spark igniters of the type studied here are widely employed to initiate combustion in aeronautical and ground-based gas turbines. Although timely flame development is important for safe and reliable engine operation, measurements of the ignition process inside a practical combustor have not been widely reported. The performance of the surface-discharge igniter, which operates differently to an air-gap igniter, is particularly poorly understood. Although the diagnostic techniques to study surface-discharge sparks have been developed previously (Gord et al., 1999), a systematic assessment of the hot gas kernels produced by these sparks has not been reported.

The optical diagnostic and visualisation methods are useful in the study of spark ignition because of the benefit of non-intrusiveness. The spark ignition and the flame kernel development processes have been investigated by different visualisation techniques. Direct visualisation by high speed camera was used to observe and calculate the flame kernel growth and flame propagation speed (Ahmed and Mastorakos, 2006). Schlieren combined with a state-of-the-art high speed camera acted as a powerful diagnostic tool for the investigation of the ignition process (Bradley et al., 2004, Ohiwa et al., 2002). Planar laser-induced fluorescence (PLIF) of the OH radical was applied to examine the flame structure and position at the early stage of the spark in (Ahmed and Mastorakos, 2006, Ahmed et al., 2007,

Spiglanin et al., 1995). Holographic method was employed to observe the generation of spherical shockwaves by laser induced spark (Gatti et al., 1988).

In this chapter, the spark induced plasma jet of a gas turbine combustor igniter (a surface discharge type) has been investigated using high speed schlieren, stereo and stereoscopic shadowgraph imaging visualisation techniques. Instead of studying the ignition process in a combustible mixture, only the spark induced plasma jet and its interaction with the ambient air is investigated in order to decouple the complex interactions of plasma jet and reactive mixtures. The schlieren imaging technique provides a means to visualise the development of the spark induced shockwave and plasma jet, especially when the jet stops to emit visible light due to the gas temperature drop. The stereo images combined with the 3D reconstruction process introduced in Chapter 3 provide quantitative 3D distribution of the visible streaks formed by the tiny melted metal bits as well as the spark kernel movement after spark initiation. The stereoscopic shadowgraph technique established in Chapter 4 is applied to reveal the 3D structures of the hot gas and ambient air interactions.

6.2 Experimental setup

A gas turbine combustor igniter was used in the experiments at atmospheric condition. It was sparked only in ambient air. The schematic of the experimental setup and an image of the igniter tip are shown in Figure 6-1. The spark input voltage was controlled by a transformer, with an adjustable voltage range from 0 V to 240 V. When the input voltage is increased, the frequency of the spark generation is increased accordingly. The schlieren imaging system was used to observe the spark induced plasma and shockwave propagation.

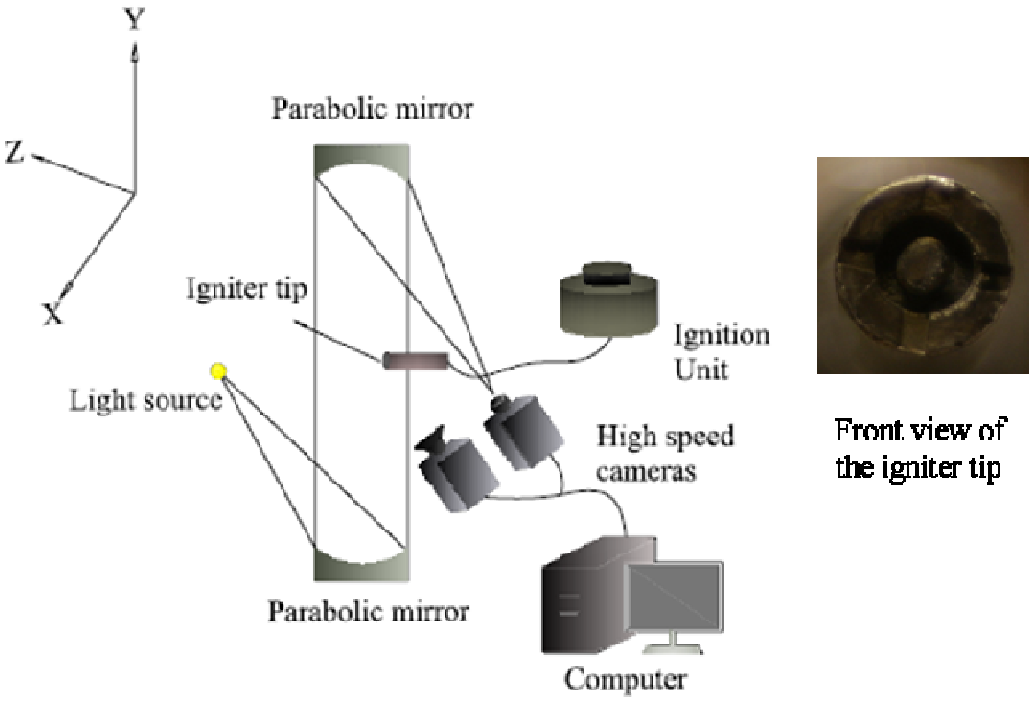

Figure 6-1 Schematic of the experimental setup and the front view of the igniter tip

The stereo adapter introduced in section 3.1 was attached to the front lens of one of the high speed camera to capture a pair of images at two slightly different view angles. Two high speed cameras (Photron SA-3) were synchronized to take schlieren and stereo pictures simultaneously. The parameters of the cameras are outlined in Table 4-1. The igniter was also investigated by the stereoscopic shadowgraph techniques. As shown in Figure 4-1 (section 4.2), the igniter was placed at the cross area of the two converging beams. The two high speed cameras were used to take two shadowgraph images at two different directions simultaneously.

6.3 Spark characteristics investigation

6.3.1 Spark initiation performance

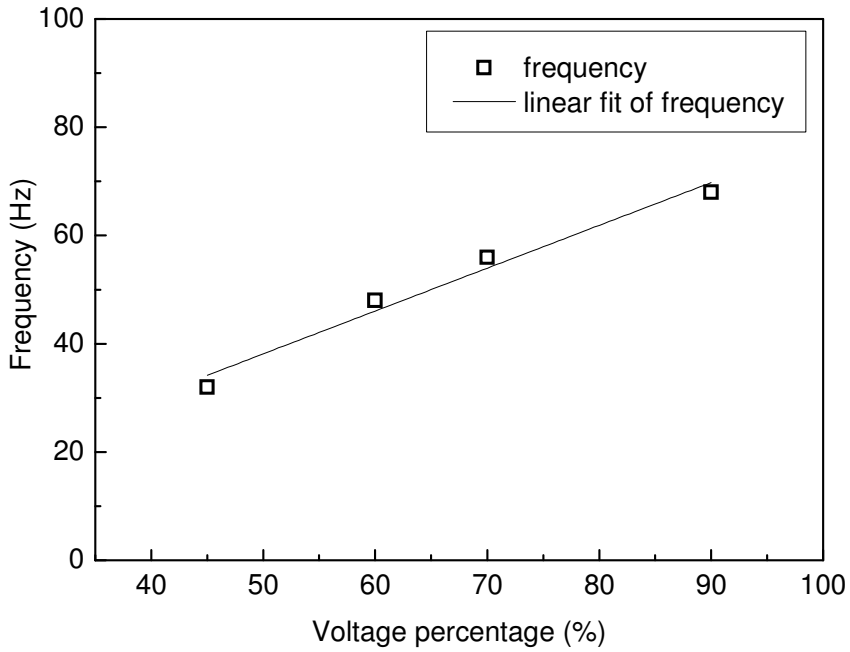

Figure 6-2 Spark frequencies versus input voltages

In the experiments, the spark was only generated in ambient air, without the presence of fuel. The spark is generated by a reservoir condenser through a high voltage rectifier. The minimum input voltage which was able to trigger a spark was found to be around 108 V. When the voltage is further increased, the frequency of the spark ignition was observed to increase accordingly. As shown in Figure 6-2, the trend between the spark frequency and the input voltage is linear.

6.3.2 Shockwave and hot gas propagation

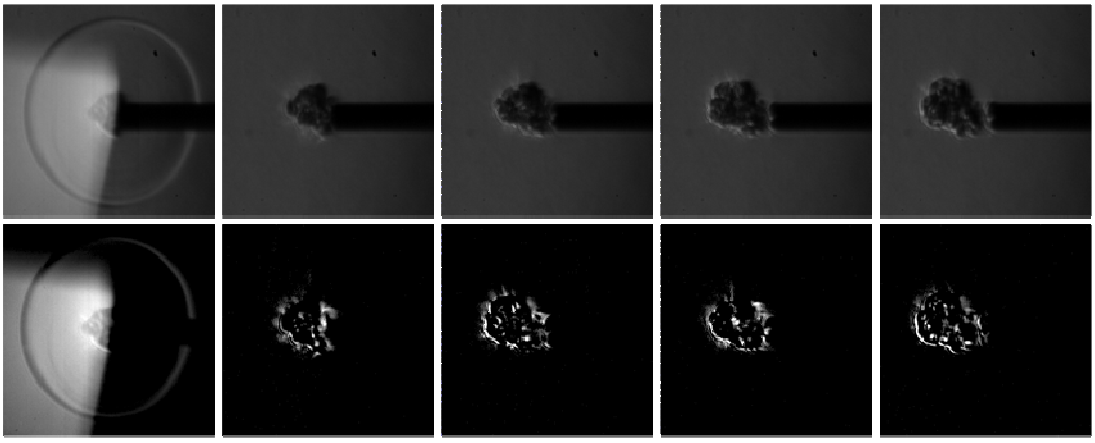

Figure 6-3 Time-resolved schlieren images of spark induced shockwave and hot gas jet (The time interval between each two images is 1 ms.) (Upper row: Original images; Bottom row: Subtracted images.)

After the spark initiation, a light flash is observed with a sharp acoustic sound. A sequence of schlieren images of the spark initiation were illustrated in Figure 6-3. The images were recorded at 2,000 fps. The electrical spark induced shockwave was captured successfully. At the same time, a hot gas jet is observed propagating along the igniter axis in the schlieren image sequence. In order to show the hot gas jet propagation more clearly, digital image processing technique is used by subtracting the two consecutive images. In this way the changes between the two consecutive images are highlighted as shown in Figure 6-3.

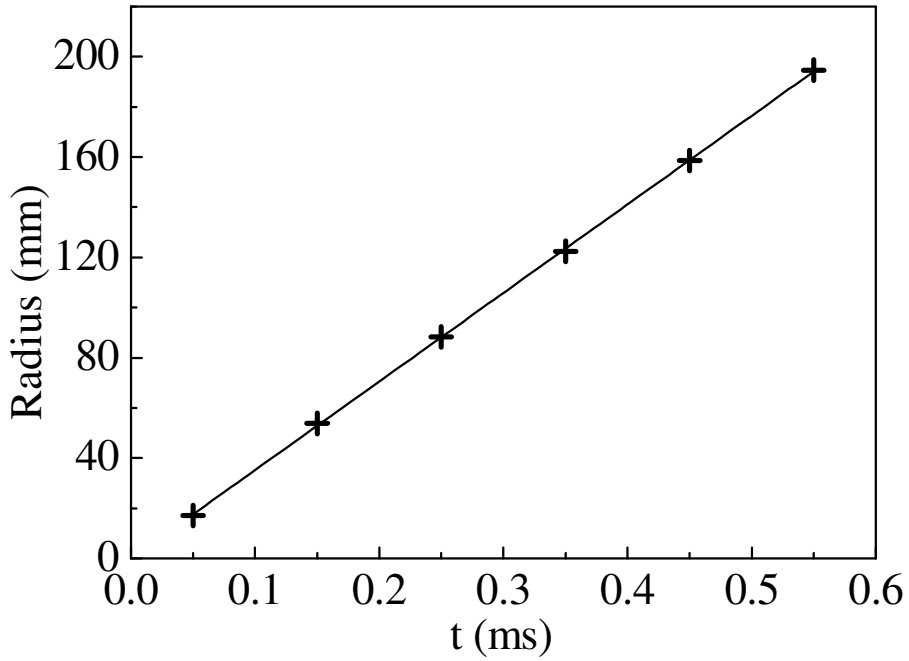

Figure 6-4 Spherical shockwave radius increasing with time

After the spark is initiated, a finite amount of energy is suddenly released in a small local volume, where a high temperature and high pressure gas pocket is generated. The gas breaks down generating a plasma kernel which expands outwards in all directions. If the expansion velocity is greater than the sound velocity, a spherical shockwave is created and propagates outwards. In order to calculate the shockwave propagation speed, another sequence of schlieren images were recorded at 10,000 fps. The radius of the spark induced shockwave was measured based on the schlieren images. As shown in Figure 6-4, the shockwave radius is observed to increase linearly with time in the scale of 0.1 ms to 0.6 ms after spark initiation. By evaluating the distance of the shockwave between two consecutive images, the average speed of the shockwave can be calculated. The result shows that the spark induced shockwave is propagating at the speed of 353 m/s, which is slightly higher than the sound speed of 343 m/s at the laboratory temperature of 21 ^{o}C.

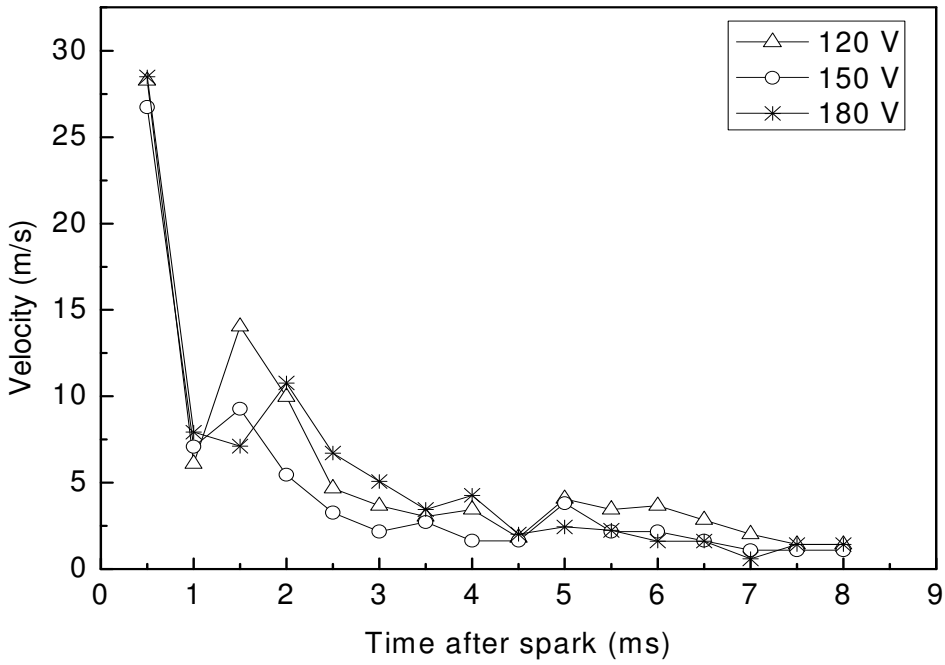

Figure 6-5 Hot gas jet front propagating speed at different input voltages

The hot gas jet is generated by the release of spark energy, which has created a high pressure zone locally. The tip of the igniter used in this study has a finite diameter of 12 mm, as shown in Figure 6-1. The blockage effect of the igniter tip leads the hot gas propagating mainly in the forward direction. The propagating speed of the hot gas front is measured through the time-resolved schlieren images. The results in Figure 6-5 present hot gas front propagation speed at three different input voltages, which were set at 120V, 150V and 180V respectively. It is shown that the maximum speed is generated at the initiation of the spark, about 28 m/s. The hot gas propagating velocities decrease dramatically in the first 1 ms and then get down to a low value less than 5 m/s after a few milliseconds. The life time of the observable hot gas in the schlieren images is about 100 ms. The results show that the input voltage does not have much effect on the evolution of the spark induced hot gas jet.

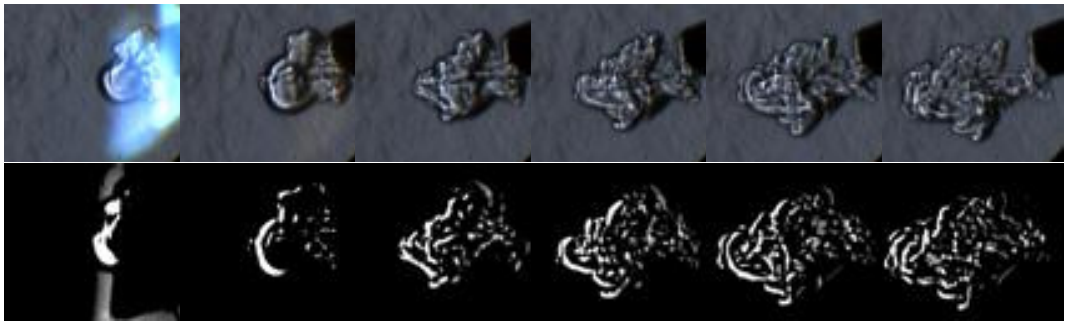

(a)

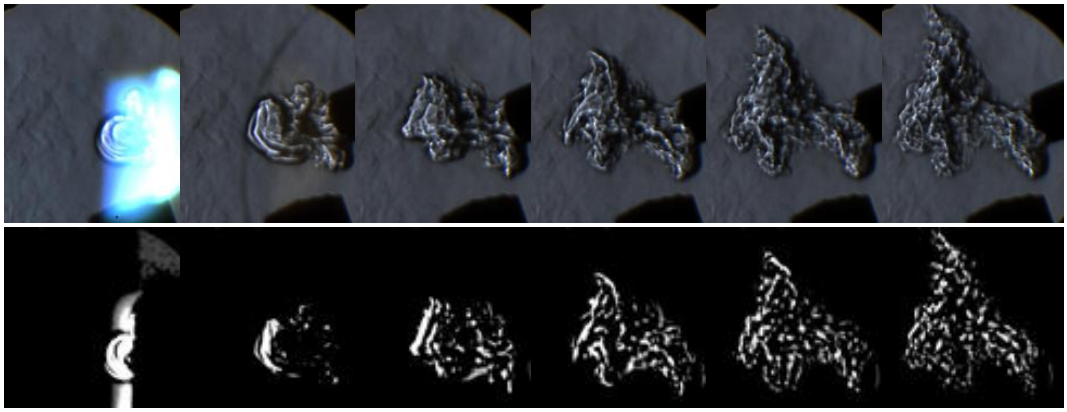

(b)

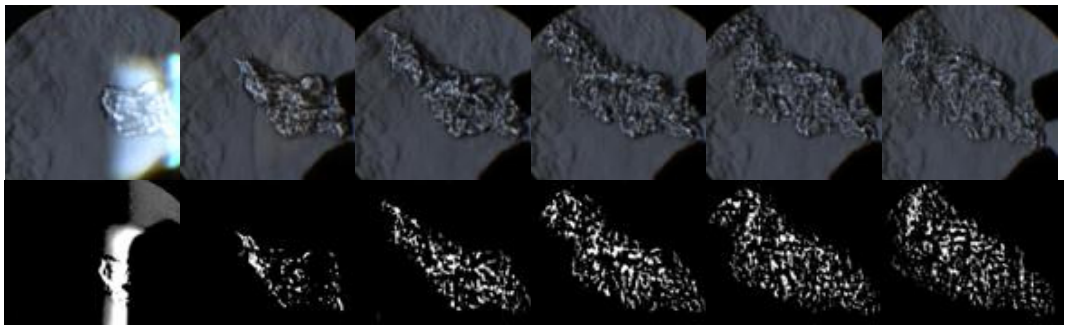

(c)

Figure 6-6 The time resolved schlieren images of the spark induced plasma jet at different air velocities (The time interval between each two images is 0.4 ms.) (a) Air jet velocity at 0 m/s; (b) Air jet velocity at 10m/s; (c) Air jet velocity at 20m/s

An air jet was introduced from the underneath of the igniter tip to investigate the hot gas development under different flow conditions. The mean air flow jet velocity is set at 0 m/s, 10 m/s and 20 m/s to investigate the plasma jet behaviours at different air velocities. Figure 6-6 shows the sequence of schlieren images of the electrical igniter induced plasma jet at different air jet velocities. The schlieren images (1024×1024) were recorded at 5,000 fps and the shutter speed was set at 1/50,000 s.

To highlight the local jet structure evolution, the resultant images of subtracting two consecutive images (with a time interval of 0.2 ms) is shown below the original schlieren images. When there is no air flow, a visible turbulent hot gas jet is observed propagating forward. While the air flow velocity is at 10 m/s, the middle part of hot gas jet is blown upward along the air flow direction. At higher air flow velocity of 20 m/s, the whole hot gas jet is pushed upward by the strong air flow. The structure and the propagating direction of the spark induced hot gas are obviously affected by the air flow.

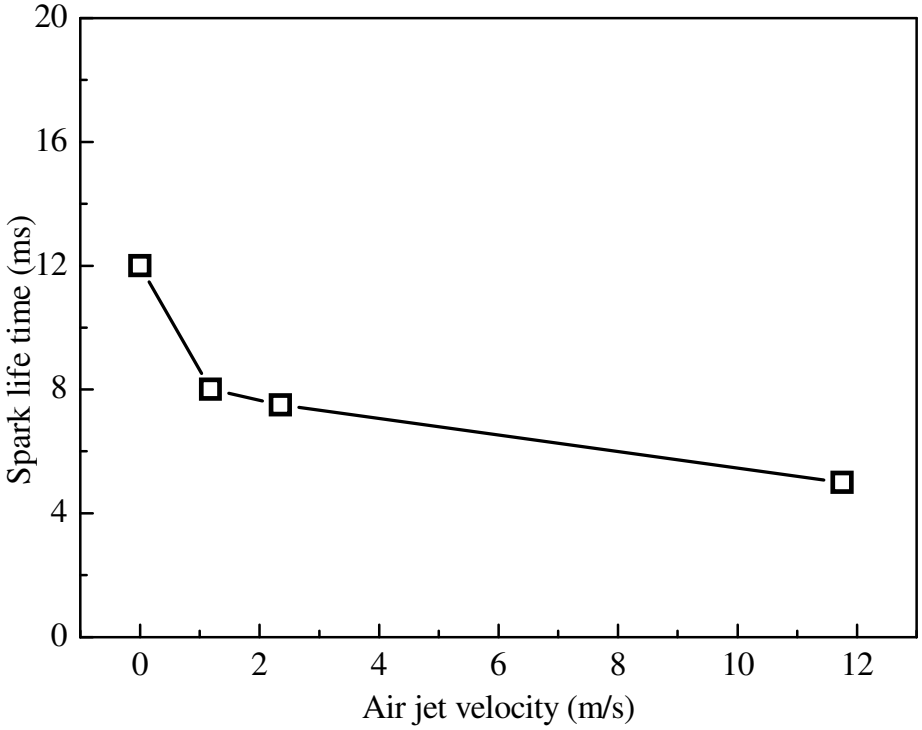

Figure 6-7 The life time of the traceable spark kernel at different air jet velocity

Besides the different hot gas structures observed at different air jet velocities, the life time of the visible spark kernel also varies with the air jet velocity. As shown in Figure 6-7, the life time of the spark decreases with the increase of the air jet velocity. This can be attributed to the air jet flow cooling to the visible hot spark kernel. Any increase in the air velocity will lead to stronger cooling of the hot spark

kernel below the threshold of temperature at which the hot kernel ceases to emit visible light.

6.4 Stereo application on spark performance investigation

6.4.1 Camera calibration

The camera calibration with the stereo adapter attached was conducted based on the procedures introduced in section 3.3. In this application, four different positions of the calibration board were used to do the camera calibration. The 3D view of the reconstructed four planes was shown in Figure 6-8. The standard deviation is then calculated based on the distances between the neighbouring points and the error is less than 5%.

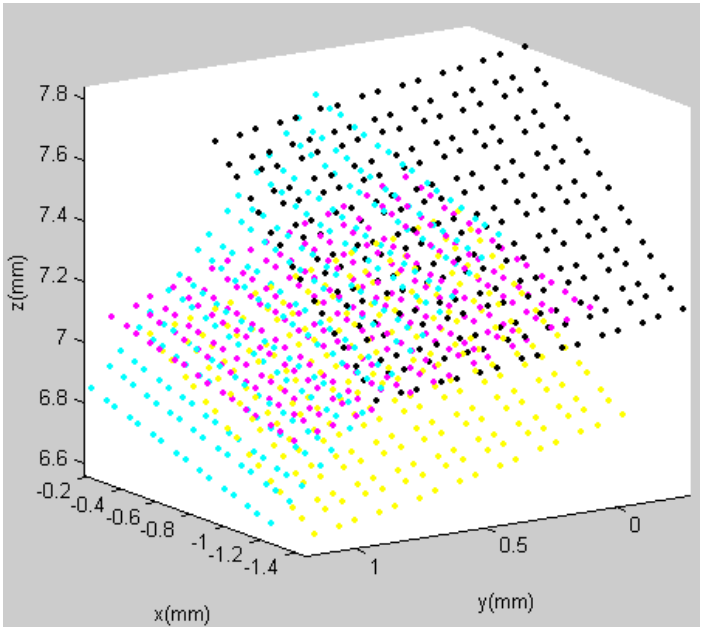

Figure 6-8 Reconstructed planes of the calibration board at different orientations

The calibration parameters are listed below, where *A1* and *A2* are the intrinsic parameters of the two virtual cameras; *R* and *t* are the extrinsic parameters indicating the motion between the two cameras. With the calibration parameters obtained, the 3D coordinates of the correspondence points in the stereo image pairs could be worked out.

$$A1 = \begin{bmatrix} 2476.1 & -8.7415 & 516.47 \\ 0 & 2492.6 & 544.41 \\ 0 & 0 & 1 \end{bmatrix}$$

$$A2 = \begin{bmatrix} 2476.1 & -8.7415 & 504.47 \\ 0 & 2492.6 & 544.41 \\ 0 & 0 & 1 \end{bmatrix}$$

$$R = \begin{bmatrix} 0.9424 & 0.011896 & 0.33426 \\ -0.0006381 & 0.99943 & -0.033771 \\ -0.33447 & 0.031612 & 0.94187 \end{bmatrix}$$

6.4.2 3D points tracing of spark kernel

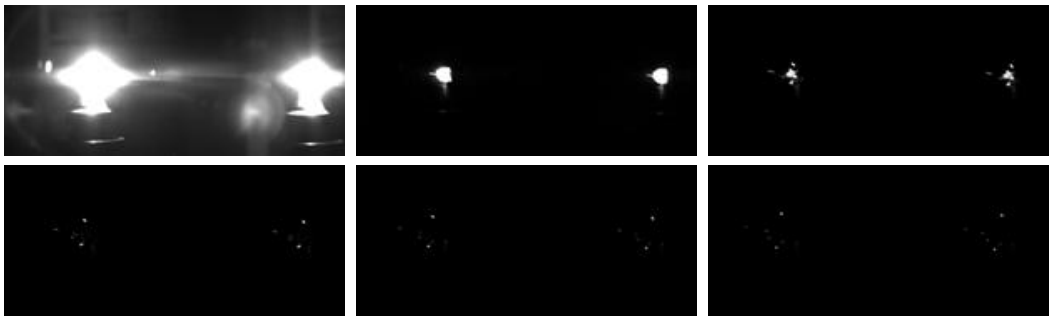

Figure 6-9 Stereo images of the ignition spark without air flow jet
(The time interval between each two images is 1 ms.)

Figure 6-9 shows the time resolved stereo imaging sequence of the visible spark in ambient air, which is formed by ions generated from the spark initiation. After the spark occurs, a light flash is observed with a sharp acoustic sound. Then the visible spark kernel diminishes gradually. Only small spots are observable after 3 ms. The small spots eventually disappear around 12 ms after the spark occurring.

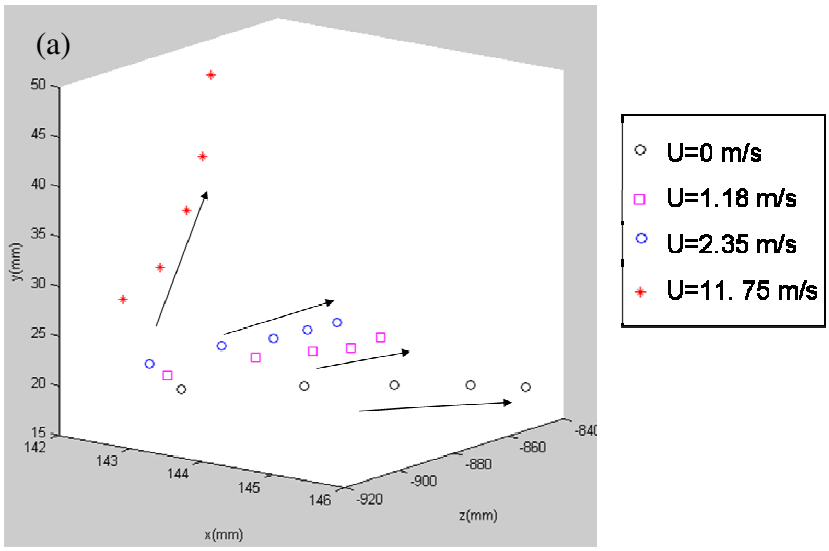

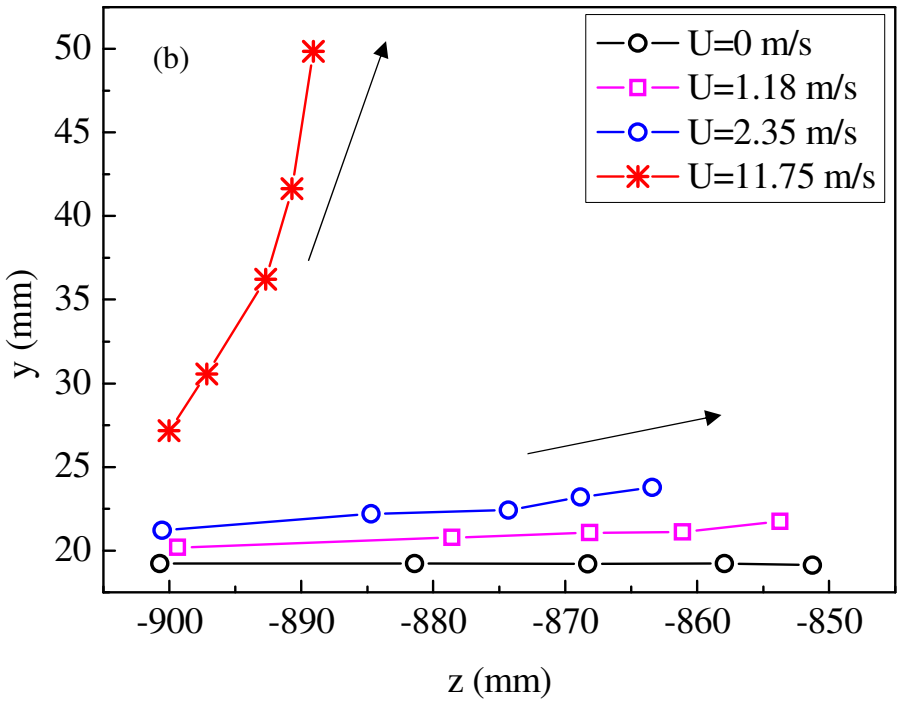

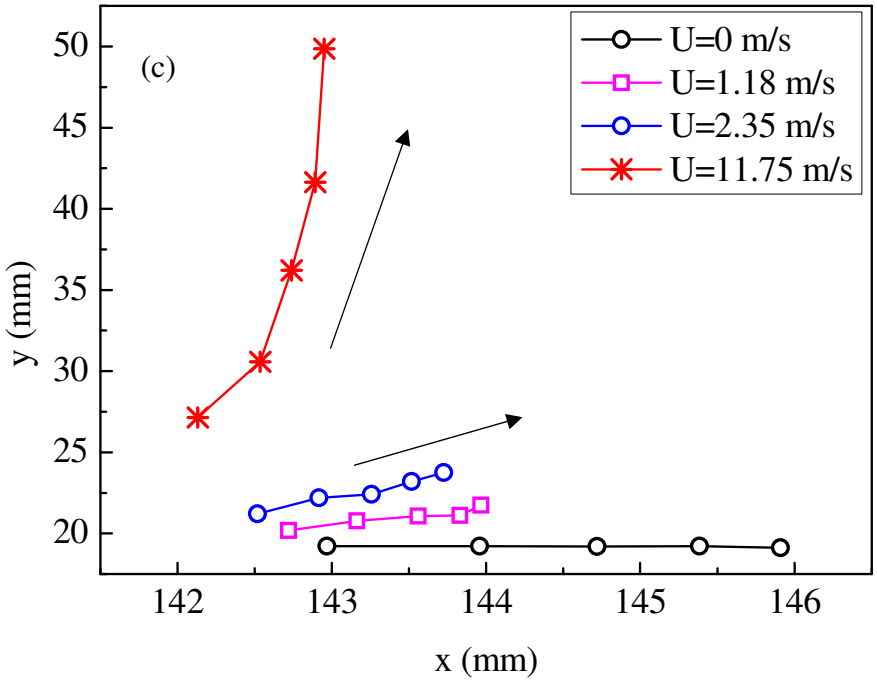

Figure 6-10 (a) 3D view, (b) side view and (c) front view of the big spark centroid trajectory for the first 5 frames at different air jet velocities

The centroid of the big spark kernel at different flow velocities are tracked and reconstructed in 3D space for the first five consecutive frames, as shown in Figure 6-10 (a). The absolute value in X, Y and Z directions are decided by the camera and the image plane. The X, Y and Z directions in real world is illustrated in Figure 6-1. In the figure the axis of the igniter rod is in XZ plane. As emphasized by the side view and front view shown in Figure 6-10 (b-c), the spark centroids are travelling in different directions with different velocities. The spark centroids at U=0 m/s, 1.18 m/s and 2.35 m/s are mainly moving in a trajectory path in XZ plane and slightly moving in Y-direction. In the higher air velocity case (U = 11.75 m/s), the spark centroid is significantly moving in the positive Y-direction due to the jet air flow effects.

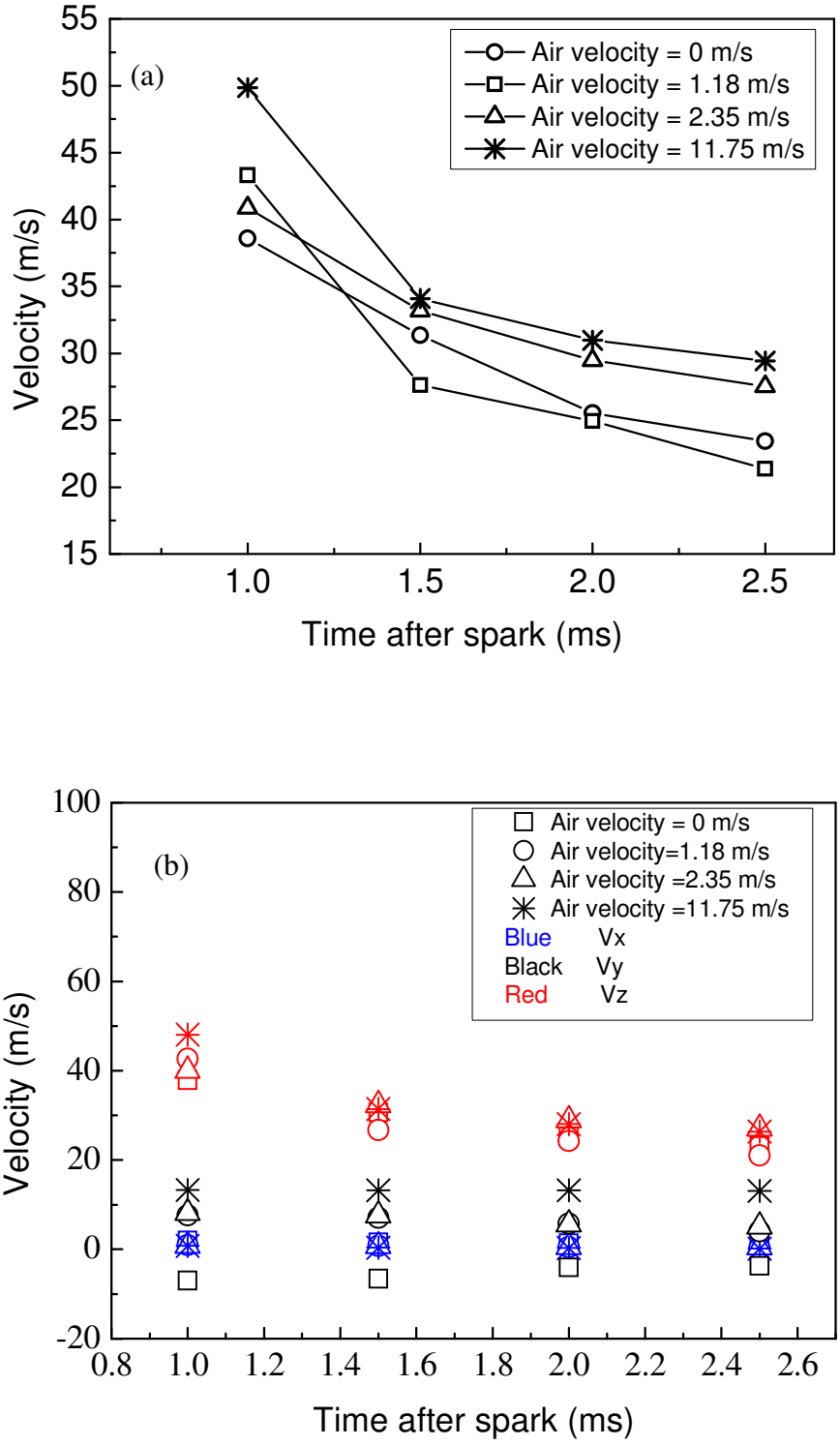

Figure 6-11 (a) The spark kernel centroid velocity and (b) velocity components in three directions at different air jet velocities

The mean velocities of the spark kernel centroid in three directions are calculated based on the 3D coordinates obtained between two consecutive stereo image pairs.

As shown Figure 6-11 (a), the overall velocities in the four cases are all decreasing as the time passes. Figure 6-11 (b) shows the velocity components of the spark kernel centroid in three dimensions with different air jet velocities. The result shows that *Vx* and *Vz* has similar trends with time at different air jet velocities. The velocity in Y-direction increases obviously with the air jet velocity.

6.4.3 3D points tracing of the ejected metal bits

It is reported that each spark causes a small bit erosion of the metal (Lefebvre, 1999). However, the generation and movement of the metal bits are lack of further investigation. In the experiments, it is interesting to note that the melted tiny metal bits leave bright streaks in the high speed images though they are not observable directly by eyes. These streaks are recordable until 12 ms after the spark initiation. A pair of the stereo images with streaks are shown in Figure 6-12. It is observed clearly that the tiny eroded metal particles have formed streaks of different lengths at the same shutter speed of 0.5 ms, indicating that the hot metal particles are travelling at different speeds. As shown in Figure 6-12, the two end points of each streak can be easily matched for 3D reconstruction. For example, the end points A and B in the left image and the end points A' and B' in the right image are corresponding points, which could be matched conveniently. The stereo technique used in this study provides an effective method to evaluate the mean 3D velocity of the particles during the image exposure time.

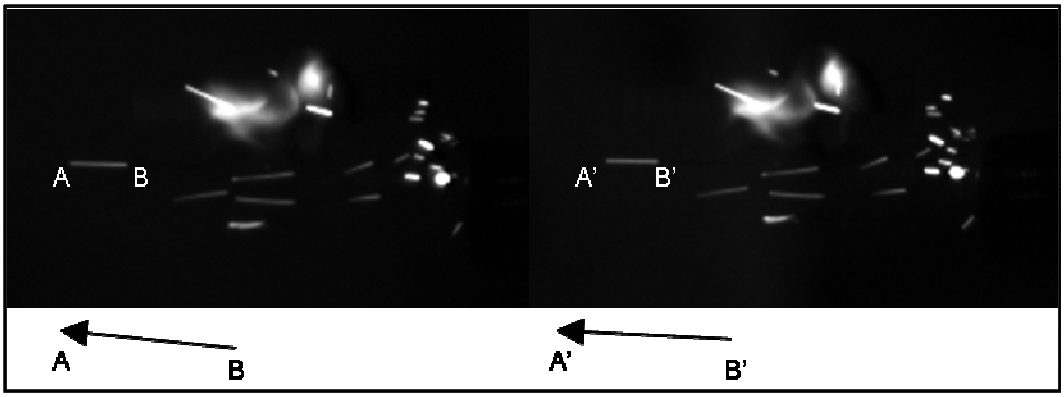

Figure 6-12 A stereo image pair of the captured streaks at 2.5 ms after spark

Combined with pre-calculated calibration parameters, the 3D coordinates of the end points of the streaks can be established. Once the two end points of each streak of the metal points are matched and the coordinates are computed, the 3D mean velocity of the metal bit during the image exposure period can be easily calculated. Then the velocity map of the various metal bits is obtained by plotting these 3D vectors on the same frame.

Three typical cases of the 3D velocity distributions of the tracked streaks have been demonstrated in Figure 6-13 (a), (b) and (c). The input voltage of the three cases is fixed at 150V. The length of the arrows is proportional to the velocity module. The arrow direction shows the spots propagating direction. It can be seen that the metal bits have very different trajectory paths and velocities after each spark initiation. The observed metal bits mainly move forward along the igniter axial direction, while some travel outwardly at very large angle and lower velocities. The histograms of the velocity distribution of the three cases are shown in Figure 6-14 (a-c). The maximum velocities of the three cases are 63 m/s, 56 m/s and 31 m/s respectively. From the images, it could be observed that the amounts of the particles are also different from spark to spark. In contrast with the similar development of the hot gas jet at different input voltages in Figure 6-5, the 3D velocity distributions of the metal particles are

different even at a fixed supply voltage. The amounts of the eroded metal particles and their velocity distributions show random tendency with the input voltage. The variations of the metal erosion at each spark may be caused by the highly localized 3D spark initiation at the very early stage. A slight variation in local geometry and surface conditions may have a significant effect on the metal eroding process. On the other hand, the gas jet development may mainly be controlled by the amount of energy released, which is almost a constant from spark to spark.

It is worth noting that the velocities of most particles are much higher than the hot gas propagation speed shown in Figure 6-5. It can also be seen from the simultaneous schlieren and direct imaging sequences that some metal bits along the igniter axis have travelled well beyond the front of hot gas propagation, which means that the hot gas jet at a later stage cannot be the driving force for the metal bits. The metal bits must have gained their energy and momentum during the short period of the intense energy release immediately after the spark initiation. Thus the energy loss caused by the metal erosion should be considered in spark performance investigation. It is also worth mentioning that it is not clear whether these metal bits will have any effect on the ignition process. Their speed, temperature and composition will play an important role in dictating its real effect.

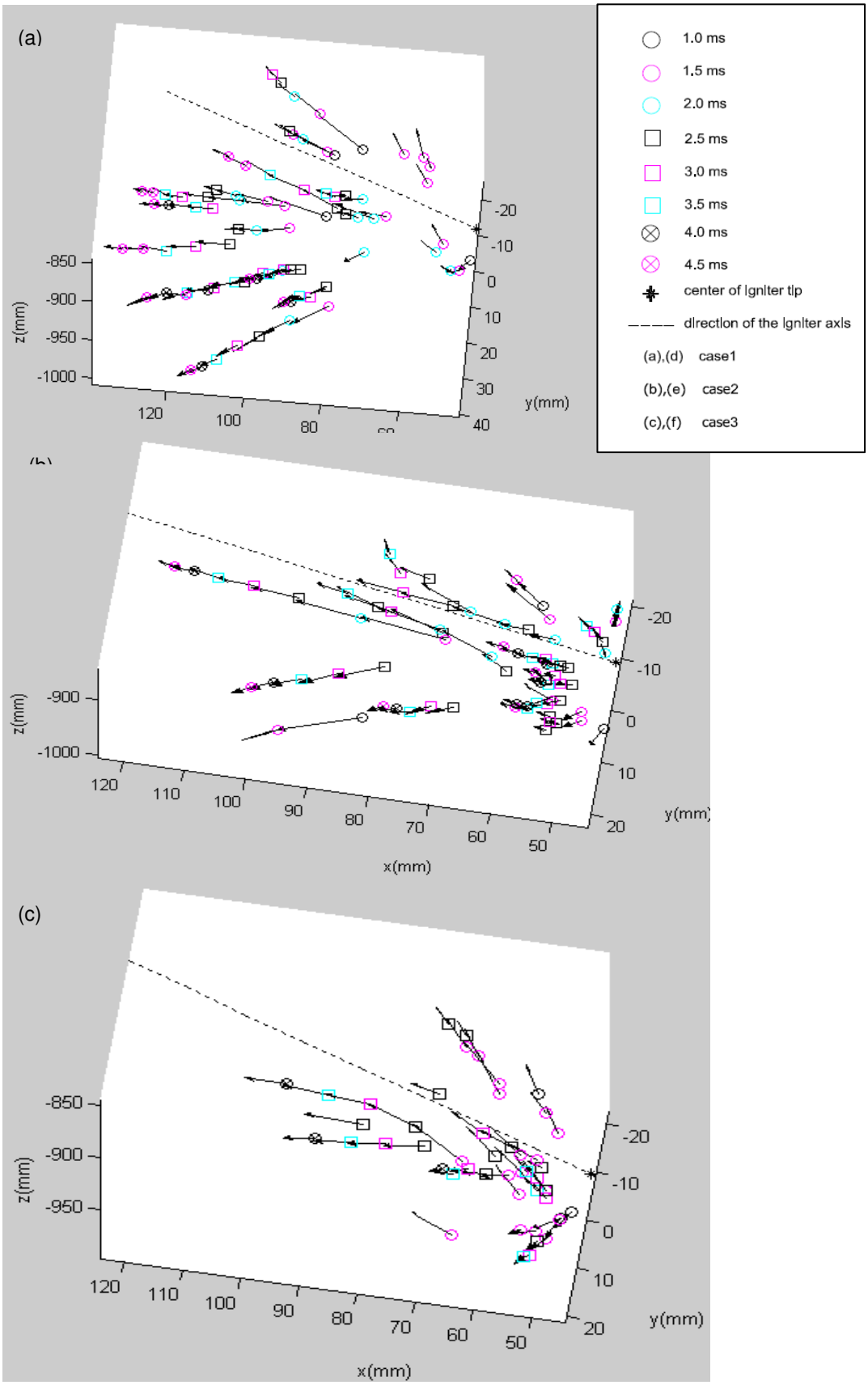

Figure 6-13 (a-c) Time resolved 3D velocity distribution of three different spark cases

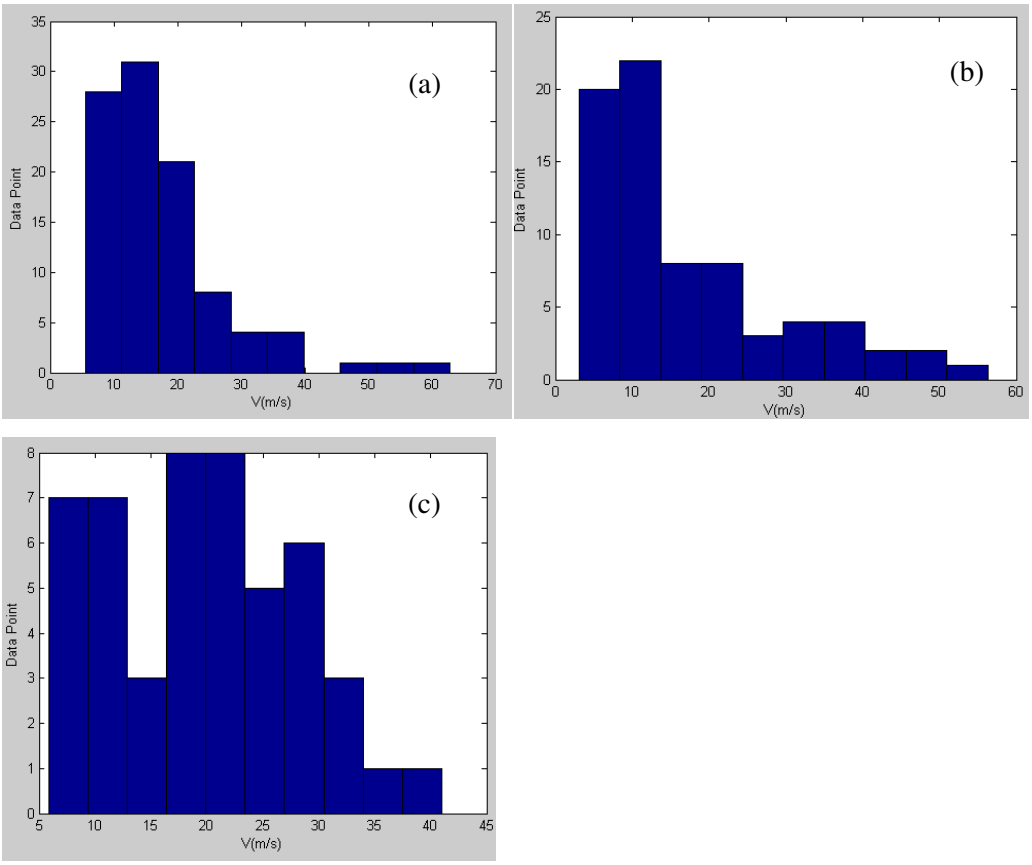

Figure 6-14 The histograms of velocity values

6.53D reconstruction of hot gas structure

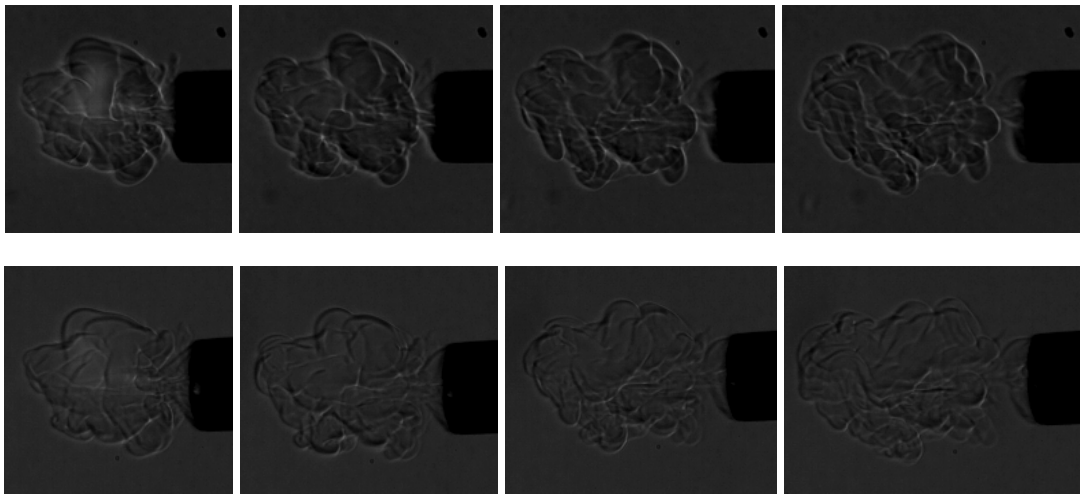

1.0ms 1.4ms 1.8ms 2.2ms

Figure 6-15 Shadowgraph sequence of spark induced hot gas propagation

The stereoscopic shadowgraph technique is then applied to investigate the 3D structure of the hot gas. The sequences of shadowgraph images at two directions are

shown in Figure 6-15. It could be observed that the interaction between the hot gas and ambient air is turbulent and has irregular structures. With careful examination, it could be observed that the curves in the two image sequences are different in detail structure. The standard stereo matching techniques which employ dense disparity matching are used to extract the correspondence points in the image pairs. The method works quite well on surfaces with texture or being non-smooth. However, the correlation approach tends to fail in smooth surfaces without features. A sample pair of images with the correspondence points extracted are plotted in Figure 6-16. The main features of the interaction interfaces are extracted successfully. With the calibration parameters given, corresponding feature points from the image pairs can be reconstructed. The raw data does not really describe surfaces, but only clouds of point coordinates in three-dimensional space. A three-dimensional mesh is applied to represent the 3D structure.

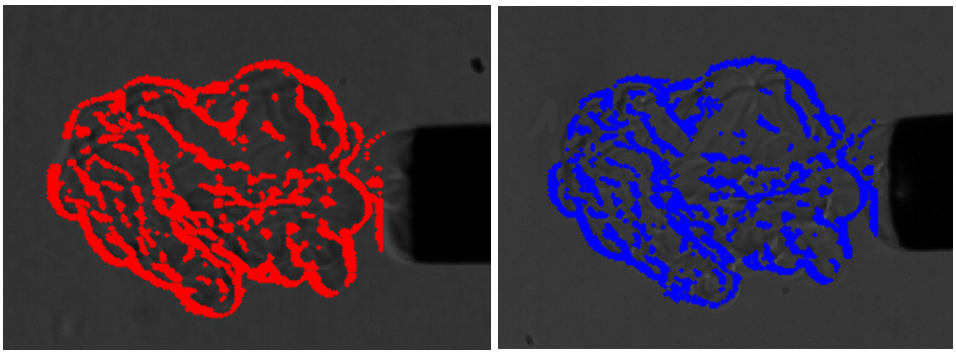

Figure 6-16 Correspondence points selected for reconstruction (t=2.2ms)

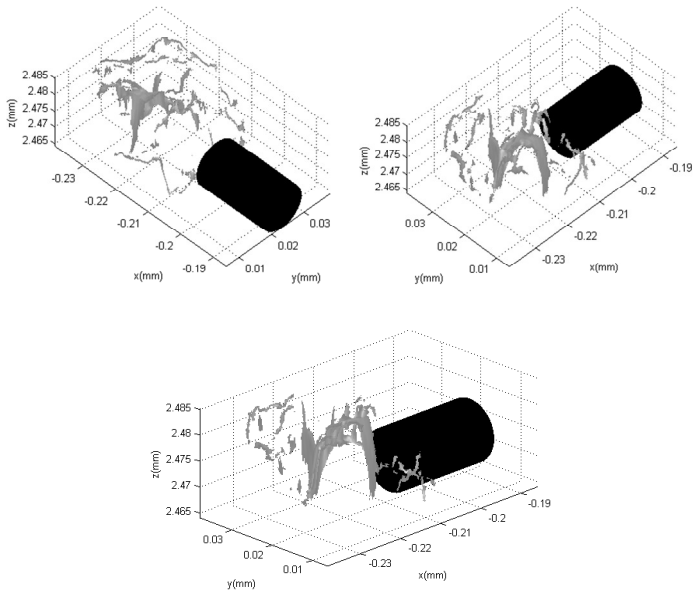
z(mm)
2.485
2.48
2.475
2.47
2.465
x(mm)
-0.23
-0.22
-0.21
-0.2
-0.19
y(mm)
0.03
0.02
0.01

(a)

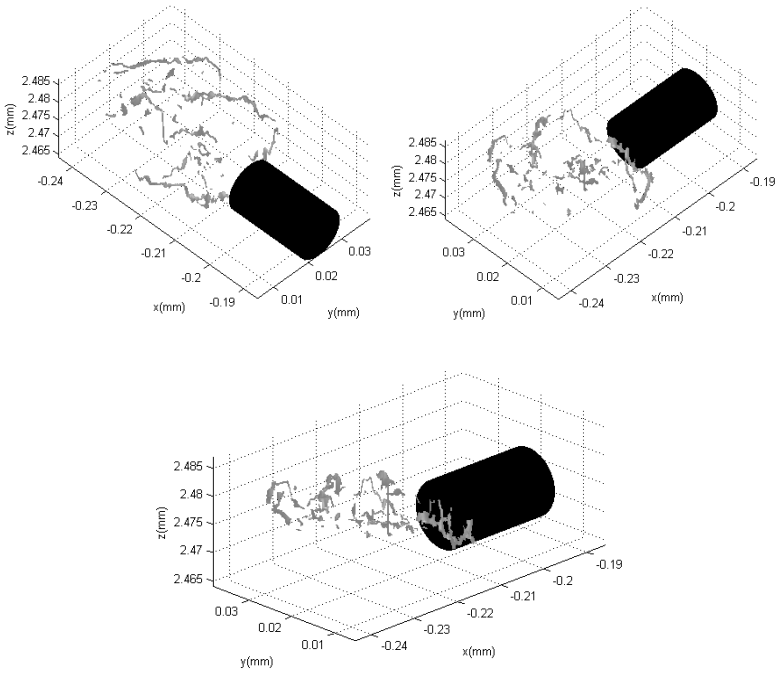
z(mm)
2.485
2.48
2.475
2.47
2.465
x(mm)
-0.24
-0.23
-0.22
-0.21
-0.2
-0.19
y(mm)
0.03
0.02
0.01

(b)

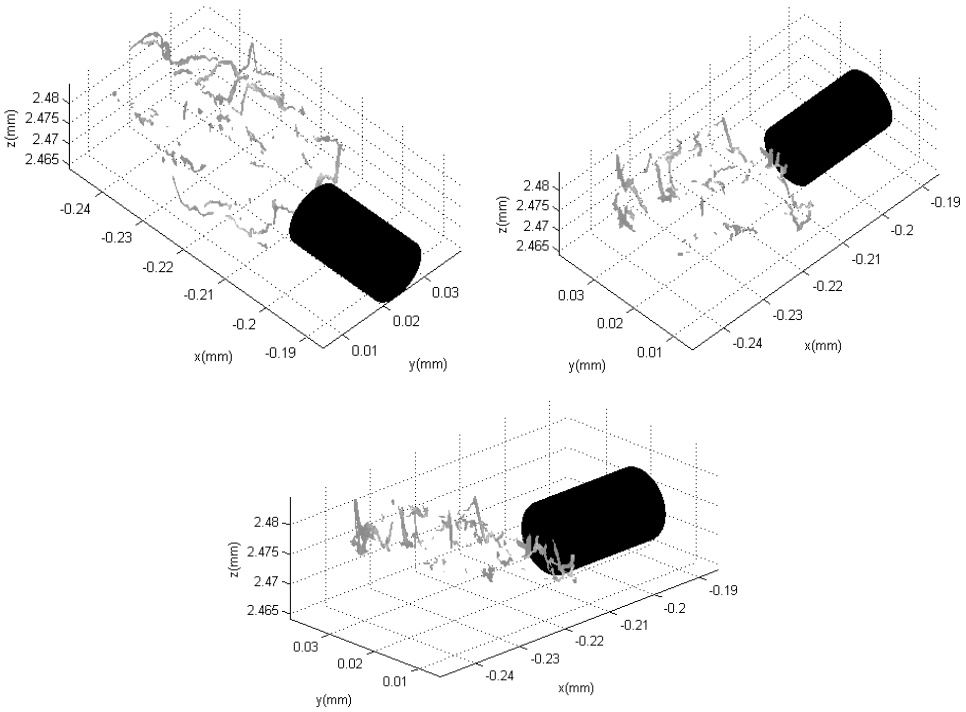

(c)

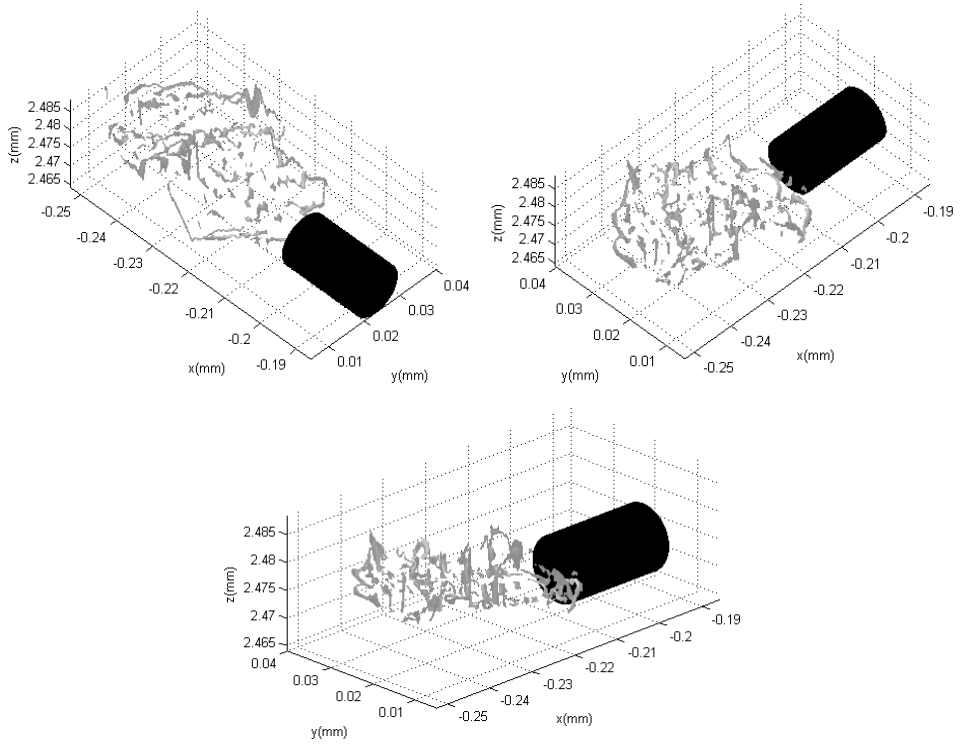

(d)

Figure 6-17 3D views of reconstructed hot gas structure at (a) t=1.0 ms, (b) t=1.4 ms, (c) t=1.8 ms, (d) t=2.2 ms

The 3D structure of the hot gas and ambient air interaction interfaces are illustrated in Figure 6-17. The 3D shape and distribution of salient features are extracted from the stereoscopic shadowgraph image pairs successfully. It can be seen that the interaction boundaries between the hot gas and ambient air shows a shape of an ellipsoid. The surface shows typical wavy structures, containing overlapping curve shapes in the 3D space. The irregular structures shown in Figure 6-17 could only be well understood through different 3D views. The 3D structure is of great help to understand the hot gas kernel development, which are difficult to be accomplished by other conventional techniques. The application of the newly proposed stereoscopic shadowgraph technique on hot gas structure indicates its ability of resolving relative weak density disturbances.

6.6 Conclusions

The characteristics of the shockwave and hot gas induced by a surface discharge igniter were investigated systematically through high speed schlieren and stereo techniques. A shockwave was captured at the early stage of the spark initiation by schlieren images. The shockwave speed in the test time scale is found to be slightly higher than the sound speed at ambient condition. The spark induced local high temperature and pressure combines with the igniter tip geometry to form a forward plasma jet. The evolution of the propagation speed of the hot gas jet front was found to be similar for all the test cases at different input voltages. The schlieren images and 3D tracing of the visible spark centroids show that the air flow jet can affect the spark performance greatly.

Stereo images were taken with a four-mirror adapter attached to the front lens of a high speed camera. The tiny metal bits eroded by the spark initiation formed streaks of different lengths and directions on the high speed stereo images. The 3D velocity vectors of the moving metal bits are reconstructed quantitatively and the details of the 3D methodology and the possible error in digital reconstruction are shown. At fixed spark generation frequency, the velocity distributions and the amount of the eroded metal bits are found varying significantly from spark to spark. Some of the metal bits propagating along the igniter axis have a much higher velocity than the hot gas front. The metal erosion will affect not only the life span of a spark igniter but also the performance of each individual spark because melting and heating of the metal will drain energy. The time resolved 3D structures of the hot gas kernel has been extracted using a newly developed stereoscopic shadowgraph technique. The quantitative information obtained in this chapter may shed light for further spark ignition performance investigation.

Chapter 7 Vortex Dynamics and Structures of Methane/Air Co-flow Diffusion Flames

7.1 Introduction

Laminar gas jet diffusion flames have been intensively studied in combustion science. The understanding of diffusion flame stabilization mechanisms is essential for industrial applications, such as engine and furnace designs, safety consideration, costs cutting, combustion efficiency improvement and pollutant emissions reduction. It is found that laminar jet diffusion flames show a typical phenomenon of flickering/oscillating at a low frequency of 10-20 Hz (Chamberlin and Rose, 1948). In a flickering flame, the flame and flow interactions show periodic and reproducible characteristics. In a cycle of flickering flame, the flame surface and outer vortical flow shows typical turbulent flame features. According to flamelet concept, laminar flame burning is pertinent to the turbulent flames. Therefore, the study of laminar

diffusion flame contributes to the understanding of not only flickering flame itself but also turbulent flames.

The experimental study by Chen *et al.* (Chen et al., 1989) has shown two distinct vortices: large toroidal vortices outside the luminous flame and small roll-up vortices inside the luminous flame. It was found that the flame oscillation frequency is correlated with the large toroidal vortex structures outside the visible flame zone due to buoyancy-driven instability (Toong et al., 1965, Katta and Roquemore, 1993, Kimura, 1965). Buckmaster et al. (Buckmaster and Peters, 1988) employed a linear instability theory and showed that the flame buoyancy could result in a modified Kelvin-Helmholtz type instability at a frequency around 17 Hz. In addition, it is underlined by Demare and Baillot (Damare and Baillot, 2001) that a lifted diffusion jet flame in the hysteresis zone is stabilized on secondary streamwise vortices rather than primary instabilities. The laminar jet diffusion flame flickering frequency is relatively independent of fuel type, nozzle dimension and jet exit velocity (Chen et al., 1989, Kimura, 1965, Lingens et al., 1996, Hamins et al., 1992). Furthermore, the experiments in low-gravity conditions show that the flame flickering frequency is proportional to the square root of the gravitational acceleration (Papas, 2002). It is reported that the flame flickering frequency increases while the ambient pressure is increased (Albers and Agrawal, 1999, Darabkhani and Zhang, 2010). In investigating the flame flickering behaviours, photomultipliers or other optical sensors are applied to collect the visible flame signals (Sato et al., 2000). Because of this, the correlation between the invisible flow field and the visible flame cannot be made.

The effects of Froude number on stability limits in flames were investigated in different literatures (Shu et al., 1997, Hamins et al., 1992, Sato et al., 2000). Shu et

al. (1997) studied the dynamic flame structure and flame-vortex interactions at different Froude numbers (*Fr*), in a fuel-rich premixed (CH_4-air) annular jet sandwiched between a central air jet on the inside and co-flowing air on the outside. They reported that, at lower *Fr* the rollup occurs closer to the burner port, resulting in flame-vortex interactions and a dynamic flame, while at high *Fr* the computed flame exhibits a steady flame structure.

The investigation of diffusion flame can be divided into lifted and non-lifted flames. A lifted jet flame can be created by increasing the fuel or surrounding air co-flow velocity for most hydrocarbon gas fuel. The lifted diffusion jet flame on co-flow model has been extensively explored recently, especially on hysteresis related characteristics (Cabra et al., 2005, Terry and Lyons, 2006, Gollahalli et al., 1988). The dynamics of non-lifted laminar co-flow diffusion flame is the main focus of this study. Co-flow model is widely used in combustion investigation, because it is a relatively simple flow field and thus amenable to study both numerically and experimentally (Liu et al., 2004, Connelly et al., 2009). However, a systematic and quantitative investigation of the co-flow effect on the interaction between the visible flame and outside vortices is not yet reported. The fundamental dynamics and structure investigation is important to understand the co-flow flame instability and is effective experimental proof for the potential comparison with numerical results.

In this study, several visualisation methods are employed to investigate the flame and outer vortex evolution at different fuel and co-flow air conditions. High speed direct imaging is a very powerful tool for the visualisation of the visible flame. High speed schlieren imaging technique is widely used to observe the global vortex evolution of the flame induced hot gas products (Davis and Rerkshanandana, 1993,

Strozzi et al., 2008). In this study, the schlieren view is much larger than the visible flame region, which provides an opportunity to assess the flow dynamics and structures not only around the visible flame but also in post combustion zone. Besides direct/schlieren visualisation to gain insights into the physical phenomena, image analysis has been carried out to extract quantitative information from the obtained image database. Laser based diagnostic techniques such as Particle Imaging Velocimetry (PIV) has been applied to investigate the flame structure and its interaction with flow field (Chew et al., 1989, Chang et al., 2001) to provide valuable insights. In this study, PIV technique is also applied to observe the structures of flame and hot gas interaction on specific planes. The velocity distribution is obtained through the PIV technique as well.

7.2Experimental setup

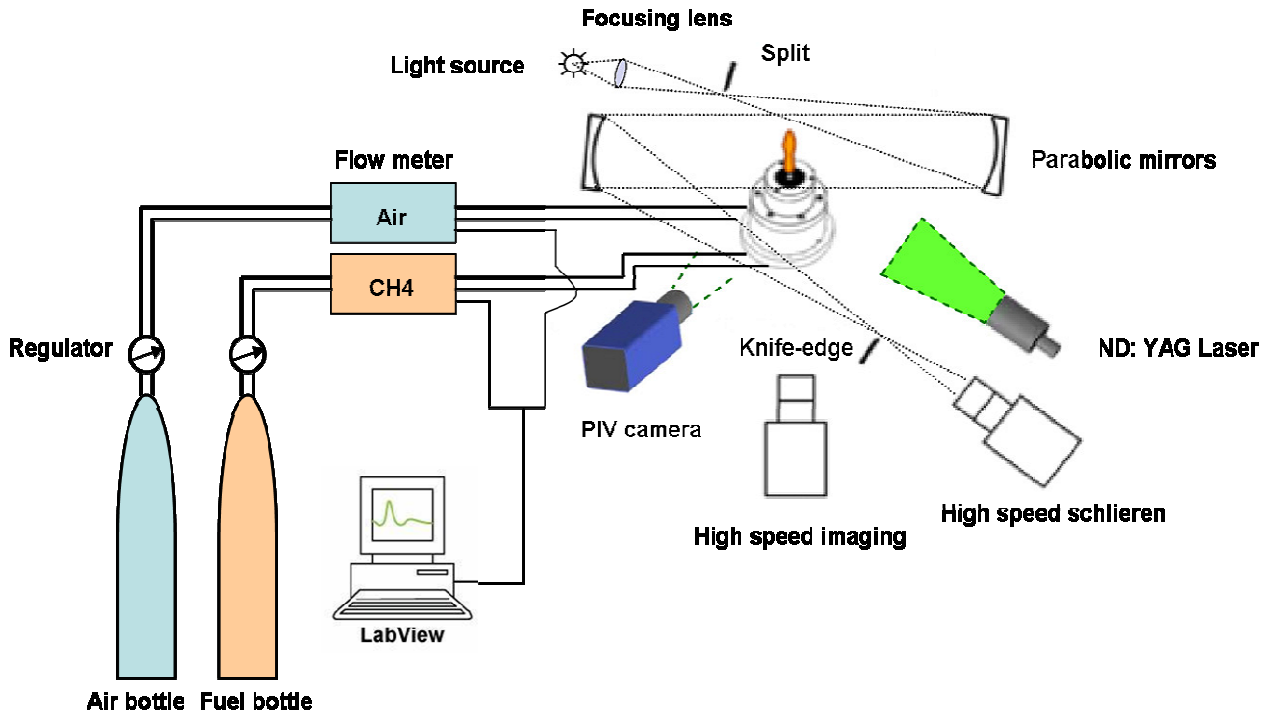

(a)

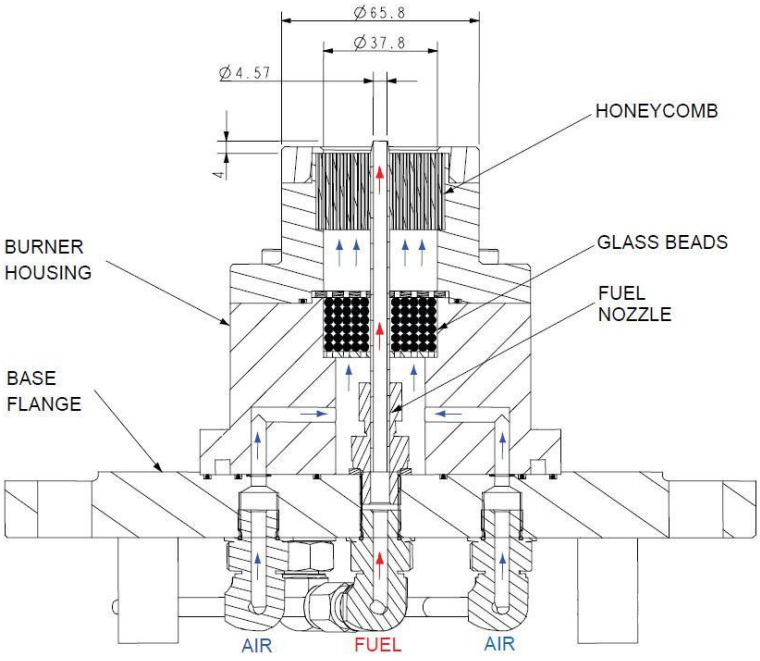

(b)

Figure 7-1 (a) Schematic of the experimental setup; (b) Cross-section of the co-flow diffusion flame burner

A schematic setup of the co-flow burner system is shown in Figure 7-1 (a). In the experiments, methane was used as the fuel. Mass flow controllers were used to control the flow rate of fuel and air separately. The cross section of the co-flow burner is illustrated in Figure 7-1 (b). The fuel jet was surrounded by a coaxial air jet. The fuel was injected through a central nozzle of 4.57 mm in diameter. The co-flow air nozzle has a diameter of 37.8 mm. The air was straightened by a fine meshed honeycomb inside the air nozzle.

The high speed schlieren imaging system was used to investigate the flow dynamics and structures. All the schlieren images (1024×1024 pixels) were recorded by a high speed camera (Photron SA-3) at a framing rate of 2,000 fps and the shutter speed was set at 1/200,000 s. The very high shutter speed provides good temporal resolution of the image and prevents the blurring caused by flame or flow movement.

A TSI PIV system is applied both for qualitative visualization and quantitative velocity measurement. It consists of a double-pulse 15 Hz ND: YAG laser and a TSI POWERVIEW™ Plus 4MP Camera which offers a pixel revolution by 2,048 × 2,048. A solid particle generator (Dantec Dynamics model 10F01) and titanium dioxide particles with a mean diameter of 3 μm were used as seeding for the PIV system. The seeding was added to the co-flow air. The interrogation area for PIV post processing is set at 32 pixels in width and 64 pixels in height. The result shows instantaneous flow patterns. Table 1 shows the test conditions of the experiment. The fuel flow rates were ranging from 0.20 l/min to 0.40 l/min. The co-flow air flow rate was set in the range from zero to 40 l/min. Froude number is calculated on basis of the equation $Fr = \frac{V}{\sqrt{gL}}$, where V is the velocity of the flow, g is the acceleration due to gravity, and L is the nozzle diameter. The air and fuel velocity ratio of the test conditions are illustrated in Table 7-2.

Table 7-1 Test conditions

Gas type	Volume flow rate (L/min)	Volume flow rate (10E-6×m^3/s)	Mass flow rate (10E-3×g/s)	Velocity (m/s)	*Re* No.	*Fr* No.
Methane (CH_4)	0.20	3.33	2.23	0.238	60.9	1.17
	0.25	4.17	2.78	0.298	76.1	1.46
	0.30	5.00	3.34	0.357	91.4	1.76
	0.35	5.83	3.90	0.417	106	2.05
	0.40	6.66	4.46	0.477	121	2.34
Air	0	0	0	0	0	0
	3	50.0	60.2	0.046	102	0.08
	5	83.3	100	0.077	171	0.13
	7	117	140	0.108	239	0.19
	10	167	201	0.154	342	0.27
	15	250	301	0.231	513	0.40
	20	333	401	0.309	684	0.54
	25	417	502	0.386	854	0.67
	30	500	602	0.463	1025	0.81
	40	667	803	0.617	1367	1.08

Table 7-2 Air and fuel velocity ratio at selected conditions

V_a/V_f		V_f (m/s)				
		0.238	0.298	0.357	0.417	0.477
V_a (m/s)	0	0	0	0	0	0
	0.046	0.19	0.15	0.13	0.11	0.10
	0.077	0.32	0.26	0.22	0.18	0.16
	0.108	0.45	0.36	0.30	0.26	0.23
	0.154	0.65	0.52	0.43	0.37	0.32
	0.231	0.97	0.78	0.65	0.55	0.48
	0.309	1.30	1.04	0.86	0.74	0.65
	0.386	1.62	1.30	1.08	0.92	0.81
	0.463	1.94	1.55	1.30	1.11	0.97
	0.617	2.59	2.07	1.73	1.48	1.29

7.3 Flame oscillation characteristics at different co-flow conditions

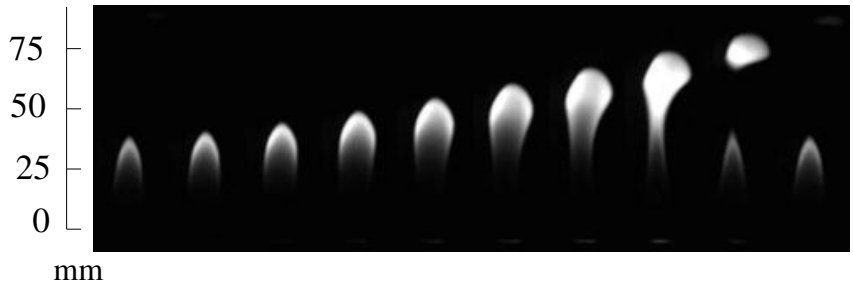

(a) Direct imaging sequence with the fuel flow rate at 0.3 l/min and no co-flow air (The time interval between each two images is 10 ms)

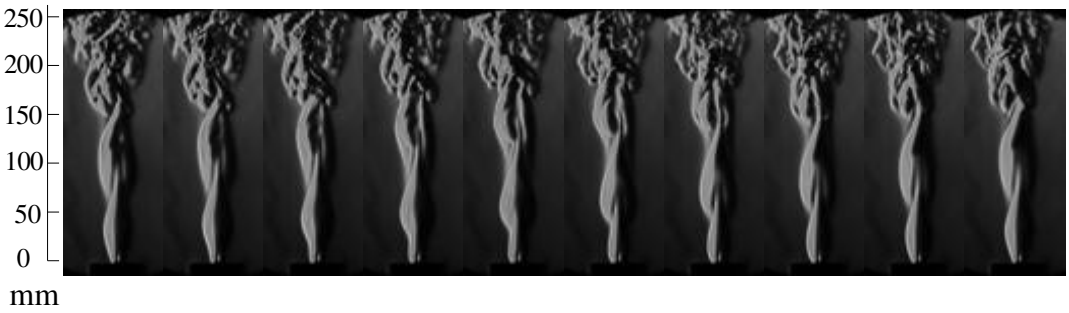

(b) Schlieren imaging sequence with the fuel flow rate at 0.3 l/min and no co-flow air (The time interval between each two images is 10 ms)

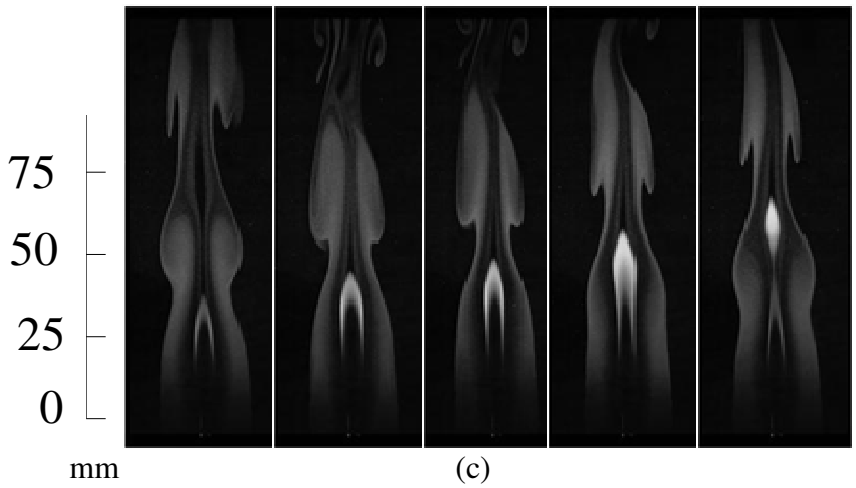

(c) PIV images of co-flow flames at fuel flow rate at 0.4 l/min and co-flow air flow rate at 10 L/ min

Figure 7-2 Flame flickering phenomena

The flame flickering phenomena is observed by high speed direct imaging, as shown in Figure 7-2 (a). The flame shows typical flickering nature driven by buoyancy and flame necking is observed. Schlieren imaging provides a method to reveal the density variations of the flow. In this study, schlieren is utilised to visualise the hot gas products and its mixing with ambient air. The contrast of the direct and schlieren images may provide valuable physical insights. The schlieren images of the same test cases as shown in Figure 7-2 (a) are presented in Figure 7-2 (b). For the flame without co-flow air, the cyclic evolution of the large toroidal vortex could be observed obviously. The initiation point of the toroidal vortex (IPTV) developed immediately at the nozzle exit. The vortex was developing and shedding in the downstream side. The large toroidal vortex structure was observed to break up into smaller vortices in further downstream of the visible flame region. The visible flame and the large toroidal vortex indicate similar evolution cycle. The PIV images shown in Figure 7-2 (c) supply further evidences of the interaction between the

visible flame and the vortices outside. It could be observed that the flame oscillation is dominated by the evolution of the large toroidal vortices.

(a) Direct imaging sequence with the fuel flow rate at 0.3 l/min and co-flow air flow rate at 7 l/min (The time interval between each two images is 10 ms)

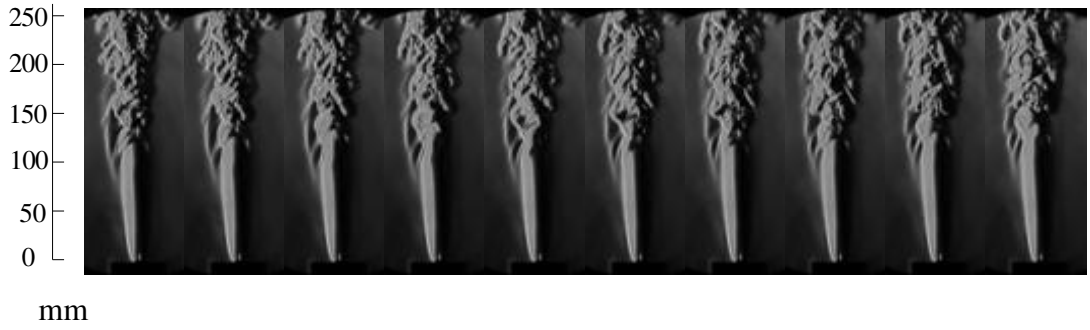

(b) Schlieren imaging sequence with the fuel flow rate at 0.3 l/min and co-flow air flow rate at 7 l/min (The time interval between each two images is 10 ms)

Figure 7-3 Flame flickering suppression by co-flow air

During the experiments, it is found that the colfow air is able to suppress the natural flame flickering completely. As shown in Figure 7-3 (a), the direct imaging sequence of the flame with an air co-flow rate of 7 l/min shows the flame keeps stable without any cyclic nature. By examining the schlieren imaging sequence in Figure 7-3 (b), a laminar pattern was observed from the nozzle exit. The height of the pattern is found to exceed the visible flame height. The vortices were formed at the end of the laminar pattern and broke up into small vortices in further downstream region. Since the flame flickering is dominated by the large toroidal vortex, the co-flow air effect

eliminates the vortex in the visible flame region and thus suppresses the flame flickering.

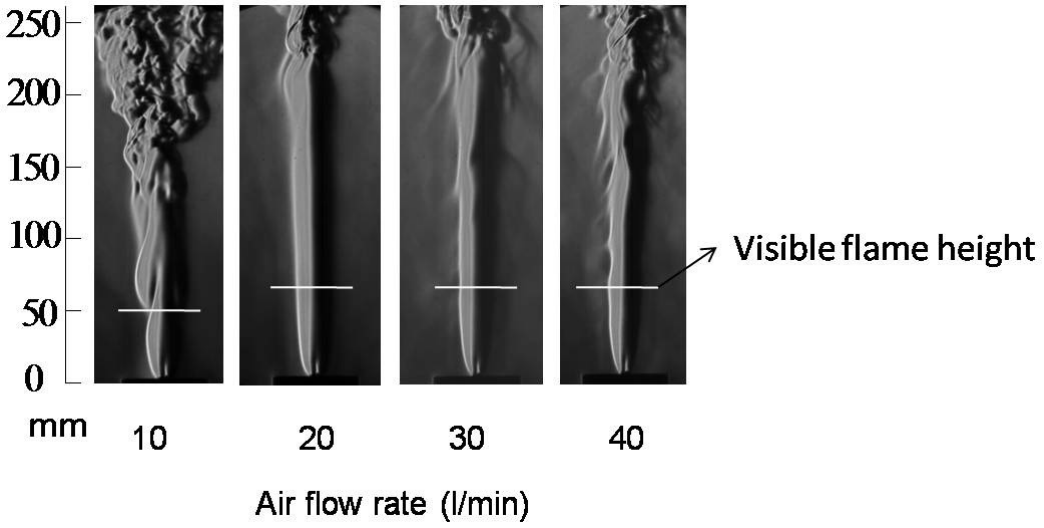

(a)

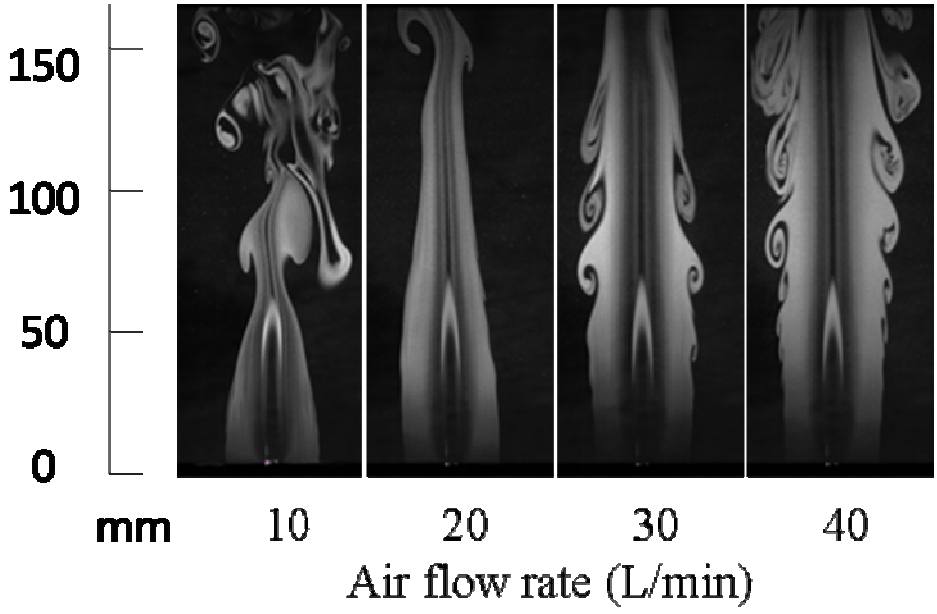

(b)

Figure 7-4 (a) Schlieren images (The line shows the height of visible flame); (b) PIV images at different air flow rates (fuel flow rate is 0.4 l/min)

The vortex evolutions at different co-flow air flow rates are investigated. Figure 7-4 shows the schlieren and PIV images at a fuel rate of 0.4 l/min with different air flow rates. It is found that the flame stops oscillating when the air flow rate exceeds 15 l/min. The schlieren sequence in Figure 7-4 (a) shows the global structure of the vortices outside the visible flame, which is caused by the buoyancy instability. It could be observed that the vortices are initiated from the nozzle exit and moving upward at the air flow rate of 10 l/min, when the oscillating exists. After the flame is stable without oscillating (air flow rate at 20 l/min, 30 l/min and 40 l/min), a stable and laminar flow pattern is observed. From the PIV images in Figure 7-4 (b), it could be seen that the height of the stable pattern is larger than the visible flame height. The initiation point of toroidal vortex (IPTV) has been pushed beyond the visible flame region by the co-flow air outside the flame. Therefore a conclusion can be drawn that the co-flow air is able to shift the location of the IPTV out of the flame region to suppress the flame flickering. The underlying reason is that in the visible flame region, the increasing co-flow air velocity counteracts with the buoyancy induced hot gas velocity. Thus the vortices can only occur in the downstream side at a position which is already over the visible flame height. Once the toroidal structure is pushed out of the flame zone the flickering of the flame will disappear naturally. It is interesting to notice that when the air flow rate is at 30 l/min and 40 l/min, roll up vortices are observed at the outer boundary of the co-flow air in the PIV images. The vortices must be generated by the velocity differences between the co-flow and ambient air, which is caused by the strong co-flow upward momentum. However the vortices are too far away from the reaction zone to affect on the flame region.

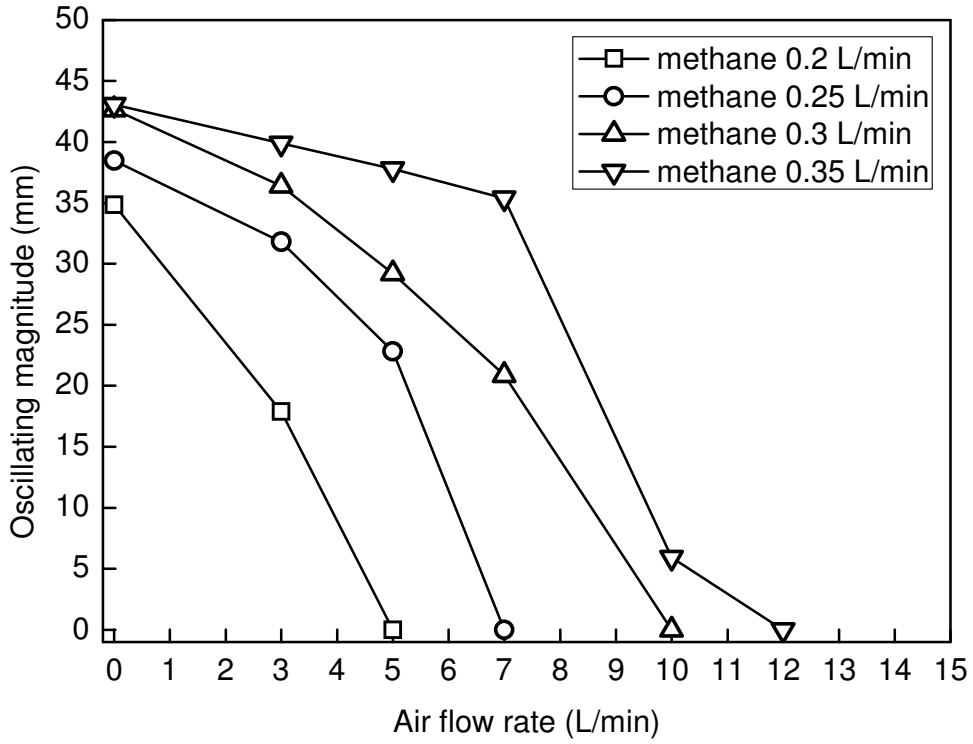

Figure 7-5 The flame oscillating magnitude L_f at different air and fuel flow rates

The oscillating magnitude L_f is defined as the difference between the maximum and minimum visible flame height. The larger the value of L_f , the more obvious oscillating could be observed. The oscillating characteristics at different fuel and co-flow air flow rates are illustrated in Figure 7-5. It could be found that at each fuel rate, the flame oscillating is inhibited by the increasing of co-flow air flow rate. The oscillating stops when the air flow rate reaches a critical value. At the same air flow rate, the flame oscillating magnitude is increased with the fuel flow rate.

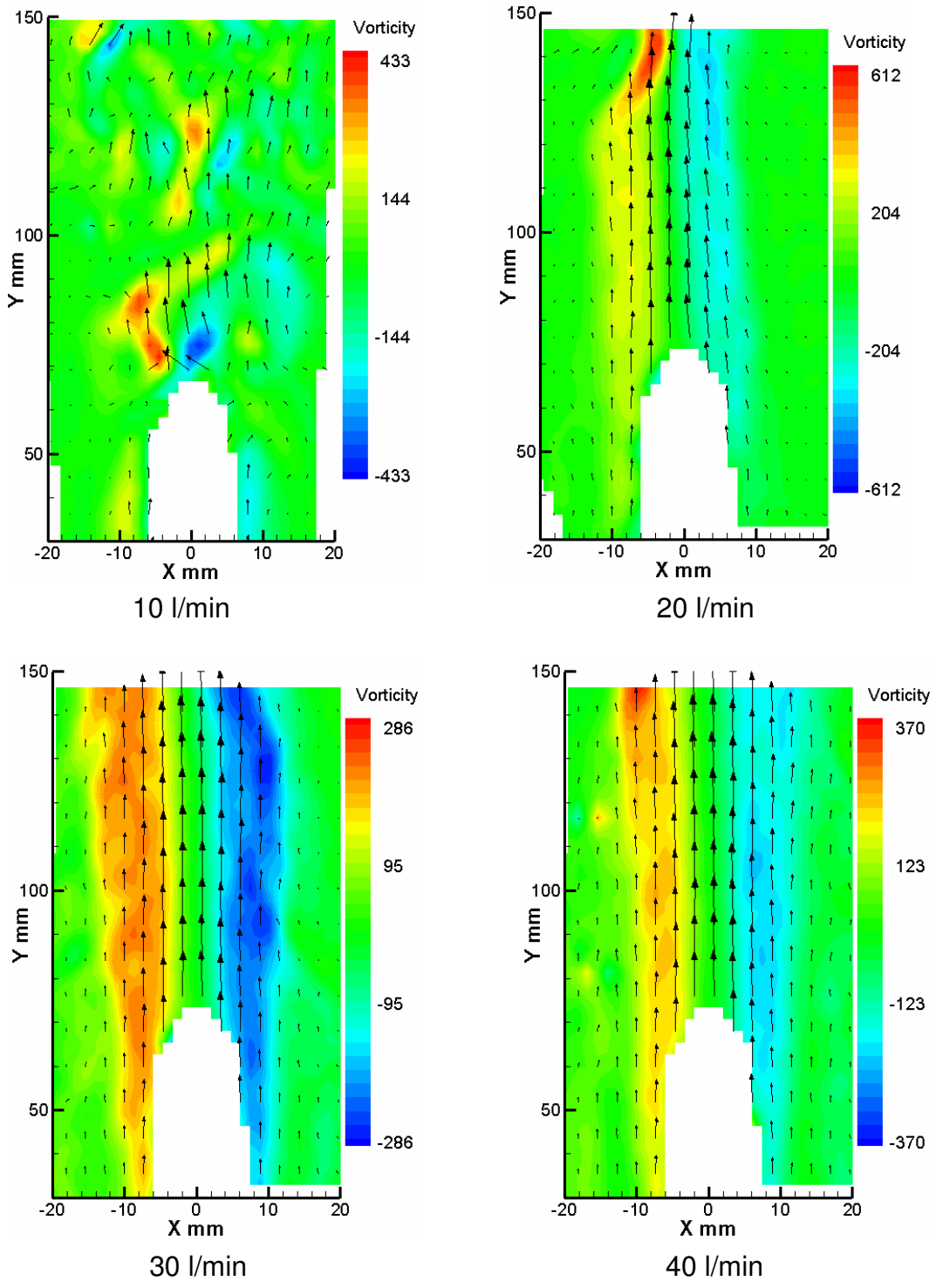

Figure 7-6 Instantaneous velocity vectors and vorticity contours at different air flow rates (fuel flow rate is 0.4 l/min)

Test cases of instantaneous velocity vectors and vorticity contours are shown in Figure 7-6. The central blank area near x-axis is the region of flame, where the seeding particles could not be traced effectively because only the co-flow is seeded.

The methane flow rate is 0.4 l/min and the air flow rate is 10 l/min, 20 l/min, 30 l/min and 40 l/min respectively. When the air flow rate is 10 l/min, the velocity magnitudes are higher in the area with strong vorticity. The vorticity distribution shows the presence of large random structures around the tip of the flame and above. When the air flow rate is increased, the strong vorticity is observed on both sides of the flame and the vorticity on the left side of the flame is positive and the right side negative. That may be caused by the vortices rotating at different directions, i.e., clockwise and anticlockwise. At air flow rate at 20 l/min, strong vorticity is seen on top left of the view field, which indicates that the co-flow air is interacting with the upward buoyant flow. When the air flow rate is increased to 30 l/min and 40 l/min, the flame becomes stable without any oscillating. The vorticity is then distributed more evenly at both sides of the flame downstream.

In all the cases shown in Figure 7-6, the velocity is found to be higher in middle and lower aside along the x-axis. The velocity magnitudes at three different z-coordinates (32 mm, 64 mm and 96 mm) are plotted in Figure 7-7. It can be seen that at all selected z-coordinates the velocity has similar trend at different air flow rates. The velocity close to the centre line is much higher, which is caused by the buoyancy effect of the flame. The velocity increases slightly with the increase of co-flow rate and z-coordinate.

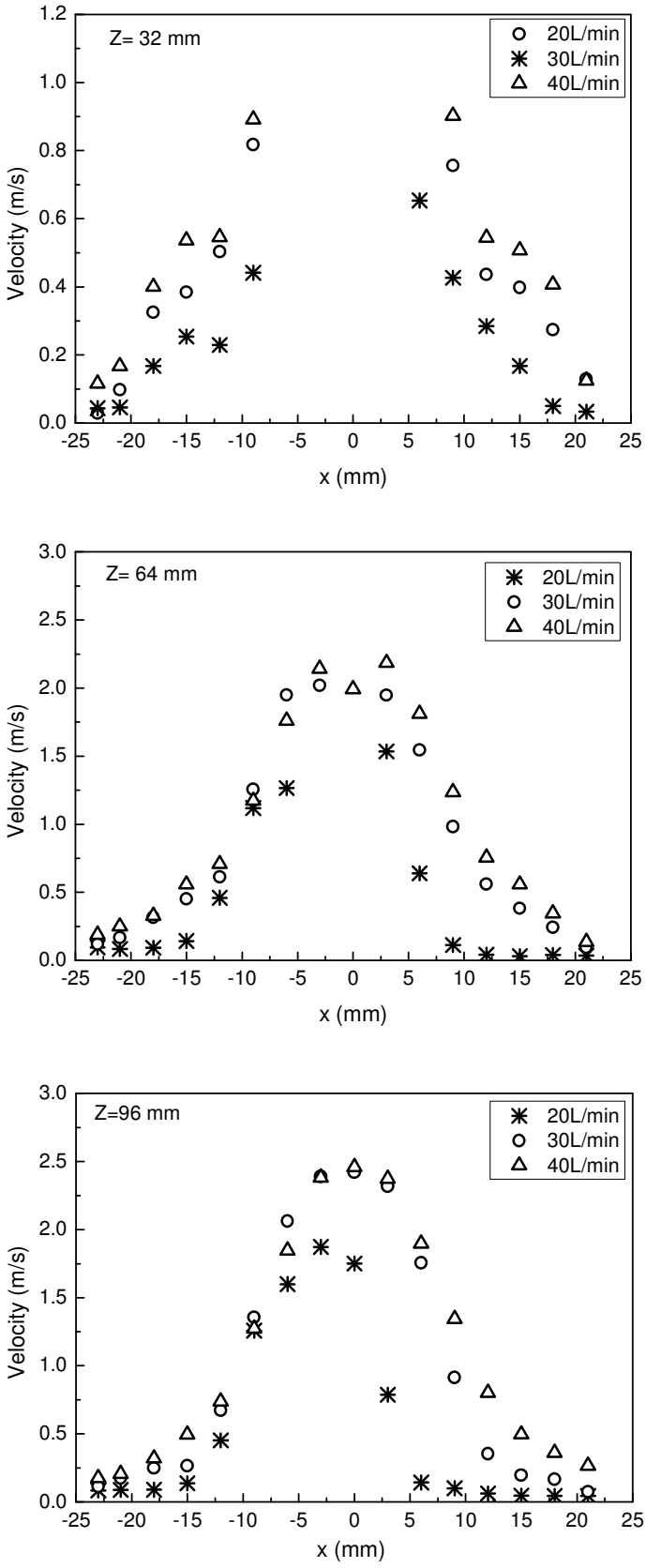

Figure 7-7 Velocity profiles at different air flow rates (fuel flow rate was 0.4 l/min)

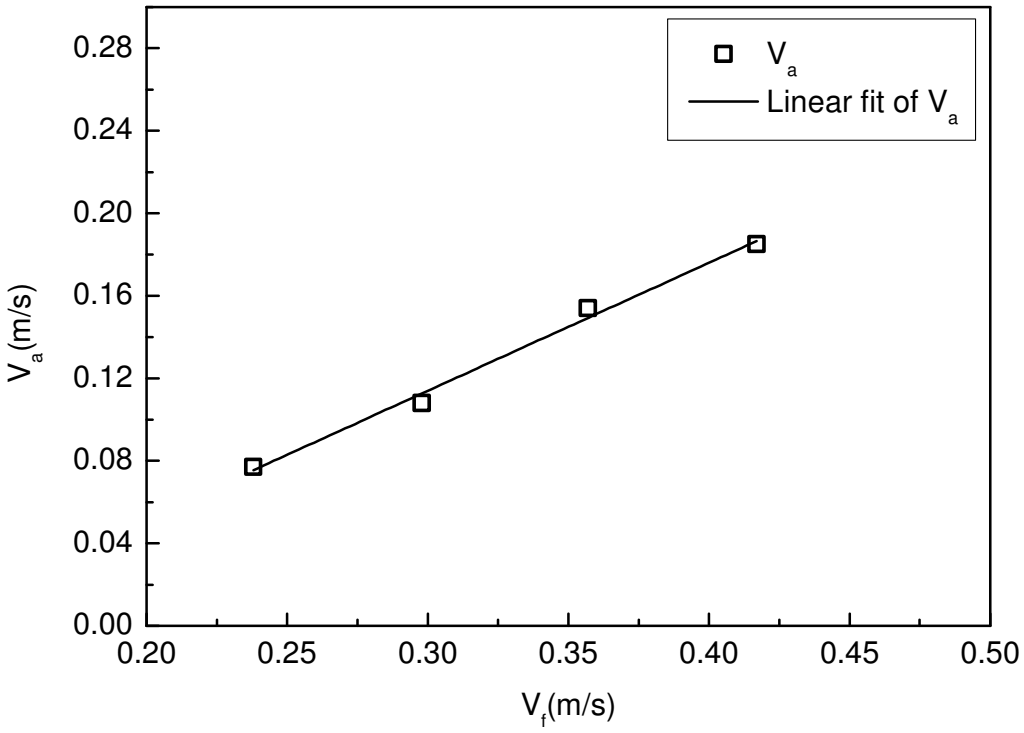

Figure 7-8 The critical air velocity versus fuel velocity

As has been discussed above, when the air flow rate exceeds a critical value, the flame is stable without any oscillations. The trend between the critical value of the mean co-flow air velocity V_a and the fuel velocity V_f at exit is plotted in Figure 7-8. The critical air flow rate increases with the fuel flow rate linearly. The trend indicates that at higher fuel flow rate the buoyancy effect is greater and it is natural that stronger co-low air momentum is required to counter the buoyancy effect. The ratio of the two velocities could be hired as a control parameter for flame stabilization. The critical value of the ratio (V_a / V_f) is 0.62 in this study. Once the air and fuel velocity ratio exceeds the critical value, the flame becomes stable. Since the velocity differences between the hot gas and co-flow air are decreasing with the increasing of co-flow velocity, the disappearance of the vortex generation in the visible flame area is also a result of the elimination of velocity gradient.

7.4 Flame and vortex structures at different co-flow conditions

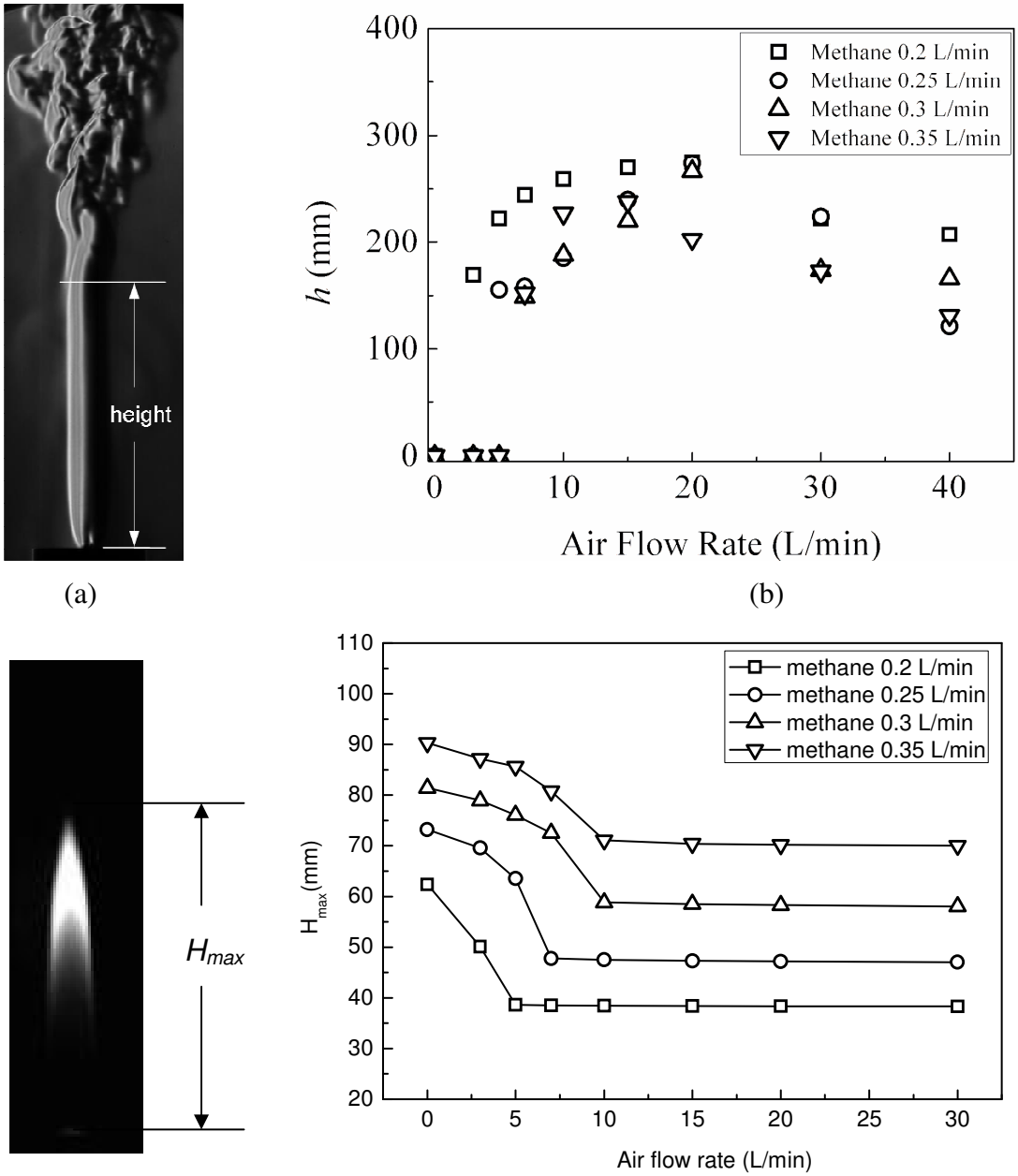

Figure 7-9 (a) Illustration of the IPTV height; (b) The IPTV height h at different fuel and air flow rates; (c)The illustration of the maximum visible flame height; (d) H_{max} at different fuel and air flow rates

The high speed direct and schlieren images provide us a chance to investigate the flame and vortex behaviours at the same time. In Figure 7-9 (a), the IPTV height h is defined as the height from nozzle exit to position of IPTV. Each IPTV height is determined by the mean value from five images and the standard deviation error is

less than 5%. The relationship between IPTV heights and co-flow rates are plotted in Figure 7-9 (b). All the test cases have shown that the value of h increases with the co-flow air flow rate initially until a maximum value is achieved. Then it starts to decrease against the air flow rate. The initial increase of the height is steep and the late on decrease is more gradual. The change of IPTV is the result of interaction of the buoyancy induced toroidal vortex and the co-flow stream momentum. The co-flow stream momentum is enhanced with the increasing air flow rates. As a result, the starting point of the buoyancy generated vortex is pushed downstream gradually. As the co-flow flow rate increases further other instability factor such as the outer layer roll-up vortices may become important and the combined effect may have pushed down the IPTV. At each fuel flow rate, a maximum IPTV height $h_{\max}$ is observed. It is found that $h_{\max}$ decreases as the fuel flow rate increases, which may be caused by the increased buoyancy effect. Meanwhile, the heights of the visible flame are evaluated at different air and fuel flow rates. As shown in Figure 7-9 (c), the flame maximum flame height H_{max} is used as the height parameter since there is oscillation in some cases. Actually, when the flame is stable, the height of the flame keeps at the same value as indicated in Figure 7-5. The trend of H_{max} at different air and fuel flow rates are plotted in Figure 7-9 (d). It could be observed that the maximum flame height is decreased with the increasing air flow rate at the oscillating stage. When the flame is stable, the flame height shows no obvious change with the air flow rate.

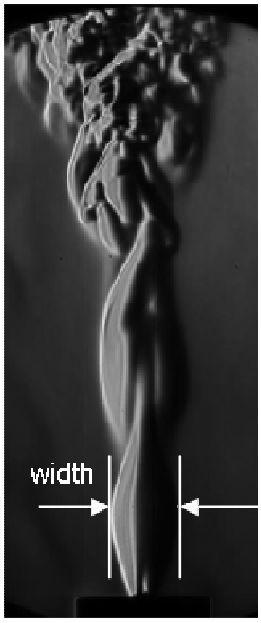

(a)

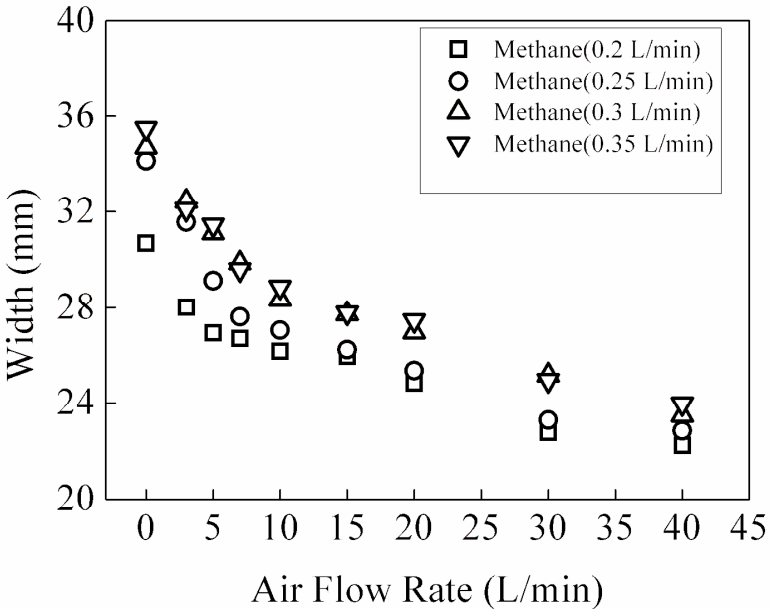

(b)

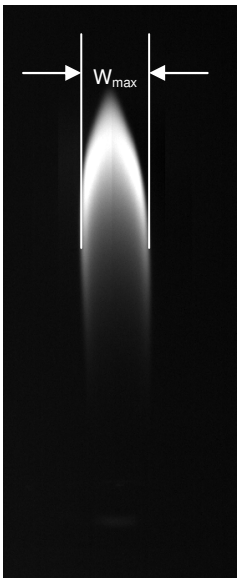

(c)

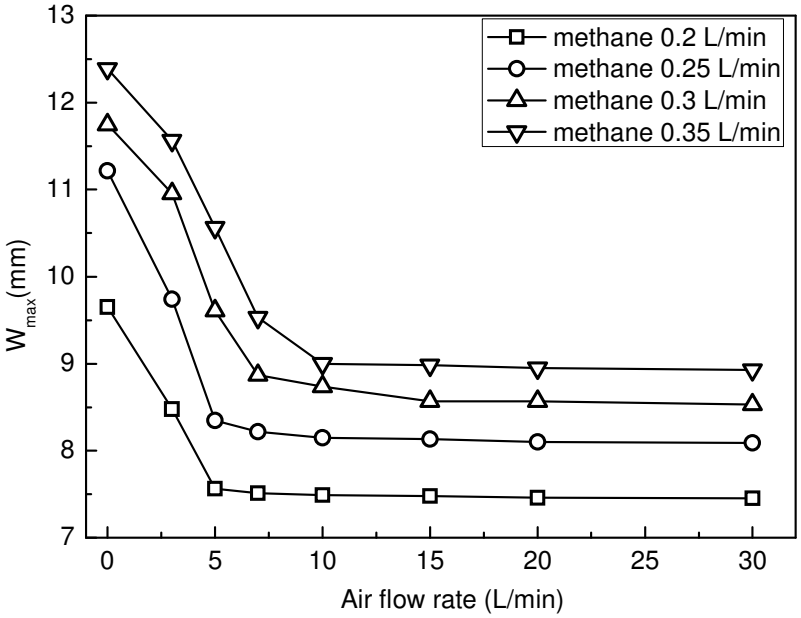

(d)

Figure 7-10 (a) Illustration of the width measurement of the first bulge; (b) Width changing trends at different air and methane flow rates; (c) Illustration of the maximum width W_{max} of the visible flame bulge; (d) W_{max} at different air and methane flow rates.

The width of the vortex and flame is evaluated following similar method. The vortex width is determined by the maximum width of the first bulge above the burner exit at oscillating cases, as illustrated in Figure 7-10 (a). While there is stable IPTV height, the width is determined by the stable flow part. The trends of the width at different

air and methane flow rates are shown in Figure 7-10 (b). It is shown that the bulge width decreases when the air flow rate is increased. The trend indicates that stronger co-flow air limits outward radial diffusion of hot gas. At the same air flow rates, the width is observed to increase with the methane flow rates slightly. This is because more fuel generates larger flames and hot gas expansion. The width of the visible flame is also measured through the high speed image sequences. The maximum width W_{max} of the flame bulge is used as the evaluation parameter, as shown in Figure 7-10 (c). The values of W_{max} are plotted in Figure 7-10 (d) at different air and fuel flow rates. In the oscillating region, W_{max} shows to decrease gradually with the increasing air flow rate. The W_{max} keeps at a similar value after the flame is stable, which is different from the trend of the vortex width.

The contrast trend between the visible flame shape (both height and width) and the outside vortices indicates that although the visible flame shows to be almost the same after reaching a stable status, the vortices outside the flame keep changing with the co-flow air flow rate. More attention should be paid on the vortex evolution besides the visible flame in practical application of the flame instability investigation.

7.5 Flame oscillation and vortex shedding frequency at different co-flow conditions

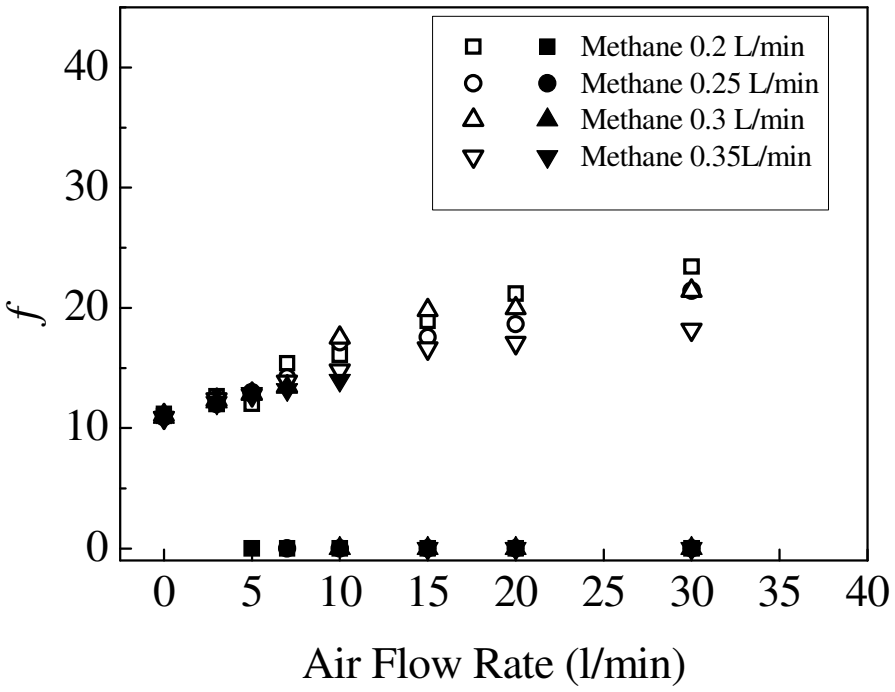

Figure 7-11 Vortex shedding frequency f at different air and fuel flow rate (Hollow symbols: results from schlieren pictures. Solid symbols: results from the photomultiplier)

Flame oscillation frequency is an important parameter to evaluate the flame periodical characteristics. Since the schlieren images taken by a high speed camera are time resolved, it is possible to estimate the large toroidal vortex shedding frequency f by observing the vortex development in an image sequence. The frequency is obtained from the arithmetic mean value of five vortex shedding cycles of each case. As shown in Figure 7-11, the vortex shedding frequency f increases with the increase of air flow rate in all the cases at different fuel flow rate. When the air flow rate is low, the vortex shedding frequency f does not change too much with the fuel flow rate. The frequencies are in good agreement with the flame flickering

frequencies obtained by a photomultiplier, which also indicates that the diffusion flame flickering frequency is dominated by the large toroidal vortex. When the air flow rate is high enough to suppress the flame oscillation completely, the large toroidal vortex is pushed out of the visible flame region. In such conditions, the flame flickering frequency obtained from a photomultiplier is zero. However, it can be seen clearly from the schlieren image sequences that although the vortex is pushed outside the visible flame region, the buoyancy induced hot gas also forms vortices at the IPTV height, which are shedding in a certain frequency. Through the schlieren image analysis the vortex shedding frequency in the hot products zone still can be evaluated. With the increase of air flow rate, the vortex shedding frequency f at different fuel flow rate was observed to become more scattered at the same air flow rate, which may imply that the increased turbulence/instability factor makes the large toroidal vortex behaviors more unstable.

7.6 Conclusions

The non-lifted methane air co-flow diffusion flames were investigated systematically by high speed direct/schlieren imaging methods as well as PIV technique. Experiments were conducted on a co-flow burner with different fuel and air flow rates. Besides direct observation from the images obtained, quantitative analysis is carried out.

It was observed that with no co-flow air or relative low air flow rates, the flame oscillates with the large toroidal vortices outside the luminous flame region. At each fuel rate, the oscillating magnitude is decreased with an increase of air flow rate. There exists a critical air flow rate at which the flame becomes very stable rather

than oscillatory. The stable status is kept while the air flow rate is increased further. The critical co-flow air velocity, at which the flame stops oscillating, is found to increase linearly with fuel flow velocity. It is also observed that the flame flickering is suppressed by co-flow air by shifting the location of the IPTV out of the flame region. The PIV measurement provides detail velocity and vorticity field. It is found that at low co-flow rate large random vorticity structure exists around the flame and the vorticity was observed to be positive on the left side of the flame and negative on the right side as the co-flow is increased further, which indicates rolling-up vortices rotating in opposite directions.

The height and width of the visible flame bulge and the outside toroidal vortices are analysed quantitatively based on the direct/schlieren images. The result shows that the visible flame height and width is increasing with the fuel flow rate. At each fuel rate, the visible flame height and width is decreasing with the air flow rate and keeps almost the same after the flame is stable. On the contrary, the IPTV height is observed to increase with the air flow rate at first, and then falling down to a lower lever after a peak value. The trend indicates the interaction between the flame induced buoyancy and the co-flow air induced upward momentum. The vortex width is decreasing with the air co-flow rates for all the test cases.

The large toroidal vortex shedding frequency f is found to be in good agreement with the flame flickering frequency obtained by a photomultiplier. The time resolved schlieren image analysis provides a means to evaluate the vortex shedding frequency beyond the visible flame zone.

Chapter 8 Nonlinear Response of Buoyant Diffusion Flame under Acoustic Excitation

8.1 Introduction

In laminar diffusion flames, in addition to the natural buoyant induced vortex oscillation, flame behaviours can be significantly altered by applying external acoustic excitation. Acoustically excited flame has been studied intensively because it permits to control the flame oscillating at specific frequencies and convenient to synchronise with other devices. Depending on the frequency and magnitude, the addition of forced acoustic field can produce considerable modification to the dynamic flame structure and movement (Farhat SA, 2005, Farhat et al.). The use of external acoustic perturbation also has an effect on combustion at chemical-level, thus resulting in the change of emissions (Saito et al., 1998), various molecular concentrations and consequently the perceptual flame colouration (Rocha et al., 2008). Furthermore, for a practical burner or combustor with high noise levels, the

acoustic perturbation sources may cause serious combustion instability phenomena (Kim et al., 2010). Therefore, the understanding of the detail physical insight of the acoustic excited combustion process is of great importance.

In acoustic excited diffusion flames, both the natural buoyant flame and excitation signal perturbation show sinusoidal wave fluctuations. In the case of a linear system, the response to a sinusoid is always a sinusoid at the same frequency and does not depend on the amplitude of excitation. In the case of a nonlinear system, it can be shown that sinusoidal forcing results in response components at frequencies other than the excitation frequency. In particular, the distribution of energy amongst these frequencies depends on the level of excitation (G. Schmidt, 1986). The buoyant diffusion flame is found to show nonlinear response to the acoustic excitation in specific conditions. Sub-harmonic flame response in pulsed buoyant diffusion flames have been previously reported in a laminar slot burner flame with air-side forcing (Thuillard, 2002) and in transitional jet flames with fuel pulsing (Stocker, 1993). The sub-harmonic phenomenon has also been found in acoustic excited premixed air/methane flames (Bourehla and Baillot, 1998). Furthermore, the 2D sub-harmonic flame structures were interrogated through the use of laser diagnostics (Timothy C. Williams, 2007). In their work, the flame oscillations at f/2, f/3, 2f/3, f/4 and even f/5 of the excitation frequency have been observed. In another experimental investigation, the diffusion flame shows half the peak frequency of that of the pure fuel when the fuel (methane and propane) is mixed (Li and Zhang, 2010). It is interesting to point out that well known nonlinear theory may well explain all the observed flame response modes. The main objective of this investigation is to apply nonlinear theory to explain the observed nonlinear response modes of an acoustically

excited diffusion flame. In the mean time, original digital flame colour image processing techniques have been applied to find further nonlinear response modes of acoustically excited diffusion flame, which can be explained by the nonlinear theory but have not been reported in the combustion community.

The local flame structure is of great help to gain physical insights into the combustion process. In practical, the flame structure is irregular and cannot be well understood by only 2D images. In this chapter, the global 3D flame structure and dynamics were investigated by high speed stereo imaging techniques, which has been demonstrated in Chatper 3. The vortex evolutions were visualised by high speed schlieren images. The results give improved phenomenological insight into the nature of the buoyant instability under acoustic excitation and should provide definitive experimental data for comparison with detailed modeling studies.

8.2 Experimental setup

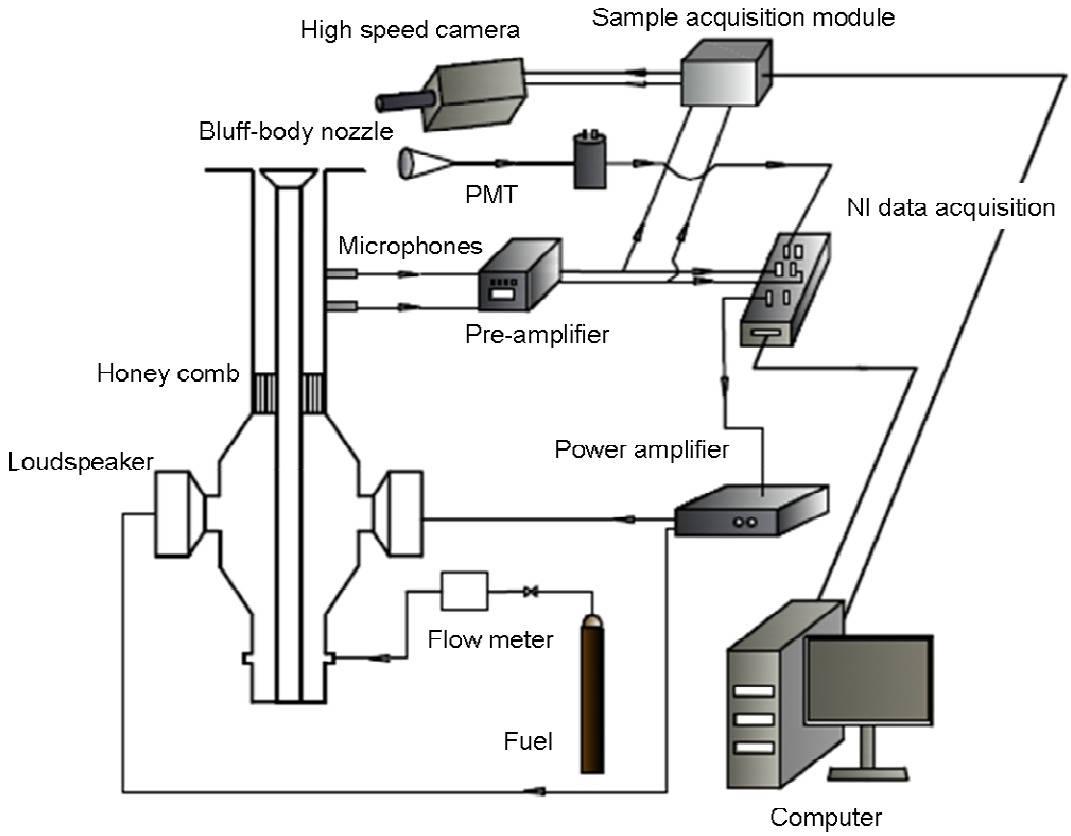

(a)

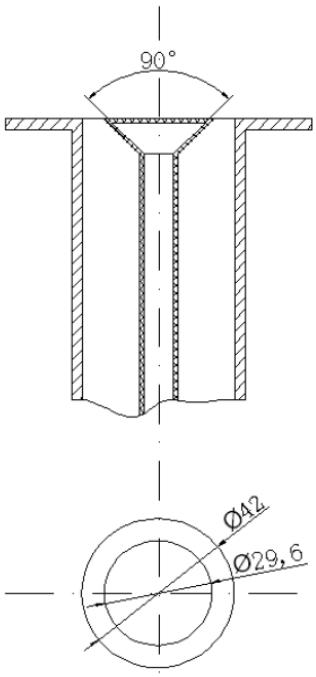

(b)

Figure 8-1 (a) Schematic of the experimental setup; (b) Dimension of the bluff body

The schematic layout of the experimental apparatus is illustrated in Figure 8-1 (a), which is similar to the design in the reference of (Balachandran et al., 2005). The burner utilised in this study is designed to establish a wide range of diffusion and premixed bluff-body stabilised flames. Gaseous fuel is supplied from a fuel bottle and controlled by a dedicated flow-meter. The range of flow rate for fuel is 0-50 slpm (standard litre per minute). The gaseous fuel enters the mixing chamber from the lower-end of the combustor. A honeycomb section is located above the mixing chamber, which straightens the flow along the burner length towards the nozzle-exit. The flame is established at the nozzle which is stabilised by a conical bluff-body structure (shown in Figure 8-1(b)) at the combustor exit. The outer diameter of the nozzle exit is 42 mm with the conical bluff-body diameter of 29.6 mm, thus giving a blockage ratio of 0.5. In this investigation, methane diffusion flame at volumetric fuel flow rate of 5 slpm was considered. External acoustic excitation was provided by two loudspeakers which are forced by a power amplifier whose amplitude and frequencies could be controlled as desired. These speakers generate periodic pressure oscillation which modulates the fuel flow conducted to the burner. In the current experiment, the flame characteristics under an acoustic excitation frequency range of 6 Hz -100 Hz were investigated. Two microphones were placed at different points of the vertical burner pipe (see Figure 8-1(a)) to detect the pressure oscillation. A photomultiplier (PMT) tube device is applied to record the flame flickering frequency based on the flame light emissions. The dynamic flame behaviours under acoustic excitations were captured by a high speed camera (Phantom V210) with a stereo adapter attached in front of the lens. The image sensor of the camera is C-MOS. The parameters of the high speed camera are outlined in Table 8-1. The stereo adapter consists of four delicate flat mirrors that can form two images at slightly

different angles on the camera focus plane. The geometry of the stereo adapter has been introduced in section 3.2.2. The framing rate is set at 1,000 fps, which has sufficient temporal resolution to resolve stereo image pairs for both the frequency analysis and 3D structure reconstruction. The high-speed imaging, the acoustic pressure measurement and PMT signals are synchronized for tractable analysis. A z-type schlieren setup, with a pair of parabolic mirrors (150 mm in diameter), is used to observe the vortex development.

Table 8-1 Frame rate versus image resolution (Phantom V210)

Frame Rate (fps)	Maximum Resolution (pixels)
2,190	1280 × 800
2,700	1024 × 800
4,060	800 × 600
26,500	256 × 256
200,000	128 × 32
300,000	128 × 8

8.3 Experimental results

8.3.1 Acoustic response test

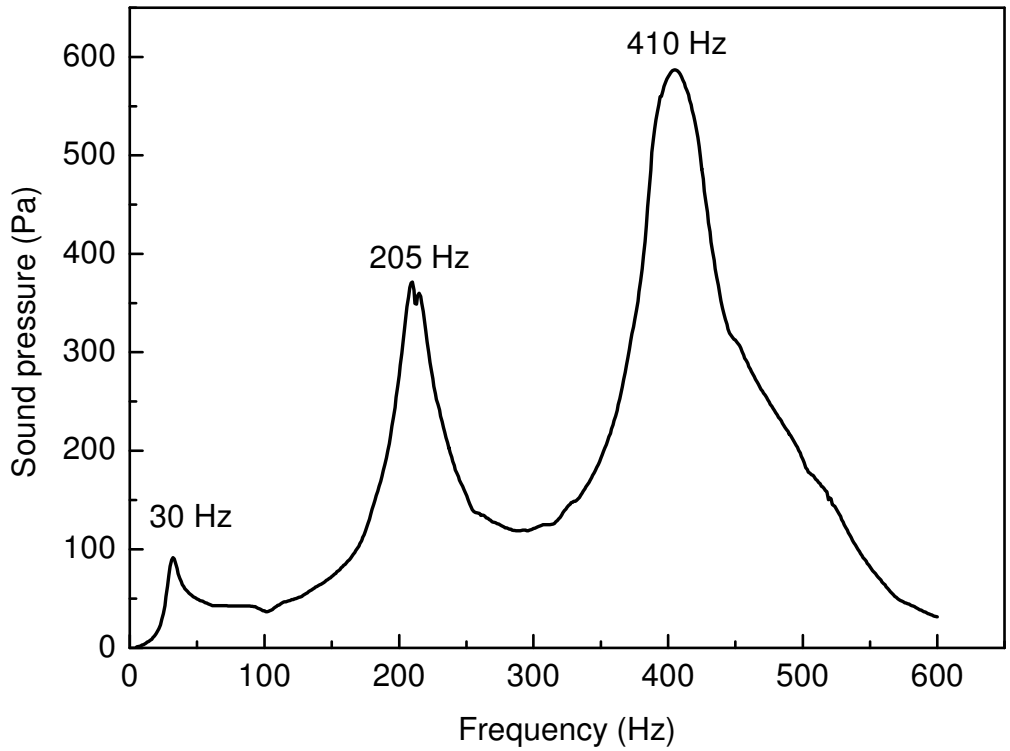

Figure 8-2 Acoustic response characteristics

The acoustic response characteristics of the tube for fuel were tested at a fixed input voltage of the loudspeakers. The test was conducted in the tube without injecting any fuel into it. The amplitude measured by the microphones on the tube is used to evaluate the response intensity. The position of the microphones has been indicated in Figure 8-1 (a). As shown in Figure 8-2, the response intensity varies greatly at different excitation frequencies. In this study, it is found that the flame response to low frequencies from 6 Hz to 20 Hz is dramatically different from the response to high frequencies. In the frequency range from 21 Hz to 500 Hz, the flame shows no obvious change with the different frequency excitations. Thus only the frequencies at

peak values at high frequencies are selected for the test cases based on the response map.

For consistency, we designate f_m as the dominant flame flickering frequency, f_e the acoustic excitation frequency and A_e the acoustic excitation amplitude. During the experiments, the fuel flow rate is kept at 5 slpm, which corresponds to a low Reynolds number at 215. The current burner has a relatively large outer diameter and a central bluff body that, without the addition of air, generate very weak annulus fuel jets. Thus the effects of forcing are manifested only in the near field region of the nozzle exit. In order to understand the acoustic excitation effect on the flame dynamics, six cases are selected to present different phenomenon and the case conditions are listed in Table 8-2. Case 1 is the natural flickering flame without acoustic excitation; and Cases 2, 3, 4, 5 and 6 are the typical flame modulated at excitation frequencies of 8 Hz, 8 Hz, 50 Hz, 30 Hz and 30 Hz.

Table 8-2 Selected case conditions

Case No.	f_e (Hz)	A_e (pa)	f_m (Hz)	Fuel flow rate (slpm)	Fuel exit velocity (m/s)	Re_D (Reynolds number based on bluff-body dimension)
Case 1	/	/	7.8	5	0.82	215
Case 2	8	1.1	8	5	0.82	215
Case 3	8	3.5	4	5	0.82	215
Case 4	50	30	7.8	5	0.82	215
Case 5	30	10	7.8	5	0.82	215
Case 6	30	90	7.8	5	0.82	215

8.3.2 PMT and acoustic signals

In the experiments, the PMT signals are recorded to show the flame perturbation, while the signal gathered from the microphones shows the acoustic external excitation. The acoustic and PMT signals of the six cases are shown in Figure 8-3. The flame flickering frequency could be evaluated from the PMT signals and analysed by applying FFT (Fast Fourier Transform) algorithm. Referring to Figure 8-3, in each case, the flame shows to oscillate periodically.

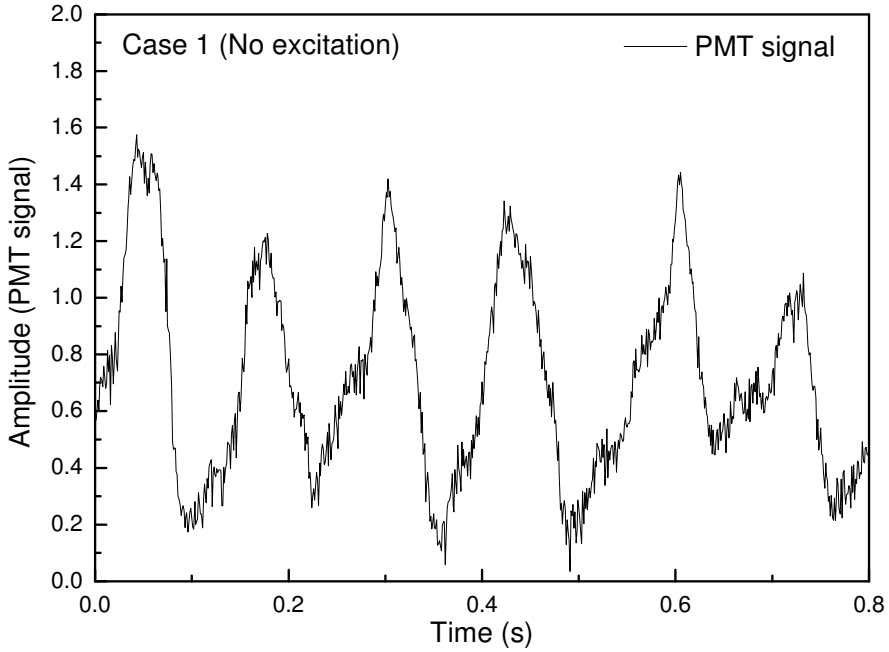

(a)

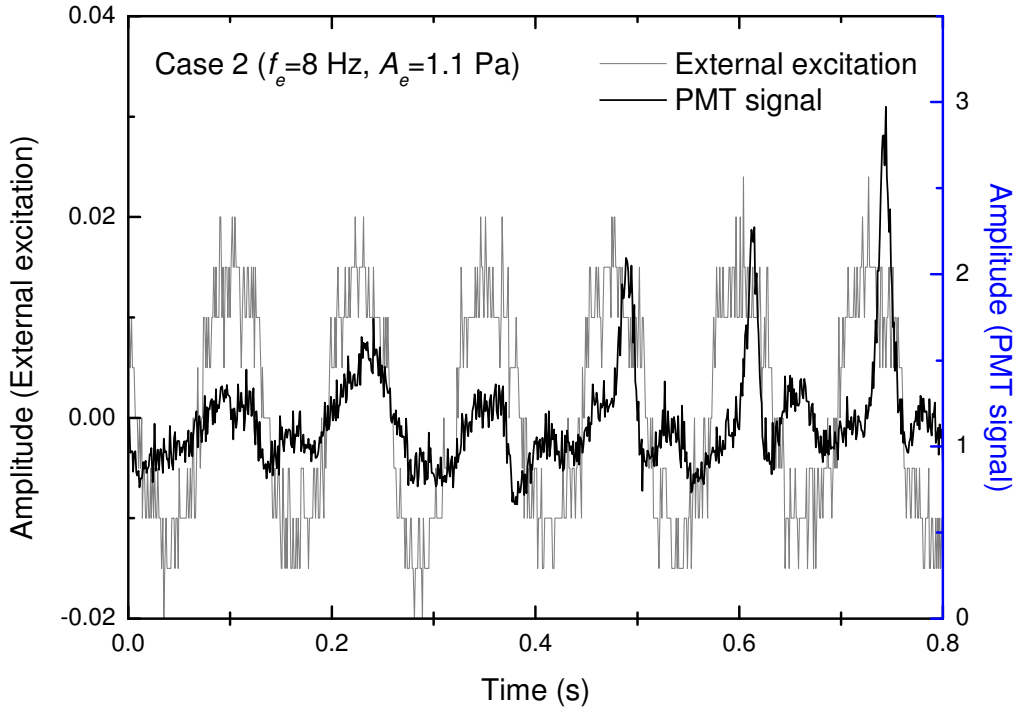
Case 2 (f_e=8 Hz, A_e=1.1 Pa)
External excitation
PMT signal
Amplitude (External excitation)
Amplitude (PMT signal)
Time (s)
0.04
0.02
0.00
-0.02
0.0
0.2
0.4
0.6
0.8
3
2
1
0

(b)

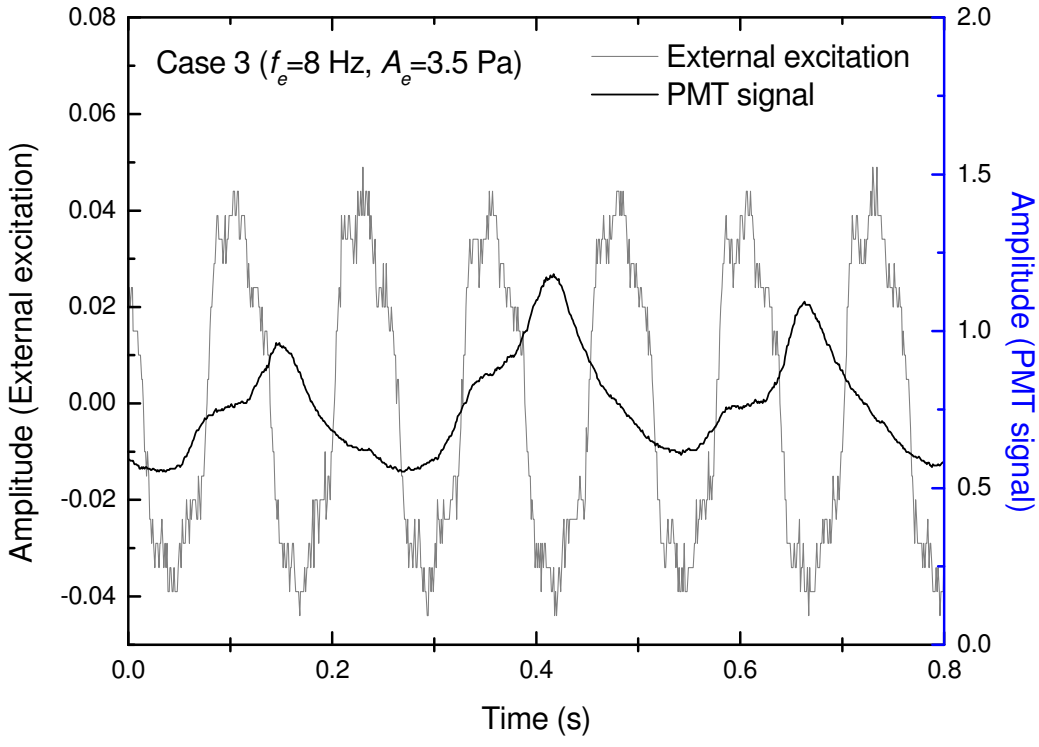
Case 3 (f_e=8 Hz, A_e=3.5 Pa)
External excitation
PMT signal
Amplitude (External excitation)
Amplitude (PMT signal)
Time (s)
0.08
0.06
0.04
0.02
0.00
-0.02
-0.04
0.0
0.2
0.4
0.6
0.8
2.0
1.5
1.0
0.5
0.0

(c)

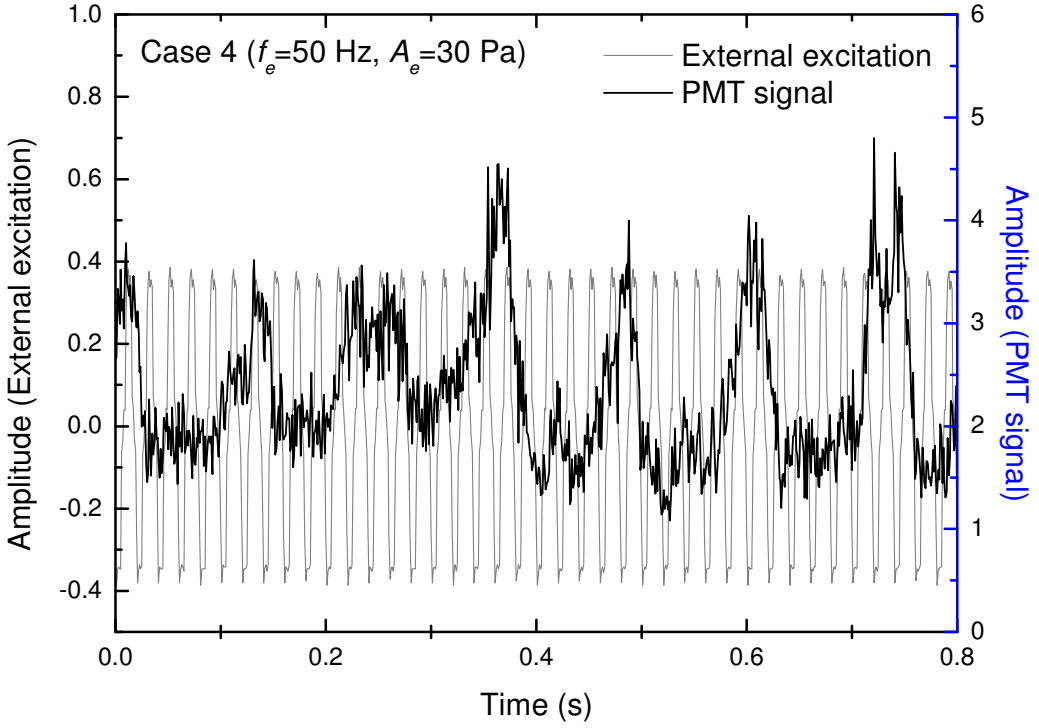
Case 4 (f_e=50 Hz, A_e=30 Pa)
External excitation
PMT signal
Amplitude (External excitation)
Amplitude (PMT signal)
Time (s)
1.0
0.8
0.6
0.4
0.2
0.0
-0.2
-0.4
6
5
4
3
2
1
0
0.0
0.2
0.4
0.6
0.8

(d)

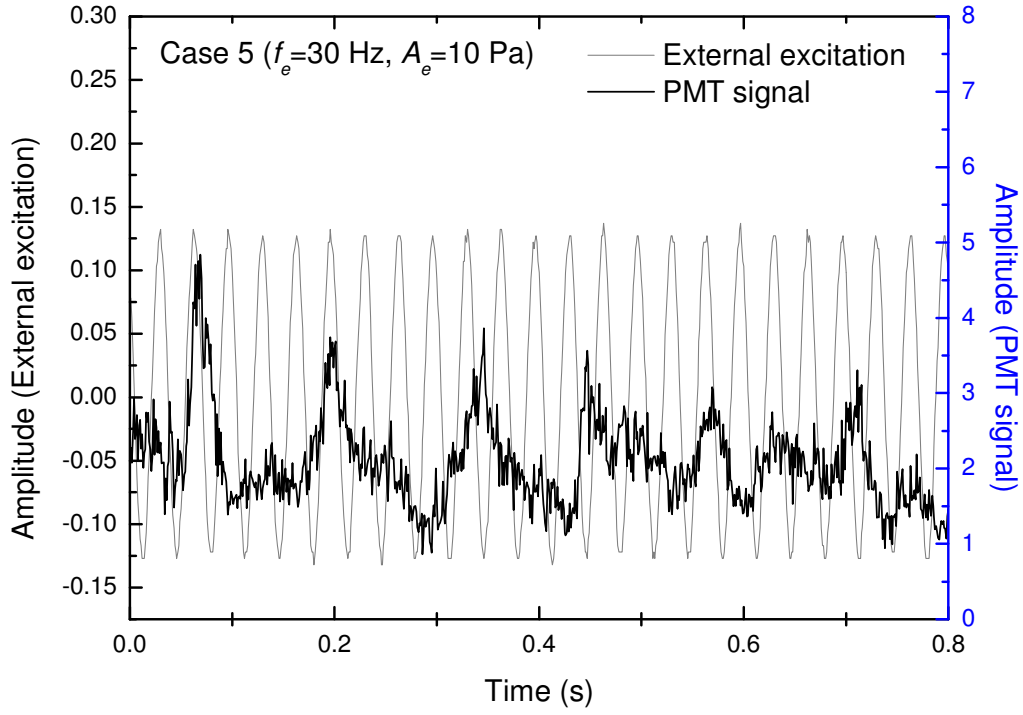
Case 5 (f_e=30 Hz, A_e=10 Pa)
External excitation
PMT signal
Amplitude (External excitation)
Amplitude (PMT signal)
Time (s)
0.30
0.25
0.20
0.15
0.10
0.05
0.00
-0.05
-0.10
-0.15
8
7
6
5
4
3
2
1
0
0.0
0.2
0.4
0.6
0.8

(e)

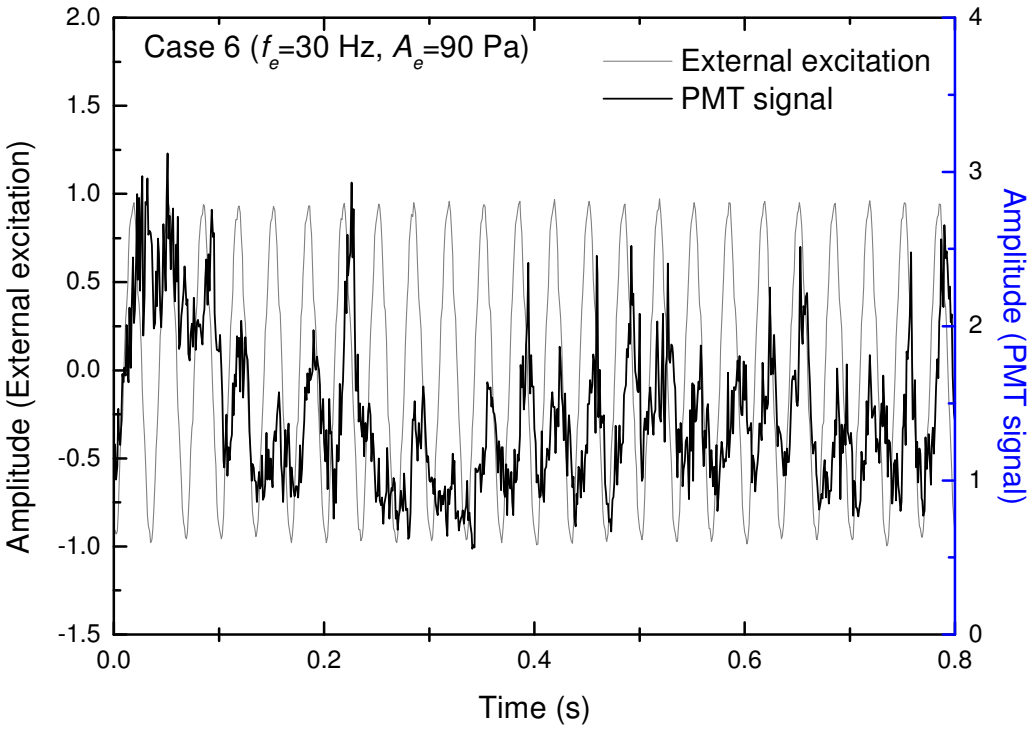

(f)

Figure 8-3 Acoustic excitation and PMT signal
(a) Case 1; (b) Case 2; (c) Case 3; (d) Case 4; (e) Case 5; (f) Case 6

8.3.3 Frequency analysis by FFT

The flame flickering frequency spectrums of the six selected cases evaluated from the PMT signals are shown in Figure 8-4. It shows that a peak frequency exists in each case. When the acoustic excitation is applied to the flame, the flame frequency changes at different frequency and amplitude of the excitation signal. The frequency results for more cases are summarised in Table 8-3. The nonlinear flame response to the acoustic excitation will be discussed in the following sections respectively.

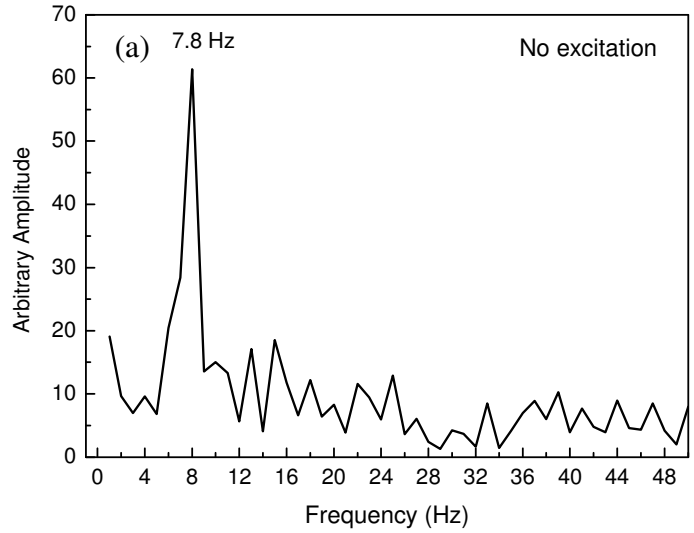
(a)
7.8 Hz
No excitation
Arbitrary Amplitude
Frequency (Hz)

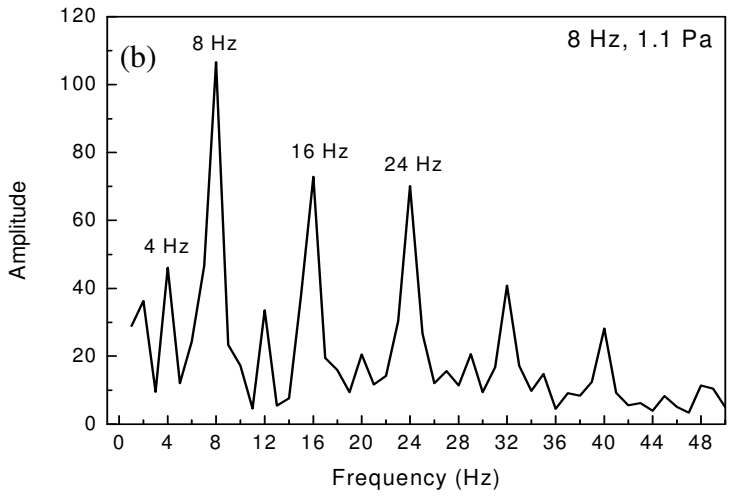
(b)
8 Hz
8 Hz, 1.1 Pa
16 Hz
24 Hz
4 Hz
Amplitude
Frequency (Hz)

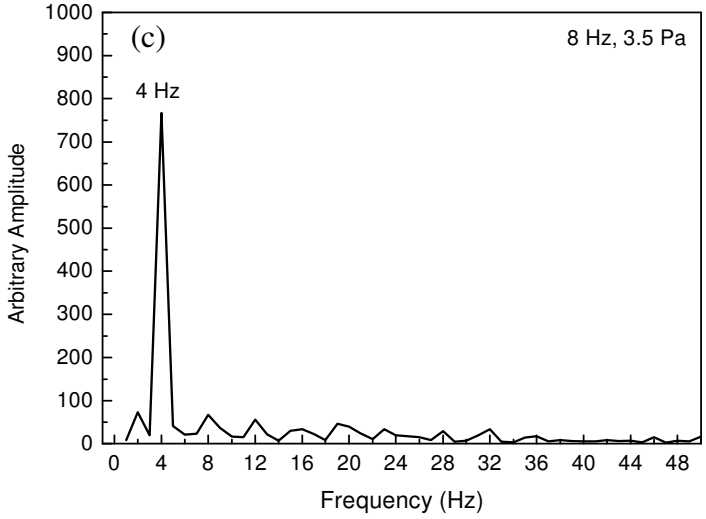
(c)
8 Hz, 3.5 Pa
4 Hz
Arbitrary Amplitude
Frequency (Hz)

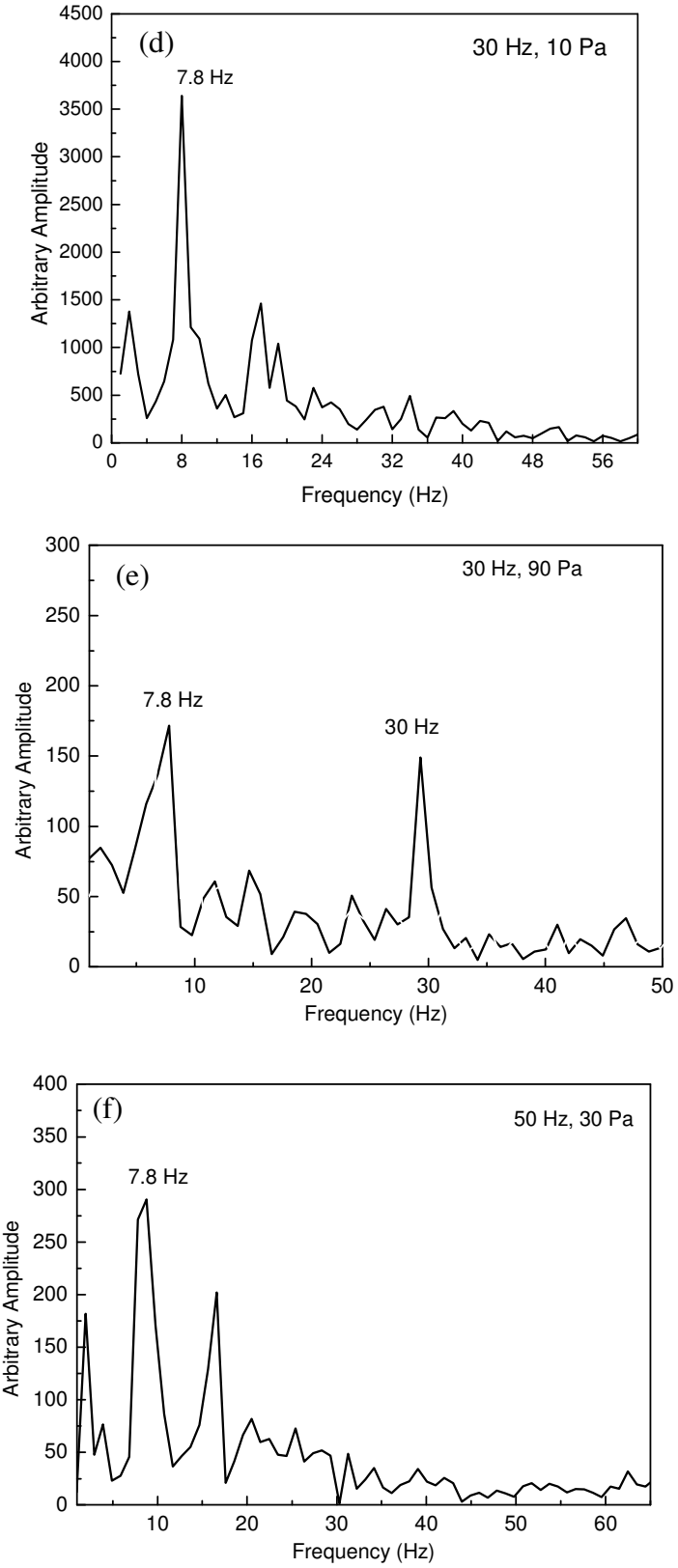

Figure 8-4 Frequency spectrum analysis from PMT signals

(a) Case 1; (b) Case 2; (c) Case 3; (d) Case 4; (e) Case 5; (f) Case 6

Table 8-3 FFT results

Case No.	f_e (Hz)	A_e (pa)	f_m(Hz)
1	/	/	7.8
2	6	0.82	6
3	6	2.05	3
4	8	1.1	8
5	8	3.5	4
6	10	0.37	10
7	10	4.1	5
8	12	5.2	6
9	14	5.6	7
10	16	7.5	8
11	18	8	9
12	20	15	10
13	30	10	7.8
14	30	90	7.8
15	50	30	7.8
16	205	250	7.8
17	410	500	7.8

Flame oscillating at natural frequency

Flame oscillating at acoustic frequency

Flame oscillating at half acoustic frequency

8.3.4 2D flame dynamics

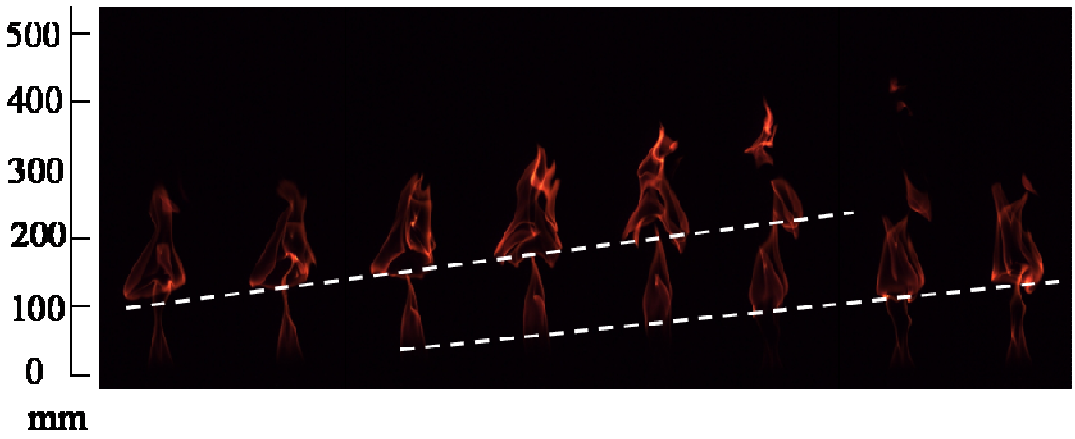

(a) Case 1 (Time interval is 20 ms)

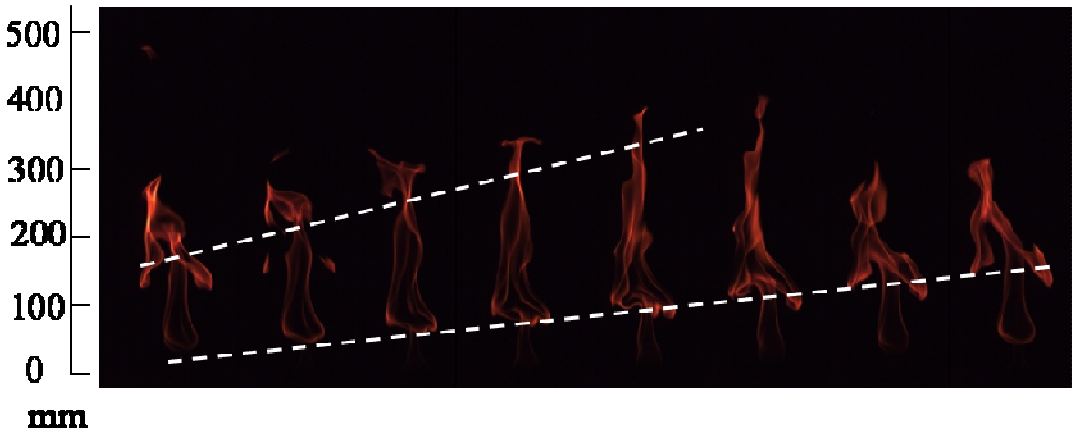

(b) Case 2 (Time interval is 20 ms)

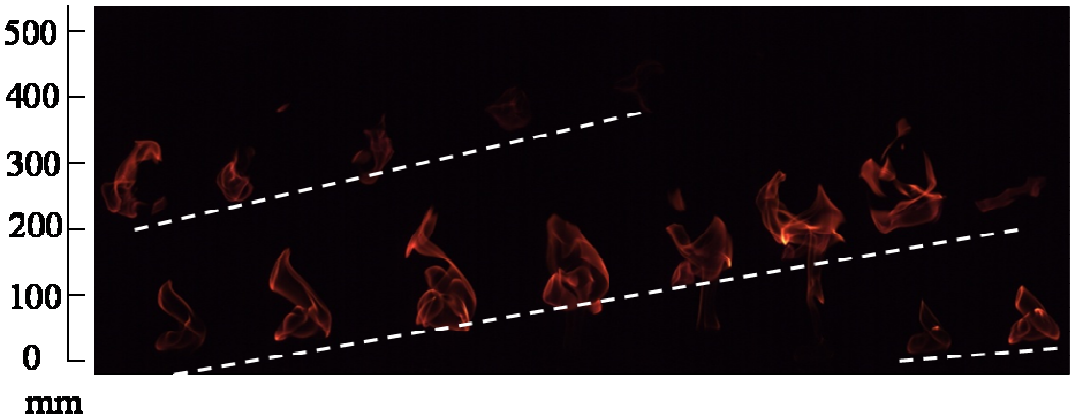

(c) Case 3 (Time interval is 40 ms)

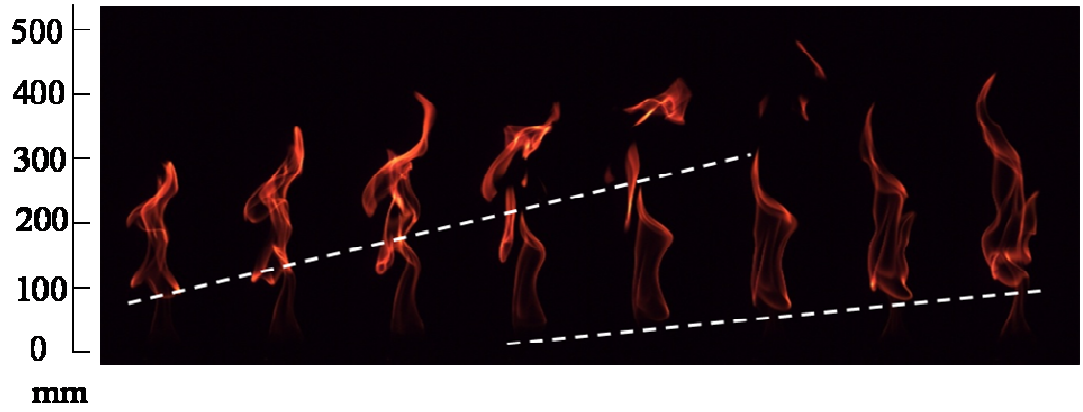

(d) Case 4 (Time interval is 20 ms)

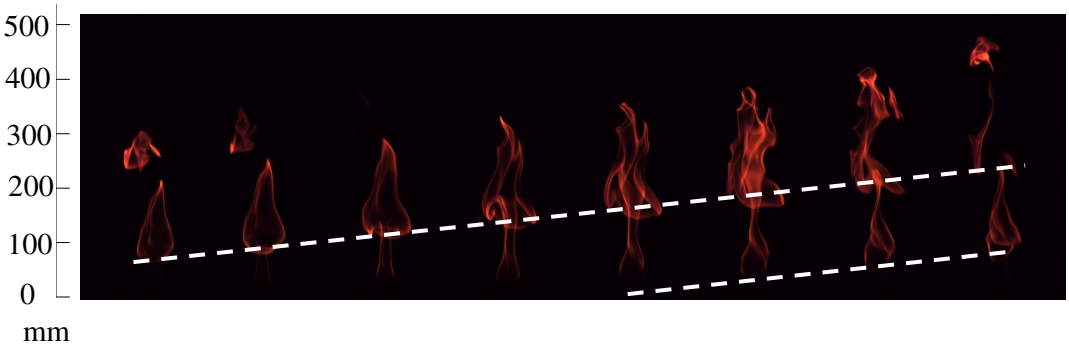

(e) Case 5 (Time interval is 20 ms)

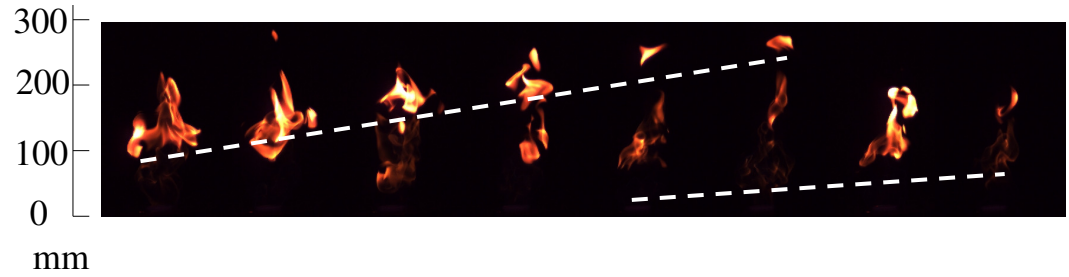

(f) Case 6 (Time interval is 20 ms)

Figure 8-5 2D flame image sequences at selected test case conditions (The dashed lines mark the approximate evolution position of flame vortices)

The high speed imaging technique supplies an effective way to depict the highly time-resolved flame development. The 2D high speed flame images for the selected cases are shown in Figure 8-5. For each case, the flame evolution in a cycle is presented. As it can be seen from the direct 2D images of Case 1, a triangle-shaped flame is formed from an initial peak shape from the burner nozzle exit. The flame shapes in Cases 2, 4 and 5 are similar to Case 1, but being narrower and longer. In

contrast, the 2D flame structures of Cases 3 and 6 are dramatically different in comparison with the Cases 2 and 5 because of the enhanced acoustic perturbation. It is observed that the visible flames of Cases 3 and 6 are shorter and wider in shape. The observed variances in different flame structures indicate that the acoustic excitation has a considerable effect on the combustion process. In each image sequence, two flame vortices are observable. It is interesting to observe that each flame vortex seems to move downstream at constant speeds, as indicated by the dashed lines. The convection velocities of the four cases are shown in Figure 8-6. In Cases 1 and 5, the two observable flame vortices move almost at the same convection velocity, while the upper vortices are moving at higher speeds than the lower ones in the other three cases. The exact causes for this difference are not clear and are worthy of further investigation. However, it is quite certain that the acoustic excitation must have played a role.

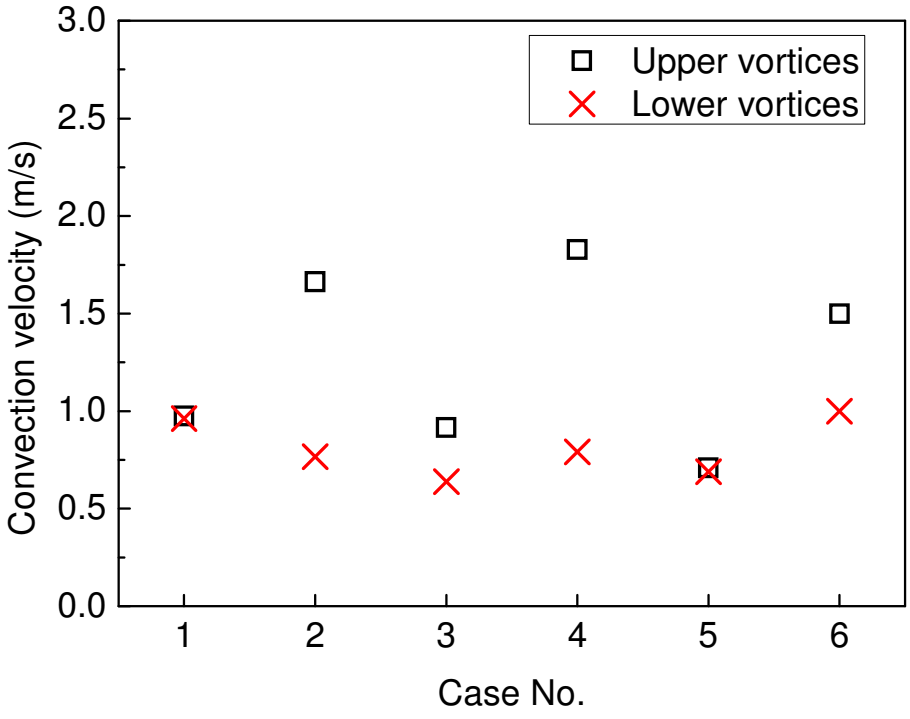

Figure 8-6 Estimated convection velocity of the flame vortices of the four test cases

8.3.5 Vortex dynamics

In this study, the vortex evolutions of the hot gas product were visualised by high speed schlieren techniques. The corresponding schlieren illustrations of vortex evolutions in the six cases are illustrated in Figure 8-7. For each case, the vortex evolution in a cycle is presented. The vortex evolutions at different cases also show great differences. As further analysed in Figure 8-8 (a-h), in Case 1 a mushroom-like structure vortex can be observed due to the shear layer effect between the hot gas and ambient air at the downstream side. In contrast, no such vortices could be observed in the other five cases, which indicate that the acoustic excitation has overcome the shear layer influence on the vortex structure. For Cases 2, 3, 4, 5 and 6, the vortex with an obvious bulge can be observed. Both the vortices in Case 1 and Case 2 are evenly distributed in size and shedding in the downstream direction one by one. In Cases 2 to 6, the counter rotating acoustic driven vortex pairs are clearly observable near the nozzle exit area.

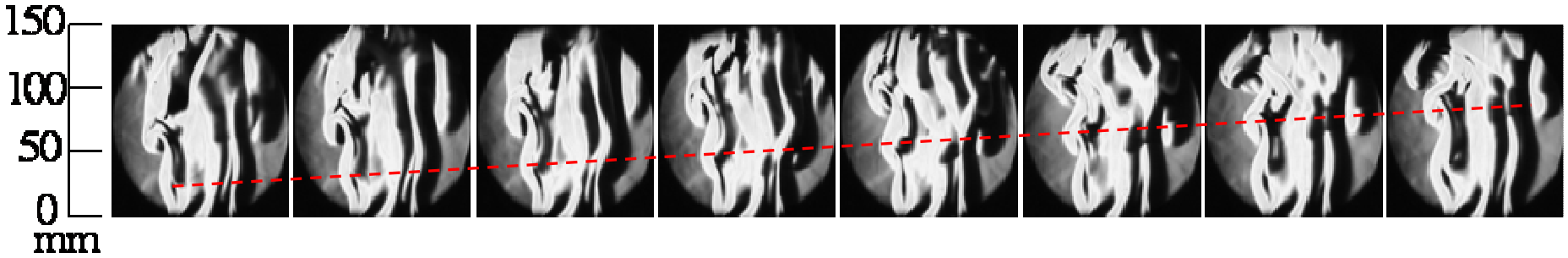

(a) Case 1 (Time interval is 20 ms)

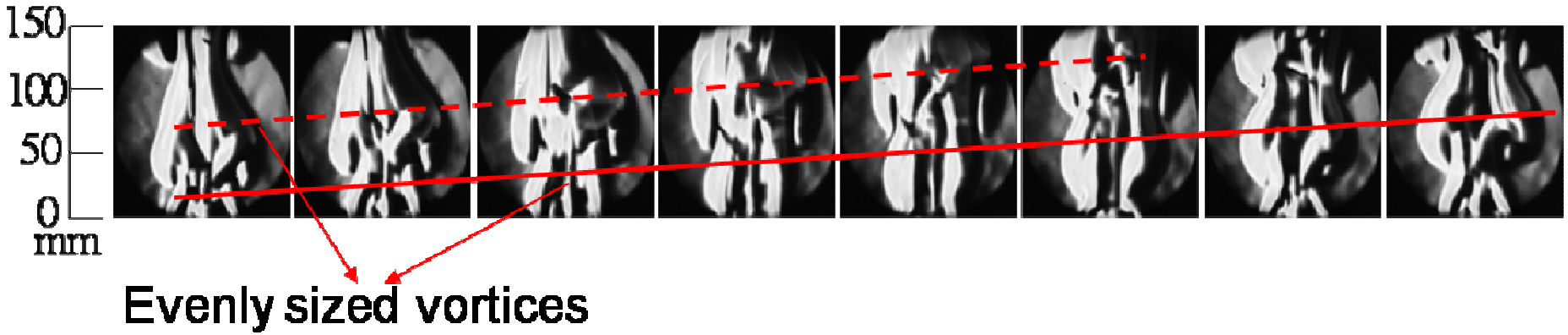

(b) Case 2 (Time interval is 20 ms)

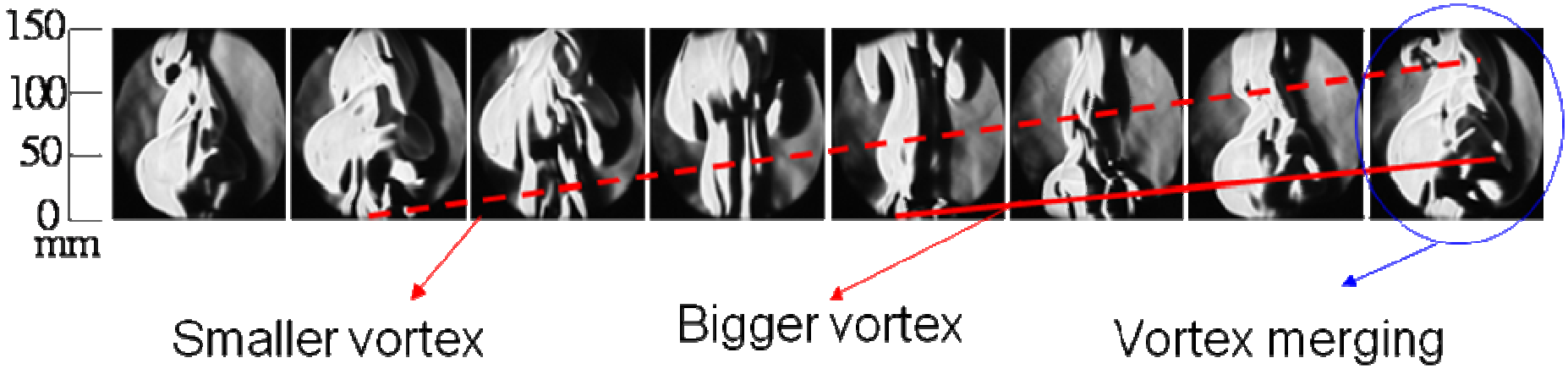

(c) Case 3 (Time interval is 40 ms)

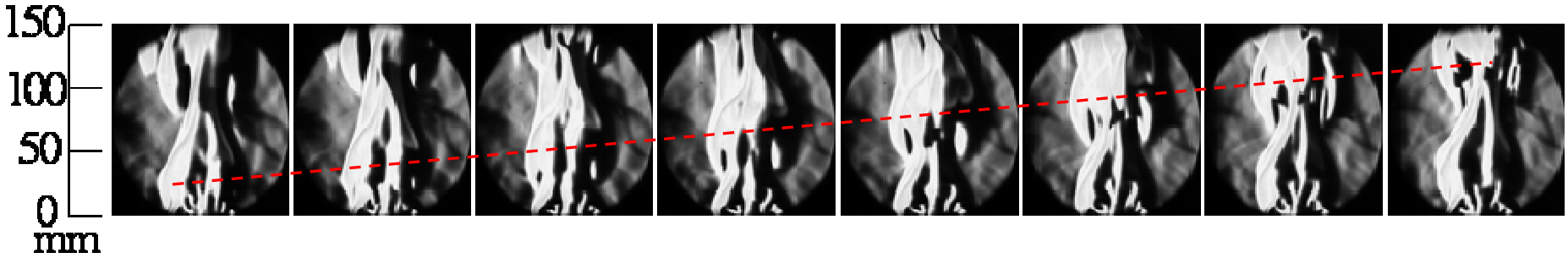

(d) Case 4 (Time interval is 20 ms)

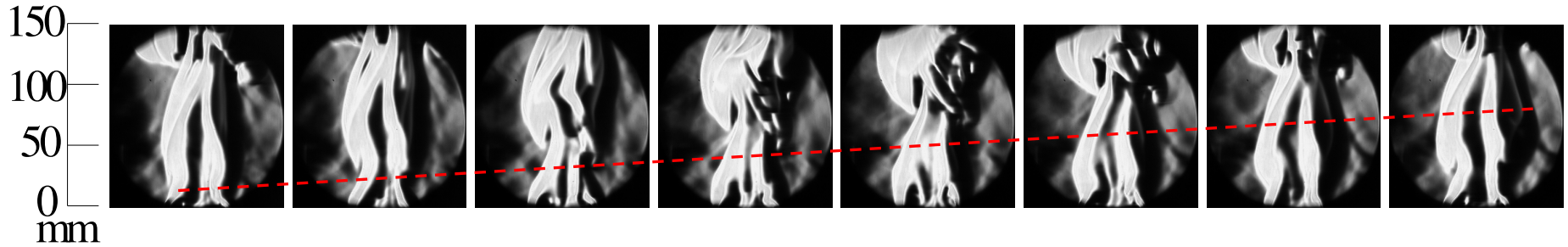

(e) Case 5 (Time interval is 20 ms)

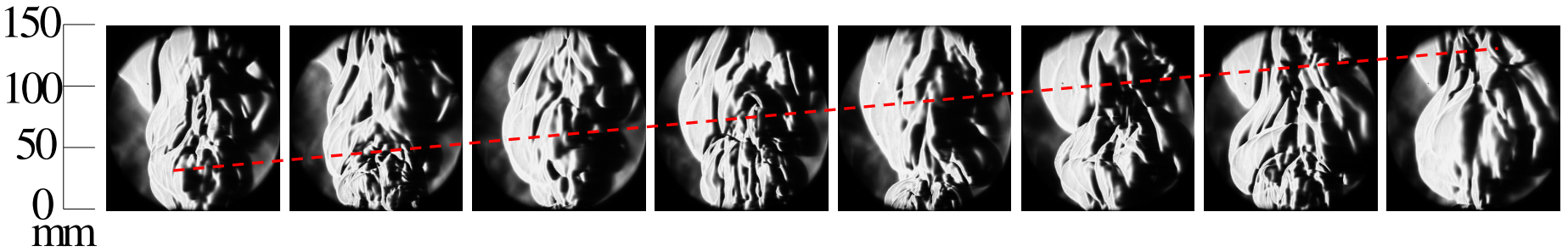

(f) Case 6 (Time interval is 20 ms)

(The line indicates the main vortex bulge evolution in one cycle.)

Figure 8-7 Schlieren images at selected case conditions (a) Case 1; (b) Case 2; (c) Case 3; (d) Case 4; (e)Case 5; (f) Case 6

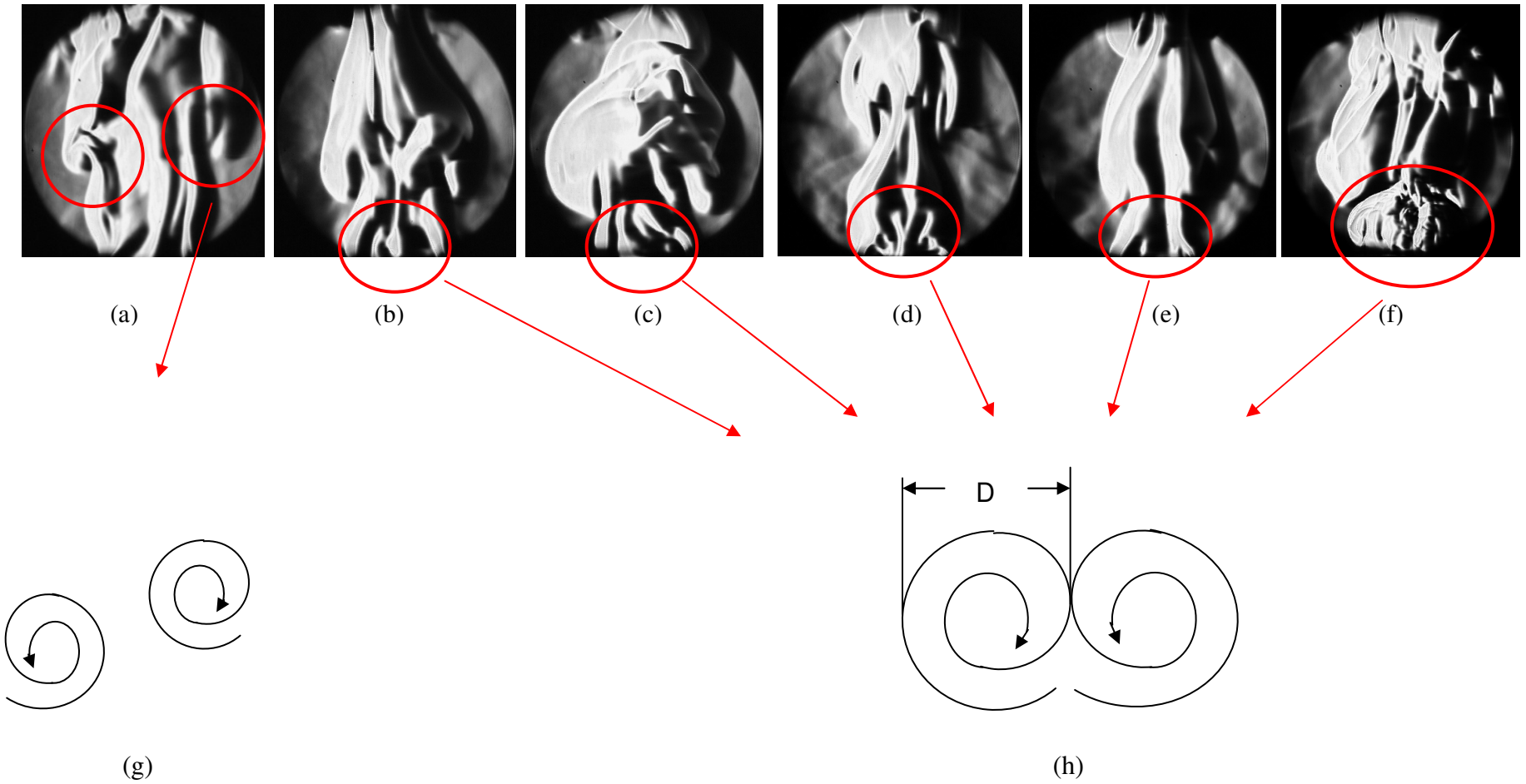

Figure 8-8 Vortex structure analysis

(a) Case 1; (b) Case 2; (c) Case 3; (d) Case 4; (e)Case 5; (f) Case 6; (g) Vortex pairing in Case 1; (h) Vortex pairing in Cases 2-6

8.4 Nonlinear response analysis

8.4.1 Frequency division

Frequency division is a common response in nonlinear systems. If the excitation signal is denoted as $x(t) = X\sin(\omega t)$, the responded signal at frequency division cases must contain the components of $y_n(t) = Y_n \sin(\omega t / n + \phi_n)$, (n=2, 3, 4, …).

8.4.1.1 Half frequency phenomena

Half excitation frequency phenomenon (f_e/2) is the most typical nonlinear response of frequency division. During this investigation, it was found that under certain conditions the flame flickering frequency became locked at precisely one-half the excitation frequency for a wide range of externally forced acoustic conditions. The natural flame flickering frequency is evaluated by the PMT signal and the value is found to be at 7.8 Hz. When the excitation frequency is in the range of 6 Hz to 20 Hz, the flame frequency shows to change with the excitation amplitude greatly. The flame frequency response map is shown in Figure 8-9. The flame frequency shows to be the same as the natural buoyant flickering frequency (7.8 Hz) when the acoustic amplitude is relatively small. The corresponding area is under the black line in Figure 8-9. In the frequency range of 6 Hz to 10 Hz investigated in this study, it was also discovered that acoustic excitation at low frequency would first shift the dominant frequency from the buoyancy driven flickering frequency to the excitation frequency and then the half excitation frequency if the excitation intensity level was increased further. The acoustic frequency range between 11 Hz and 20 Hz, there is an area of the transition flame, whose frequencies keep changing and no stable flame status could be observed. When the acoustic signal is enhanced further, a stable half

excitation frequency flame appears again. The amplitude range of the half frequency phenomenon is increased with the excitation frequency. However, the range is relatively small at the frequency of 15 Hz, which may be because the excitation frequency is just close to twice of the natural flame frequency and response function is different with other frequencies. In this study, the observed flame frequencies under acoustic excitation are in the range from 3 Hz to 10 Hz. The appearance of half frequency indicates the nonlinear response of the flame oscillation to the external forcing function. In the frequency range of 6 Hz to 20 Hz, a half frequency is observed in each case.

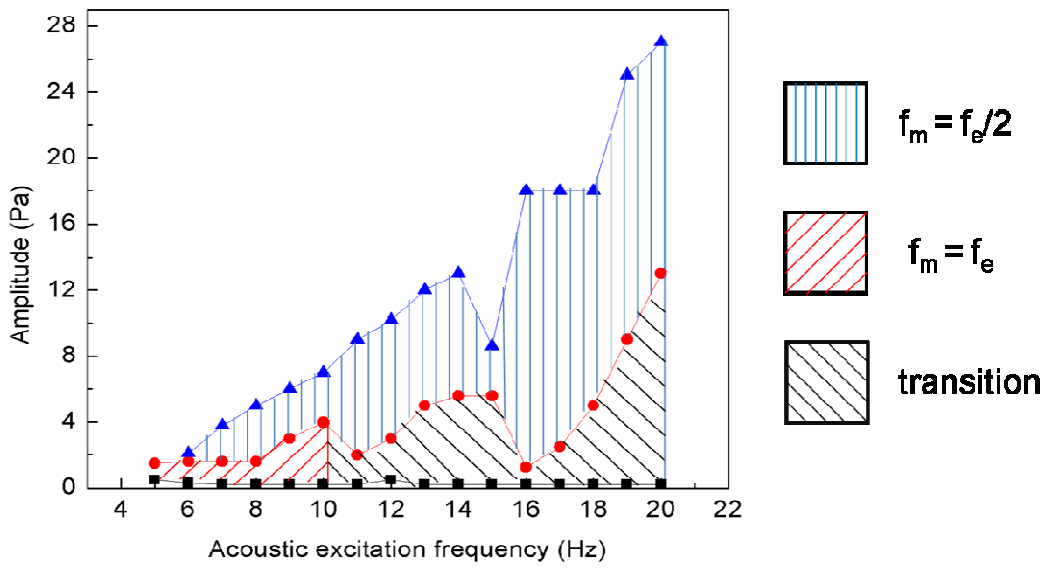

Figure 8-9 Regime of dominant flame flickering frequency under different acoustic excitation frequency and amplitudes

The appearance of half frequency indicates the nonlinear response of the flame oscillation to the external forcing function. Cases 2 and 3 are two typical cases in which the flame is oscillating at f_e and $f_e/2$ respectively. As listed in Table 8-2, the acoustic excitation frequency of the two cases is the same at 8 Hz, but with different amplitudes, i.e. 1.1 pa for Case 2 and 3.5 Pa for Case 3. As it can be seen from

Figure 8-3 (b) and (c), the PMT signal shows the same time period with the acoustic pressure signal for Case 2. In Case 3, the period of the PMT signal is double the acoustic excitation signal, which indicates that the flame frequency is half the excitation frequency. As shown in Figure 8-3 (d) and (e) and Table 8-3, the dominant frequency of the two cases is 8 Hz and 4 Hz respectively.

Referring to the vortex evolution shown in Figure 8-7 (b) and (c), it can be seen that there are two vortices formed and shedding in Case 2, as indicated by two lines. The shape of the neighbouring vortices is very similar. The vortices are evenly distributed and shedding in the downstream direction one by one. By observing the time-resolved schlieren images in Case 3 carefully, it is found that the initiation frequency of the vortex at the nozzle exit in Case 3 is shown to be the same as that of Case 2. However, the neighbouring vortices are different in size and shape, with one is much bigger than the other. During the vortex evolution process, the bottom bigger vortex merges with the upper smaller vortex under the function of buoyancy. Thus a much bigger vortex is formed and the vortex shedding frequency in Case 3 is reduced to half of Case 2. As emphasized in Figure 8-8 (c), a much bigger bulge in Case 3 is observed due to the vortex merging phenomenon.

8.4.1.2 3D flame structure investigation of Cases 2 and 3

Since the diffusion flame itself is turbulent in local structure, the 3D structure of the flame is worthy of exploration to gain physical insights. In order to investigate the acoustic excitation effect on flame structure, two typical cases are selected for 3D structure comparison. Regarding the dramatic difference of the 2D flame structures of Case 2 and Case 3, as shown in Figure 8-5 (b) and (c), the 3D flame structures of

the two cases at four phase angles in a cycle are reconstructed to gain more physical insights of the actual flame structure. The reconstruction was conducted based on the algorithm introduced in Chapter 3. Although only the part with textures could be reconstructed, it may still provide useful information to evaluate the 3D structure of the flame. The flame surface is represented by the 3D mesh grid method based on the clouds of point coordinates.

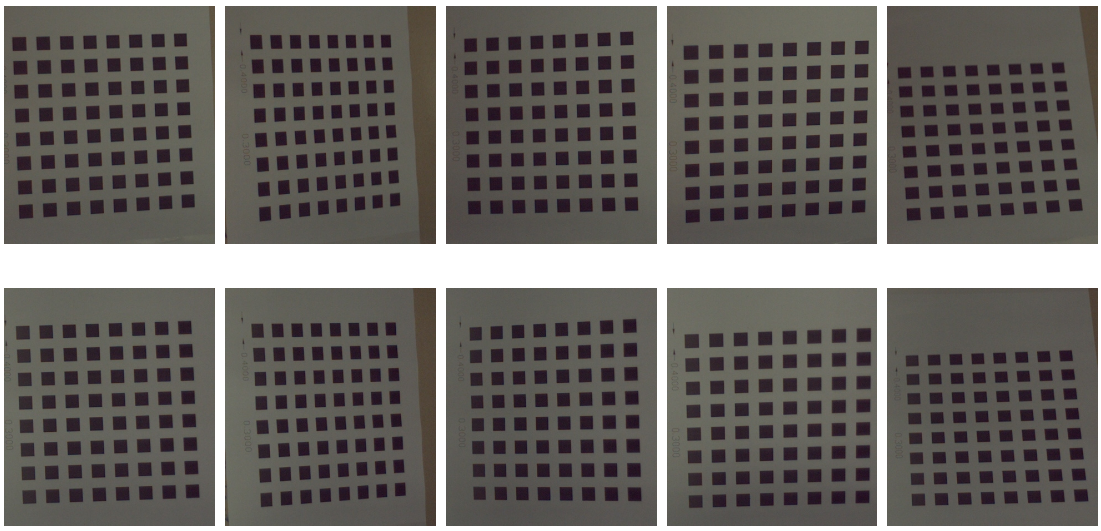

Figure 8-10 Five positions of the calibration board
(Upper sequence: left images; lower sequence: right images)

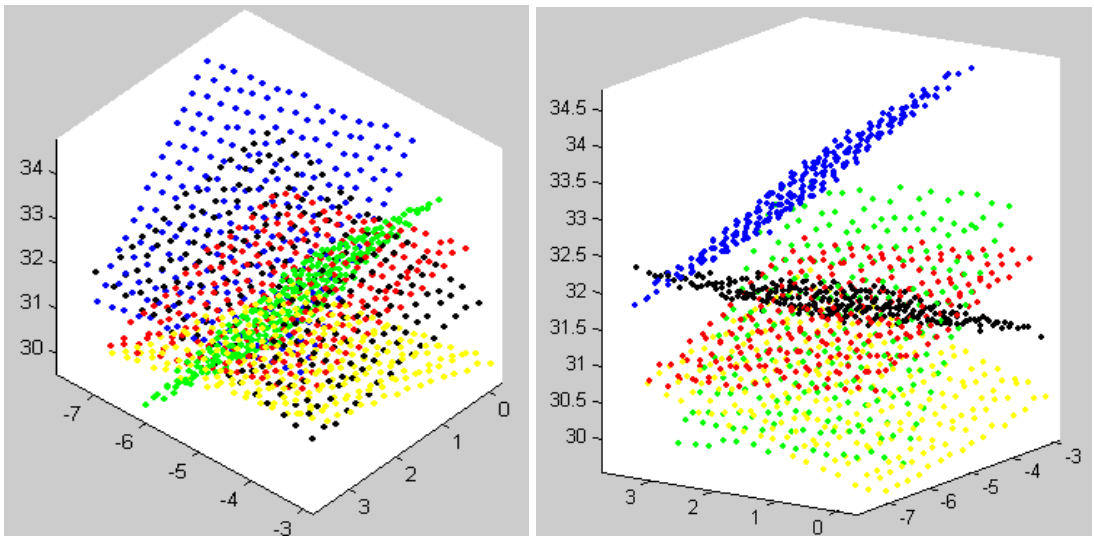

Figure 8-11 Reconstructed planes of the calibration board at different orientations

The calibration pattern shown in Chapter 3 (Figure 3-8) is printed and attached on a flat board surface. The calibration board is placed at five different positions, as shown in Figure 8-10. Following the procedures in Chapter 3, the camera calibration parameters are obtained. The reconstructed points at five positions are illustrated in Figure 8-11. The obtained calibration parameters are listed below, where A1 and A2 are the intrinsic parameters, R and t the extrinsic parameters.

$$A1 = \begin{bmatrix} 2647.4 & -3.046 & 630.61 \\ 0 & 2657.8 & 379.58 \\ 0 & 0 & 1 \end{bmatrix},\ A2 = \begin{bmatrix} 2647.4 & -3.046 & 230.61 \\ 0 & 2657.8 & 379.58 \\ 0 & 0 & 1 \end{bmatrix}$$

$$R = \begin{bmatrix} 0.93675 & 0.0064221 & 0.34995 \\ -0.0029517 & 0.99994 & -0.010449 \\ -0.34999 & 0.0087556 & 0.93671 \end{bmatrix}$$

$$t = \begin{bmatrix} -0.99124 & -0.016355 & 0.13102 \end{bmatrix}^T$$

The 2D flame images and the reconstructed flame structures visualised at three different view angles are presented in Figure 8-12 and Figure 8-13 respectively. The view angle in the second image of each group is the same as the 2D image (first image of each group) taken by the camera. It could be observed that most part of the flame structures have been reconstructed and the principle features are presented. The similarity of the reconstructed image and the original 2D image shows the reasonable accuracy of the stereoscopic reconstruction. The images at different view angles clearly show the flame distribution in 3D space. The highly contrasting visual perceptions obtained from viewing the flame at different view angles demonstrate the advantage and necessity for 3D visualisation. As shown in Figure 8-12 (a), the upper part of the visible flame in Case 2 is in a shape of three dimensional flame

sheet, with complicated distortion structures. The flame has then formed a long and narrow conical-like structure in Figure 8-13 (b-d). In contrast, the half excitation frequency flame of Case 3, the flame shape is dramatically different from Case 2 from the early stage. The flame is in an s-shape at first and then the main flame body is formed, biasing on one side in the 3D space. It is plausible to suggest that the dramatic change in the 3D flame structures is caused by the strong pressure perturbation induced by the acoustic excitation. On the one hand, the fuel/air mixing and combustion process is influenced by the acoustic wave. On the other hand, the coupling between the buoyancy and the excitation induces the vortex evolution change and thus affects the flame structure consequently.

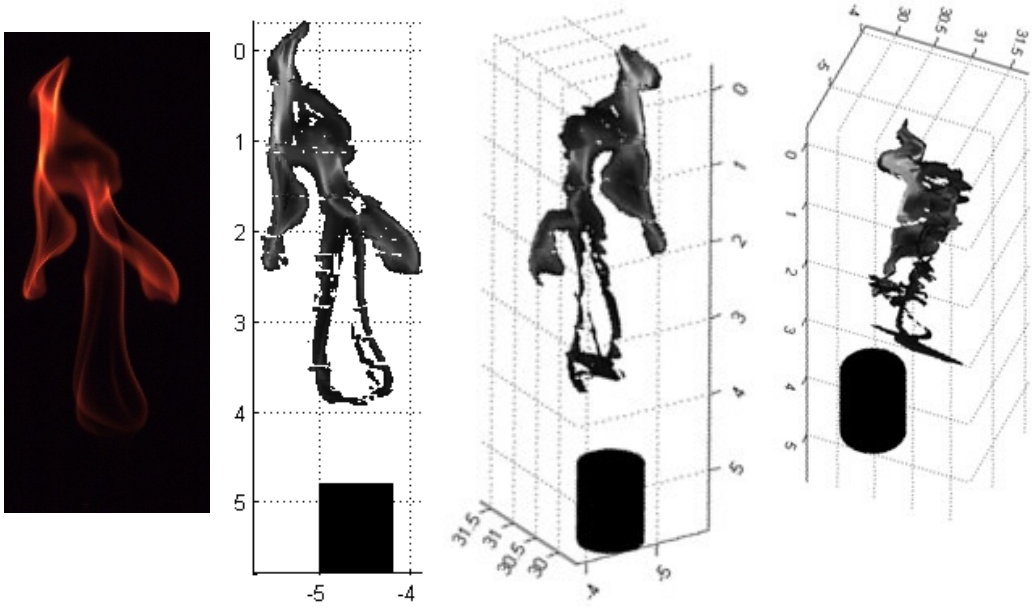

(a)

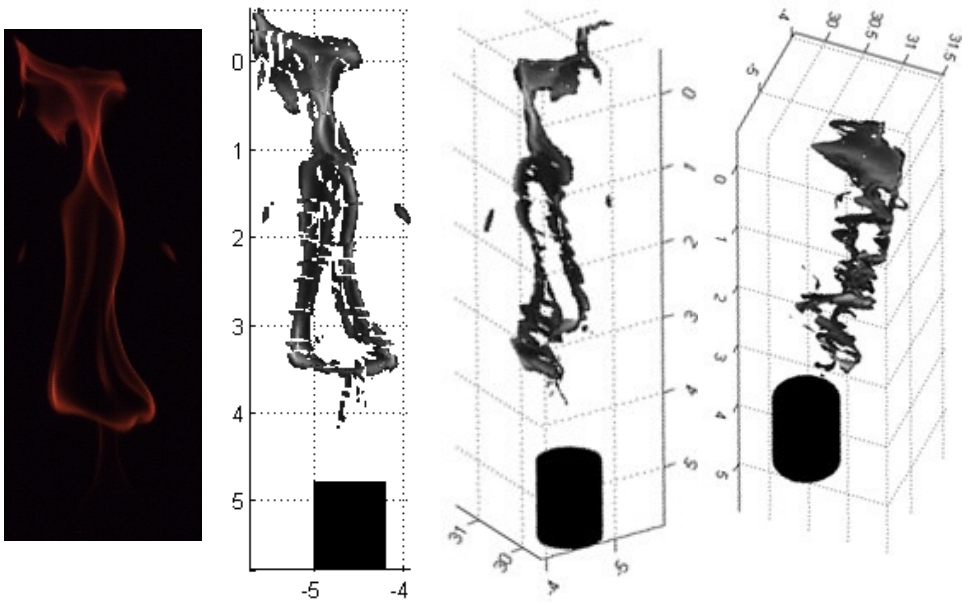

(b)

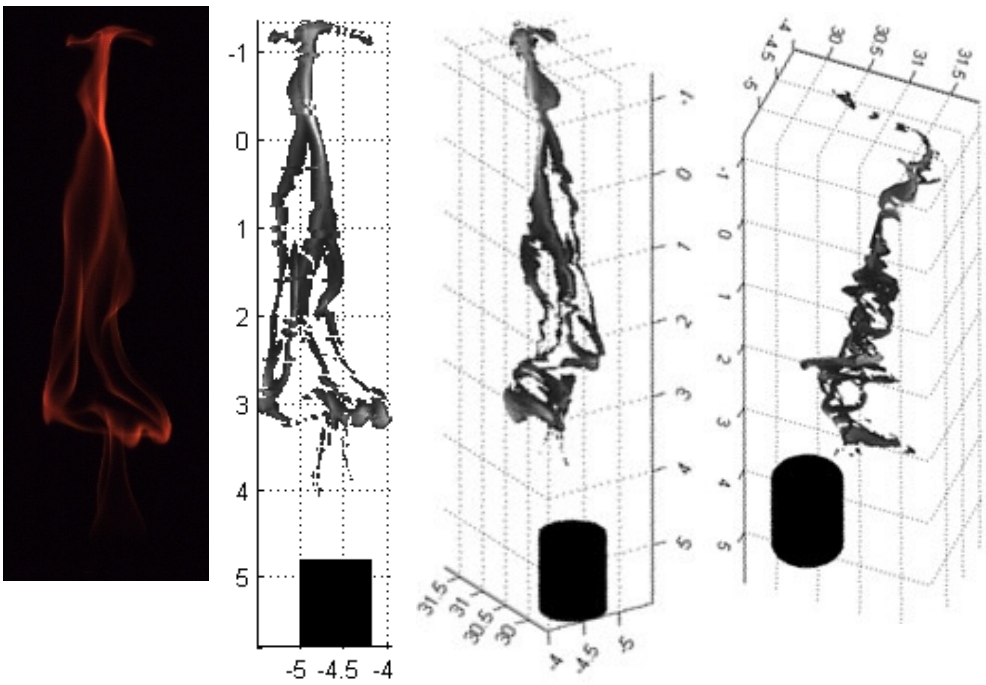

(c)

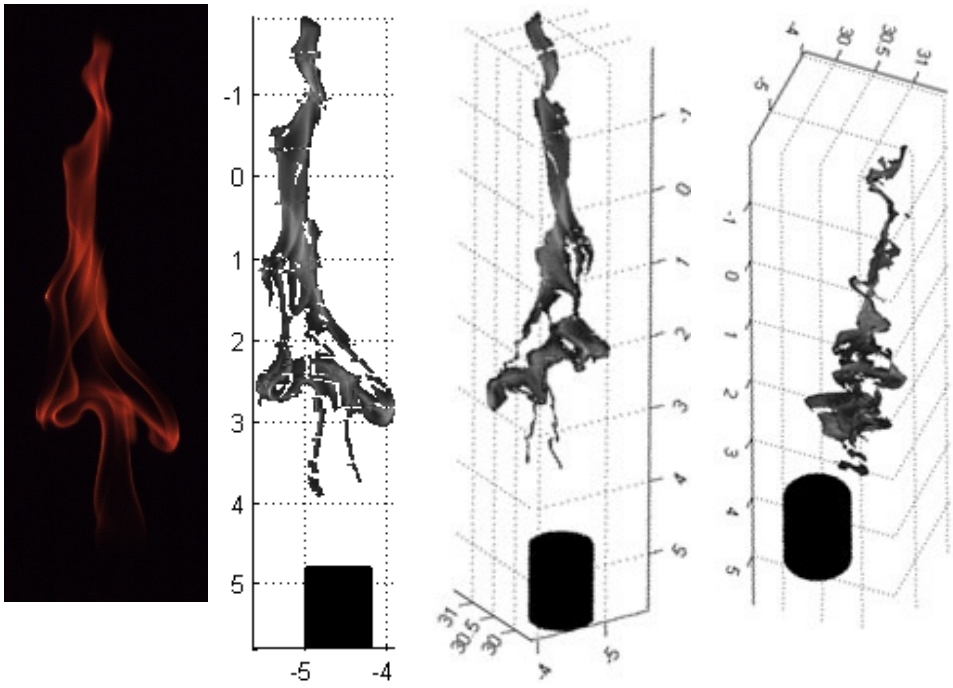

(d)

Figure 8-12 Reconstructed 3D flame structure at different view angles of Case 2 at phase angle (a) 0; (b) 90; (c) 180; (d) 270 degree

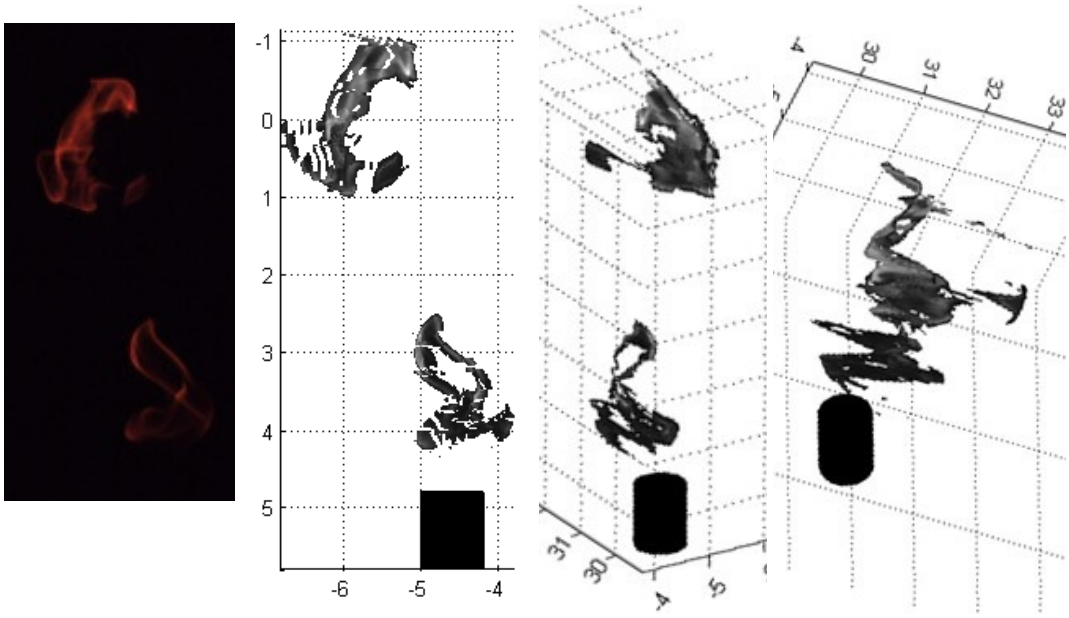

(a)

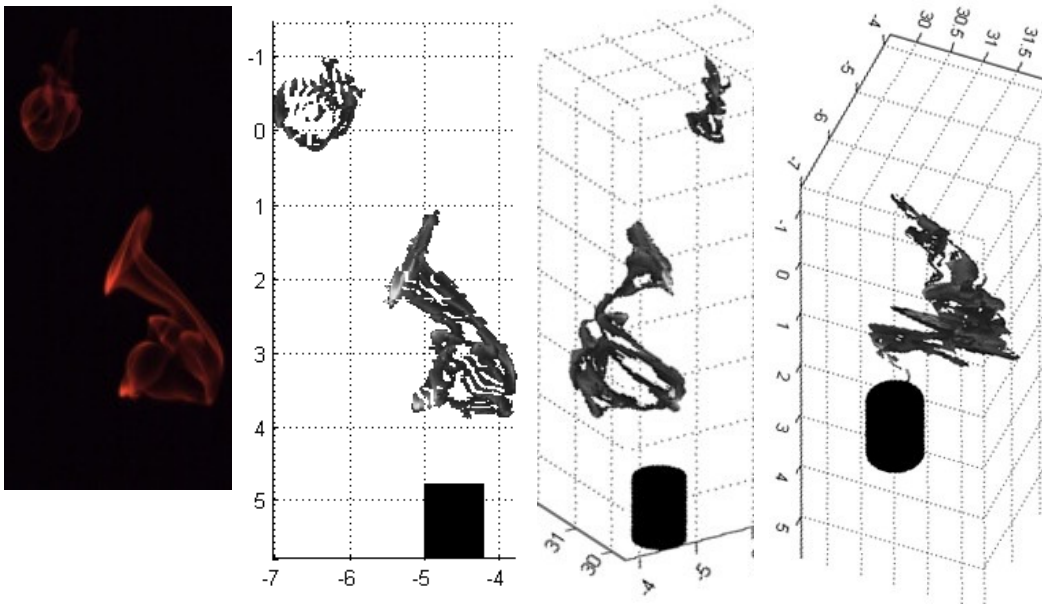

(b)

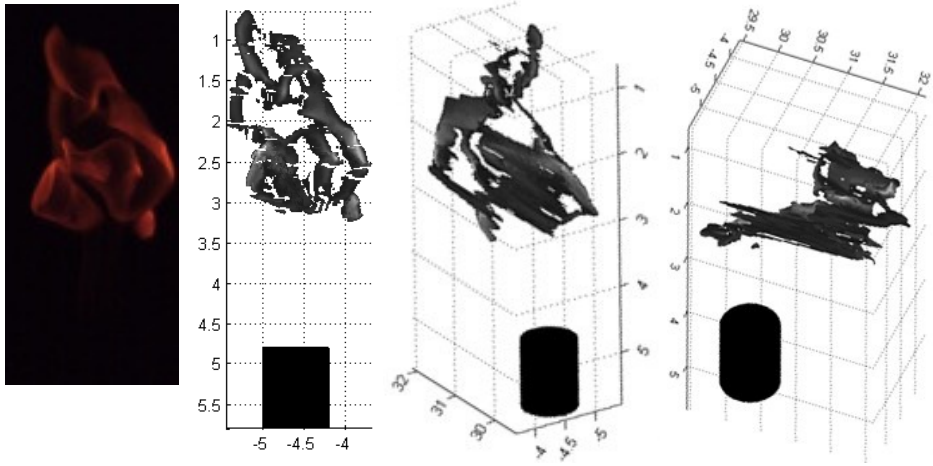

(c)

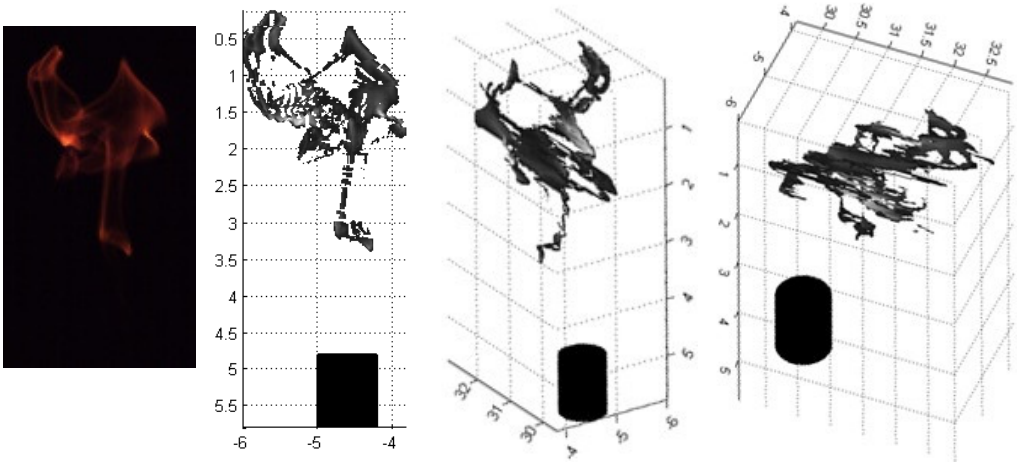

(d)

Figure 8-13 Reconstructed 3D flame structure at different view angles of Case 3 at phase angle (a) 0; (b) 90; (c) 180; (d) 270 degree

8.4.1.3 Other frequency division phenomena

Besides half frequency, $f_e/3$, $2f_e/3$, $f_e/4$ and $f_e/5$ components have been reported by Timothy C. Williams et al (Timothy C. Williams, 2007) in acoustic excited diffusion methane flames. Their study also pointed out that the air co-flow is also able to stimulate the frequency division under acoustic excitations. These higher subharmonic resonances are expected based on the nonlinear theory though further investigations are required in pinpointing the exact physical mechanisms in forming these modes. It is believed that the time-resolved vortex visualisation can be of great help in understanding the phenomena.

8.4.2 Frequency doubling

The doubling frequency harmonics are also common nonlinear response to external excitation signals. In this case, the components of $y_n(t) = Y_n \sin(n\omega t + \phi_n)$, (n=2, 3, 4, …) may exist during the signal coupling. In this study, no dominant doubling frequency is found among the test cases. However, the doubling frequency harmonics are found in Figure 8-4 (d) and (e). In Figure 8-4 (d), there are peaks at 16 Hz, 24 Hz, 32 Hz and 40 Hz, which are 2, 3, 4 and 5 times of the dominant frequency 8 Hz. In Figure 8-4 (e), the doubling harmonics at 8 Hz, 12 Hz, 16 Hz, 24 Hz, etc., can be observed. The doubling frequency may be caused by the vortex division phenomena in the combustion process. Since no vortex division happened to the large toroidal vortex, it is not able to find a dominant doubling frequency in this study. However, there are many other small vortices forming and breaking accompany with the evolution of the large toroidal vortex, which causes the doubling harmonics in the frequency spectra.

8.4.3 The phenomenon of sub frequency peaks at $f_e \pm f_m$ and $2f_e \pm f_m$

In the coupling of two signals $x_1(t) = X_1 \sin(\omega_1 t)$ and $x_2(t) = X_2 \sin(\omega_2 t)$, a component $k \sin(\omega_1 t)\sin(\omega_2 t)$ may appear at nonlinear response, where k is an arbitrary parameter. Then it can be decomposed into harmonic using elementary trigonometry as follows: $k \sin(\omega_1 t)\sin(\omega_2 t) = k(\cos([\omega_1 - \omega_2]t) - \cos([\omega_1 + \omega_2]t))/2$. Thus, the sum and difference of the two coupled frequencies may show up in the frequency spectrum.

It was found that when the acoustic frequency is increased to greater than 21 Hz, no stable half excitation frequency flame could be observed. The flame is oscillating at a frequency around the natural flickering frequency. The frequency obtained from PMT signal is similar when the excitation frequency is in the range of 21 Hz to 100 Hz. Case 4 is a typical case with the acoustic excitation frequency f_e at 50 Hz and is selected for further analysis. The PMT and acoustic signals in Case 4 are illustrated in Figure 8-3 (d) and a dominant peak frequency of 7.8 Hz is found from PMT signals in Figure 8-4 (d).

Referring to both the direct and schlieren image sequences shown in Figure 8-5 (d) and Figure 8-7 (d), the flame shape and the evolution of the large toroidal vortices in Case 4 is similar to that in Case 2. Moreover, some small vortices are formed at the exit of the nozzle, as shown in Figure 8-7 (d). Being different with the outward paring vortices formed in Case 1 Figure 8-8 (g)), the small vortices caused by the excitation is circling inward, as shown in Figure 8-8 (h). The recirculation zone is formed due to the bluff body blockage effect of the acoustic perturbation at the

nozzle exit (Shanbhogue et al., 2009). Through the observation made from time-resolved schlieren images, the frequency of the small vortices is found to match the excitation frequency exactly, which indicates that the acoustic effect on the flame is maintained mainly around the upstream flame region as estimated. The main flame body and vortex evolution at downstream region is still dominated by the natural buoyancy.

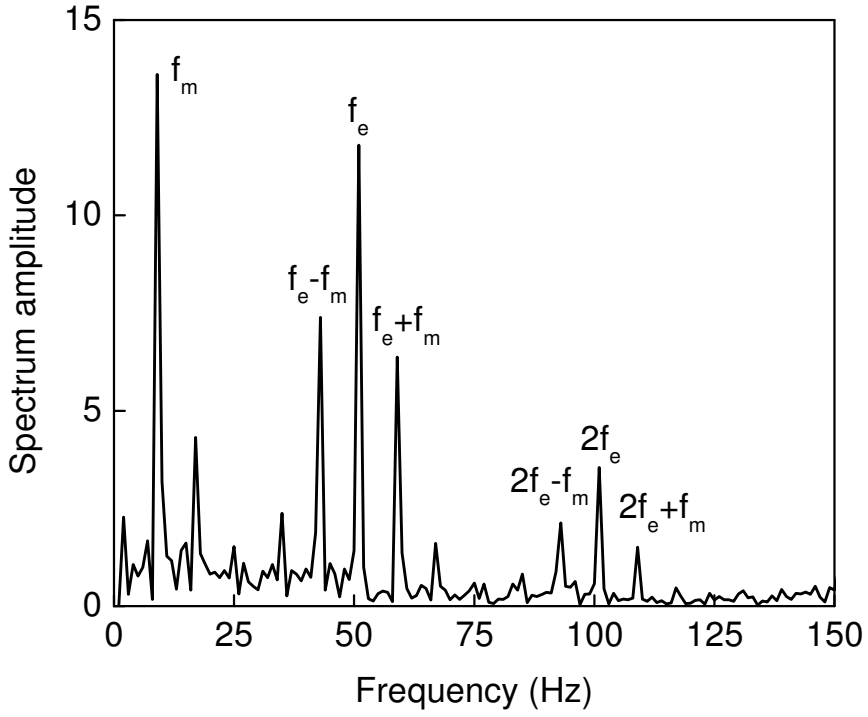

Figure 8-14 Premixed-colour filtered frequency analysis at f_e =50 Hz

Although PMT signals do not show obvious changes under acoustic excitation at high frequencies, the schlieren images indicate that the excitation effects are mainly confined to a small area. Due to the enhanced fuel/air mixing under acoustic excitation, the colour of the flame close to the nozzle exit is blue, which shows premixed flame characteristics. In order to investigate the flame dynamics in that region, the blue flames are separated from the flame images using colour processing methodology (Huang HW, 2008, Huang HW, 2011). A FFT algorithm is then

applied to the colour filtered image data, and the frequency spectra are plotted to illustrate the oscillation trends of the blue part (Huang HW, 2010). An example of the premixed-colour filtered frequency spectrum is illustrated in Figure 8-14. It can be observed from the figure that besides the peak at flame flickering frequency f_m, the excitation frequency f_e is also observable. It is worthy to mention that sub peaks of f_e-f_m and f_e+f_m are observed on the left and right side of f_e. When the acoustic excitation frequency is in the range of 21 Hz to 100 Hz, frequency peaks of f_m, f_e, f_e-f_m, f_e+f_m are observable. Particularly in Case 4, a doubling frequency $2f_e$ and the sum and difference frequency of $2f_e$-f_m and $2f_e$+f_m could also be observed. Such characteristics have not been reported in previous studies on acoustically modulated buoyant diffusion flames. When buoyancy induced vortices and acoustically driven vortices exist in the same region, the interactions of these vortices are unavoidable. The much slower buoyancy induced vortices can either help to accelerate or decelerated the faster acoustically driven vortices depending on the rotational directions of the two type vortices are in phase or not. As demonstrated in Figures 6d and 6h, the counter rotating acoustic driven vortex pairs are clearly observable. Therefore, there is the possibility of forming the plus or minus frequency modes. The blue flame colour is also an indication of strong local fuel air mixing prior to combustion, which implies the possibility of stronger interactions of the acoustically driven vortices with the buoyancy induced vortices, resulting in variations at local equivalence ratio and chemicale rates as suggested by other researchers (Saito et al., 1998, Rocha et al., 2008).

8.4.4 The effect of sound intensity on flame frequency spectrum

When there are two signals $X_1\cos(\omega_1 t - k_1)$ and $X_2\cos(\omega_2 t - k_2)$ in the system, there will be two peaks in the frequency spectrum f_1 and f_2 at different amplitudes X_1 and X_2. If the amplitude of one signal (X_2) is increased, the corresponding amplitude of the signal in the frequency spectrum should also increased.

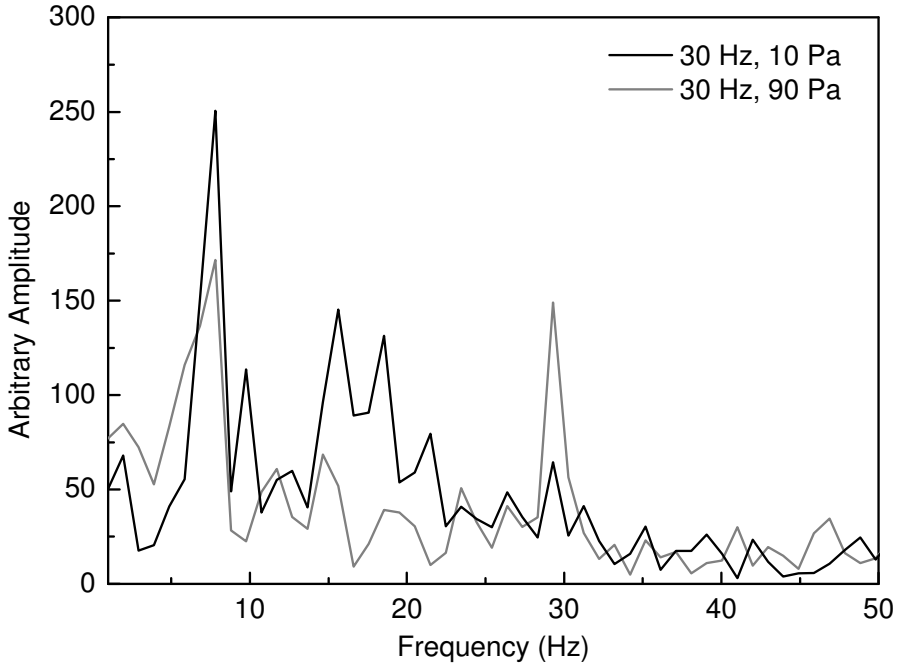

Figure 8-15 PMT signal frequency analysis at different excitation amplitudes at f_e=30 Hz

In the excitation frequency range from 21 Hz to 100 Hz, the PMT signal frequency spectrum also shows variations with the increase of the excitation amplitudes. Cases 5 and 6 are two cases with the same acoustic excitation frequency of f_e=30 Hz but at a sound intensity of 10 Pa and 90 Pa respectively. The PMT and acoustic signals of the two cases are shown in Figure 8-3 (e) and (f). The PMT signals show that the

flame oscillation of Case 5 seems still dominated by buoyancy, similar with Case 4. However, in Case 6, where the acoustic excitation intensity is increased from 10 Pa to 90 Pa, the flame fluctuation frequency almost matches the acoustic excitation frequency. The frequency spectra of Cases 5 and 6 are presented in Figure 8-15. At both frequency spectra, the peaks at 7.8 Hz and 30 Hz could be observed. The slightly peak deviation from 30 Hz may be caused by the interaction between buoyancy and acoustic excitation. It is worth noting that the peak at 30 Hz is much stronger in Case 6 than that in Case 5, which is as high as the peak at 7.8 Hz. By observing the high speed schlieren images, it is found that the excitation generated vortices in Cases 5 and 6 at a frequency of 30 Hz and form counter rotating vortex pairs as shown in Figure 8-8 (h). However, the vortex diameter D in Case 6 is much bigger than that of Case 5. The stronger sound intensity has increased the size of acoustically driven vortices and formed much stronger amplitude at 30 Hz in the frequency spectrum.

8.5 Conclusions

In this chapter, the nonlinear response of acoustic modulated methane diffusion flame frequencies were investigated using high-speed direct/schlieren imaging and digital image processing techniques. The acoustic excitation results in changes in the observed flame oscillation frequency and vortex evolutions in accordance to the varying frequency and amplitude of the excitation signals. It is found that the flame response shows a variety of expected nonlinear properties at different external excitation frequencies and amplitudes. Four types of nonlinear responses are observed and analysed in this study. Firstly, at low excitation frequencies (6 Hz-20

Hz), a vortex merging phenomenon is observed to be responsible for the flame oscillating at half the excitation frequency, which is a common nonlinear phenomenon of frequency division. Secondly, the vortices breaking down during the combustion process may cause the doubling frequency harmonics in the frequency spectra. Thirdly, in high frequency cases, typical sub peaks which are equal to the sum and difference of the excitation harmonics and the natural flickering frequency are observed in the nozzle region due to the interactions of the buoyancy induced vortices and acoustically driven vortices. Finally, the excitation frequency peak amplitude is increased at stronger excitation perturbations, which is due to increased acoustic excitation affected area through bigger size vortices generation.

The investigation has demonstrated that the coupling between the thermal buoyancy and acoustic excitation in the upstream flame region is complex and shows typical nonlinear responses. On the one hand, the fuel/air mixing and combustion process is influenced by the acoustic wave. On the other hand, the coupling between the buoyancy and the excitation induces the vortex evolution change and thus affects the flame frequency consequently. The observed nonlinear frequency modes can all be explained by the nonlinear theory. The physical mechanisms in forming these nonlinear frequency modes have been attempted.

Chapter 9 Summary and Future Work

One of the main objectives of this study was to develop an innovative 3D diagnostics by combining two widely used techniques: stereo and schlieren/shadowgraph. In addition, several issues related to combustion and fluids have been investigated by applying a combination of optical methods. In this chapter, the contributions of this research are summarised together with suggestions for future work.

9.1 Summary on contributions

- An innovative stereoscopic schlieren/shadowgraph apparatus has been established successfully. The technique has enabled the digital 3D schlieren/shadowgraph for the first time. Its ability to obtain 3D dimension/structures based on density variation is unique because this setup enables the successful digital 3D reconstruction of shadowgraph for the first time. The technique overcomes the deficiency of the early attempts (Hett, 1951, Veret, 1952), which are not real 3D by nature and very complex in

optical setup. This is achieved by changing the test section from the typical cross section of the two parallel beams formed by the two pair parabolic mirrors to the cross section of the two converging beams towards the cameras. As a result, the connection between stereo and schlieren/shadowgraph has been established successfully. Based on the projective geometry, the calibration and 3D reconstruction can be achieved digitally. After extensive searching and testing, a high precision steel grid manufactured by acid etching is chosen as a target for camera calibration. The standard deviation error of the camera calibration is only about 2%, which is quite accurate for further application. The point, curve and surface 3D reconstructions are tested on different models. With the application of high speed cameras, the unique technique has been applied successfully to study the bubble bursting dynamics and the reconstruction of hot gas jet formed by spark initiation. The stereoscopic schlieren/shadowgraph technique has shown great potential in combustion and fluid research.

- The electrical spark characteristics have been investigated by using high speed imaging techniques including direct imaging, shadowgraph, stereo and stereoscopic shadowgraph. The spark induced shockwave and hot gas propagation has been captured by high speed schlieren images. The hot gas structures and visible spark kernel movements have been found to be strongly affected by an introduced air flow. The visible metal bits eroded at each spark show different 3D velocity vectors distribution from case to case, while their effects on the ignition process still need to be further investigated. The 3D geometry of the hot gas introduced by spark has been reconstructed for the

first time using high speed stereoscopic shadowgraph technique. The fundamental study on the spark characteristics can provide valuable information for the future study of ignition and combustion process in a real combustor.

- The non-lifted methane air co-flow diffusion flames have been investigated systematically using high speed schlieren and PIV techniques. The multi optical methods reveal clearly how the flame and vortex interaction under different flow conditions. The co-flow air is observed to push the IPTV height beyond the visible flame height and thus suppress the flame flickering completely. The vortex shedding frequency observed from the schlieren images are in good agreement with the result obtained from a photomultiplier. The quantitative evaluation of flame and vortex structures is valuable for further understanding of flame and hot gas characteristics.

- The acoustically-excited diffusion flame behaviours were investigated using high speed schlieren and stereo techniques. The flame response shows a variance of nonlinear properties at different external excitation frequencies and amplitudes. The nonlinear theory is introduced to explain the flame response to the external excitations. Several nonlinear modes have been observed, some of which have never been reported before in combustion community. The 3D flame structures of typical cases are reconstructed to visualise the real flame shapes. The vortex evolutions are visualised by high speed schlielren images, which are found to be responsible for the variance of flame dynamics.

9.2 Future work

9.2.1 Improvement of the programs

There are many aspects of the programs which may be improved further, such as using correlation technique to match colour pixels rather than gray pixels. More feature extraction and matching techniques could be adopted to broaden the area of the stereo techniques. Also there are many multi view techniques that can be applied to make the reconstruction more reliable. Although 3D flame structure and 3D hot gas geometry have been reconstructed in this study, more quantitative analysis is possible by exploring the 3D coordinates.

9.2.2 Industrial application of stereo imaging technique

In practical industrial applications, the combustion chamber may be large in size and the flame is turbulent and more complicated than that of the lab-based burners. Most laser-based diagnostics are difficult to apply in practical burners. The stereo imaging technique only requires an optical window, which is advantageous for easy application.

9.2.3 Application of stereoscopic shadowgraph technique

Since the stereoscopic shadowgraph technique proposed in this study is developed on the basis of conventional schlieren system, thus the application of the new method is as wide as conventional schlieren and shadowgraph. Several main potential applications are outlined as follows:

- 3D flame vortex investigation

Conventional schlieren and shadowgraph has been applied widely in combustion research, for the sharp density variance during the combustion process. However, few techniques are able to resolve the 3D structures of the flame vortex. Most particle seeding diagnostics are effective in planar investigation of the vortex structure but fail to tackle the global 3D geometry. The newly developed high speed stereoscopic shadowgraph technique is believed to have great potential in studying 3D flame vortex evolutions. For example, there is few report on 3D vortex structure of flickering flame. The visible flame structures under acoustic excitation has been investigated in Chapter 8. However, the 3D vortex evolution is not explored yet. An initial study on hydrogen impinging flame shows that the vortices are more complicated than flickering flame, which is also valuable research work worthy of 3D investigation.

- Ignition process

  The flow field at the initial stage of an ignition process is three dimensional and complex, especially for turbulent flames. Thus coventional 2D techniques are not sufficient to resolve the real flame propagation process. The 3D visualisation of the flow field is of significant importance, both in lab apparatus an in industrial applications.

- Particle tracing in multi phase flows

  The study on bubble bursting in Chapter 5 indicates that the stereoscopic shadowgraph technique is effective at particle tracing in multi phase flows. The technique then can also be applied in similar phenomena, such as droplet trajectory tracing, spray structure reconstruction and solid particle tracing. The

curve reconstruction ability makes it also feasible to trace meaningful curve features in fluids.

- Application in wind tunnel experiments

  Schlieren is a standard technique in wind tunnel experiments to visualise the shockwaves. With the stereoscopic schlieren/shadowgraph method, it is then able to advance the visualisation from 2D to 3D. More complicated models especially with irregular structures could be studied more effectively.

9.2.4 Stereo IR technique

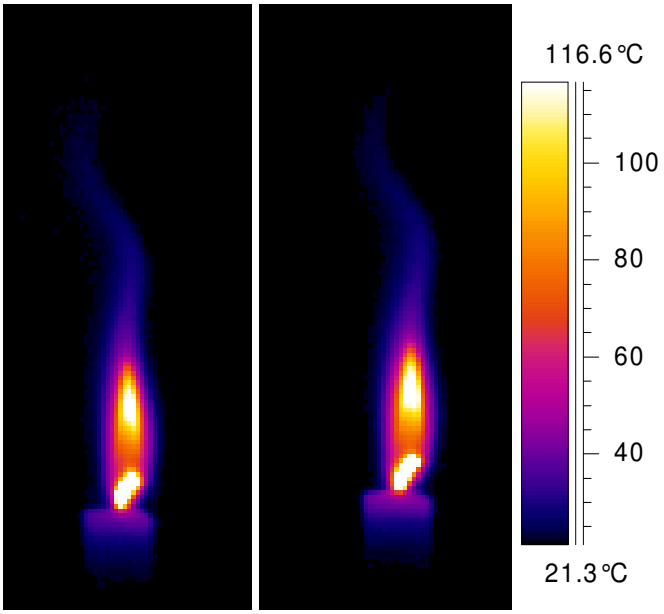

Figure 9-1 A pair of stereo IR images of candle flame

Another promising approach for 3D visualisation technique is to combine IR (infrared) imaging and stereo imaging together. IR imaging is a widely used diagostic tool to investigate the temperature field. The stereo adapter introduced in Chapter 3 is tried to be attached to the front lens of an IR camera (FLIR SC3000). A pair of stereo IR images are presented in Figure 9-1. It can be seen that two IR images could be obtained through the stereo adapter, which shows the possibility to

establish a stereo IR system. Since the images formed on the screen also based on the pinhole camera model, with a particular calibration board, the camera calibration and 3D reconstruction could be conducted based on the algorithm introduced in Chapter 3. Thus the stereo technique and IR technique can be combined to enable 3D surface temprature exploration.

References

ADELSON E, A. P. (1990) Ordinal characteristics of transparency. *AAAI-90 Workshop on Qualitative Vision, Boston, MA*.

AHMED, S. F., BALACHANDRAN, R., MARCHIONE, T. & MASTORAKOS, E. (2007) Spark ignition of turbulent nonpremixed bluff-body flames. *Combustion and Flame,* 151**,** 366-385.

AHMED, S. F. & MASTORAKOS, E. (2006) Spark ignition of lifted turbulent jet flames. *Combustion and Flame,* 146**,** 215-231.

ALBERS, B. W. & AGRAWAL, A. K. (1999) Schlieren analysis of an oscillating gas-jet diffusion flame. *Combustion and Flame,* 119**,** 84-94.

ALVAREZ-HERRERA, C., MORENO-HERNANDEZ, D., BARRIENTOS-GARCIA, B. & GUERRERO-VIRAMONTES, J. A. (2009) Temperature measurement of air convection using a Schlieren system. *Optics and Laser Technology,* 41**,** 233-240.

ANGENENT, L. T., KELLEY, S. T., ST. AMAND, A., PACE, N. R. & HERNANDEZ, M. T. (2005) Molecular identification of potential pathogens in water and air of a hospital therapy pool. *Proceedings of the National Academy of Sciences of the United States of America,* 102**,** 4860-4865.

ATCHESON, B., IHRKE, I., HEIDRICH, W., TEVS, A., BRADLEY, D., MAGNOR, M. & SEIDEL, H. P. (2008) Time-resolved 3D capture of non-stationary gas flows. *ACM Transactions on Graphics,* 27.

B. LYOT, M. F. (1948) Observation des defaut de poli et homogeneite au stereoscope par la method du contraste de phase. *Revue d' Optique,* 27**,** 397-398.

BALACHANDRAN, R., AYOOLA, B. O., KAMINSKI, C. F., DOWLING, A. P. & MASTORAKOS, E. (2005) Experimental investigation of the nonlinear response of turbulent premixed flames to imposed inlet velocity oscillations. *Combustion and Flame,* 143**,** 37-55.

BASCLE, B. & DERICHE, R. (1993) Stereo matching, reconstruction and refinement of 3D curves using deformable contours. *1993 IEEE 4th International Conference on Computer Vision.*

BAYLE, P., BAYLE, M. & FORN, G. (1985) Blast wave propagation in glow to spark transition in air. *Journal of Physics D: Applied Physics,* 18**,** 2417-2432.

BHEEMUL, H. C., LU, G. & YAN, Y. (2001) Three-dimensional Monitoring and Characterisation of Gaseous Flames Using Digital Imaging Techniques. *International conference on Energy, Automation and Information Technology*.

BIRD, J. C., DE RUITER, R., COURBIN, L. & STONE, H. A. (2010) Daughter bubble cascades produced by folding of ruptured thin films. *Nature,* 465**,** 759-762.

BOUREHLA, A. & BAILLOT, F. (1998) Appearance and stability of a laminar conical premixed flame subjected to an acoustic perturbation. *Combustion and Flame,* 114**,** 303-318.

BOUYER, R. A. C., C. (1956) Application of Phase Contrast to the study of High-speed Gas Jets. *Proceedings of the 3rd International Congress on High-speed Photography*.

BRADLEY, D., SHEPPARD, C. G. W., SUARDJAJA, I. M. & WOOLLEY, R. (2004) Fundamentals of high-energy spark ignition with lasers. *Combustion and Flame,* 138**,** 55-77.

BUCKMASTER, J. & PETERS, N. (1988) The infinite candle and its stability-A paradigm for flickering diffusion flames. *Symposium (International) on Combustion,* 21**,** 1829-1836.

BURTON, R. A. (1949) A Modified Schlieren Apparatus for Large Areas of Field. *J. Opt. Soc. Am.,* 39**,** 907-907.

CABRA, R., CHEN, J. Y., DIBBLE, R. W., KARPETIS, A. N. & BARLOW, R. S. (2005) Lifted methane-air jet flames in a vitiated coflow. *Combustion and Flame,* 143**,** 491-506.

CHAMBERLIN, D. S. & ROSE, A. (1948) The flicker of luminous flames. *Proceedings of the Symposium on Combustion,* 1-2**,** 27-32.

CHANG, N. W., SHY, S. S., YANG, S. I. & YANG, T. S. (2001) Spatially resolved flamelet statistics for reaction rate modeling using premixed methane-air flames in a near-homogeneous turbulence. *Combustion and Flame,* 127**,** 1880-1894.

CHEN, L. D., SEABA, J. P., ROQUEMORE, W. M. & GOSS, L. P. (1989) Buoyant diffusion flames. *Symposium (International) on Combustion,* 22**,** 677-684.

CHEW, T. C., BRITTER, R. E. & BRAY, K. N. C. (1989) Laser tomography of turbulent premixed bunsen flames. *Combustion and Flame,* 75**,** 165-174.

CONNELLY, B. C., LONG, M. B., SMOOKE, M. D., HALL, R. J. & COLKET, M. B. (2009) Computational and experimental investigation of the interaction of soot and NO in coflow diffusion flames. *Proceedings of the Combustion Institute.*

CULICK, F. E. C. (1960) Comments on a ruptured soap film *J Appl Phys* 31**,** 1128-1129.

DALZIEL, S. B., HUGHES, G. O. & SUTHERLAND, B. R. (2000) Whole-field density measurements by 'synthetic schlieren'. *Experiments in Fluids,* 28**,** 322-335.

DAMARE, D. & BAILLOT, F. (2001) The role of secondary instabilities in the stabilization of a nonpremixed lifted jet flame. *Physics of Fluids,* 13**,** 2662-2670.

DARABKHANI, H. G. & ZHANG, Y. (2010) Methane Diffusion Flame Dynamics at Elevated Pressures. *Combustion Science and Technology,* 182**,** 231-251.

DAVIDHAZY, A. (2011) *[image available online]* http://people.rit.edu/andpph/photofile-b/shadowgraph-bullet-1.jpg. *Access on 07 Apr 2011.*

DAVIS, M. R. & RERKSHANANDANA, P. (1993) Schlieren measurement of turbulent structure in a diffusion flame. *Experimental Thermal and Fluid Science,* 6**,** 402-416.

DE GENNES, P. G., BROCHARD-WYART, F. & QUERE, D (2004) Capillarity and Wetting Phenomena. *Springer*.

EGGERS, J. & VILLERMAUX, E. (2008) Physics of liquid jets. *Reports on Progress in Physics,* 71**,** 036601:1-79.

FARHAT, S. A., NG, W. B. & ZHANG, Y. (2005) Chemiluminescent emission measurement of a diffusion flame jet in a loudspeaker induced standing wave. *Fuel,* 84**,** 1760-1767.

FARHAT SA, N. W., ZHANG Y. (2005) Chemiluminescent emission measurement of a diffusion flame jet in a loudspeaker induced standing wave. *Fuel,* 84**,** 1760-1767.

FAUGERAS, O. (1993) Three-dimensional computer vision: a geometric viewpoint. . *MIT Press, Cambridge*.

FIEDLER, H., NOTTMEYER, K., WEGENER, P. P. & RAGHU, S. (1985) Schlieren photography of water flow. *Experiments in Fluids,* 3**,** 145-151.

G. SCHMIDT, A. T. (1986) Non-Linear Vibrations. *Cambridge Univ. Press, Cambridge, Chap. 1.*

GARG, S. & CATTAFESTA III, L. N. (2001) Quantitative schlieren measurements of coherent structures in a cavity shear layer. *Experiments in Fluids,* 30**,** 123-134.

GATTI, M., PALLESCHI, V., SALVETTI, A., SINGH, D. P. & VASELLI, M. (1988) Spherical shock waves in laser produced plasmas in gas. *Optics Communications,* 69**,** 141-146.

GAYHART, E. L. A. P., R. (1949) Interference Phenomenon in the Schlieren System. *J. Opt. Soc. Amer. ,* 39**,** 546-549.

GEORGE PAPADOPOULOS, R. A. B., WILLIAM M. PITTS (2001) Particle Image Velocimetry in Flickering Methane/Air Diffusion Flames. *Second Joint Meeting of the United States Sections of the Combustion Institute***,** 1-16.

GILABERT, G., LU, G. & YAN, Y. (2007) Three-dimensional tomographic reconstruction of the luminosity distribution of a combustion flame. *IEEE Transactions on Instrumentation and Measurement,* 56**,** 1300-1306.

GOLLAHALLI, S. R., SAVAS, HUANG, R. F. & RODRIQUEZ AZARA, J. L. (1988) Structure of attached and lifted gas jet flames in hysteresis region. *Symposium (International) on Combustion,* 21**,** 1463-1471.

GORD, J. R., TYLER, C., GRINSTEAD JR, K. D., FIECHTNER, G. J., COCHRAN, M. J. & FRUS, J. R. (1999) Imaging strategies for the study of gas turbine spark ignition. *Proceedings of SPIE - The International Society for Optical Engineering.*

GOSHTASBY, A. & GRUVER, W. A. (1993) Design of a single-lens stereo camera system. *Pattern Recognition,* 26**,** 923-937.

H.C.HOTTEL, W. R. H. (1949) Diffusion in laminar flame jets. *Symposium on Combustion and Flame, and Explosion Phenomena,* 3**,** 254-266.

HAMINS, A., YANG, J. C. & KASHIWAGI, T. (1992) An experimental investigation of the pulsation frequency of flames. *Symposium (International) on Combustion,* 24**,** 1695-1702.

HETT, J. H. (1951) A high-speed stereoscopic schlieren System. *J. Soc. Motion Picture Engineers,* 56**,** 214-218.

HUANG HW, Z. Y. (2008) Flame colour characterization in the visible and infrared spectrum using a digital camera and image processing. *Meas. Sci. Tech.,* 19**,** 085406.

HUANG HW, Z. Y. (2010) Dynamic application of digital image and colour processing in characterizing flame radiation features. *Measurement Science and Technology,* 21.

HUANG HW, Z. Y. (2011) Digital colour image processing based measurement of premixed CH4 + air and C2H4 + air flame chemiluminescence. *Fuel,* 90**,** 48-53.

HULT, J., MEIER, U., MEIER, W., HARVEY, A. & KAMINSKI, C. F. (2005) Experimental analysis of local flame extinction in a turbulent jet diffusion flame by high repetition 2-D laser techniques and multi-scalar measurements. *Proceedings of the Combustion Institute,* 30**,** 701.

INABA, M., HARA, T. & INOUE, H. (1993) Stereo viewer based on a single camera with view-control mechanisms. *1993 International Conference on Intelligent Robots and Systems.*

ISENBERG, C. (1978) The Science of Soap films and Soap Bubbles. *Dover Publications*.

KATTA, V. R. & ROQUEMORE, W. M. (1993) Role of inner and outer structures in transitional jet diffusion flame. *Combustion and Flame,* 92**,** 274-282.

KIM, K. T., LEE, J. G., QUAY, B. D. & SANTAVICCA, D. A. (2010) Response of partially premixed flames to acoustic velocity and equivalence ratio perturbations. *Combustion and Flame,* 157**,** 1731-1744.

KIMURA, I. (1965) Stability of laminar-jet flames. *Symposium (International) on Combustion,* 10**,** 1295-1300.

KLEINE, H. & GRONIG, H. (1991) Color schlieren methods in shock wave research. *Shock Waves,* 1**,** 51-63.

LAURENTINI, A. (1994) Visual hull concept for silhouette-based image understanding. *IEEE Transactions on Pattern Analysis and Machine Intelligence,* 16**,** 150-162.

LEE, D. & KWEON, I. (2000) A novel stereo camera system by a biprism. *IEEE Transactions on Robotics and Automation,* 16**,** 528-541.

LEE, D. H., KWEON, I. S. & CIPOLLA, R. (1999) Biprism-stereo camera system. *Proceedings of the IEEE Computer Society Conference on Computer Vision and Pattern Recognition,* 1**,** 82-87.

LEFEBVRE, A. H. (1999) Gas Turbine Combustion *2nd ed. Taylor & Francis***,** 167-190.

LI, J. & ZHANG, Y. (2010) Fuel mixing effect on the flickering of jet diffusion flames. *Proceedings of the Institution of Mechanical Engineers, Part C: Journal of Mechanical Engineering Science*.

LINGENS, A., NEEMANN, K., MEYER, J. & SCHREIBER, M. (1996) Instability of diffusion flames. *Symposium (International) on Combustion,* 26**,** 1053-1061.

LIU, F., THOMSON, K. A., GUO, H. & SMALLWOOD, G. J. (2004) Numerical and experimental study of an axisymmetric coflow laminar methane-air diffusion flame at pressures from 5 to 40 atmospheres. *International Symposium on Combustion, Abstracts of Works-in-Progress Posters.*

MACINTYRE, F. (1972) Flow patterns in breaking bubbles. *Journal of Geophysical Research,* 77**,** 5211–5228.

MENG, H., ESTEVADEORDAL, J., GOGINENI, S., GOSS, L. & ROGUEMORE, W. M. (1998) Holographic flow visualization as a tool for studying three-dimensional coherent structures and instabilities. *Journal of Visualization,* 1**,** 133-144.

MENG, H., PAN, G., PU, Y. & WOODWARD, S. H. (2004) Holographic particle image velocimetry: From film to digital recording. *Measurement Science and Technology,* 15**,** 673-685.

MORTENSEN, T. (1950) An improved schlieren appratus employing multiple slit-gratings. *Rev Sci Instrum,* 21**,** 3-6.

NENE, S. A. & NAYAR, S. K. (1998) Stereo with mirrors. *Proceedings of the IEEE International Conference on Computer Vision.*

NG, W. B. & ZHANG, Y. (2003a) Stereoscopic imaging and reconstruction of the 3D geometry of flame surfaces. *Experiments in Fluids,* 34**,** 484-493.

NG, W. B. & ZHANG, Y. (2003b) Stereoscopic imaging and reconstruction of the 3D geometry of flame surfaces. *Experiments in Fluids,* 34**,** 484.

NISHIMOTO, Y. & SHIRAI, Y. (1987) Feature-based stereo model using small disparities.

OHIWA, N., ISHINO, Y., IKARI, M. & YAMAGUCHI, S. (2002) Simultaneous and two-directional high speed schlieren observation of effects of ignition points on vortex-flame interaction. *Proceedings of SPIE - The International Society for Optical Engineering.*

PAPAS, P. (2002) Normal and microgravity experiment of oscillating lifted flames in coflow: Comments. *Proceedings of the Combustion Institute.* 1 ed.

PEACOCK T. AND WEIDMAN, P. (2005) The effect of rotation on conical wave beams in a stratified fluid. *Experiments in Fluids,* 39**,** 32-37.

PETERS, F., KURALT, T. & SCHNIDERJAN, J. (1992) Visualization of water flow by sugar schlieren. *Experiments in Fluids,* 12**,** 351-352.

PHUOC, T. X. (2005) An experimental and numerical study of laser-induced spark in air. *Optics and Lasers in Engineering,* 43**,** 113-129.

PRASAD, A. K. (2000) Stereoscopic particle image velocimetry. *Experiments in Fluids,* 29**,** 103-116.

PU, Y. & MENG, H. (2005) Four-dimensional dynamic flow measurement by holographic particle image velocimetry. *Applied Optics,* 44**,** 7697-7708.

RAFFEL, M., RICHARD, H. & MEIER, G. E. A. (2000) On the applicability of background oriented optical tomography for large scale aerodynamic investigations. *Experiments in Fluids,* 28**,** 477-481.

RAFFEL M., W. C., WERELEY S., KOMPENHANS J. (2007) Partical Image Velocimetry: a practical guide. *Springer-Verlag Berlin Heidelberg, 2nd Edition***,** 3-8.

REEVES, M. & LAWSON, N. J. (2004) Evaluation and correction of perspective errors in endoscopic PIV. *Experiments in Fluids,* 36**,** 701.

RICHARD SZELISKI, P. G. (1999) Stereo Matching with Transparency and Matting. *Int. J. Comput. Vision,* 32**,** 32.

RM (2011) Bunsen burner [image available online]. *http://www.talktalk.co.uk/reference/encyclopaedia/hutchinson/m0033660.html. Access on 29 May 2011.*

ROBERT, L. & FAUGERAS, O. D. (1991) Curve-based stereo: Figural continuity and curvature.

ROCHA, A. M. A., CARVALHO JR, J. A. & LACAVA, P. T. (2008) Gas concentration and temperature in acoustically excited Delft turbulent jet flames. *Fuel,* 87**,** 3433-3444.

SAITO, M., SATO, M. & NISHIMURA, A. (1998) Soot suppression by acoustic oscillated combustion. *Fuel,* 77**,** 973-978.

SAKAI, S. (1990) Visualisation of internal gravity waves by Moire method. *Kashika-Joho,* 10**,** 65-68.

SATO, H., AMAGAI, K. & ARAI, M. (2000) Diffusion flames and their flickering motions related with Froude numbers under various gravity levels. *Combustion and Flame,* 123**,** 107-118.

SAUDERS, M. J. A. S., A. G. (1956) Phase Contrast Observations of Flames. *J. Appl. Phys. Soc. Amer. ,* 27.

SCHARDIN, H. (1942) Schlierenverfahren und Ihre Anwendungen. *Ergebnisse der exakten Naturwissenschaften,* 20.

SETTLES, G. S. (1985) Colour-coding schlieren techniques for the optical study of heat and fluid flow. *International Journal of Heat and Fluid Flow,* 6**,** 3-15.

SETTLES, G. S. (2002) Schlieren and Shadowgraph Techniques.

SHANBHOGUE, S. J., HUSAIN, S. & LIEUWEN, T. (2009) Lean blowoff of bluff body stabilized flames: Scaling and dynamics. *Progress in Energy and Combustion Science,* 35**,** 98-120.

SHU, Z., AGGARWAL, S. K., KATTA, V. R. & PURI, I. K. (1997) Flame-vortex dynamics in an inverse partially premixed combustor: The Froude number effects. *Combustion and Flame,* 111**,** 276-295.

SPIGLANIN, T. A., MCILROY, A., FOURNIER, E. W., COHEN, R. B. & SYAGE, J. A. (1995) Time-resolved imaging of flame kernels: Laser spark ignition of H2/O2/Ar mixtures. *Combustion and Flame,* 102**,** 310-328.

STOCKER, D. P. S., J.C.; CHEN, L. D. (1993) Preliminary Observations of the Effect of Microgravity on a Pulsed Jet Diffusion Flame. *Fall Meeting of the Western States Sec., The Combustion Inst. Paper 93-065.*

STROZZI, C., SOTTON, J., MURA, A. & BELLENOUE, M. (2008) Experimental and numerical study of the influence of temperature heterogeneities on self-ignition process of methane-air mixtures in a rapid compression machine. *Combustion Science and Technology,* 180**,** 1829-1857.

SUTHERLAND BR, D. S., HUGHES GO, LINDEN PF (1999) Visualisationand measurement of internal waves by "synthetic

schlieren". Part I: Vertically oscillating cylinder. *J Fluid Mech,* 290**,** 93-126.

SZELISKI, R., AVIDAN, S. & ANANDAN, P. (2000) Layer extraction from multiple images containing reflections and transparency. *Proceedings of the IEEE Computer Society Conference on Computer Vision and Pattern Recognition.* Hilton Head Island, SC, USA, IEEE.

TANAHASHI, M., MURAKAMI, S., CHOI, G.-M., FUKUCHI, Y. & MIYAUCHI, T. (2004) Simultaneous CH-OH PLIF and stereoscopic PIV measurements of turbulent premixed flames *International Symposium on Combustion*.

TAYLOR, G. I. (1959) The dynamics of thin sheets of fluid III. Disintegration of fluid sheets. *Proc R Soc London Ser A* 253**,** 313.

TEOH, W. & ZHANG, X. (1984) An inexpensive stereoscopic vision system for robots. *Robotics and Automation. Proceedings. 1984 IEEE International Conference on.*

TERRY, S. D. & LYONS, K. M. (2006) Turbulent lifted flames in the hysteresis regime and the effects of coflow. *Journal of Energy Resources Technology, Transactions of the ASME,* 128**,** 319-324.

THUILLARD, M. (2002) A new flame detector using the latest research on flames and fuzzy-wavelet algorithms. *Fire Safety Journal,* 37**,** 371-380.

TIMOTHY C. WILLIAMS, C. R. S., ROBER W. SCHEFER, PASCALE DESGROUX (2007) The response of buoyant laminar diffusion flames to low-frequency forcing. *Combustion and Flame,* 151**,** 676-684.

TOONG, T. Y., RICHARD F, S., JOHN M, S. & GRIFFIN Y, A. (1965) Mechanisms of combustion instability. *Symposium (International) on Combustion,* 10**,** 1301-1313.

VAN VLIET, E., VAN BERGEN, S. M., DERKSEN, J. J., PORTELA, L. M. & VAN DEN AKKER, H. E. A. (2004) Time-resolved, 3D, laser-induced fluorescence measurements of fine-structure passive scalar mixing in a tubular reactor. *Experiments in Fluids,* 37**,** 1-21.

VENKATAKRISHNAN, L. (2005) Density measurements in an axisymmetric underexpanded jet by background-oriented schlieren technique. *AIAA Journal,* 43**,** 1574-1579.

VERET, C. (1952) La strioscopie stereoscopique *La Recherche Aeronautique,* NO.29**,** 3-7.

WANG, R. (2009) Digital Stereo Imaging and Reconstruction of Flame Dynamics and Structure. *Manchester University. PhD thesis*.

WARNATZ J., M. U., DIBBLE R.W. (2006) Combustion: physical and chemical fundamentals,modelling and simulation, experiments, pollutant formation. *Springer-Verlag Berlin Heidelberg, 4th Edition***,** 1-8.

WATERFALL, R. C., HE, R., WOLANSKI, P. & GUT, Z. (2001) Flame visualizations using electrical capacitance tomography (ECT). *Proceedings of SPIE - The International Society for Optical Engineering.*

WOODCOCK, A. H., KIENTZLER, C. F., ARONS, A. B. & BLANCHARD, D. C. (1953) Giant condensation nuclei from bursting bubbles. *Nature,* 172**,** 1144-1145.

WU, J. (1981) Evidence of sea spray produced by bursting bubbles. *Science,* 212**,** 324-326.

XIAO, Y. J. & LI, Y. F. (2005) Optimized stereo reconstruction of free-form space curves based on a nonuniform rational B-spline model. *Journal of the Optical Society of America A: Optics and Image Science, and Vision,* 22**,** 1746-1762.

YANG, W. J. (1989) Handbook of Flow Visualization. *Hemisphere Publishing Corporation*.

ZHANG, Z. (1997) A new multistage approach to motion and structure estimation: From essential parameters to Euclidean motion via fundamental matrix. *J. Opt. Soc. Am. A* 14.

ZHANG, Z. (2000) A flexible new technique for camera calibration. *IEEE Transactions on Pattern Analysis and Machine Intelligence,* 22**,** 1330-1334.